Effect of Grain Size Distribution and Nb Addition on the Recrystallisation Avrami exponent of Fe- 30Ni Model Alloy

By

Mo Ji

A thesis submitted in partial fulfilment of the requirements for the degree of

Doctor of Philosophy in Engineering

University of Warwick,
Warwick Manufacturing Group, August 2018

Contents

Acknowledgements

I would like to acknowledge the University of Warwick, EPSRC and Tata Steel to give me the opportunity and the support to undertake this research. Also, I would like to express my gratitude to my supervisors Prof. Claire Davis, Dr. Martin Strangwood and Dr. Carl Slater for the countless times of corrections and discussions about the project. Additionally, I am very much thankful to my industrial supervisor Dr. Sally Parker for the industrial support and insight. Thank you for the support on my project.

Thank you and recognition must also be given to:

Dr. Richard Beanland, Dr. Geoff West, Prof. Barbara Shollock, Steve York and Steve Hindmarsh for the training of TEM and FIB. It has been a privilege to have your guidance.

To Dr. Vit Janik and Dr. Daniela Proprentner for the support of EBSD and In-Situ EBSD. I really appreciate your technical support and your precious knowledge.

To the University of Warwick technical support staff, thank you for the technical support.

And finally,

Thank you all for the encouragement, advice and support.

Declaration

This thesis is presented in accordance with the regulations for the degree of Doctorate of Philosophy. It has been written and complied by myself and has not been submitted anywhere else. The work in this thesis has been undertaken by me except where otherwise stated.

Signed: Date:

Abstract

Recrystallisation is an important process for grain size control in steel, which is affected by the material grain size, alloy content, temperature, strain and strain rate. A crucial parameter for recrystallisation prediction is known as the Avrami exponent as this affects the recrystallisation rate. The Avrami exponent is independent of strain and strain rate, providing that the recrystallisation mechanism remains the same, but is affected by microstructure. In this thesis an austenitic Fe-30 Ni model alloy, with and without Nb addition, has been used to investigate the role of grain size distribution and Nb addition (through solute drag and strain induced precipitation) on the recrystallisation Avrami exponent.

As-rolled Fe-30Ni with/without 0.044 wt.% Nb alloy was provided which was homogenised at 1150 °C for 4 hours to remove Nb segregation and the deformation bands present. To determine the influence of grain size distribution on recrystallisation Avrami exponent, two different grain size distributions, one with a mode grain size of 160µm and wider distribution and one with a mode grain size of 100µm and narrower distribution were generated by heat treatment. Both cold and hot deformation (to a range of strains from 0.2 to 0.45 and temperatures from 850 – 950 °C) have been used to examine the effect of grain size distribution. The cold deformation and annealing tests allowed the in-situ and ex-situ observation of recrystallisation nucleation and growth mechanism, also provided a more uniform macroscopic deformation. Hot deformation tests were used to validate the proposed recrystallisation Avrami exponent prediction model for a wider range of conditions.

The hot and cold deformed microstructures were examined, and similar microband containing structures were observed, although the stored energy varied for the different deformation modes for the same applied strain, this was due to different amounts of recovery occurring (during reheating to the annealing temperature for cold deformed at annealed samples and during deformation (dynamic recovery) for hot deformed samples). Local strain inhomogeneity after both cold and hot deformation were also observed in the deformed microstructure of Fe-30Ni, attributed to the effect of grain size variation. Both intra- and inter-granularly inhomogeneity was seen: triple points and grain boundaries had a higher local misorientation than the grain interior; and smaller grains showed higher local misorientation than coarser grains. In-situ EBSD and interrupted recrystallisation characterisation showed that impingement of recrystallised grains along the grain boundary occurs at an early stage of recrystallisation due to the non-randomly distributed nuclei, and that finer grains recrystallise faster than coarser grains due to both their higher stored energy and larger number of potential nucleation sites. A reduced Avrami exponent was seen for the larger mode/wider grain size distribution and an equation to predict the Avrami exponent from the grain size distribution is proposed.

A delay in the onset of recrystallisation due to the Nb addition was observed in the cold deformed and annealed as well as the hot deformed and annealed samples. In both conditions, the Avrami exponent was not affected by the Nb addition if the strain induced precipitates rapidly coarsened reducing the pinning force on recrystallisation. A decreased Avrami exponent was only seen for one deformation condition (cold deformation to 0.3 strain and annealing at 850°C) and this was attributed to the slow growth of the strain induced precipitates meaning that they remained fine in size and high in number density resulting in a larger pinning force reducing the recrystallisation rate.

List of Figures

List of Tables

Chapter 1 Introduction

Many metal and alloy products, such as aluminium alloys, copper and steels, are produced by thermomechanical processing, including forging, rolling and extrusion, to achieve their final shape or dimensions [1]. The deformation can be carried out either hot, above and/or below the recrystallisation stop temperature (RST), or cold, generally followed by an annealing heat treatment to promote recrystallisation. For example, high strength low alloy (HSLA) steels are produced by hot rolling with the material in an austenitic state, with complete recrystallisation occurring between each roughing pass to achieve grain refinement. Furthermore, grain elongation during the finish rolling passes (below the RST) provides multiple nucleation sites for ferrite formation from the deformed austenite grains on cooling [2]. Other materials with an austenitic (face centred cubic) structure, such as austenitic stainless steels and aluminium alloys can be cold-rolled then annealed at elevated temperatures to give recrystallisation to achieve better ductility than in the cold rolled state [3-5].

During deformation, stored energy is introduced in the form of crystalline defects, e.g. dislocations, which provide the driving force for recovery and recrystallisation. Recrystallisation occurs after the rearrangement of dislocations into sub-grains by the nucleation and growth of dislocation-free grains via boundary migration at the expense of the deformed / recovered matrix [6]. In hot deformation, recovery can occur during deformation, i.e. dynamic recovery, the rate of which depends on the deformation temperature, strain rate and applied strain. Recovery is rare during cold deformation, but may occur during reheating prior to recrystallisation, dependent on the heating rate and the annealing temperature, as well as the cold strain imparted. In both cases, the stacking fault energy (SFE) of the material will affect the ease of the recovery process [7]. As recrystallisation significantly affects the grain size and the texture, which affects the final mechanical properties, it is of great importance to understand microstructure evolution during and after deformation through the process of recrystallisation.

The most widely accepted model for recrystallisation kinetics is the Johnson- Mehl-Avrami- Kolmogorov (JMAK) model, which assumes the recrystallisation nuclei are

randomly distributed and the matrix is homogeneous i.e. uniform composition and strain and a narrow grain size distribution, as recrystallisation kinetics (following both cold and hot deformation) generally follow a sigmoidal time-behaviour, which is well fitted by JMAK-type equations. However, experimental observations suggest that recrystallisation is rather inhomogeneous in terms of both nucleation site distribution and matrix strain as well as composition and local grain size [8- 12]. For example, Figure 1-1 shows the partially recrystallised microstructure after 40% cold compression of an aluminium alloy on annealing where the recrystallising grains, numbered 1-19, were observed to be primarily nucleated along the deformation bands. Region B, on the right bottom side, has little or no recrystallisation compared to the grain boundary area and the deformation band region between regions A and B. It is known that the strain distribution within polycrystalline materials after deformation is inhomogeneous, and the grain size is almost never uniform. Currently there are limited models available to take the inhomogeneous nature of recrystallisation due to strain variation into consideration [13- 16]. There is little information on the effect of any inhomogeneity in grain size on stored energy and none on its effect on the recrystallisation behaviour [17].

A further factor to consider is precipitation as this can affect the recrystallisation process, as well as acting as a strengthening mechanism in the final product [16]. For example, HSLA microalloyed steels often contain small quantities of Nb, V and/or Ti, i.e. strong carbo-nitride formers, which can retard recrystallisation by precipitate pinning and/or solute drag [16]. Niobium is the most influential element in HSLA steels [17]. It is well known that the presence of crystalline defects (dislocations) can considerably accelerate precipitation rates, i.e. strain-induced precipitation (SIP). This is due to the dislocations acting as nucleation sites for precipitates to form, and thus, the precipitation nucleation rate, density, size and dispersion properties for SIP differ from precipitation in undeformed material. In addition, the interaction between SIP and deformation substructures inevitably affects the recrystallisation process. Therefore, prediction of precipitation evolution preceding or during recrystallisation is also of great importance. The interaction between precipitation and recrystallisation is still not well understood because of difficulties in making direct observations of the austenitic microstructure in HSLA steels, which transforms during cooling eliminating the deformation substructures [18]. Moreover, the fine size of SIP (-5nm) and the

different detecting techniques used in the literature to quantify precipitation also leads to varying results between different groups [9].

Therefore, in this project, Fe- 30%Ni with 0.044 wt. % Nb or Nb- free have been chosen to investigate the effect of grain size distribution as well as strain induced precipitation on the evolution of recrystallisation after both cold and hot deformation. The reasons to choose Fe- 30Ni moded alloy are its austenitic microstructure at both elevated and room temperature, also the comparable stacking fault energy of Nb- free model alloy to C- Mn steels in the austenitic state, according to a recent XRD line profile study, which could give an indication of the austenitic deformation/ recrystallisation microstructure in C- Mn steels [19]. The cold deformation and annealing study provided a fundamental understanding of recrystallisation nucleation and growth mechanism via both in- situ and ex- situ study, which enables the observation of the deformed microstructure and early stage of recrystallisation. The knowledge could then be applicable for recrystallisation of FCC metals in general. The hot deformation study was then to extend the knowledge gained from cold deformation, and to validate the proposed models for the microalloyed steels in the hot deformed conditions.

The effect of grain size distribution on recrystallisation kinetics has been studied for both cold and hot deformation conditions. A reason for using cold deformation in this case was to avoid the barrelling effect seen during hot deformation (for uniaxial compression in the Gleeble thermo-mechanical simulator [20]), i.e. macroscopic strain inhomogeneity, therefore the effect of local strain inhomogeneity due to grain size variation on recrystallisation kinetics could be studied. Additionally, using cold deformation allowed subsequent in-situ SEM-EBSD observation (using an SEM with heating stage) of recrystallisation evolution. Hot deformation tests have been applied to validate the knowledge gained in the cold deformation studies, also to compare the recrystallisation kinetics between the cold and hot deformation conditions. As it is possible for the amount of stored energy at the onset of recrystallisation to vary (for the same initial applied strain) due to differing amounts of recovery (e.g. occurrence of dynamic recovery during hot deformation compared to recovery during heating to the annealing temperature after cold deformation).

In terms of the strain induced precipitation study, both cold deformation and annealing tests and hot deformation have been used to examine the SIP kinetics and the influence of SIP on recrystallisation. Cold deformation has been applied for Nb containing model alloy to estabilish the same condition as the Nb free alloy, therefore the retarding effect caused by strain induced precipitation and solute drag could be studied. Hot deformation tests have also been carried out to determine the influence of initial dislocation structures also to compare the precipitation and recrystallisation kinetics to the cold deformation and annealing tests. It is worth noting that the precipitation kinetics (and hence recrystallisation kinetics) measured may not represent the HSLA steel industrial processing route and microstructure because of potential differences in the initial dislocation distribution (due to the different recovery processes that occur for cold deformation followed by annealing compared to hot deformation) and differing solubility Nb limits (due to the high Ni content in the Fe- 30Ni steel). However, useful insights into the required number density and size of SIP that affect recrystallisation can be gained. The results are also relevant to precipitation in other systems such as cold deformed and annealed austenitic steels, such as Fe-Mn-C austenitic steels [5].

The thesis is divided into the following chapters:
In chapter 2, literature review concerning models and kinetics of recrystallisation in austenite are reviewed. Additionally, the microstructure evolution during and after hot and cold deformation are discussed.

In chapter 3, reported models for, and kinetics of, precipitation of Nb (C, N) in austenite are reviewed, the effect of cold and hot deformation on the strain induced precipitation kinetics is discussed.

In chapter 4 and 5, the aims and objectives are proposed and the experimental materials and methods used to observe the recrystallisation and precipitation behaviour are outlined, respectively.

In chapter 6, the analysis of the as-rolled, as-homogenised and deformed microstructures is discussed, and the heat treatments used for the Fe-30Ni Nb-free model alloy to generate different starting grain size distributions are given. Also, the differences between the hot and cold deformed microstructures are discussed.

In chapter 7, experimental measurements of recrystallisation during isothermal holding in the Fe-30Ni Nb-free model alloy via optical, hardness and EBSD are discussed. The effects of strain, starting grain size distribution and temperature on the recrystallisation kinetics are summarised and the effect of hot and cold deformation on the recrystallisation kinetics investigated.

In chapter 8, the strain induced precipitation kinetics and the SIP size evolution at various temperatures after cold deformation to 0.3 strain are presented along with an analysis of the hot and cold deformation strain induced precipitation kinetics and the recrystallisation kinetics.

In chapter 9, conclusions and further work are given. The potential translation from the cold deformation and annealing recrystallisation kinetics to hot deformation recrystallisation kinetics is discussed.

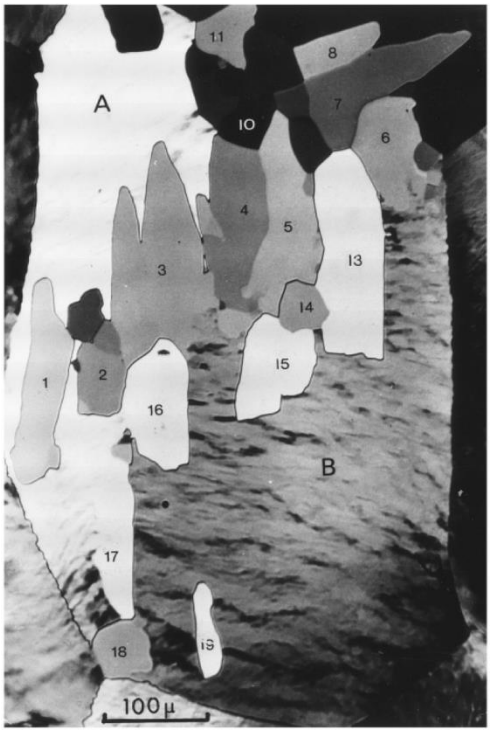

Figure 1-1 Optical micrograph of partially recrystallised grains in pure aluminium cold deformed to 40% compression then annealed. A and B are two regions in one grain with different misorientation after deformation. The numbers represent the recrystallising grains [8].

Chapter 2 Recrystallisation kinetics and models of austenite

2.1 Microstructure evolution of deformed austenite

Annealing of deformed metals is crucial to restore the ductility and refine the grain size [1]. The mechanisms for the restoration are recovery and recrystallisation. Both mechanisms can occur during and/ or after the deformation, depending on the temperature, strain and strain rate. Restoration taking place during deformation is referred to as dynamic, and that which occurs after deformation is called static.

The driving force for the restoration is the stored energy, which is induced during deformation in the form of crystalline defects, e.g. dislocations, stacking faults. At temperatures higher than the recrystallisation stop temperature (RST), recrystallisation occurs after recovery, i.e. the rearrangement of dislocations into sub-grains, by the nucleation and growth of dislocation free grains via boundary migration [6].

The definition of these two processes are listed as follows:

1) Recovery: microstructure change prior to recrystallisation that partially restores the properties. The process includes the rearrangement and annihilation of dislocations through dislocation climb and cross slip. As a result of recovery, subgrain boundaries form within the deformed matrix.

2) Recrystallisation: eliminating dislocations in large numbers simultaneously to restore the microstructure into the annealed state via high angle grain boundary migration. The process includes the nucleation and growth of recrystallised nuclei.

Since both processes are driven by stored energy, recovery and recrystallisation are competing processes. Obviously, recovery consumes the stored energy prior to recrystallisation, which decreases the driving force for recrystallisation. When recrystallisation starts, recovery will no longer be able to proceed [1] .

Figure 2-1 summarises the effect of the potential softening mechanisms on the stress level of the deformed austenite. Dynamic recovery and recrystallisation will reduce the stress level during deformation, and static recovery and recrystallisation affect the strength of the material after deformation. It can be seen that linear work hardening is

expected during deformation if there is no dynamic restoration. That is, cold deformation at room temperature, with limited dynamic recovery, is expected to result in a higher dislocation density than hot deformation at elevated temperature after same strain level if dynamic processes occur. Additionally, a higher amount of energy is required to deform the sample under cold deformation compared to hot deformation, which could also leads to a higher stored energy for the cold deformed samples deformed to the same strain level.

Controlling recrystallisation is important in generating a fine and homogeneous grain microstructure, i.e. to avoid any inhomogeneity after this process. It has been widely accepted that recrystallisation primarily nucleates at grain boundaries and is driven by the stored energy, and its reaction kinetics can be expressed as a function of nucleation and growth [1]. Nucleation is considered as the first appearance of new grains in the microstructure and growth is when the new grains replace the deformed matrix [1, 12]. Deformed microstructure and recovery are also of great importance. The amount of deformation determines the stored energy level and recovery controls the rearrangement and annihilation of dislocations, both of which affects the recrystallisation driving force and kinetics directly.

The initial grain size distribution has a significant influence on recrystallisation, as it determines the number density of recrystallisation preferential nucleation sites (grain boundaries and triple points) and influences strain inhomogeneity [1,18, 21], which means that the recrystallisation process can vary in different grains. In order to model the recrystallisation process to be able to optimise processing it is important to understand the role of grain size distributions on the recrystallisation process and to be able to predict behaviour. It is also important to understand the effect of other influences on inhomogeneity, for example macroscopic strain inhomogensity. These factors will be discussed int he following sections, along with observations on the effect of the deformed microstructure inhomogeneity on the recovery and recrystallisation driving force, nucleation, growth mechanisms and kinetics.

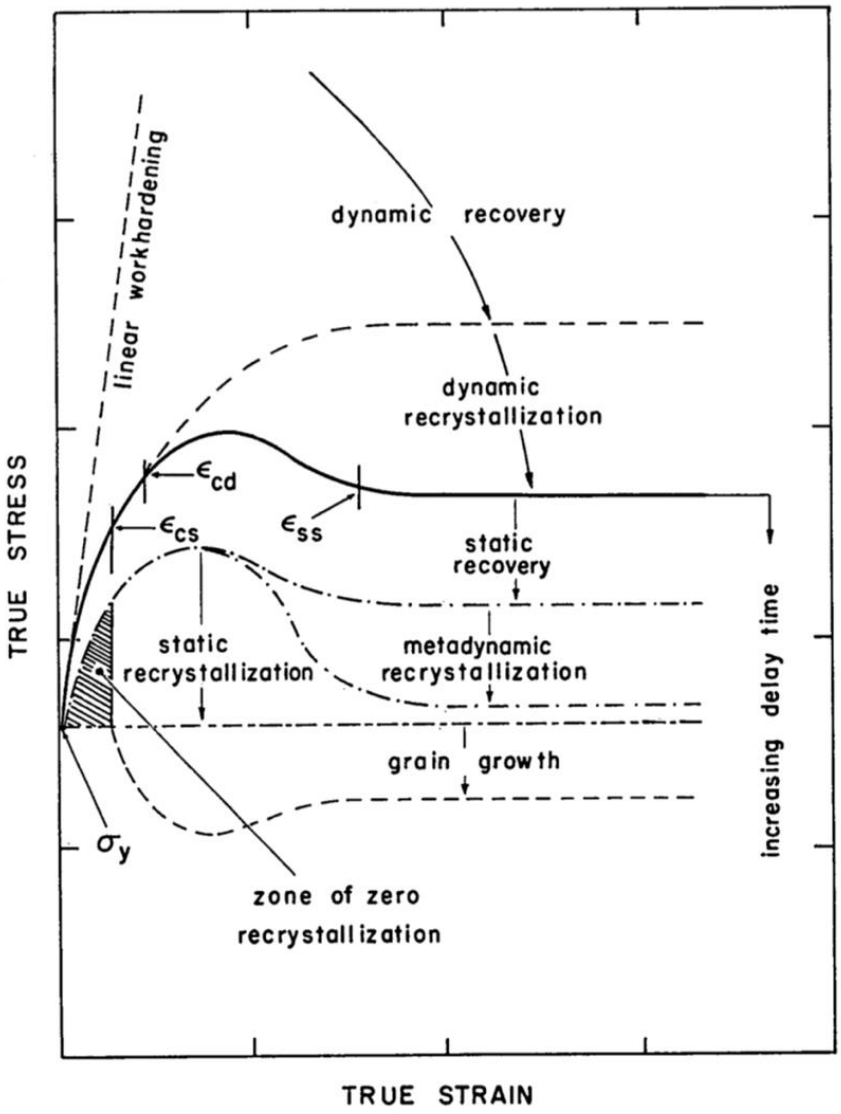

Figure 2-1Schematic diagram showing the effect of the five softening mechanisms that can happen during / after deformation on stress levels. The dashed lines above the solid line represent linear work hardening if there is no recovery occurring, also the stress level where dynamic recovery occurs during deformation. The flat dotted line is the yield strength of the undeformed material, and the broken lines below the solid line, i.e. static recovery, metadynamic recrystallisation, static recrystallisation and grain growth, represents the maximum softening achievable for each softening mechanism [22]. ε_{cs} ε_{cd} and ε_{ss} are the critical strain for static recrystallisation, dynamic recovery and steady state respectively.

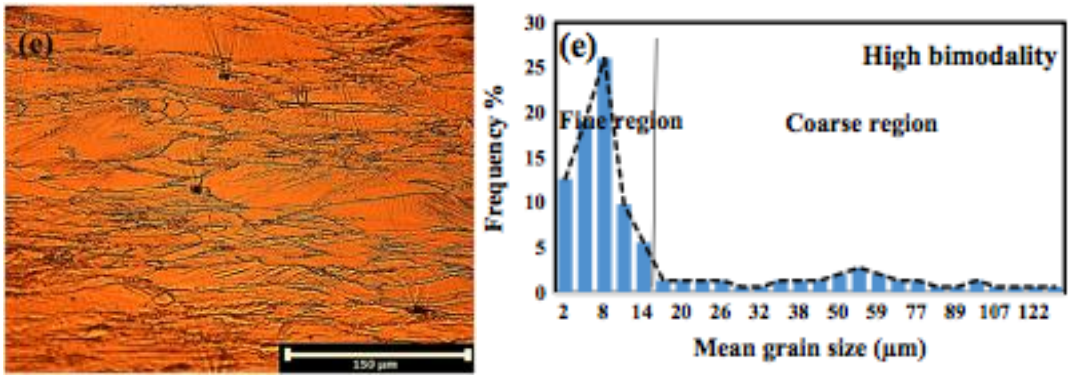

Figure 2-2 Microstructure and grain size distribution of a TWIP sample deformed at 1100 °C, 60% reduction, then air cooled showing a bimodal grain size distribution [23]

2.2 Deformed state

The study of deformed state is of great importance as it determines the amount and the distribution of the driving force for recrystallisation. The driving force for recovery and recrystallisation is the dislocations introduced into the microstructure during deformation. Thus, the morphology of the dislocation network and its spatial distribution directly determines the recrystallisation kinetics. In addition, the deformed microstructure affects the strain-induced precipitates spatial distribution significantly [24], which will be discussed in the next chapter.

2.2.1 Stored energy estimation

During deformation, the microstructure has to change to accommodate the macroscopic applied stress. Grains become elongated and the grain boundary area increases via accumulating dislocations. Dependent on the strain level, the internal deformed structures, i.e. dislocations, cell blocks, deformation bands, microbands and shear bands start to appear within the grain [25].

If no restoration occurs during deformation, the dislocation density increases with increasing strain, thus increasing the internal energy. The strain energy for a dislocation is the existence of distortion around it [26]. The strain energy of one dislocation, E_0, can be expressed by:

$$\mathrm{E}_0 = \frac{Gb^2}{4\pi}\ln\left(\frac{R}{r}\right) = \alpha G b^2 \quad \ldots 1$$

Where G is shear modulus, b is burgers vector, and α = 0.5 - 1 depending on the dislocation distribution. R is the cut off radius of a dislocation, r is the core radius.

Then, the stored energy, E, for a material with a dislocation density of $\Delta\rho$

$$E = \alpha G b^2 \Delta\rho \quad \ldots 2$$

Where $\Delta\rho$ is dislocation density. The work hardening, i.e. the increase in flow stress during deformation, is due to the increase in dislocation density, thus, the dislocation density can be estimated by a Forest Hardening type relation [27]:

$$\sigma = \sigma_0 + M\alpha G b\sqrt{\Delta\rho} \quad \ldots 3$$

Where σ_0 is initial flow stress, M is the Taylor factor, 3.1 for isotropic f.c.c. crystals, and α is a constant taken to be 0.15. Burgers vector is 2.52×10^{-10} m, and shear modulus at 900°C is 45 GPa [28].

If the deformation microstructure contains cell like microstructure and subgrains, the stored energy can also be expressed by the misorientation between subgrains and the subgrain diameter [1], which is given by,

$$E = \frac{A\theta}{d} \quad \ldots 4$$

Where A is a constant, θ is the misorientation between adjacent subgrains and d is the diameter of the subgrain. It can be seen that the stored energy increases with increasing misorientation. For 0.3 strain, the stored energy measured by multiple different authors have been reported within the range of 0.6 – 7 J/ mol for FCC materials [29, 30, 31, 32].

2.2.2.1 Effect of grain size distribution on stored energy

Strain is not homogeneous across the material or even within a grain since local lattice curvatures exist. Also, the texture of a grain leads to different deformation behaviour depending on the direction of straining relative to the grain [34]. In fact, the inhomogeneity of strain distribution is crucial for recrystallisation nucleation, and will be discussed in section 2.3.2.

The inhomogeneity of stored energy distribution has been widely observed within and among grains. Ashby has pointed out that for a polycrystalline material, each individual grain has to accommodate the shape change from the neighbouring grains during deformation, as a result, extra geometrically necessary dislocations (GND) have to form along the grain boundaries, Figure 2-3 [18].. Ashby gave an equation for estimating the GNDs.

$$\rho^G \approx \frac{\bar{\varepsilon}}{4bD} \quad \ldots 5$$

Where $\bar{\varepsilon}$ is the mean strain, b is the burgers vector, D is the grain size.

Due to the phase transformation during cooling, measurement of the effect of the austenite grain size on stored energy for HSLA steels is extremely challenging. Most studies have been carried out in austenitic steel, copper and aluminium. Cizek and Palmiere have reported that the grain boundaries and triple points have a higher distortion compared to the grain interior for Fe-30Ni and 304 stainless steel [10, 35]. At low and medium strain level, less than 0.5, it has been reported that the stored energy level increases with decreasing grain size, which is consistent with additional GNDs being required to accommodate the differential strain in neighbouring grains [36].

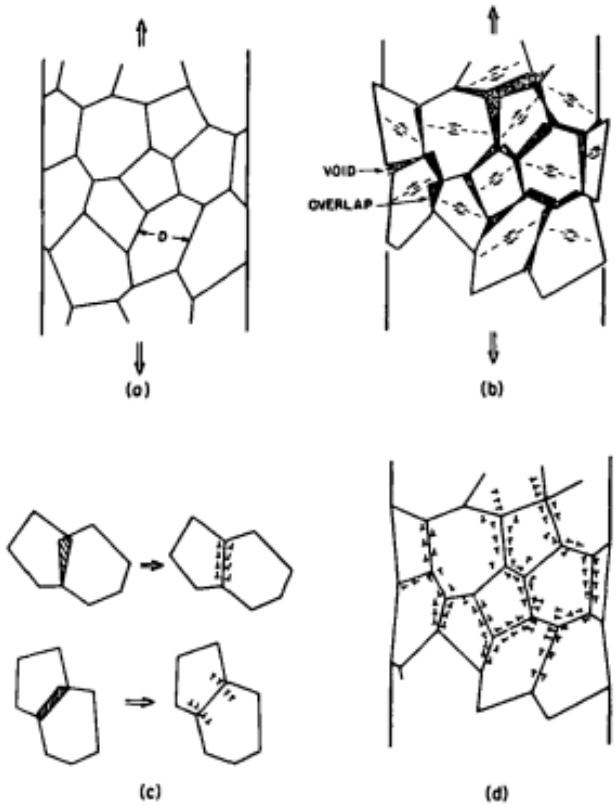

Figure 2-3 Schematic diagram of the geometrically necessary dislocations along the grain boundaries. [18] (a) onset of deformation (b) overlap and voids occur if there is no local deformation (c) geometrically necessary dislocations are introduced to accommodate the local distortion along the grain boundary (d) extra GNDs are located along the boundaries

It has been reported that the stored energy variance across the grain size range of 60 - 760 μm was between 6 - 30% in copper [37, 38, 30]. Williams reported that the stored energy increased by 0.59 MPa in copper for a grain size decrease from 300 to 30 μm. Baker gives an equation of the effect of grain size on stored energy [39].

$$\mathrm{E} = \alpha G b^2(\rho^S + \rho^G) = \frac{\alpha G b M \varepsilon}{D}\left(\frac{1}{\alpha_s + C}\right) \quad \ldots 6$$

Where α, α_s and C are materials constants, G is shear modulus, M is the Taylor factor, ε is the applied strain, D is the grain size.

2.2.2 Fe-30Ni model alloy

Fe-30Ni, as a model alloy, was originally developed to study the austenitic microstructure development during and after hot deformation, due to its fully austenitic microstructure being retained to room temperature and being representative of the high temperature austenitic structure for C-Mn steels with respect to deformation structure [10, 35, 40, 41]. The suitability of Fe-30Ni as a model alloy of C-Mn steel has been studied extenisively and summarised by Black and Abdollah-Zadeh [11, 40]. The addition of Ni above 28 wt.% leads to a stable austenite microstructure at room temperatrure. Therefore, other compositions, such as Fe- 70Ni and Fe- 50Ni, have also been developed as a model alloy. However, the addition of Ni does not only influence the stacking fault energy (SFE), but also affects the solubility of other alloying elements, such as Nb.

Nb has also been added into the Fe-30Ni alloy to study strain induced precipitation kinetics in a deformed austenite microstructure [40- 42] and its feasibility as a model alloy for precipitation studies will be discussed in chapter 3.

In this project, the application of the Fe- 30Ni as a model alloy has been extended to investigate the effect of grain size distribution on the recrystallisation behaviour after both cold and hot deformation in austenite. Due to its fully austenitic microstructure, the deformed, prior and post recrystallisation microstructure at same region could be revealed via in- situ observation. Therefore, this study is to gain the fundamental understanding of recrystallisation mechanism, and it is not necessarily to simulate the deformation and recrystallisation behaviour of C- Mn steels.

Materials with different stacking fault energy (SFE) can have different deformation mechanisms. That is, materials with high SFE tend to be deformed only by slip, whereas twinning can occur in materials with low SFE. Nickel is added to iron in the Fe-30Ni alloy to retain the austenitic microstructure to room temperature, however, the SFE changes with Ni content. The variation of SFE with different Ni content has been measured by different authors and the results are summarised in Table 2-1. Das has summarised the SFE data for austenitic steels from literature [43]. Charnock and Nutting measured the stacking fault energy for Fe-Ni alloys by measuring the frequency of occurrence of annealing twins. Schramm et al. measured the stacking

fault energy of Fe-Ni alloys with different Ni content by XRD line profile analysis, which gave a value of 160 mJ/ m^2 for Fe-30.2 Ni, 121 mJ/ m^2 for Fe-30.9 Ni, and 142 mJ/ m^2 for Fe-65.5 Ni, Figure 2-4 [19] – It can be seen from the figure that they corrected their data by changing the lattice parameter for each composition after cold deformation. Even with the adjustment the reported values from Schramm vary significantly with little change in composition at compositions around Fe-30Ni, i.e. Fe-30.2 Ni and Fe-30.9 Ni. The data quoted from Butakava for Fe- 30Ni is around 100 mJ/ m^2 and Zaefferer reported a value of 122 mJ/ m^2 for Fe- 36Ni alloy [44]. Hence, from the data reported it can be seen that a range of SFE values have been determined for Fe-30Ni, from 60 – 160 mJ/ m^2 (ignoring the low value of 35 mJ/ m^2 determined by Charnock and Nutting as optical analysis of annealing twins is not an accurate method and the more recent literature is likely to be more appropriate). The C-Mn steels stacking fault energy has been reported to be 75 mJ/ m^2 [41]. Therefore, whilst there is some scatter in the reported SFE values it appears that the SFE for Fe-30Ni is in the same range for C-Mn steels [41]. This suggests that the deformation mechanism will be the same in both steels, making Fe-30Ni an appropriate material to use to study recrystallisation mechanisms relevant for C-Mn steels.

To further consider the applicability of using Fe-30Ni as a model alloy for C-Mn steels, its flow stress behaviour and deformation microstructure under hot deformation have been considered by multiple authors. Hansen summarised that typical deformed microstructures of cells, microbands and subgrains have been observed in austenite with different SFE [25]. Fe-30Ni shows a dislocation structure consisting of tangled dislocations, cells and microbands, which is comparable to FCC metals with medium SFE (40- 100 mJ/ m^2 i.e. values similar to those reported and discussed above) [45, 46, 47]. Poths et. al [42] and Cizek [10] have claimed that the deformation microstructures and the flow stress behaviour are comparable between Fe-30Ni and microalloyed steels. Additionally, Palmiere and Black compared the flow stress behaviour between Fe-30Ni-0.09 wt. % Nb and microalloyed steel with similar Nb content. All tests were carried out under uniaxial compression with the same strain, strain rate and temperature. It was reported that there was no dynamic recrystallisation occurring within the temperature range 900-1050 °C at strain rate of 10 s^{-1} (strain 0.45), Figure 2-5. The higher flow stress observed under same strain in Fe-30Ni was attributed to the higher Ni content [40, 41]. Dynamic recrystallisation has been

observed for C-Mn steels at a strain rate lower than $2s^{-1}$, at a temperature above 900 °C, strain 0.45 [48]. Whereas Fe-30Ni showed no sign of dynamic recrystallisation with strain rate down to 0.7 s^{-1}, Figure 2-6 [45], for the same strain. These observations suggest that the high Ni content in Fe-30Ni could retard the onset of recrystallisation. Therefore, the recrystallisation kinetics, i.e. the absolute values of recrystallisation starting and finishing time, measured from Fe-30 Ni model alloy might not be directly transferrable to C- Mn steels.

Hurley and Beladi have used Ni-30Fe to investigate austenite hot deformation behaviour and microstructures as they considered its SFE to be comparable to austenite iron [49, 50]. They found that Ni-30Fe and Fe-30Ni both show comparable deformed microstructures, Figure 2-7, 2-8, which indicates that if there are differences in SFE these are not sufficient to cause differences in the deformation microstructures, which also supports the proposal that Fe-30Ni can be considered to represent HSLA microalloyed steels in terms of deformation behaviour.

Therefore, it can be seen that Fe-30Ni has been used extensively as a model alloy for austenitic iron with regard to representing the deformed microstructure and flow stress behaviour and has been studied extensively for deformation in the strain range between 0.2 – 0.45, strain rate 10 s^{-1}, and temperature range 850 – 1050 °C.

Table 2-1 Summary of literature data of stacking fault energy of Fe- 30Ni

References	Materials	SFE (mJ/ m^2)	Detecting method
[43]	Fe- 30Ni	60- 95	Literature review
[51]	Fe- 30Ni	35	Optical microscope
[19]	Fe- 30Ni	121- 160	XRD line profile analysis
[44]	Fe- 36Ni	122	TEM

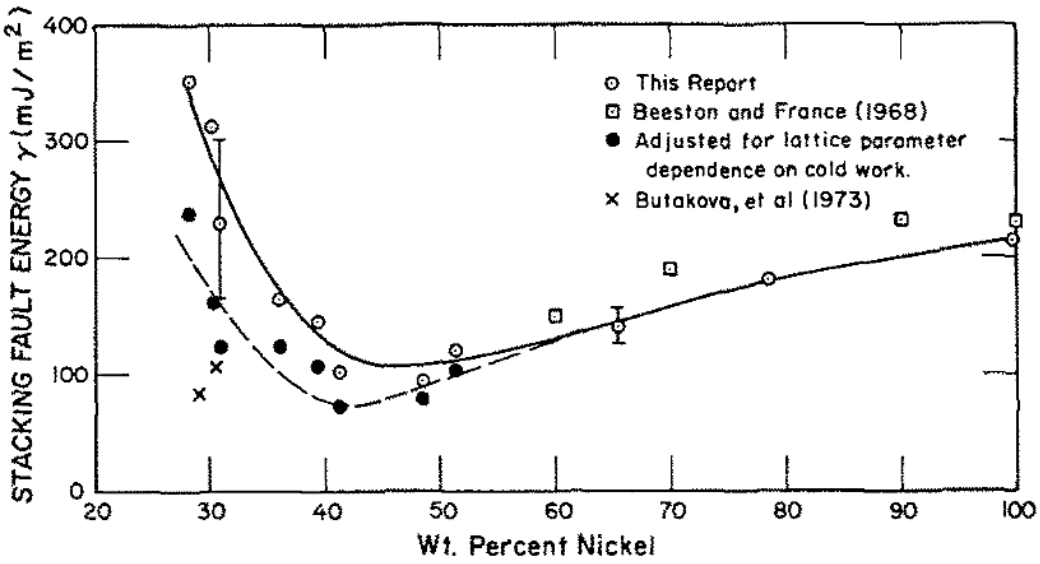

Figure 2-4 Variation of stacking fault energy across the iron-nickel system. Error bars show 95 % confidence on experimental parameters [19].

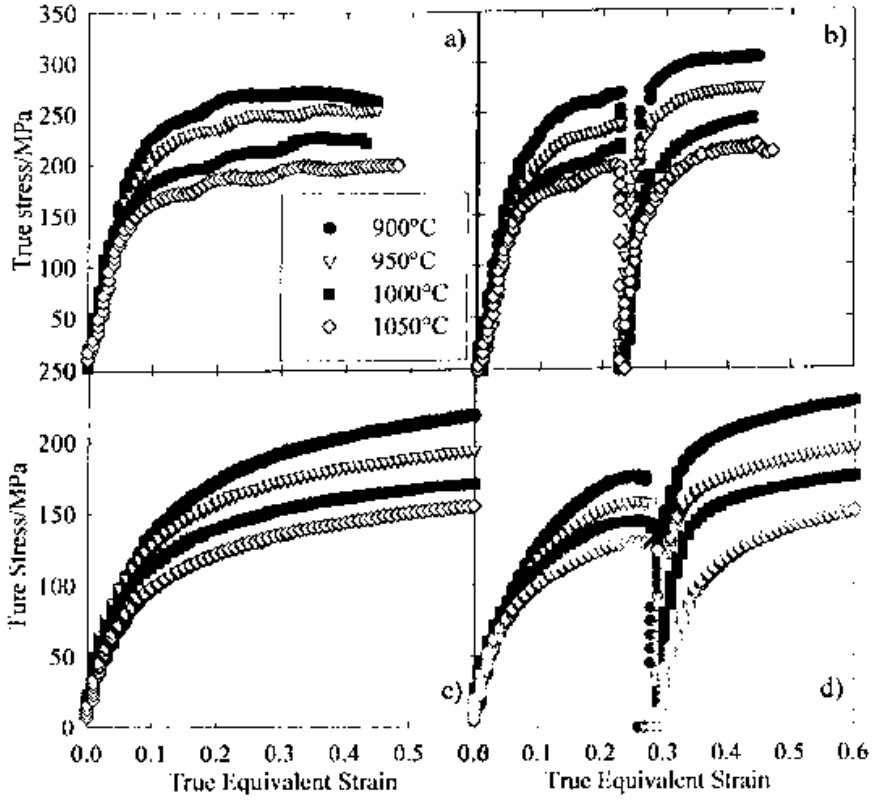

Figure 2-5 Single hit and double hit flow stress curves at various temperatures for Fe-30Ni- 0.1Nb (a)(b) and Fe-1.43Mn-0.09Nb (c)(d), deformed at a strain rate of 10/s [40].

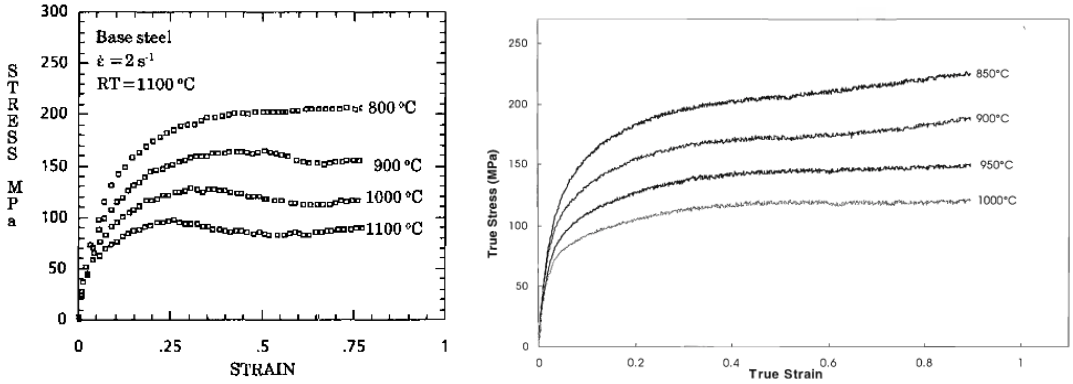

(a) (b)

Figure 2-6 Flow stress curve for (a) C-Mn steel, strain rate $2s^{-1}$ [50] and (b) Fe-30Ni, strain rate $0.7s^{-1}$ [48].

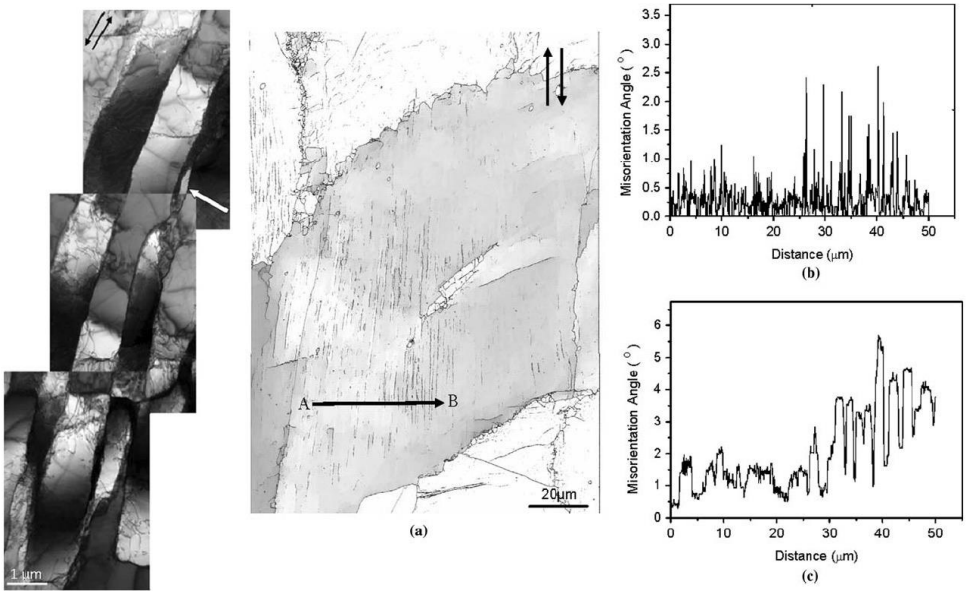

Figure 2-7 TEM and EBSD images of the deformed microstructure of Ni-30Fe at strain 0.5 at 1000°C, parallel arrows refer to the deformation direction (b), (c) represent the point to point and cumulative misorientation respectively [50]

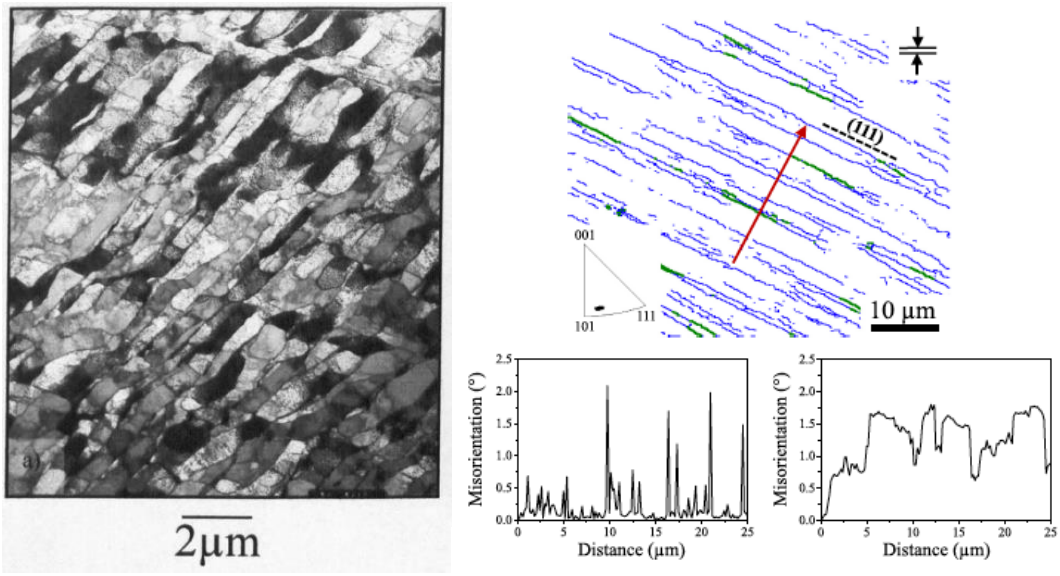

Figure 2-8 Typical deformed microstructure in Fe-30Ni. TEM work (Fe-30Ni-0.1Nb, 950 °C, 0.5 strain) [10]; and EBSD work (Fe-30Ni- 0.098Nb, 950C, 0.2 strain) [47]

2.3 Recovery

Recovery is a thermally activated process, which is driven by the stored energy. It refers to the annihilation and rearrangement of dislocations to achieve a lower energy configuration [1, 34]. During hot deformation, recovery can happen during and/or after deformation, and in materials where recovery occurs during deformation, i.e. dynamic recovery, the working hardening rate decreases, and the flow stress reaches a plateau with increasing strain, which is called steady state [8]. During the cold deformation and annealing process, recovery could occur during reheating and therefore prior to recrystallisation, and its extent will be dependent on the strain, the heating rate and annealing temperature [1].

Recovery and recrystallisation are competing processes, as the driving force for both processes is the stored energy. Recovery can occur separately after small strains, while at higher strains, the onset of recrystallisation can halt the recovery progress. Therefore, many authors have shown that recovery affects the recrystallisation kinetics as it alters the stored energy through dislocation annihilation [33, 36, 52, 53]. The microstructure evolution during recovery is shown in Figure 2-9. The tangled dislocations form cells by climb and cross-slip. Then dislocation annihilation occurs within the cell, and misorientation between cells increases, until the cell wall develops into a low angle

grain boundary, i.e. LAGB, such that the recovered microstructure consists of subgrain boundaries surrounding the nearly strain-free subgrains. The stored energy of the recovered structure after subgrain formation is still large compared to a fully-annealed state, thus subgrain growth can occur [1]. It can be seen from Figure 2-10 that the subgrain size increases with increasing annealing time, whereas it decreases with increasing in strain.

The extent of recovery is dependent on the amount of deformation, i.e. strain; strain rate; temperature; time, and more importantly, the nature of the material, i.e. its stacking fault energy (SFE). With increasing strain, the stored energy increases thus promoting recovery [8, 12]. The SFE determines the extent of dislocation dissociation, which affects dislocation climb and cross slip rate [1, 52]. The higher the SFE, the easier it is for dislocations to slip. As seen in Figure 2-11, aluminium tends to show extensive softening due to recovery, because dislocations slip easily due to the high SFE. Whereas in low stacking fault energy materials, for example copper, there is little recovery before recrystallisation, Figure 2-11 [52]. Stuwe also compared the softening fraction and recrystallisation fraction for cold deformed copper and aluminium within the temperature range of 700 - 1100 °C [54]. It can be seen from Figure 2-12 that 40 - 50 % of softening occurred prior to recrystallisation in aluminium, whereas no softening occurred for copper.

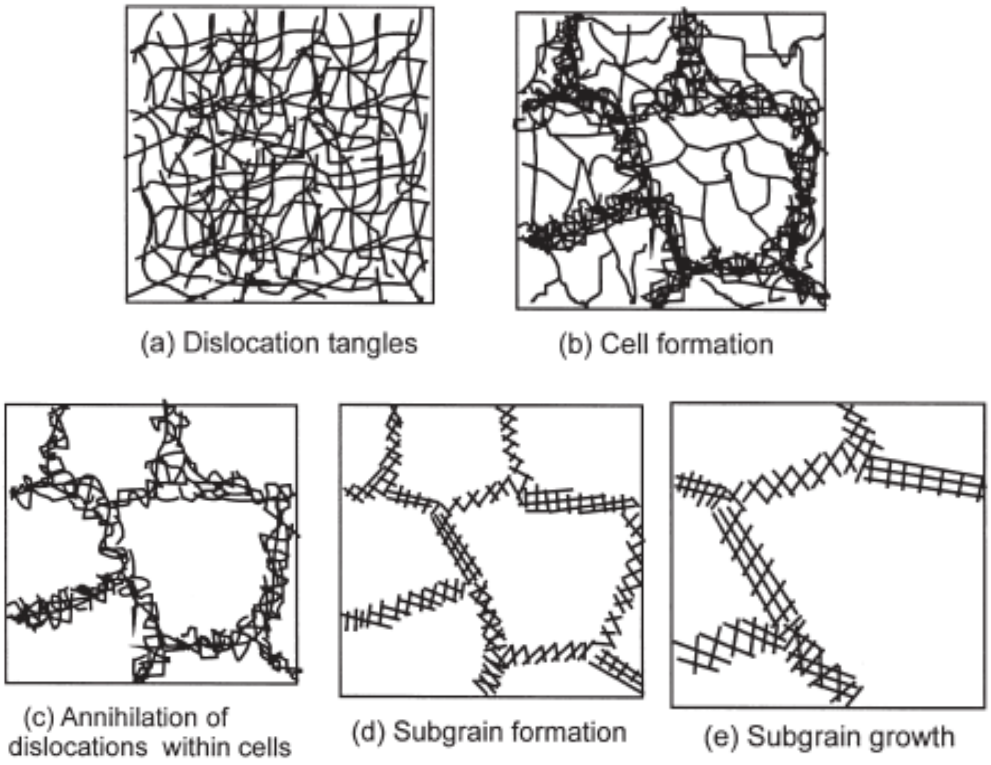

Figure 2-9 Schematic diagrams of the stages during recovery of a deformed material [1]

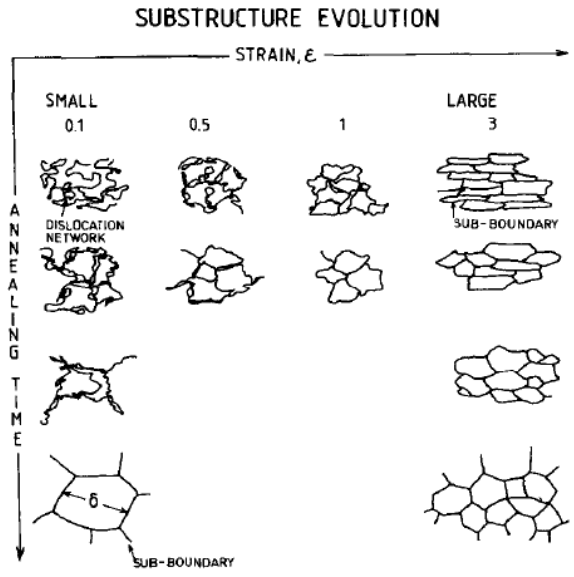

Figure 2-10 Schematic diagram of the substructure evolution by recovery with increasing strain and the annealing time [55]

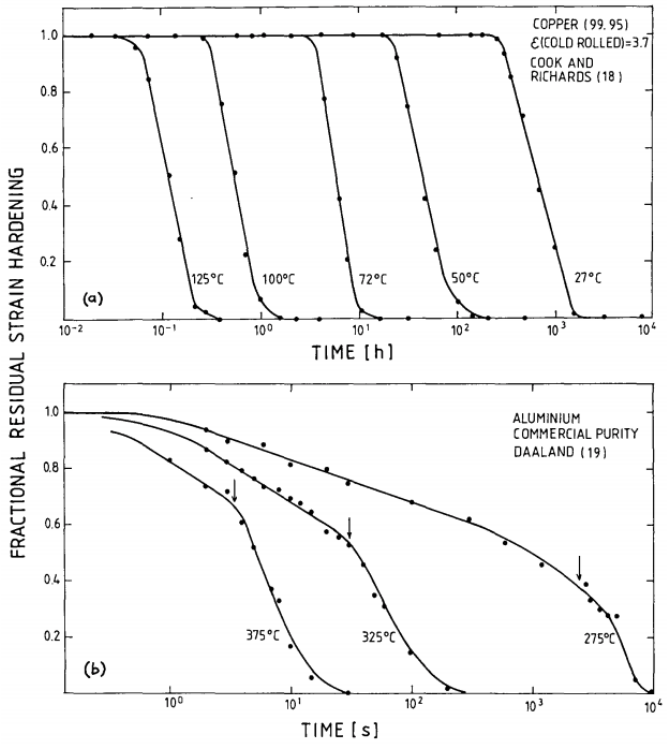

Figure 2-11 The residual strain hardening comparison during annealing for (a) cold worked copper (b) commercial purity aluminum, the arrow indicates the onset of recrystallisation [52]

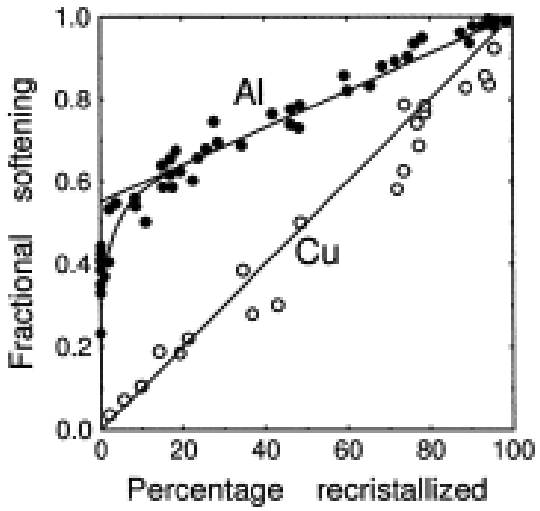

Figure 2-12 Comparison between softening fraction and recrystallisation fraction in copper and aluminium [54]

2.4 Recrystallisation

Recrystallisation is a nucleation and growth process of strain-free grains consuming the deformed / recovered microstructure via high angle boundary migration [59]. Unlike other (phase) transformations, the recrystallisation driving force is stored energy, which is independent of temperature. In addition, recrystallisation is irreversible and no phase transformation is involved [11, 40].

Recrystallisation nucleation occurs at sites of high internal energy, such as grain boundaries, twin boundaries, and deformation bands [49, 52, 56]. The microstructure at any time is divided into recrystallized or non-recrystallized regions, and growth of recrystallised grain boundaries will occur when the growing boundary bulge is stable and the misorientation angle across the interface has become high.

2.4.1 Recrystallisation driving force

The driving force for recrystallisation, F_R, is the difference in the stored energy across the moving boundary. The model was initially developed by Beck and Sperry and was subsequently advanced through Bailey and Hirsch [9, 34, 53]. In the absence of an applied stress, the driving force for grain boundary migration in a deformed matrix is the strain energy difference between deformed and non-deformed regions, and therefore a function of the difference in dislocation density between the growing grain and the deformed materials. Thus, the recrystallisation driving force is given by,

$$F_R = \frac{Gb^2\Delta\rho}{2} \qquad \ldots 1$$

Where G is the shear modulus, b is the Burgers vector, and $\Delta\rho$ is the dislocation density gradient between the recrystallised and the deformed region. As strain inhomogeneity widely exists in the deformed microstructure, therefore, the recrystallisation driving force varies across the materials accordingly [56].

2.4.2 Recrystallisation nucleation

Recrystallisation nucleation refers to the process of the formation and migration of the high angle grain boundaries in the deformed microstructure [12, 36, 52, 56]. As mentioned in section 2.1, the stored energy after 0.3 strain of any polycrystalline metals is of the magnitude of 1J/ mol, which is considerably lower than the driving force for other processes, for example solidification of copper near to 0K, i.e. 13 kJ/mol [57], and ferrite to austenite phase transformation of iron, i.e. 0.92 kJ/mol [1]. Therefore, due to the low driving force and high interfacial energy (0.5 MJ/ m^{-2}) between the recrystallised and unrecrystallised region, the nuclei size has been calculated in the region of 1 μm, i.e. 10^{10} atoms. Therefore, the classical theory for nucleation, i.e. the formation of stable nuclei generated by thermal fluctuations, is unlikely to occur during recrystallisation.

Recrystallisation nuclei form preferentially in a region with a large strain gradient due to the larger driving force. Therefore the larger the strain, the more nuclei can be formed due to the larger misorientation and more nucleation sites [34]. However, it is worth noting that a large strain gradient does not necessarily mean a high macroscopic strain. Humphrey mentioned that a single crystal of zinc could be deformed by single glide to strain of 100% without forming a recrystallisation nucleus at the annealing temperature due to the lack of a local strain gradient [1]. Hutchinson has observed heterogeneous recrystallisation nucleation in iron, Furu in aluminium, and Cizek in Fe-30Ni [10, 52, 58]. The new grains form in the localised high strained regions, and the sites of these nuclei are determined during deformation; the potential nucleation sites for recrystallisation are listed in Table 2-2. Three mechanisms have been proposed for recrystallisation nucleation (for example at the nucleation sites identified in Table 2-2) and are given in Table 2-3. Strain-induced boundary migration (SIBM) is generally accepted as the mechanism operating for rolling deformation of steels, this is due to the low reduction of each pass during rolling.

a) Subgrain rotation and coalescence

This mechanism involves rotation of the subgrains. The boundary between two subgrains can be eliminated by a relative rotation of the two subgrains. The rotation can be done through the diffusion of atoms, along the subgrain boundaries [1]. The model is thermodynamically feasible, and it has been observed in aluminium thin foils

heated in the TEM. However, Humphrey, Rios and Hassner pointed out that there is little evidence that this mechanism plays a significant role in recrystallisation nucleation of bulk materials [49, 56, 59].

b) Subgrain-boundary migration

The model mentions that a heavily localized deformed region will generate nuclei that are misoriented to the neighbouring subgrains and therefore, could grow into them, Figure 2-13 [59]. The highly deformed region evolves into a strain-free cell by dislocation rearrangement and climb, and the subgrain growth can consume the surrounding dislocations. The misorientation of the growing subgrain increases until the formation of a high angle grain boundary [56]. Due to the heterogeneous nature of deformation, the stored energy, subgrain sizes and the misorientation vary with strain level. The subgrain migration mechanism have been observed under high strains, large spread in the subgrain size distribution and preferentially in low SFE metals. Ray has observed the subgrain – boundary migration in copper at true strain of 3 [60]. The higher the level of strain, the larger is the misorientation between neighbouring subgrains [59]. Therefore, the critical radius for subgrain formation is smaller and the subgrain growth rate is higher.

c) Strain induced grain boundary migration (SIBM)

In the SIBM mechanism it is proposed that recrystallisation nucleation is achieved by a pre-existing high angle grain boundary bulging into a neighbouring grain due to the local strain energy gradients, i.e. difference in dislocation density between neighbouring grains, Figure 2-14 [40]. A subgrain with a low dislocation density will bulge into one with higher dislocation density, and during the bulging process, the dislocations will be swept up. This nucleation mechanism usually applies when the strain is low (<40%), because strain inhomogeneity from grain to grain is more significant at low strains [59].

The number of nuclei per unit volume is a crucial parameter as it determines the final microstructure and recrystallisation kinetics. It has been reported that different initial grain sizes affect the recrystallisation nucleation process significantly [36]. Ashby reported that a fine grain sized material has a faster recrystallisation nucleation rate and higher number of nuclei per unit volume than a coarse grain sized material for the

same deformation and time. This is due to more preferred nucleation sites being available, i.e. grain boundary area, in the fine grain material. In addition, if recrystallisation nucleation occurs primarily at grain boundaries at low strains, a fine grained material should give more homogeneous recrystallisation than a coarser grained material given the same number of nuclei, Figure 2-15 [1].

Table 2-2 The nucleation sites for recrystallisation [6]

Nucleation sites	Mechanisms
Deformed austenite grain boundaries	Local strain energy gradients which are more pronounced at lower deformation levels
Recrystallised-unrecrystallised interface	Effective pinning of the interface by precipitates allowing nucleation of new grains
Deformation bands	Local strain energy gradients are found in heavily deformed austenite
Undissolved precipitates (>0.5μm)	The strain gradient developed around the particle and its interfacial energy

Table 2-3 Summary of recrystallisation nucleation mechanisms

Subgrain coalescence	Subgrain-boundary migration	Strain induced boundary migration (SIBM)
• Moderate strain • Low temperature • High SFE metals	• High strain (95% reduction) • High temperature • Low SFE metals	• Low strain (up to 40% reduction)

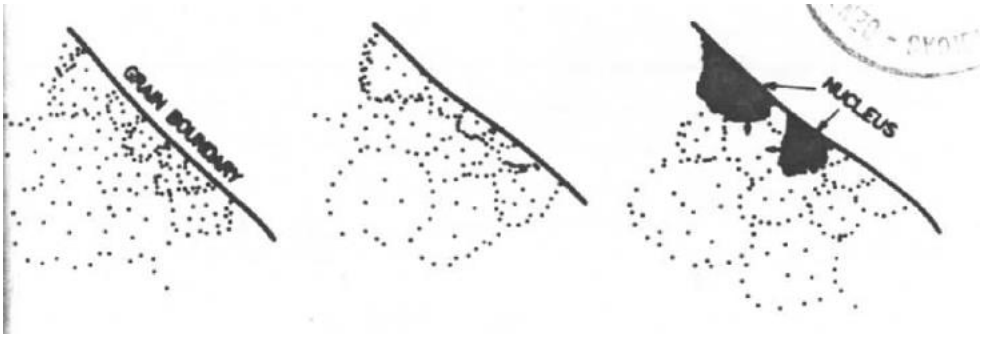

Figure 2-13 Schematic diagram of the subgrain boundary migration mechanism [59]

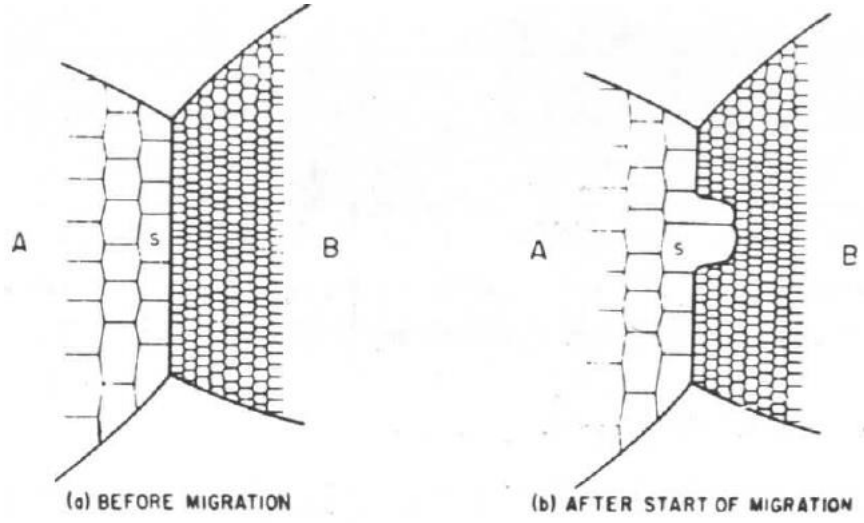

Figure 2-14 Schematic diagram of the SIBM mechanism [59]

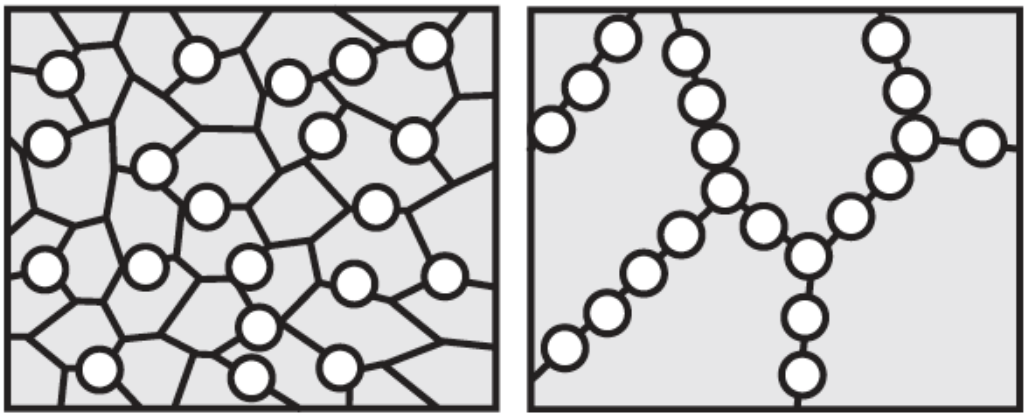

(a) (b)

Figure 2-15 Schematic diagram of the effect of the grain size on the heterogeneity of recrystallisation nucleation in (a) fine grained material (b) coarse grained material [1]

2.4.3 Recrystallisation growth

Recrystallisation growth is a process where the high angle grain boundaries migrate into the deformed matrix, leaving a strain-free matrix behind. It is generally accepted that the velocity of a high angle grain boundary, which is also the growth rate ($\dot{G}$) is given by [1],

$$\dot{G} = MP \quad \ldots 2$$

Where M is the boundary mobility and P is the net pressure on the boundary. It can be seen that the recrystallisation rate is dependent on an intrinsic mobility of the boundary, and the net pressure, i.e. stored energy.

The mobility of grain boundaries is temperature dependent and is usually found to follow an Arrhenius relationship.

$$M = M_0 \exp(-\frac{Q}{RT}) \quad \ldots 3$$

Where $M_0$is the intrinsic mobility and Q is the activation energy. The crystallographic orientations of the deformed matrix and the orientation of the boundary plane also affect the activation energy for boundary migration [34]. For example, it has been reported that the <111> tilt boundary with a misorientation of 40 ° has the maximum migration rate in a lightly deformed fcc material [56]. Therefore, microscopically speaking, each migration grain boundary could have a different migration rate. In most cases, the average boundary migration rate has been applied, which assumes the boundaries have random orientation [61]. Zhou has estimated the mobility from grain growth experiments in C-Mn steels [27]:

$$M_{pure} = \frac{0.192}{T} \exp(\frac{-20837.14}{T}) \quad \ldots 4$$

Due to the inhomogeneous nature of deformation, the growth rate of recrystallisation varies accordingly. That is, the initial growth of the nuclei will be fast following recrystallisation nucleation in high stored energy regions, and once these regions are consumed, the recrystallisation growth rate will decrease. Several authors have

observed that recrystallisation firstly consumes the heavily deformed regions, and the lightly deformed regions recrystallise at a latter stage or are left unrecrystallised due to a lack of driving force [36, 52, 62, 63].

Nakamichi reported that the recrystallising grains have different growth rates in IF steels at 1020K, 80% reduction. The stored energy has been represented via misorientation, and it clearly indicates that the stored energy variation contributed to the variation in recrystallisation growth rate, Figure 2-16 [64]. Le Gall has also used in-situ SEM on cold rolled nickel to study the recrystallisation growth rate at strain level of 0.25 - 1.12, isothermal holding temperature of 455 °C. It was observed that the recrystallisation growth rate (G) is not a constant, but decreases with time [65]. The reason was attributed to the variation in the stored energy, as discussed above, and boundary mobility variation due to a crystallographic orientation effect, which was stated to have a minor effect. Hutchinson investigated the inhomogeneous recrystallisation in cold rolled copper and observed that the regions with high stored energy recrystallised first [58]. The measured growth rate of the recrystallising grains decreased with time. Vandermeer and Hutchinson summarised a time-dependent equation for the boundary migration rate [58, 66],

$$\dot{G} = At^{-m} \qquad \ldots 5$$

Where A and m are constants.

In practice, the global growth rate has been used to give an indication of how fast the recrystallisation growth is. Cahn and Hagel proposed that the global growth rate is influenced by the interfacial area between the recrystallised and unrecrystallised matrix per unit volume as a function of time. The equation is given by [67],

$$G = \frac{1}{S_V}\frac{dX_V}{dt} \qquad \ldots 13$$

Where S_v is the interfacial area between recrystallised and unrecrystallised regions, and X_v is the recrystallisation fraction.

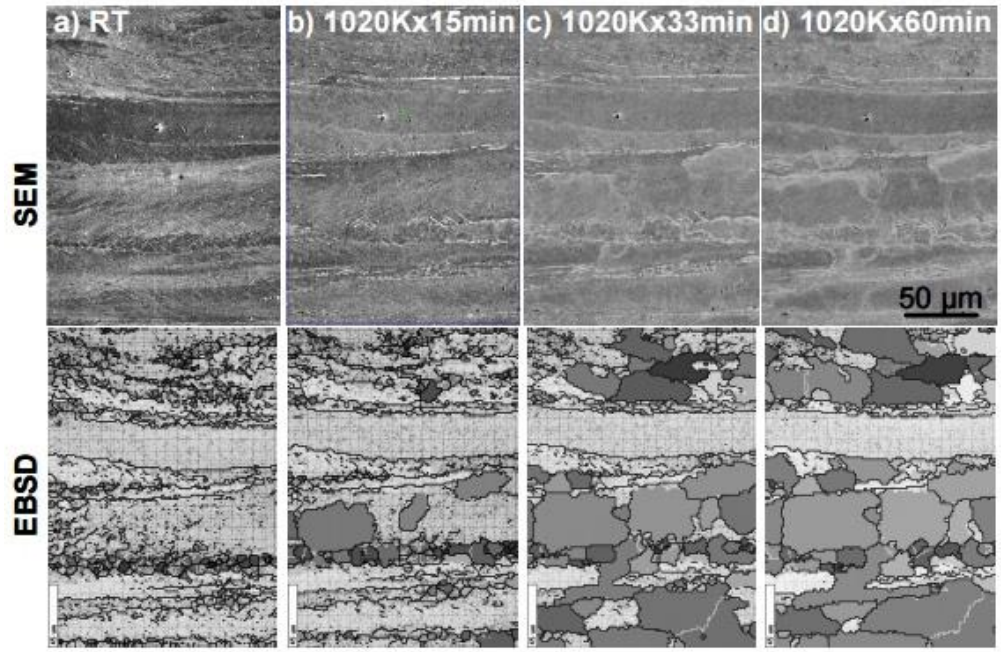

Figure 2-16 Microstructure evolution of IF steel that were rolled 80% reduction showing the effect of stored energy variation on recrystallisation growth. The dark line shown in EBSD is the LAGB and HAGB with misorientation larger than 1 degree [64]

2.4.4 Recrystallisation kinetics

2.4.4.1 JMAK model

The most widely applied model for recrystallisation kinetics is the Johnson-Mehl-Avrami-Kolmogorov (JMAK) model, which describes the sigmoidal time dependence of recrystallised volume fraction, Figure 2-17 [59]. The rate of onset of recrystallisation is slow due to the nucleation process, i.e. formation of HAGB, and the rate at the end of recrystallisation decreases, which is attributed to the impingement of the recrystallising grains.

JMAK model has made three significant assumptions to describe the recrystallisation kinetics:

1. Nucleation occurs homogeneously and the nuclei are randomly distributed over the deformed matrix.
2. Growth rate is constant and independent from the extent of recrystallisation fraction.

3. Growth rate is isotropic, i.e. remains the same rate in all directions.

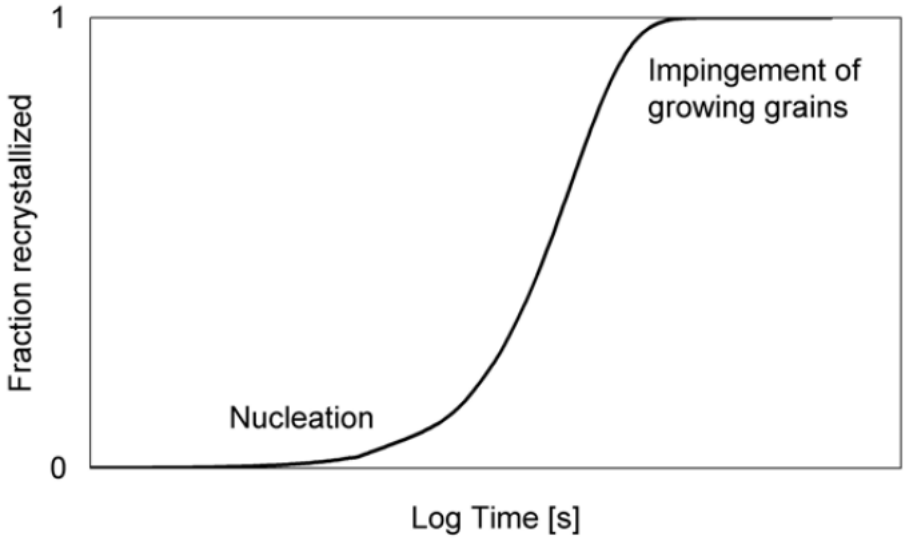

Figure 2-17 Schematic diagram of the recrystallisation fraction versus time [34]

The derivation of the JMAK model is shown as follows. At any given time, the recrystallised volume fraction is set to be V, then the unrecrystallised volume fraction is (1-V). During the time between t and t + Δt, the increased recrystallisation volume is given as,

$$dV_\beta = (1 - V)dV_\beta^e \quad \ldots 14$$

Where dV_β is the recrystallised volume fraction during the time Δt and dV_β^e is the "extended" recrystallised volume fraction. The extended volume fraction refers to the recrystallised fraction assuming recrystallisation could occur anywhere in the matrix, i.e. in both recrystallised and unrecrystallised regions.

After the integration, the equation is:

$$V_\beta = 1 - \exp(V_\beta^e) \quad \ldots 15$$

Then, the volume of a grain after time t, can be expressed by:

$$V_1 = \frac{4}{3}\pi \dot{G}^3 t^3 \quad \ldots 16$$

Where V_1 is the volume of the nuclei at time t, and G is the recrystallisation growth rate.

Assuming the recrystallisation nucleation rate is N and it is constant, so the number of new nuclei forming between t and Δt is $N\Delta t$. The change in the extended volume fraction during the time Δt_1 is given by,

$$dV_\beta^e = \frac{4}{3}\pi\dot{G}^3(t)^3\dot{N}\Delta t \quad \ldots 17$$

Therefore, the recrystallised fraction can be expressed as,

$$V_\beta = 1 - \exp(-\frac{1}{3}\pi\dot{N}\dot{G}^3\, t^4) \quad \ldots 18$$

It is worth noting that the recrystallisation nucleation and growth rate within the above equation are constant. This is referred to as constant nucleation.

In the case that the nucleation rate is so high that all nuclei form at the onset of recrystallisation, the recrystallised fraction is given by,

$$V_\beta = 1 - \exp(-\frac{1}{3}\pi N_0\dot{G}^3\, t^3) \quad \ldots 19$$

Where N_0 is the number of nuclei; this is called site saturated nucleation. Therefore the recrystallised fraction X can be expressed as:

$$X = 1 - \exp(-kt^n) \quad \ldots 20$$

Where, $k = \frac{f\dot{N}\dot{G}^n}{4}$ is the rate parameter (f is shape factor, $\frac{4\pi}{3}$ for a spherical nucleus) and n is the Avrami exponent. As seen, the rate parameter is only determined by the HAGB migration rate assuming site saturated nucleation for recrystallisation.

It can be seen that the Avrami exponent can be altered by the nucleation and growth

mechanisms depending on the nucleation rate and growth dimension, the ideal exponents are listed in Table 2-4.

The n value can be experimentally determined by plotting equation 20 in a double logarithmic form and taking n to be the slope of log (ln(1/(1-X_V)) vs. log(t) plot. Where Xv is the recrystallised fraction measured at time t.

The Avrami exponent "n" is only time-dependent on the nucleation and growth rate of recrystallisation (nominally temperature independent). In addition, Sellars et.al reported that the exponent showed independence of temperature and strain rate [68]. Given the assumption of continued / site saturated nucleation and three-dimensional growth with a constant rate for recrystallisation, then the n value should be 4 or 3, respectively [52]. In practice, the Avrami exponents that are larger than three have only been observed in light deformed fine grained metals [21]. Whereas the majority of the published data gave the exponent to be lower than two or one even for recrystallising grains growing in three dimensions [69].

Table 2-4 Summary of Avrami exponents for different nucleation and growth mechanisms

Growth dimensionality	Site saturated nucleation	Constant nucleation rate
3-D	3	4
2-D	2	3
1-D	1	2

In terms of the recrystallisation rate dependent parameter "k", many models have been developed, but all based on the same concept as proposed by Sellars for C-Mn steels [2, 70].

Then at 50% of recrystallisation, the equation can be written as,

$$0.5 = 1 - \exp(-kR_{50\%}{}^{n}) \quad \ldots 21$$

Where $R_{50\%}$ is the time for 50% recrystallisation, then k is

$$k = \frac{\ln(0.5)}{R_{50\%}^{n}} \quad \ldots 22$$

That is,

$$X = 1 - \exp(-\ln(0.5)(\frac{t}{R_{50\%}})^{n}) \quad \ldots 23$$

It can be seen that any recrystallisation kinetics can be described by JMAK model once 50% recrystallisation time is obtained. Recrystallisation is a thermally activated process and it follows the Arrhenius equation.

Sellars and Barraclough observed that the Avrami exponent is between 1 and 2 [71]. Luton and Ruibai found constant n value smaller than two over a range of temperature and strain rate for copper and steels, Vandermeer and Gordon on 40% cold rolled and annealed aluminium gave a number of 1.7. Medina, Laasraoui and Jonas tested microalloyed steels over 900 - 1100 °C and reported that the n value is lower than 1 [48, 72]. Moreover, n is in many cases not a constant but decreases as the recrystallisation progresses [21, 52].

Galibois and Dube reported Avrami exponents of 2.4 to 4.3 for ultra low carbon steel recrystallisation. The stored energy in this case was induced through quenching, that is, the dislocation microstructure induced via martensitic transformation, which is expected to be more uniform compared to the plastic deformed microstructure [14].

Recovery has been considered causing the low Avrami exponent, but recently many experiments showed that low Avrami exponents have still been observed even in the absence of recovery [1, 21].

Some authors have proposed that the lower Avrami exponents than theoretically predicted can be attributed to the heterogeneous distribution of stored energy and grain boundaries (potential nucleation sites for recrystallisation) [71], and, in some cases, that crystallographic texture in the material might be the reason [73]. Nevertheless, there has not been a conclusion for the causes of lowered Avrami exponent for recrystallisation kinetics.

JMAK modelling can also be expressed as the time for 50% recrystallisation. The derivation is shown as below. For site saturated nucleation with three-dimensional growth with constant growth rate, the equation can be written as,

$$X = 1 - \exp(-\frac{4\pi}{3} N G^3 t^3) \quad \ldots 24$$

Where N is the number density of the nucleation sites and G is the growth rate. Then, 50% recrystallisation can be given as,

$$0.5 = 1 - \exp(-\frac{4\pi}{3} N G^3 {R_{50\%}}^3) \quad \ldots 25$$

Then,

$$R_{50\%} = A N^{-\frac{1}{3}} G^{-1} \quad \ldots 26$$

Where,

$$G = MP \quad \ldots 27$$

Therefore,

$$R_{50\%} = A N^{-\frac{1}{3}} P^{-1} M^{-1} \quad \ldots 28$$

Where A is a constant, the density of nucleation sites per unit volume is N, the stored energy per unit volume is P, and the grain boundary mobility is M. The grain boundary mobility is temperature dependent, which is given as,

$$M_{gb} = M_0 \exp(\frac{-Q}{RT}) \quad \ldots 29$$

Where M_0 is a constant, and Q is the activation energy for boundary migration.

Therefore,

$$R_{50\%} = A N^{-\frac{1}{3}} P^{-1} M_0 \exp(\frac{-Q}{RT}) \quad \ldots 30$$

The equation for 50 % recrystallisation time is applicable for samples either deformed cold and annealed or deformed hot and held at temperature given the assumption of site saturated nucleation with constant growth rate.

2.4.4.2 Effect of annealing temperature on recrystallisation kinetics

Recrystallisation is a thermally activated process, therefore, the recrystallisation rate follows the Arrhenius equation, which is given as,

$$Growth\ Rate = C \exp\left(-\frac{Q_{rex}}{RT}\right) \quad \ldots 31$$

Where C is a constant, Q_{rex} is the recrystallisation activation energy, R is the universal gas constant and T is the temperature. The recrystallisation activation energy has been reported by Sellars and Whiteman to be 310 kJ/ mol for C-Mn steels, and Speich reported 290 kJ/mol for Fe-3.5 Si [36], whereas Barraclough reported a value of 425 kJ/mol for Type 304 stainless steel [71]. It has been reported that the Fe-30Ni has a low recrystallisation activation energy of 192 kJ/mol [11]. Therefore, faster recrystallisation kinetics is expected for Fe-30Ni compared to C-Mn steels.

During recrystallisation, the nucleation and growth mechanisms are independent from temperature, thus, the Avrami exponent is a constant that is not affected by temperature. Figure 2-18 shows recrystallisation curves of a plain C-Mn steel at different temperatures from 1200 - 850 °C, deformed to 0.2 strain at a strain rate of $1s^{-1}$. It can be seen that all curves follow a sigmoidal shape and have a comparable slope, which indicates the same Avrami exponent [74].

However, Vandermeer reported a constant Avrami exponent values in pure iron after cold deformation to 70% and annealing at 600- 500 °C, and a decreasing Avrami exponent at 475- 450 °C, Figure 2-19 [75]. Llanos has reported a decreasing Avrami exponent with decreasing temperature at strain 0.16 - 0.36, strain rate $1s^{-1}$. The Avrami exponent changed from 1 to 0.3 from 1100 °C to 800 °C. The steels consist of 20 - 30 wt. % Mn, 0 - 0.1 wt. % V and 0 - 0.1 wt. % Nb [76]. No reason for the decrease in Avrami exponent was given, however, the effect of the alloying elements on recrystallisation kinetics via solute drag and / or precipitation, which is temperature

sensitive, could have lead to the decrease of n value, this is further discussed in section 2.4.4.5.

Therefore, recrystallisation rate increases with increasing temperature, whereas the recrystallisation mechanism, i.e. Avrami exponent, is considered as independent from annealing temperature for both cold and hot deformation isothermal annealing process.

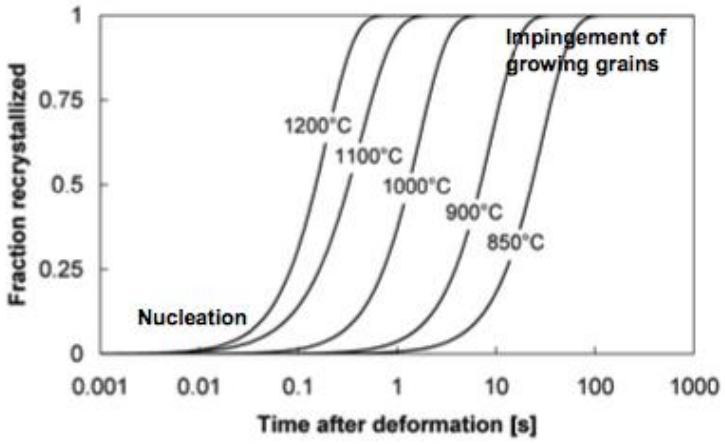

Figure 2-18 Recrystallisation curves of a plain C- Mn steel, temperature range 1200-850 °C, deformed to strain 0.2, strain rate $1s^{-1}$, measured by stress relaxation tests [74]

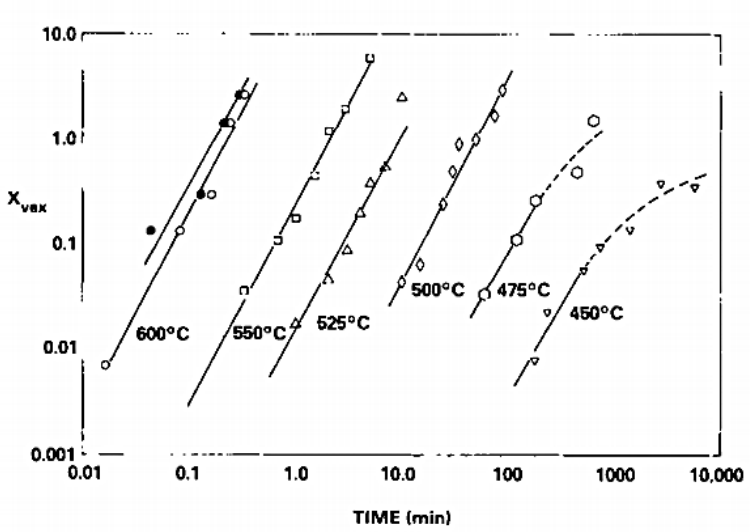

Figure 2-19 Avrami plots of recrystallisation kinetics in pure iron after 70% reduction, reproduced from Vandermeer and Rath [75]

2.4.4.3 Effect of initial grain size distribution on recrystallisation kinetics

Grain size affects the austenite grain boundary length per unit area, which determines the nuclei number density, i.e. the recrystallisation rate and final microstructure. The grain size effect on recrystallisation has been extensively studied for aluminium and copper and the primary effects have been summarised by Humphreys [1]:

1. The stored energy in the material deformed to a low strain (<0.5) tends to increase with a decrease in grain size.
2. Inhomogeneities such as deformation and shear bands are more readily formed in the coarser grains.
3. Grain boundaries are favoured recrystallisation nucleation sites, thus, the number of available nucleation sites is greater for a fine-grain material.

The effect of initial grain size on the Avrami exponent in the JMAK model has also been studied. Hutchinson reported that under the same temperature and strain conditions, fine-grained copper (15 μm), gave an n value of 2.7 whereas the coarse-grain copper (50 μm) gave an n value of 1.7 [58]. Similar observations have been reported by Barraclough and Sellars, Figure 2-20: the Avrami exponent decreased from 2 to 1 by increasing the initial grain size from 140 – 530 μm at 0.5 strain [71].

The decrease of Avrami exponent could be due to the inhomogeneous recrystallisation nucleation [1]. As discussed in section 2.4.2, grain boundaries are the primary recrystallisation nucleation sites. Therefore, a microstructure with a fine average grain size tends to have a more uniform spatial distribution of nuclei compared to a microstructure with a coarse grain size.

In the past 40 years, generally it is the mode / average grain size values that has been considered in recrystallisation modelling. In practice, the initial microstructure includes a range of grain sizes, i.e. grain size distribution. If the grain size distributions all have the same shape (e.g. log-normal) then the models will generally be widely applicable (i.e. should be correct for steels / conditions the models were not originally developed for). Kundu investigated the validity of predicting final grain sizes using the different grain size models and found that significant discrepancies existed, but

that improved agreement could be obtained by considering the entire grain size range rather than just the average grain size [12].

Cram and Zurob have proposed a model of dynamic recrystallisation that has taken the grain size distribution into consideration [77]. It assumes that each grain has different stored energy after deformation dependent on its orientation / Taylor factor and the grain size, Figure 2-21. Therefore, the recrystallisation nucleation and growth rate in each grain is expected to vary. In theory, the grain size and orientation distribution after recrystallisation could also be obtained, Figure 2-22. However, the model did not fit well with the experimental observed dynamic softening behaviour at strain rate above 0.2 s^{-1}. This might be due to an underestimation of the nucleation rate [77].

Rehman extended the model into describing static recrystallisation behaviour [27, 78]. An example has been given with a mode grain size of 600 μm, with the maximum and minimum of grain size being 925 and 275 μm. The deformation condition is 0.3 strain, $10s^{-1}$ with isothermal holding temperature of 1100 °C. It was predicted that larger grains carry less stored energy after deformation due to its lower yield strength compared to the finer grains, thus, the larger grains recrystallise later, Figure 2-23. No comparison between the predicted and experimental results have been mentioned in the thesis, but the potential of applying the approach into considering recrystallisation inhomogeneity has been confirmed [78].

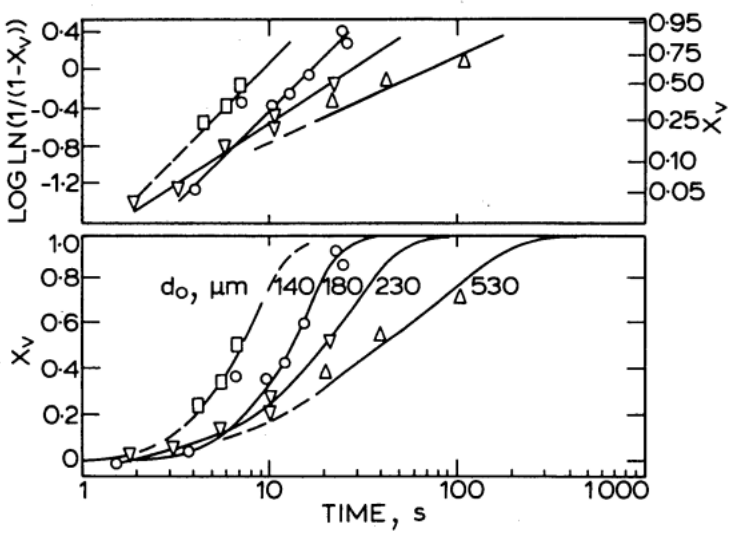

Figure 2-20 Effect of grain size on static recrystallisation kinetics, samples deformed at 0.5 strain, 1050 °C and 1 s^{-1} [71]

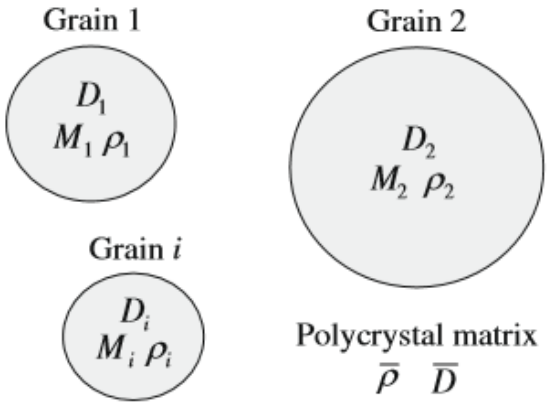

Figure 2-21 Schematic diagram of grains with different dislocation density after deformation due to different sizes, D_i, and orientation/ Taylor factor, M_i. [77]

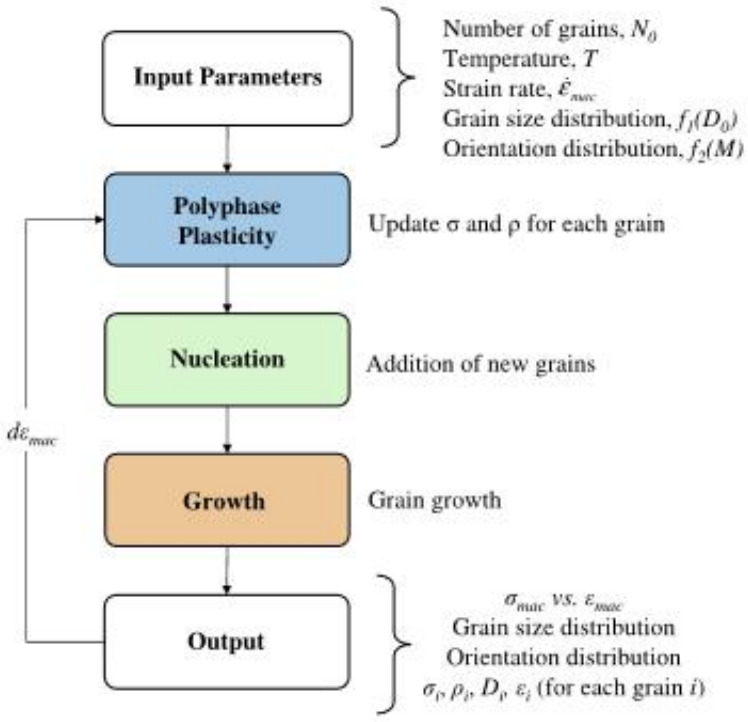

Figure 2-22 Summary of the model proposed by Cram et. al [77]

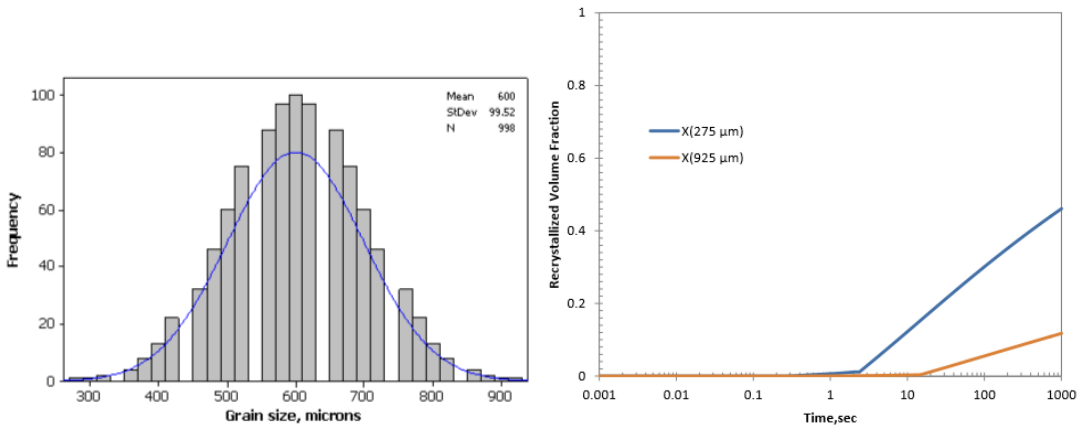

(a) (b)

Figure 2-23 (a) plot of grain size distribution proposed by Rahmen (b) recrystallised fraction evolution for the maximum and minimum grains, i.e. 975 µm and 275 µm. 0.05 wt. % Nb microalloyed steel at 1100 °C, strain 0.3, strain rate 10 s^{-1}. [77]

Attempts have been made to model the recrystallisation kinetics for heterogeneous nucleation and growth condition. Rollett proposed a modified JMAK model of dividing the recrystallising matrix into M classes giving different recrystallisation rates of each class [14]. That is,

$$X = \sum_1^M X_i = \sum_1^M [1 - \exp(-k_i t^{n_i})] \quad \ldots 32$$

Where X is the overall recrystallisation fraction, X_i is the recrystallisation fraction of each class, k_i and n_i is the rate dependent parameter and the Avrami exponent for each class individually.

As seen in Figure 2-24, the overall recrystallisation rate has been decreased due to the heterogeneous recrystallisation kinetics and, as a consequence, the overall Avrami exponent is lower than 3. Rollett pointed out that the various recrystallisation rates within the matrix could be either due to various recrystallisation nucleation incubation times or various local strain distributions [14]. Luo proposed the same approach while assuming a normal distribution of the local strain within the deformed matrix [79]. Luo also demonstrated a decrease in Avrami exponent with increasing local strain variation after deformation, however, no comments have been made on the validity of this model compared to experimental data for recrystallisation rate.

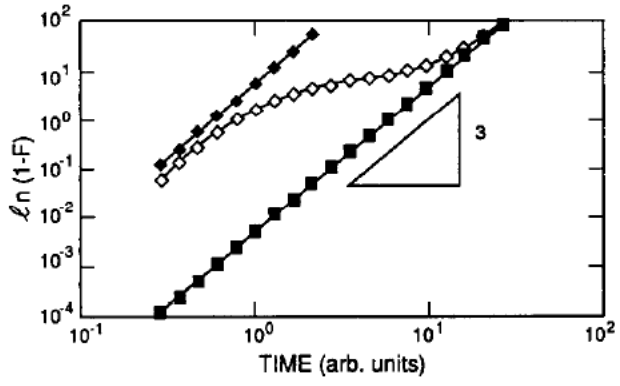

Figure 2-24 JMAK plot of recrystallisation kinetics of Rollett's model. The two lines with black dots represent the recrystallisation rate of two different regions. The curve with hollow dots represents the overall recrystallisation rate [14].

2.4.4.4 Effect of strain inhomogeneity on recrystallisation kinetics

Strain levels determine the nuclei per unit volume and the driving force for recrystallisation. With increasing strain, the recrystallisation nuclei density and the recrystallisation growth rate increase. However, as discussed section 2.2, strain is not homogeneously distributed and this affects the recrystallisation kinetics and hence will affect the Avrami exponent [80]. The stored energy varies locally after deformation, with the heavily deformed regions, i.e. grain boundaries, triple points and deformation bands, recrystallising considerably faster than the lightly deformed regions, which leads to a variation of the recrystallisation rate. Once the more highly deformed regions have been consumed, the recrystallisation rate decreases. Furu observed that heavily deformed regions tend to recrystallise quicker than less deformed regions in aluminium [52]. Humphrey has observed faster recrystallisation in the more deformed regions in copper [1]. Therefore, a faster recrystallisation rate at the beginning and a much slower recrystallisation rate later leads to a lower overall Avrami exponent that predicted by the theory assuming uniform strain.

2.4.4.5 Effect of solute atoms on recrystallisation kinetics

Solute drag is an effect where alloying elements segregate towards the grain boundaries and dislocations and affect their motion. Moving boundaries are therefore expected to contain a higher Nb concentration than the matrix, and the migration of the grain boundary will lead to an asymmetric segregation profile developing. This profile leads to a net force on the grain boundary, opposing the migration, which reduces the boundary migration rate, i.e. recrystallisation rate. Solute drag is more effective during recrystallisation growth than at the nucleation stage, though a retardation effect on recrystallisation nucleation has also been observed [81]. Nb is the most effective alloying element for solute drag during recrystallisation during hot rolling [81].

The quantitative model describing the influence of solute drag on the rate of grain boundary migration is Cahn's model [28]. This model proposes that the drag force depends on the interaction energy between the grain boundary and the solute atoms

and on the diffusion rate of the solutes in and near the grain boundary [82]. The equation proposed by Cahn for the driving force for migrating boundary is given by:

$$F = \frac{v_{GB}}{M_0} + \frac{\alpha X_s v_{GB}}{1+\beta^2 v_{GB}^2} \quad \ldots 33$$

Where F is the driving force for grain boundary migration, v_{GB} is the migration rate, M_0 is the grain boundary mobility in pure metal, and Xs is the atom fraction of solute in the bulk. α and β are dependent on both the interaction energy between the solute and the grain boundaries and on the diffusivity of the solute in the vicinity of the grain boundaries.

Zurob has extended this model into high angle grain boundary mobility during recrystallisation [83],

$$M(t) = (\frac{1}{M_0} + \alpha_m C_{Nb})^{-1} \quad \ldots 34$$

Where

$$\alpha_m = \frac{\beta N_v (kT)^2}{E_0 D} (sinh \frac{E_0}{kT} - \frac{E_0}{kT}) \quad \ldots 35$$

M_0 and C_{Nb} is the intrinsic grain boundary mobility and the concentration of Nb in solution, β is the grain boundary width (approx. 1nm), N_v is the number of atoms per unit volume, E_0 is the solute boundary binding energy, and D is the cross-boundary diffusion coefficient.

Vervynckt and Jonas have investigated the solute drag effect by using a designed steel with very low carbon content (11 ppm) and 0.16 wt. % Nb [84]. They found that the effect of solute on 50% softening follows an exponent law,

$$t_{50\%} = A \exp(SRP_{0.5}[Nb]) \quad \ldots 36$$

Where A is a constant, $SRP_{0.5}$ is a solute retardation parameter, which could be determined by comparing the time of 50% recrystallisation with and without [Nb] in

a no precipitation state, i.e. carbon / nitrogen free and / or at temperatures close to Nb(C, N) solubility temperature. SRP values for different conditions has been summarised in Table 2-5.

The effect of solute drag on recrystallisation kinetics has also been studied by Yamamoto in a steel with 0.1 wt. % Nb and 0.002 wt% C at 900 °C, Figure 2-25 [85]. Due to its low carbon content, no precipitation is expected to form. The retardation of the onset of recrystallisation increases with the increasing Nb content, that is, the initial stage of the softening becomes sluggish with Nb addition. Whereas the overall slope of the softening curves did not change up to 0.097 wt. % Nb, indicating that solute drag has little / no effect on recrystallisation mechanisms.

Table 2-5 Solute retardation parameters for static recrystallisation [84]

Element	SRP_a	SRP_w
V in		
V steel	12	13
V-Nb steel	23	25
V-Mo-Nb steel	19	21
Mo in		
Mo steel	33	20
Mo-Nb steel	33	20
Mo-Nb-V steel	35	21
Ti in		
Ti steel	70	83
Nb in		
Nb steel	235	222
Nb-V steel	403	275
Nb-Mo steel	390	265
Nb-Mo-V steel	346	236

Note: SRPa and SRPw refer to the retardations produced by 0.1 atomic percent and 0.1 weight percent of addition respectively.

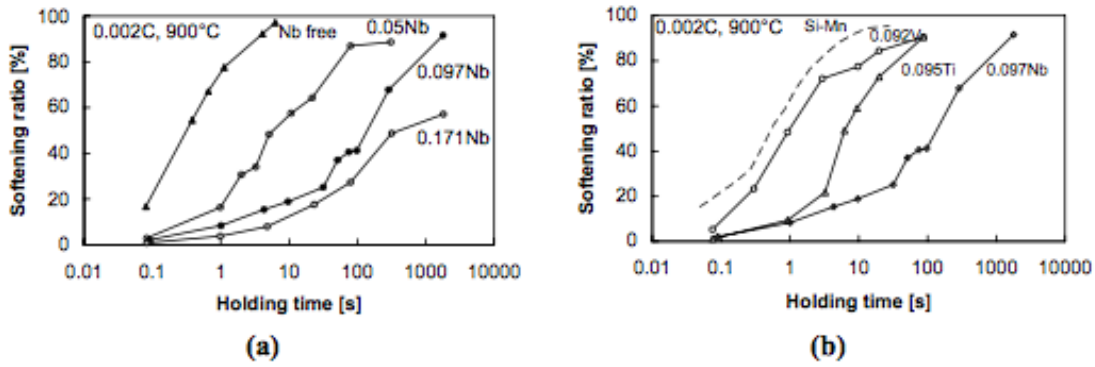

Figure 2-25 Effect of solute drag (a) Nb (b) Nb, V and Ti from Yamamoto [85]

2.5 Cold and hot deformation comparison

Cold or hot deformation can be defined by the deformation temperature being below 0.3 or above 0.6 of the melting temperature respectively [86]. Hot deformation testing has been used as lab simulation for industrial hot rolling / forging processing routes for metals and alloys, especially for HSLA steels and Fe-30Ni [87- 89]. The most common hot deformation testing involves uniaxial compression testing, whilst plane strain compression and torsion testing have also been reported [11, 40, 72, 90]. Recrystallisation during or following hot deformation can be studied by using stress relaxation, double hit deformation testing or interrupted tests with microstructural observation [33, 40, 90, 91]. Alternatively, cold deformation followed by annealing can be considered for recrystallisation studies. It is important that any differences in the two approaches are considered to determine when knowledge transfer between the two situations is appropriate. In particular the following aspects need to be considered: whether the deformed microstructures (i.e. dislocation structures) are comparable; what level of stored energy is imparted into the deformed material due to cold or hot deformation; the extent of dynamic recovery that may occur during hot deformation; the extent of static recovery that may occur during heating to the annealing temperature; and any strain inhomogeneity that can occur in the sample. These factors are discussed below:

2.5.1 Deformed microstructure comparison

Any differences in the deformed microstructure under different deformation temperatures need to be considered. Hughes and Hansen have studied the microstructure evolution during cold and hot deformation in FCC materials with medium to high stacking fault energy, i.e. > 40 mJ/ m^{-2} [92]. In both cold and hot deformed samples, groups of cells in cell blocks surrounded by dense dislocation walls or microbands have been observed at small strains, i.e. strain 0.1 - 0.35. With increasing deformation, the misorientation between the microbands increases and the spacing between microbands decreases [92]. However, Hughes commented that more equiaxed cells and subgrains with a reduced frequency have been observed in hot deformed Al alloys at 300 - 500 °C, strain 0.8, compared to the samples deformed at room temperature, which was attributed to more dynamic recovery occurring during hot deformation [92]. Taylor reported that hot deformed austenite microstructures display characteristics qualitatively similar to those obtained during cold deformation of FCC metals with medium-to-high stacking fault energy [93]. The data used by Taylor has been summarised in Table 2-6, where both cold and hot deformation across a wide range of strains gave deformed microstructures with microbands and cell blocks. Zaefferer et. al studied the cold deformed microstructure for Fe-36 Ni alloy, Figure 2-26. It was reported that the spacing between microbands is approximately 1 μm at a strain of 0.5. The cold deformed microstructure showed comparable microbands features as the hot deformed microstructure, Figures 2-7 and 2-8.

Additionally, both cold and hot deformed microstructures have been observed to show inhomogeneity within the grains: for example Cizek observed, in hot deformed Fe-30Ni alloy, that the grain boundaries and triple points are generally more deformed, i.e. carry a higher local stored energy, than the grain interior [89]. Hansen observed the cold deformed microstructure for FCC metals with medium to high SFEs, i.e. Al, Ni and Cu and found that the grain boundary regions are more deformed than the grain interior [25]. Randle also observed this in cold deformed aluminium [94]. EBSD images showed that both the cold and hot deformed samples were more deformed at grain boundaries and triple points, a banded structure was also formed in the grain interior. Whereas the cold deformed sample carried a higher stored energy, i.e. denser subgrains and dislocation walls, compared to the hot deformed samples via EBSD observation.

Therefore, microbands and cell blocks deformed microstructure are shown in both cold and hot deformation. Additionally, grain boundary regions are more deformed than the grain interior for both deformation conditions.

Table 2-6 Summary of the strain and temperature levels reported similar deformed characteristics, i.e. microbands and cell blocks in FCC metals

Reference	Materials	Strain	Temperature (°C)
[95]	Ni-30Fe	1.2	800
[96]	Fe-30Ni-20Cr	0.18 - 1.38	900 - 1050
[97]	Fe-11Ni-17Cr	0.3, 0.7	900
[89]	Fe-30Ni	0.2 - 0.8	950
[98- 100]	Aluminum	0.05 - 0.8	Room temperature
[85, 99]	Copper	0.1 - 0.8	Room temperature
[100]	Nickel	0.45	Room temperature

Using cold deformation of Fe-30Ni enables observations of the initial deformed microstructure and the very early stages of static recrystallisation, i.e. the recrystallisation nucleation process. Using hot deformation, recrystallisation nucleation has also been observed but mostly for Fe-30Ni containing microalloying elements, i.e. Nb and Mo as these are required to retard the recrystallisation process in order to retain the microstructure at the early stage of recrystallisation [11, 89]. Abdollah-Zadeh has investigated the deformed microstructure of Fe-30Ni deformed to 0.25- 0.9 strain within the temperature range of 1000- 850 ºC. The deformed samples were quenched directly after deformation, nevertheless, recrystallised grains were observed in all samples and it was impossible to distinguish whether these grains formed during deformation or during the time at temperature before and during quenching, i.e. dynamic or static recrystallisation, Figure 2-27 [11]. Cizek deformed Fe-30Ni-1.51Mo at 950 ºC to strains of 0.2 to 0.8 with a strain rate of 10/s with samples being quenched after deformation at a cooling rate of 80 ºC/s. Recrystallised grains were observed after a strain of 0.2 and the sample had already fully recrystallised after a strain of 0.8, Figure 2-28 [89]. This strongly suggests that what is seen in these ‘deformed’ microstructures has actually already significantly recovered or even partially recrystallised, which limits the study of the early stage of recrystallisation kinetics and mechanisms, i.e. the early impingement of recrystallisation nuclei.

Figure 2-26 TEM image showning the dense dislocation walls (DDW) / microbands in Fe-36 Ni alloy after cold deformation to a strain of 0.5 [44]

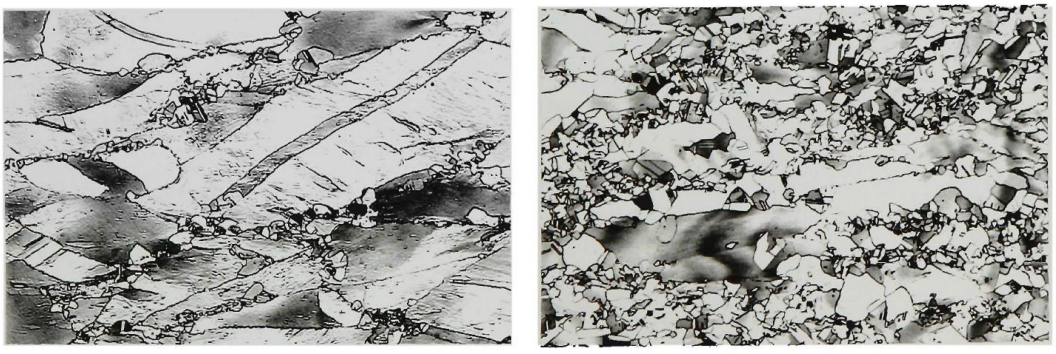

(a) (b)

Figure 2-27 Optical image of a partially recrystallised sample showing the grain boundaries and triple points acting as the preferential nucleation sites for recrystallisation. The sample is Fe-30Ni-0.02 Nb alloy, hot deformed at 950 ºC to 0.5 strain (a), 0.9 strain (b), strain rate $0.7s^{-1}$, then quenched [11].

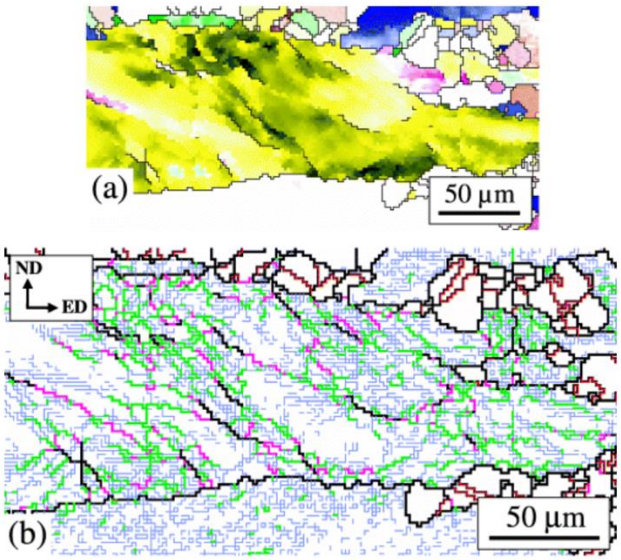

Figure 2-28 EBSD image of deformation band within a Fe-30Ni-1.51Mo grain hot deformed to 0.4 strain at 950 ºC, strain rate 10/s, then quenched. Recrystallised grains can be seen at the right top corner, also along the high angle grain boundaries [89]

2.5.2 Stored energy comparison

Kaonda investigated the stored energy equivalence between hot and cold deformation via calculating the area under the flow stress curve excluding elastic work. Figure 2-29 shows an example for the calculation, it can be seen that a cold deformation of strain 0.17 would be equivalent to a hot deformation of strain 0.3. Other strain equivalences were also determined via this approach, Table 2-7 [90]. This approach provides an insight into cold and hot strain equivalence and indicates that the for the same applied strain during hot and cold deformation it is expected significant differences in the stored energy in the samples, even if there was no dynamic recovery, which is what has been observed when researchers have calculated stored energy values, as discussed above. However, it is worth noting that the dislocation density, i.e. stored energy, has not been measured/ given for either cold or hot deformed samples in this case, which could provide more insight on the strain distribution and deformed microstructure variation between the cold and hot deformed samples. Additionally, Kaonda investigated the recrystallised grain size for both cold deformed and annealed and hot deformed Fe-30Ni alloy, at various temperatures within the range of 850 – 950 °C, to the same equivalent strain (hot strain values of 0.15 – 0.7). It was found that the grain size distributions were the same indicating that the use of

equivalent strain allows direct comparison between hot and cold deformation since strain (i.e. stored energy) is known to affect the recrystallised grain size. One example has been given at Figure 2-30, the cold deformed sample to 0.17 strain shows a comparable recrystallised grain size distribution to the hot deformed sample to 0.3 strain. Other recrystallised grain sizes at equivalent strain between cold and hot deformation have been summarised in Table 2-8. These results suggest that cold deformed samples will have higher stored energy than hot deformed samples if deformed to the same strain and that an equivalence of stored energy, by considering the work done in deforming the sample, can be applied. However, there was no discussion on any effect of heating rate or strain rate on potential static or dynamic recovery respectively, which might affect the stored energy (see later discussion).

Wu and Jensen have estimated the stored energy for cold and hot deformed aluminium alloys at a strain of 2 by measuring the subgrain size and misorientation between subgrains. It was found that the stored energy for the cold deformed sample is four times higher than the sample deformed at a temperature of 400 °C [66, 101]. There was no discussion on whether dynamic recovery or recrystallisation occurred for the hot deformed samples, which might be expected for such a high strain level. Therefore it is not possible to determine whether the higher stored energy in the cold deformed samples is due to the difference in flow stress and work done during deformation (as suggested by Kaonda) or because of the loss in stored energy due to recovery, or due to both factors.

Kolupaeve et. al reported a stored energy difference for deformation in the temperature range between 23-523 ºC for copper based on the flow stress curves for deformation with a strain rate 1000 s^{-1}, which should limit any dynamic recovery effects [102]. It can be seen from Figure 2-31 that the stored energy in the material deformed at 23 ºC is about one order of magnitude higher than in material deformed at 523 ºC for 0.3 strain. This also supports the assumption that greater stored energy for the same strain is imposed during cold deformation.

Therefore, from the discussion above it is clear that a cold deformed sample will have a higher stored energy than the hot deformed sample at same strain. However recovery effects also need to be considered and are discussed in the next section.

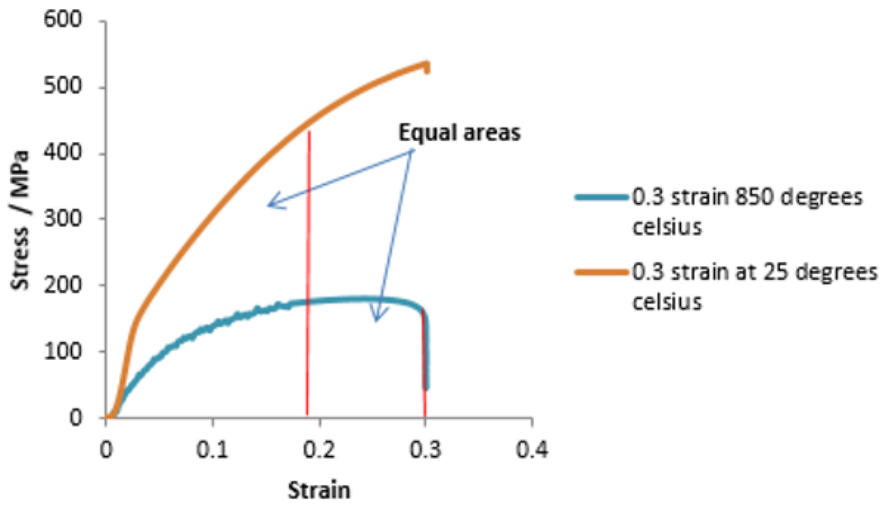

Figure 2-29 Stress- strain curves of Fe-30 Ni alloy deformed to 0.3 strain at 25 ºC (room temperature) and 850 ºC. Strain rate is 2 minutes for cold deformation and 1/s for hot deformation [90].

Table 2-7 Summary of equivalent hot strain by Kaonda's approach [90]

Cold strain	Equivalent hot strain
0.08	0.15
0.12	0.22
0.17	0.3
0.22	0.45

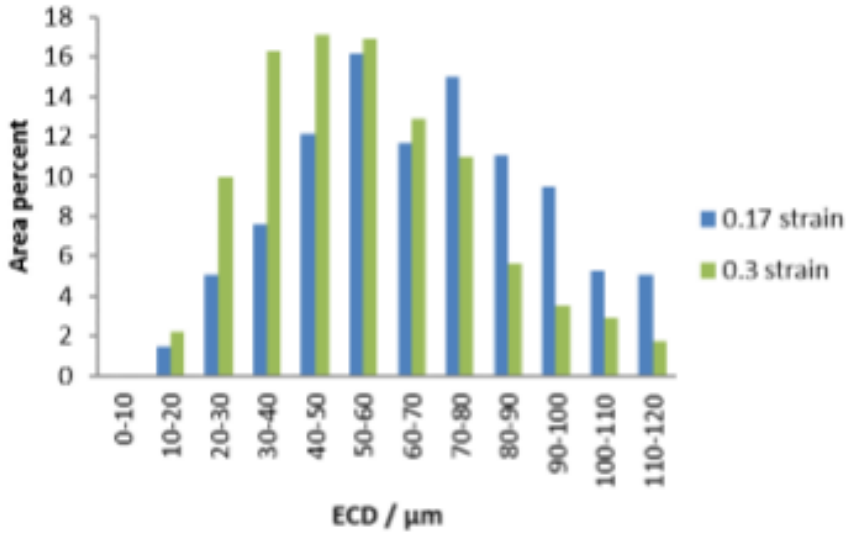

Figure 2-30 Grain size distribution of fully recrystallised samples deformed to 0.17 strain at room temperature or 0.3 strain at 850 °C by uniaxial compression testing [90]

Table 2-8 Measured recrystallised mode grain size following cold (room temperature) and hot (850 °C) deformation, initial grain size 110 μm [90]

Cold deformation		Hot deformation	
Strain	Recrystallised grain size (μm)	Strain	Recrystallised grain size (μm)
0.08	80- 90	0.15	70- 80
0.17	50- 60	0.3	40- 50
0.22	40- 50	0.45	30- 40

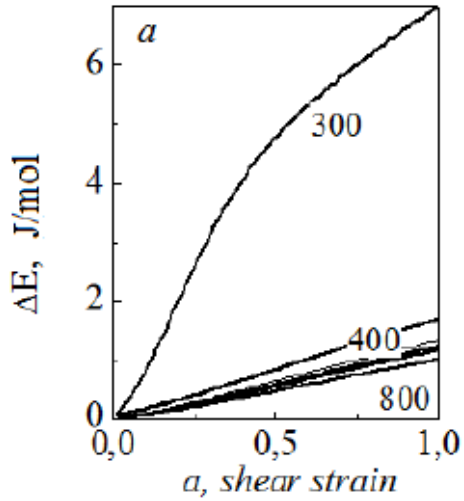

Figure 2-31 Stored energy dependence on the deformation temperature (K) for copper within the temperature range of 23 - 523 ºC for deformation at 1000 s^{-1} (300 – 800 K) [102]

2.5.3 Effect of recovery on recrystallisation kinetics

Dynamic recovery can occur during deformation, which leads to the formation of the subgrain and dislocation walls. Static recovery can occur prior to static recrystallisation either isothermally or non- isothermally [103]. These factors are considered below:

Mukuthan et. al studied the effect of heating rate, i.e. different extent of recovery, on recrystallisation kinetics in cold deformed interstitial-free steel after 80% reduction cold reduction. Recovery consumed 50% stored energy prior to recrystallisation with a heating rate of 0.025 °C/s, whereas less than 20% softening was attributed to recovery prior to recrystallisation at a heating rate of 20.2 °C/s. It was also found that

the recrystallisation starting time was delayed with decreasing heating rate, whereas the recrystallisation mechanism, i.e. the Avrami exponent, was not changed [104]. Mukuthan also found that the recrystallisation Avrami exponent did not change when recrystallizing within the temperature range of 600 - 760 °C with a heating rate of 80 °C/s for isothermally annealing where different amounts of recovery might be expected from heating to the different annealing temperatures, Figure 2-32 [104].

Barraclough and Sellars investigated the effect of strain rate on recrystallisation recrystallisation kinetics for the hot deformed austenitic stainless steels. It has been found that the recrystallisation Avarmi exponent is independent from the strain rate (range between 4.7×10^{-2} and 1 s^{-1}) at 950 °C, 0.25 strain. Abbod et. al studied the relationship between strain rate (0.1- 10 s^{-1}) and the dislocation density at 950 °C, up to 0.8 strain, Figure 2-33. It can be seen that the dislocation density increases with increasing strain rate significantly, which leads to a higher driving force for recrystallisation, i.e. faster recrystallisation kinetics [105].

Therefore, it can be seen that different amounts of recovery can occur during cold deformation and annealing (static recovery during reheating dependant on the heating rate and annealing temperature) and during hot deformation (dynamic recovery dependant on strain rate and temperature), which affects the recrystallisation kinetics but not the recrystallisation mechanism i.e. recrystallisation start and finish times are not comparable but Avramic exponents are.

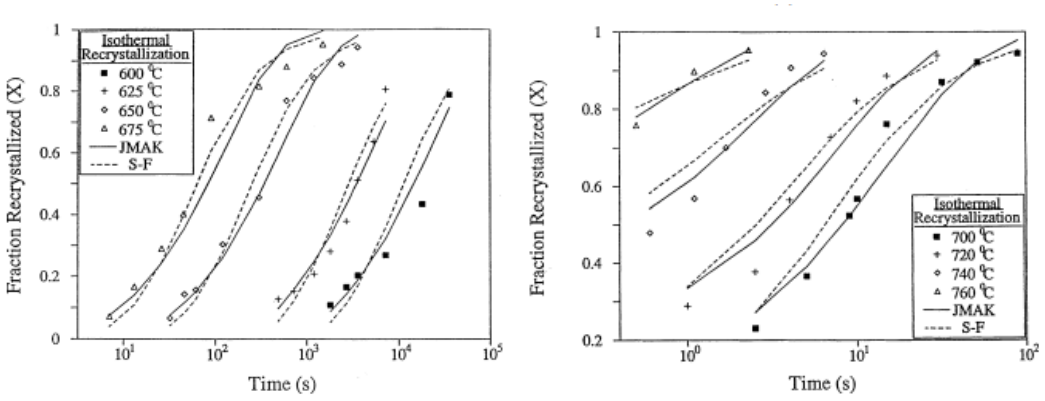

Figure 2-32 Recrystallisation kinetics of IF steels cold deformed (80% reduction) then annealed at various temperatures with a heating rate of 80 °C/s [104]

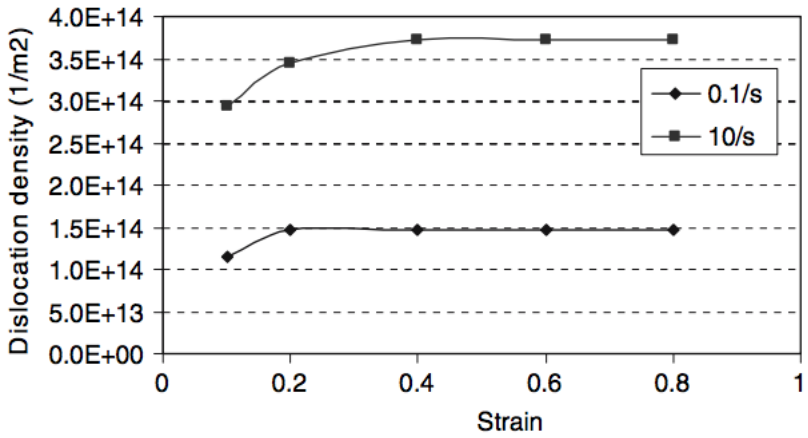

Figure 2-33 Estimated dislocation density proposed by Abbod et. al for Fe- 30Ni deformed at 950 °C, strain rate 0.1 or 10/s to various strains [105].

2.5.4 Barrelling and macroscopic strain inhomogeneity

A barrelling effect during deformation of uniaxial compression samples can be caused by temperature gradients across the sample and friction between the sample and test anvils, and leads to a macroscopic strain inhomogeneity throughout the sample. Barrelling has been observed even when little temperature gradient (< ±10 °C) was present [106], which will be caused by friction at the anvil-contacting surfaces generating circumferential tensile stresses. Whilst friction can be minimised using friction modifiers (for example graphite and / or tantalum foil for Gleeble testing [21, 90, 107]), it is generally higher for hot testing than cold testing [90]. Therefore, a location-dependent strain within the specimen is generated. The strain decreases along the axis from the sample centre to the platen face indicating little stored energy at the anvil-contacting region (strain <0.1), which is known as the 'dead zone' [107]. Watson investigated the strain distribution in a 9Cr forging steel deformed to strain of 1, strain rate $1s^{-1}$ via Q-form software using the measured amount of barrelling, Figure 2-34 [108]. It can be seen that the highest strain of 1.1 is predicted at the centre of the sample (higher stored energy hence finer resulting recrystallised grain size), whereas only 0.5 strain is predicted near the anvil. Bhadeshia et. al investigated the effect of barrelling on strain distribution for C-Mn steels deformed to 0.18 - 0.8 strain at 600 °C [107]. Figure 2-35 shows the microstructure and hardness of samples deformed to 0.18 and 0.36 strain. It can be seen that the barrelling leads to a non-uniform strain distribution within this strain range for C-Mn steels. Ji observed the effect of barrelling on the strain distribution for HSLA steels deformed to 0.3 strain at 990 °C, strain rate

10 s^{-1}. The microhardness map showed that the dead zone is nearly 1.5 mm wide at the anvil, Figure 2-36 [106].

Kaonda compared the barrelling effect for both cold and hot deformed samples [90]. Fe-30Ni was deformed to strains of 0.08 - 0.22 (room temperature) or strains of 0.15 - 0.45 (at 850 °C), which were determined to be the equivalent strain to give the same stored energy (see discussion in section 2.2.3.2). PTFE film was used as the lubricant for cold deformation, and graphite foil was used for hot deformation. . Li reported that the friction coefficient for steel- graphite foil at 800- 1200 °C is 0.3- 0.35 [109], whereas the friction coefficient for steel- PTFE at room temperature is 0.06 [110]. More severe barrelling is expected for deformation with a higher friction coefficient. As a result, the cold deformed samples showed less barrelling compared to the hot deformed sample within the strain range tested. Also with increasing strain, the barrelling was more significant. Therefore, the strain distribution is expected to be more inhomogeneous by using hot uniaxial compression compared to cold deformation for an equivalent stored energy.

Macroscopic strain inhomogeneity does not only exist in uniaxial compression tests; Black investigated the effect in plane strain tests [40]. Figure 2-37 shows the deformed microstructure and the partially recrystallised microstructure in plane strain samples. It can be seen that the deformation bands present mostly at the centre of the deformed samples, the grains are also more elongated in this region. Whereas the grains near the anvil region showed much less deformation. Additionally, recrystallisation has been observed proceeding quicker in the centre compared to the anvil contacting regions.

Therefore, macroscopic strain inhomogeneity can cause uneven recrystallisation through the sample, which, in theory also could lead to a decrease in Avrami exponent. Therefore investigations of recrystallisation (for example microstructural effects such as grain size distribution on the Avrami exponent) should be carried out in samples with minimal macroscopic strain inhomogeneity.

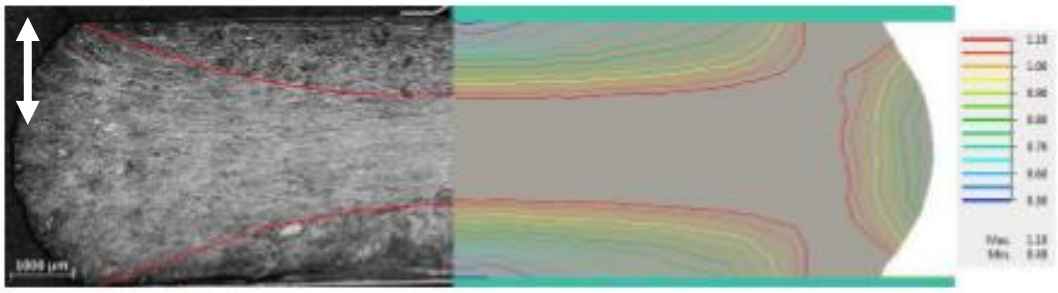

Figure 2-34 Example of non-uniform strain distribution prediction in uniaxial compression samples using Q-form software and an optical image showing flow lines for a deformed 9Cr forging steel at 900 °C to a strain of 1, strain rate of 1/ s. The arrow indicates the deformation direction [108]

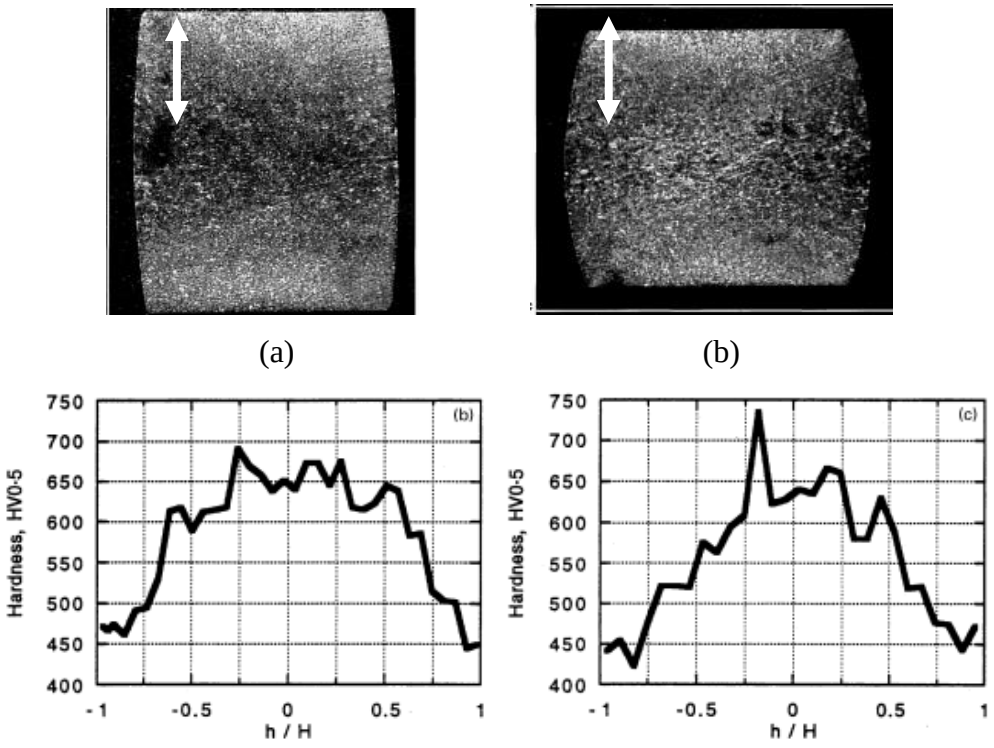

Figure 2-35 C-Mn steel samples deformed at 600 °C to strain 0.18, microstructure (a), hardness profile through thickness (c), and strain 0.36, microstructure (b), and hardness profile through thickness (d) The arrow indicates the deformation direction [107]

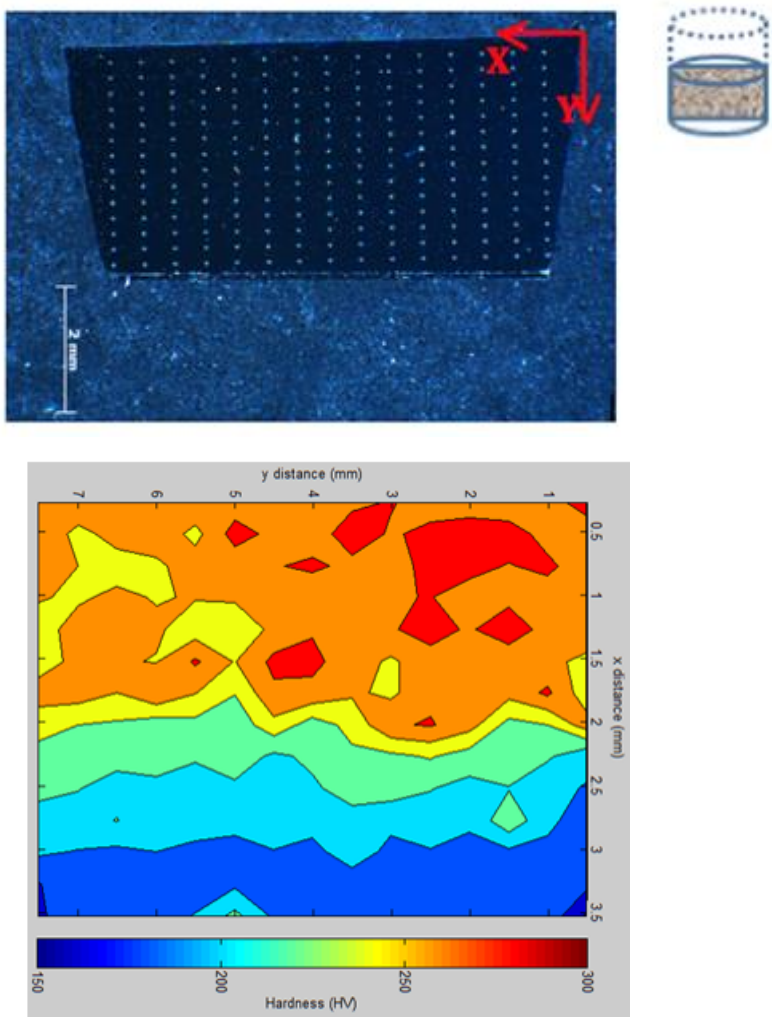

Figure 2-36 Micro-hardness mapping of HSLA steel sample deformed at 990°C, strain 0.3, strain rate $10s^{-1}$. Examined region and X-Y axis shown in the macrograph [106].

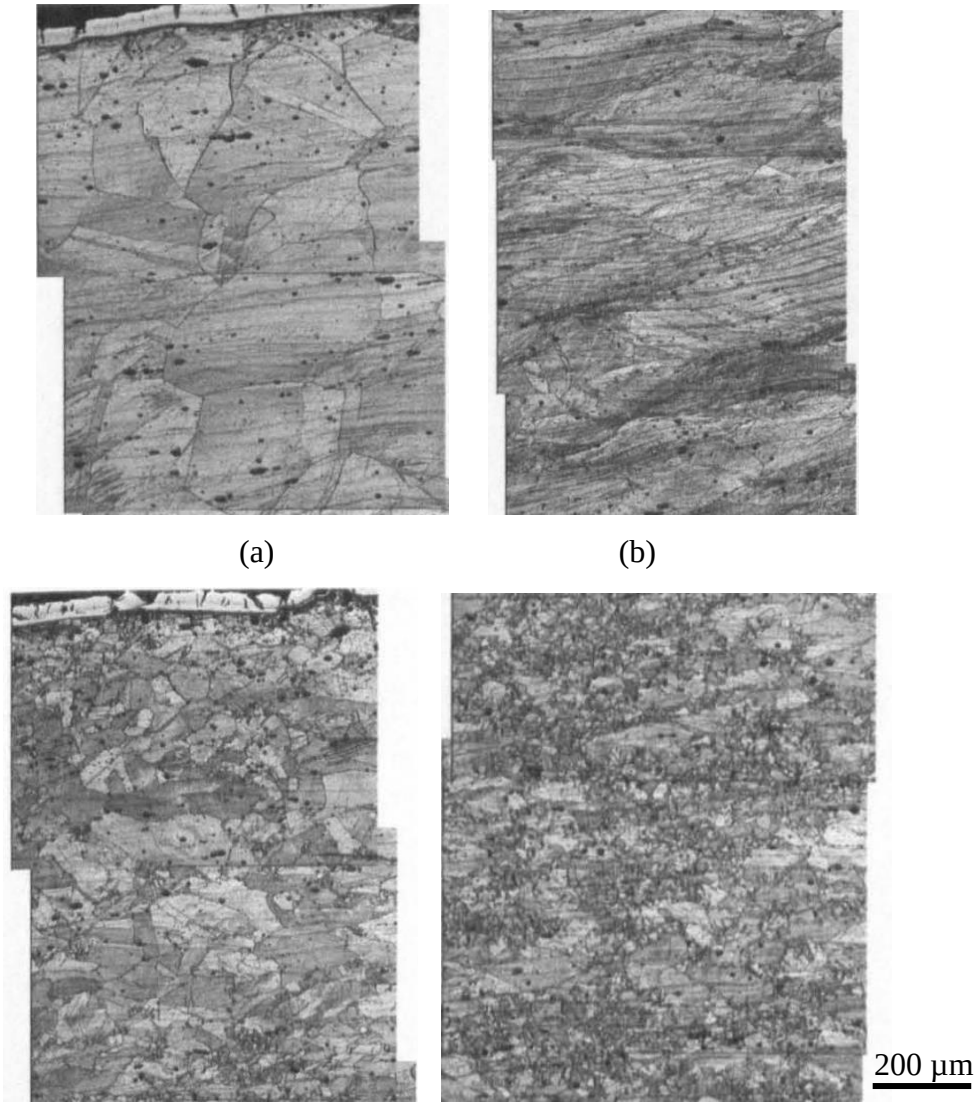

Figure 2-37 Microstructure deformed to 0.5 strain at 900 °C, no recrystallisation occurred (a) anvil contacting region (b) central region. Microstructure deformed to 0.5 strain at 1000 °C and held for 1000 s, 40 % recrystallised (c) anvil contacting region (d) central region. [40]

2.5.5 Strain induced martensite

Another concern for using cold deformation with Fe-30Ni austenitic steel is the potential for strain induced martensite to form. The martensitic starting temperature for Fe-30 Ni alloy has been reported to be within the temperature range of – 70 °C to – 40 °C depending on the carbon content and the grain size [88, 109]. Maxwell reported little strain induced martensite formation at 0 °C for Fe-32 Ni during tensile testing to failure, Figure 2- 38. Also, Zaefferer deformed Fe-36 Ni at room temperature

and found no martensite via TEM [44]. Thus, the effect of strain induced martensite formed during the deformation of Fe-30 Ni at room temperature is expected to be negligible.

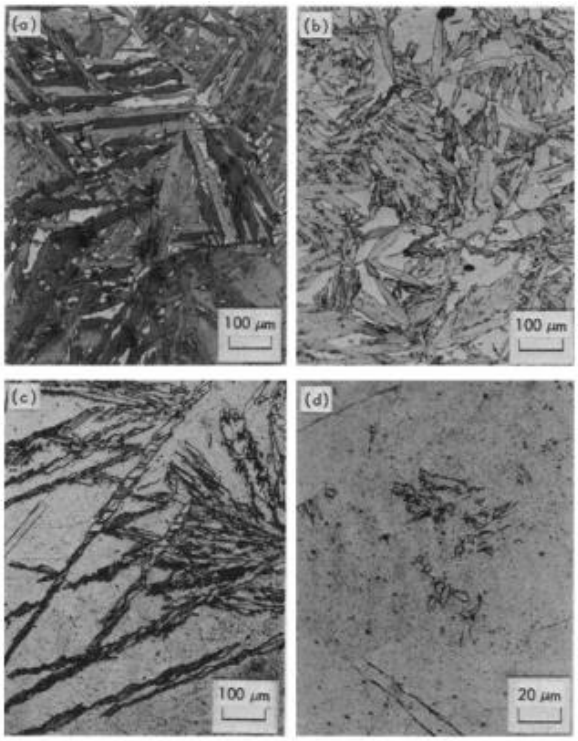

Figure 2-38 Optical images showing a Fe-32Ni-0.02 C alloy tested in tension to failure with strain induced martensite formation at (a) -72 °C (b) -50 °C (c) -30 °C and little strain induced martensite formed at (d) 0 °C [111]

2.5.6 Summary on cold and hot deformation

Therefore, based on the discussion above it has been shown that the cold and hot deformed microstructure for Fe-30Ni are similar in terms of the formation of dislocation cells and microbands. In the absence of any dynamic or static recovery then an equivalent hot deformation strain for a given cold deformation strain, based on equivalence of area under the stress strain curve, may be appropriate to allow comparison betweenthe approaches. However, even at relatively low strains (<0.3), recovery can occur in hot deformed samples (dynamic recovery, dependant on strain rate, strain and deformation temperature) and in cold deformed and annealed samples (static recovery during reheating dependant on the heating rate, strain and the annealing temperature), which leads to a different driving force for recrystallisation. As a result, the recrystallisation rates determined from hot and cold deformation

studies even for the same (equivalent) applied strain might not be directly comparable unless recovery is accounted for. However, it has been shown the as the deformation microstructures are similar and the recrystallisation mechanisms remain the same for both cold deformed and annealed and hot deformed samples any study on the recrystallisation mechanisms (and hence the Avrami exponent) will be comparable between the two approaches.

2.6 Cold and hot deformation recrystallisation kinetics comparison

As mentioned in chapter 2.5, cold and hot deformed microstructures are similar for Fe-30Ni alloy, i.e. observations of more deformed regions adjacent to grain boundaries and triple points, also microband dislocation structures after deformation, along with the same locations for recrystallisation nuclei on prior austenite grain boundaries, triple points and deformation bands. However, differences in the amount of stored energy in the hot and cold deformed samples can arise if the same strain is applied because of the different flow stresses and/ or differences in the amount of recovery that could occur (dynamic recovery during hot deformation compared to recovery during heating to the annealing temperature for cold deformed and annealed samples). The resulting differences in stored energy could affect the recrystallisation start times/ kinetics, but, it is not expected that the recrystallisation mechanisms and Avrami exponents will be effected.

Vandermeer compared the recrystallisation growth rate of hot and cold deformed aluminium alloy after a strain of 2. The hot deformation was carried out at 400 °C, at a strain rate of 2 s^{-1}, and the cold deformation was at room temperature, heating rate was not specified. The growth rate of the cold deformed sample was found to be over one magnitude faster than for the hot deformed samples, and the recrystallised grain size after cold deformation and annealing was 3- 4 times smaller than for the hot deformed sample, Figure 2-39 [66, 101]. This result is consistent with there being higher stored energy in the cold deformed samples when deforming to the same strain (see section 2.5.2) without significant reduction in stored energy due to recovery on reheating to the annealing temperature.

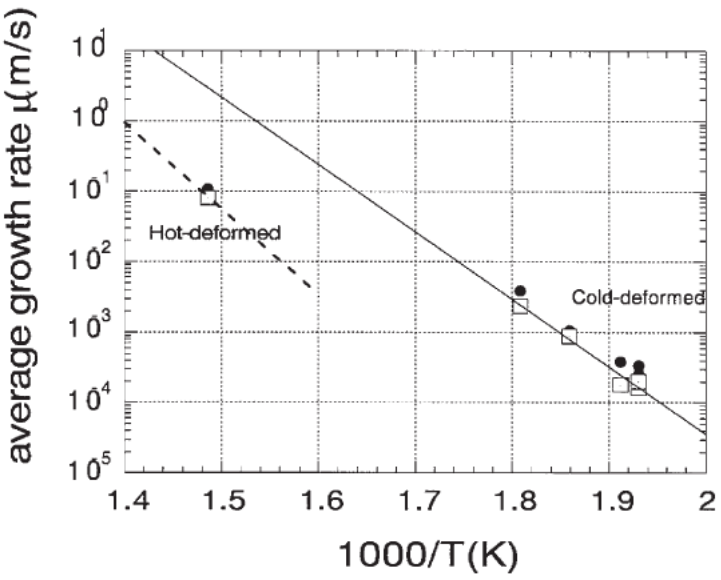

Figure 2-39 Comparison of average growth rate by hot and cold deformed samples. The sample is aluminium alloy, deformed to strain of 2 either cold (room temperature) or hot (400 ºC). Cold deformed sample was annealed at 260 ºC, hot deformed sample was annealed at 400 ºC. The square points and the filled circles represent the different models for calculating the average growth rate [66]

2.6.1 Hot deformation recrystallisation JMAK modelling

Sellars further simplified the recrystallisation model by replacing the parameters of nucleation site density, stored energy and boundary mobility the constant A, the strain, strain rate and initial grain size in the Arrhenius equation for recrystallisation. Then the time of 50% recrystallisation can be modelled as:

$$R_{50\%} = AZ^{-m} d_0^p \varepsilon^{-q} \exp\left(\frac{Q_{rex}}{RT}\right) \quad \ldots 37$$

where A, m, p and q are constants, Z is the Zener-Hollomon parameter, i.e. a strain rate compensation parameter, d_0 is the initial grain size, ε is the strain, R is the gas constant, Q_{rex} is the activation energy for recrystallisation, and T is the isothermal holding temperature. Initial grain size represents the available nucleation sites density for recrystallisation, strain represents the stored energy level for recrystallisation, and recrystallisation activation energy represents the materials recrystallisation property. Sellars developed the model to fit the experimental data from different research groups

rather than based on a single grade using the same experimental technique. Additionally, the initial grain size considered was from 100 – 450 μm, and only mode grain size has been taken into consideration, also the model is applicable within the range of 0.06 - 0.17 wt. % C, 0.005 - 0.015 wt. % N, 0.03 - 0.045 wt. % Nb. The Avrami exponent has been experimentally fitted to 2, no physical explanation or prediction is available for the Avrami exponent [87].

Sellars gave p a value of 2 for microalloyed steels [87]. However, deviations from a linear relationship have been reported for both fine and coarser grain size material, Figure 2-40. Li reported a value of 1.7 for microalloyed steels containing 0.055 wt. % Nb with a grain size range between 12 - 83 μm [112]. Fernandez gave a grain size dependent exponent for Nb, Ti microalloyed steels [2]: when the initial grain sizes are smaller than 160 μm, the exponent is given as 2, but when the initial grain size is larger than 160 μm, an exponent of 1 gave the best fit to their experimental data.

Sellars gave q a value of 4 for C-Mn and microalloyed steels, 2.7 for Al-Mg alloys and 1.5 for the pure Al [71, 87]. Medina reported that the strain exponent is between 1.3 - 2.3 for microalloyed steels with grain sizes between 180 - 430 μm at 0.3 strain. Fernandez proposed that the strain exponent to be dependent on the initial grain size for HSLA steels, i.e. $q = 5.6D_0^{-0.15}$. Therefore it appears that the strain exponent is dependent on the material properties and its initial grain size. Hodgson proposed that the Nb content affects the strain exponent, and q is given as (-4 + 77 [Nb]) [113].

The Avrami exponent is one of the most crucial parameters in JMAK modelling, which affects the recrystallisation starting / finishing time prediction significantly. Nevertheless, it has been empirically fitted, and lacks fundamental understanding. The ideal Avrami exponent for site saturated nucleation with three-dimensional growth with constant growth rate is 3, however these empirically fitted values were lower than 3 without observation of growth occurring in less than three dimensions. Abdollah gave a value of 1.5 for Fe-30 Ni alloy [11], Sellars gave a value of 2 for type 304 austenitic steel [71], Medina gave a range of 0.6- 1.5 for microalloyed steel [72], Fernandez gave a range of 0.9- 2 for microalloyed steels [2]. As mentioned in section 2.4.4, the microstructure inhomogeneity is believed to be the reason, which has already been observed in aluminium in-situ EBSD test [1]. However, there has not been a

direct observation of recrystallisation inhomogeneity affecting the Avrami exponent for microalloyed steels in austenite.

The relationship among the recrystallisation starting time, time and temperature can be represented by an RTT curve. It can be seen in Figure 2-41 that the recrystallisation starting time (5% of recrystallisation) and finishing time (85% of recrystallisation) under certain strain is plotted against temperature.

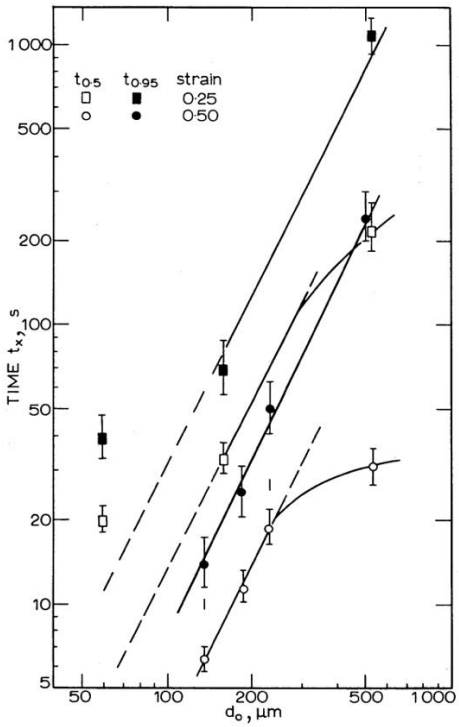

Figure 2-40 Effect of average initial grain size on the 50% and 95% of recrystallisation time [71]

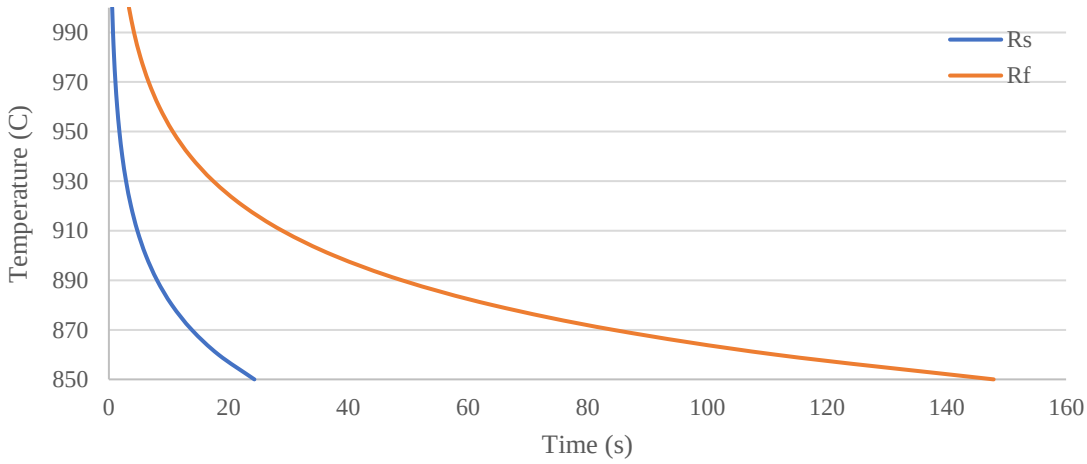

Figure 2-41 A schematic diagram of recrystallisation-temperature-time (RTT) curve

Kundu et al found that the different models, fitted for a given set of experimental data, do not work well when considering all the experimental data available in the literature, shown in Figure 2- 42. It can be seen from Figure 2- 42 (a) that the Dutta-Sellars model fitted well with the experimental data within the valid range, i.e. Nb level: 0.03 - 0.04 wt. %, strain at 0.3. Whereas poor agreements have been shown when considering a wider range of Nb content, Figure 2- 42 (b).

Abdollah investigated the validity of the Dutta-Sellars model on predicting recrystallisation kinetics of Fe-30Ni-0.02 Nb after hot deformation [11]. Poor agreements have been observed over the strain range of 0.25 - 0.9, temperature range of 1000 - 900 °C with an initial grain size of 310 μm. A modified model has been given as,

$$R_{50\%} = (-26.25 + 2750[Nb]) \times 10^{-18} d_0^2 \varepsilon^{-(-4+77[Nb])} \exp\left(\frac{Q}{RT}\right) \quad \ldots 38$$

The recrystallisation activation energy used for the Fe-30Ni-0.02 Nb alloy is 270 kJ/ mol, and 190 kJ/ mol for Fe-30Ni Nb free alloy measured by Abdollah [11].

To sum up, there are two aspects of recrystallisation JMAK modelling that remains unclear. Firstly, the variation in fitting parameters indicates that this is still limited fundamental understanding about each parameter and how it is affected by material parameters. This limits how well the empirically fitted parameters can describe the recrystallisation kinetics for a wide range of steels. Secondly, whilst the causes of the lowered Avrami exponent for C-Mn steels has been suggested to be due to grain size differences or macroscopic strain variation a more precise prediction is highly desirable.

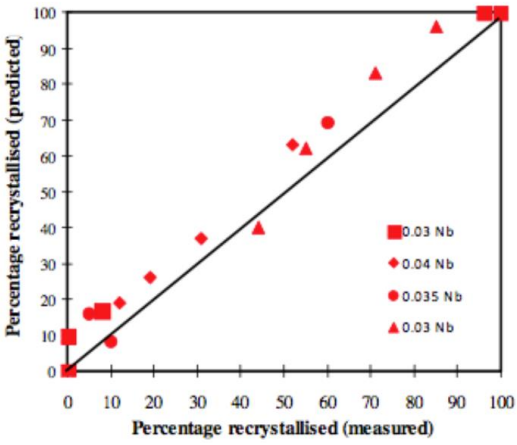

(a)

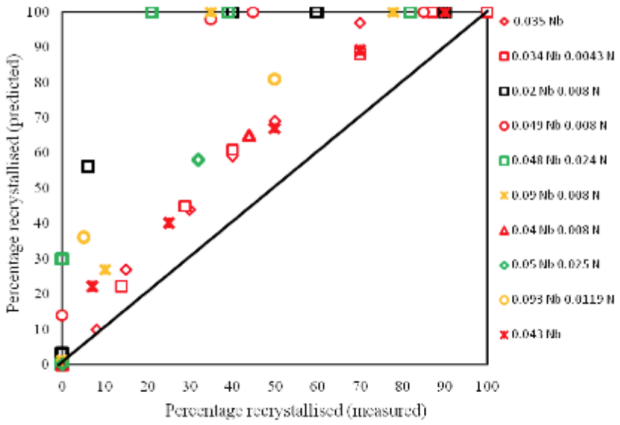

(b)

Figure 2-42 (a) The predictions by the D-S model and measured results of recrystallisation evolution at different Nb levels in HSLA steels, 0.3 strain (b) The comparison of D-S prediction and measured results in a wider range of Nb level at 0.3 strain, summarised by Kundu [12]

2.6.2 Cold deformation and annealing recrystallisation JMAK modelling

As discussed in section 2.4.4.1, the JMAK equation for cold deformation is the same as for hot deformation. Multiple authors have applied the JMAK model for cold deformation recrystallisation conditions, where a lower that theoretically predicted Avrami exponent has also been observed. Lu et.al gave the Avrami exponent a range of 0.7 - 1.37 for Fe-21Mn steel annealed within the temperature range of 560 - 700 °C, following cold reduction to 50 % (true strain of 0.7) [114]. Lu has proposed a decreasing growth rate with time,

$$G = Ct^{-r} \quad \ldots 39$$

Where C is a constant, t is the isothermal holding time and r is an exponent.

Torabinejad gave the Avrami exponent a range of 0.9- 1.5 for Fe-30Mn-5Al steel within the annealing temperature range of 600 - 700 °C, cold reduction 40 - 70 % (true strain 0.5- 1.2) [115]. Zaefferer et. al has investigated the recrystallisation kinetics for Fe-36Ni cold deformed to 69 % - 94% reduction (true strain 1.2 - 3.3), then annealed at 600 °C for various times. The recrystallisation kinetics were examined by hardness testing. It was found that the recrystallisation kinetics follow the JMAK model, the Avrami exponents were also determined, i.e. 1.06 - 1.38, Figure 2-43 [44]. Tsuji et. al also studied the recrystallisation kinetics for cold rolled Fe-36 Ni to 70% reduction (true strain of 1.2) then annealed at 700 °C for over 7000s. The initial average grain size was 220 μm. The Avrami exponent was measured to be 0.9 [116].

It can be seen that whilst the JMAK model has been widely used to describe the recrystallisation kinetics for cold deformed and annealed samples, there is yet to be a more generalised model to describe the effect of strain, initial grain size and composition on recrystallisation kinetics after cold deformation. It has been mentioned in chapter 2.5 that the main difference between cold and hot deformation for Fe-30Ni alloy is the stored energy level. Therefore, it is not unreasonable to consider that the Sellars approach could be used for austenitic model alloy recrystallisation kinetics prediction after cold deformation, although it is recognised that the occurrence of recovery on heating to the annealing temperature (and hence the heat rate) would need to be considered.

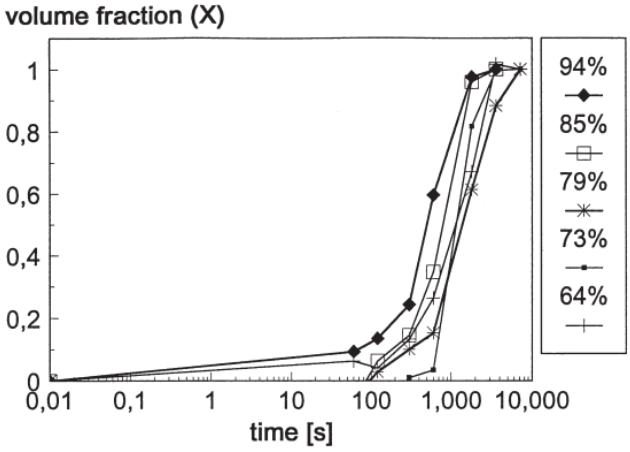

Figure 2-43 Isothermal recrystallisation kinetics for cold deformed Fe-36Ni to 64 - 94% reduction, then annealed at 600 °C. [44]

2.7 Recrystallised grain size prediction

It is very desirable to precisely control the grain size distribution during the rolling process to avoid bimodal grain size distributions in the final product [16]. Recrystallisation is the mechanism for controlling the grain size evolution, and most work has been done on predicting the mean recrystallised average grain size [16, 71].

The recrystallised grain size has been found to be dependent on strain and the initial austenite grain size. The relationship between recrystallised grain size, starting grain size and strain is given by Sellars and Barraclough [70, 71]:

$$D_{rex} = D' D_0^{0.67} \varepsilon^{-1} \quad \text{(C-Mn steels)} \qquad \ldots 40$$

$$D_{rex} = D' D_0^{0.67} \varepsilon^{-0.67} \quad \text{(Nb-bearing steels)} \qquad \ldots 41$$

Where D' is a fitting parameter which has been found to vary with different grades of steels, Table 2-7. The equations indicate that the initial grain size and strain levels play dominant roles in the final recrystallised grain size. These equations are valid for average grain size predictions, and the empirically fitted equation only fits limited conditions, for example poor agreements have been reported for Nb microalloyed steels at 0.3 strain [12].

Recently predictions of grain size distributions have been carried out. Kundu proposed the "halved grain size distribution" method to predict the recrystallised grain size distribution for Nb-microalloyed steels after deformation to 0.3 strain [12]. The idea is to treat each grain class in the distribution individually, and the recrystallised grain size is halved compared to its original grain class. Good agreements have been reported at 0.3 strain, 975 - 1075 °C for Nb microalloyed steels, Figure 2-44 [12]. Strangwood and Kaonda further extended the Sellars approach to predict recrystallised grain size distribution by introducing a variable D' for different grain size classes. That is, three different D' values have been applied to fit the finest grain size class (5% of distribution), the mode grain size class and the largest grain size class (95% of distribution) respectively. It has been reported that better fits than using equations 41 or 42 have been seen for C-Mn steel, high aluminium steels and forging steels at strain 0.15 - 0.7, mode grain size 25 - 380 μm. Nevertheless, discrepancies were still seen at

low strains and high contents of alloying elements [117]. Shon et. al recently studied the recrystallised grain size for Fe-32 Ni samples that were cold deformed then annealed [118]. The strain range was between 0.36 - 2.3, annealing temperature was 800 °C and the annealing time was 1 hour, the starting grain size was not specified in this case. The strain exponent for Shon's data is about -0.6, which is lower than -1. This may be due to the strains being much higher than those used during the development of Sellars model.

Uranga also proposed a model to predict the recrystallised grain size distribution. The idea is to consider each grain class individually and assumes that each grain size class would form a log-normal grain size distribution after recrystallisation, Figure 2-45 [119]. The mode recrystallised grain size is predicted by a modified equation 41. It has been reported that the predicted grain size distribution fitted better by using Uranga's model compared to simply applying the Sellars equation (equation 41) onto each grain size class, Figure 2-46 [119].

Table 2-9 Values of D' for various grades of steels summarised by Kundu [12]

Composition (wt.%)	D'
C- 0.17, Mn- 0.53, Si- 0.11	0.35
C- 0.17, Mn- 1.36, Si- 0.36	0.83
C- 0.15, Mn- 0.66, Si- 0.23	0.5
C- 0.15, Mn- 0.66, Nb- 0.044, Al- 0.017, N- 0.017	0.66
C- 0.16, Mn- 1.41, Nb- 0.041, Al- 0.02, N- 0.0054	1.1
C- 0.17, Mn- 1.25, Nb- 0.015, Al- 0.005, N- 0.0057, Ti- 0.025	1.86
C- 0.04, Nb- 0.04	0.9

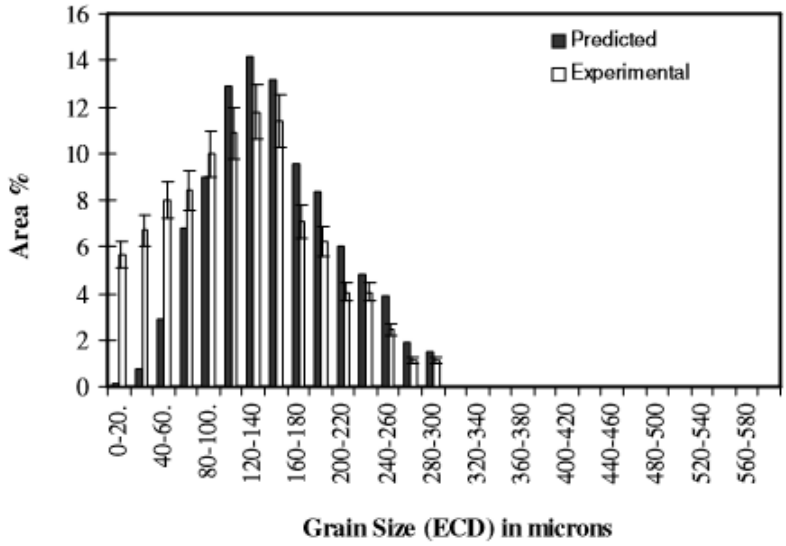

Figure 2-44 Predicted and measured recrystallised grain size distribution by using "halved grain size distribution" method for Nb-microalloyed steels at 0.3 strain, 1075 °C [12]

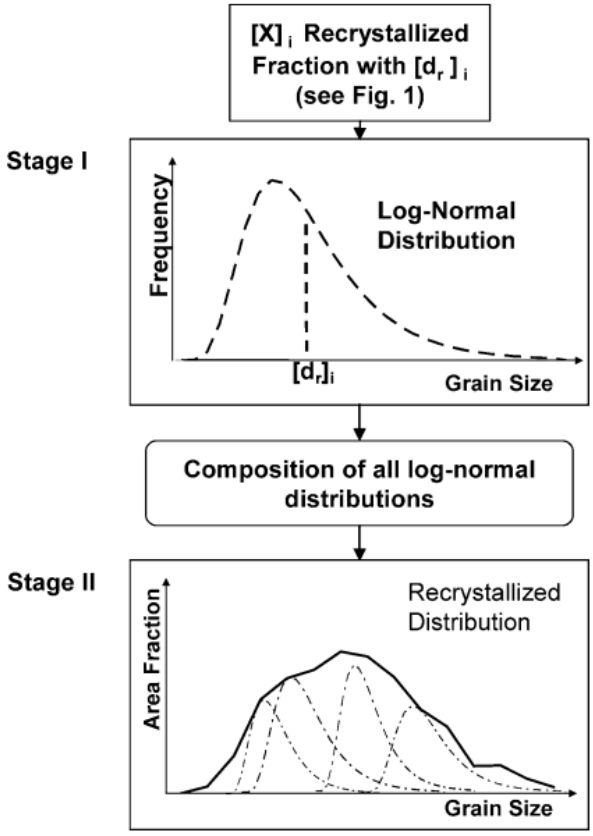

Figure 2-45 Schematic diagram of determining the recrystallised grain size distribution by Urganda's model [119]

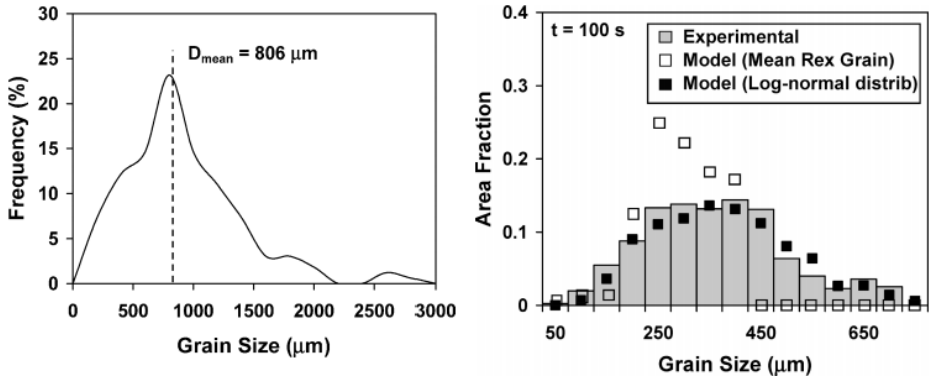

(a) (b)

Figure 2-46 (a) Initial grain size distribution of the homogenised sample (b) Experimental result and the predicted recrystallised grain size distribution by Urganda's model (log-normal distribution) and simply applying the Sellars equation onto each grain size class (Mean Rex Grain) [119]

2.8 Summary

The JMAK model has been widely used in describing the recrystallisation kinetics for metals and alloys deformed either cold or hot. A random distribution of recrystallisation nuclei and a constant recrystallisation growth rate are fundamental assumptions in the model. The Sellars approach further simplified the JMAK model, which is able to predict the recrystallisation starting and finishing time of steels within a certain range of composition, strain and temperature, that covers typical Nb-microalloyed steels and hot rolling deformation strains.

However, the nature of recrystallisation is inhomogeneous. It is widely accepted that the recrystallisation nucleation sites are located at grain boundaries and deformation bands rather than being randomly distributed. The recrystallisation nucleation mechanism requires a local stored energy variation and the nuclei density is dependent on the grain size and the strain level. In addition, the strain is inhomogeneously distributed and recrystallisation nucleates predominately in the heavily deformed regions, then the recrystallisation growth rate will be high in these regions, but then decrease when these high stored energy regions are consumed. It has been mentioned in recrystallisation studies on Al and Cu that the microstructure inhomogeneity could lead to a decrease in the Avrami exponent. Yet there is no comprehensive study in terms of the grain size effect on recrystallisation behaviour, and no model available to predict any connection between the microstructure inhomogeneity and the

recrystallisation kinetics.

The effect of cold and hot deformation on the dislocation density and dislocation arrangement has been considered. It has been shown that Fe-30Ni alloy has a comparable deformed microstructure, i.e. microbands and locally high strain regions at triple points and grain boundaries, after both hot and cold deformation. It has been reported that the stored energy after hot and cold deformation to the same strain is different and this has been suggested to be due to a number of reasons: differences in the flow stress during cold and hot deformation and therefore differences in the work done to achieve a given strain; possibility of dynamic recovery during hot deformation reducing the stored energy; and possibility of recovery during heating to the annealing temperature after cold deformation, also reducing stored energy. It has also been reported that the recrystallisation mechanism and Avrami exponents do not change due to different extents of recovery (and hence differing stored energy levels) prior to recrystallisation. However, if there are differences in stored energy levels between cold and hot deformed samples it is expected that the recrystallisation kinetics will be different. Using the equivalent strain method for hot and cold deformation proposed by Kaonda and using a fast heating rate, i.e. above 20 °C/s (as discussed in chapter 2.5.3), to the annealing temperature following cold deformation (to minimize recovery on reheating) and for relatively low strains and high strain rates during hot deformation (to avoid dynamic recrystallisation) may allow recrystallisation kinetics to be compared. In either case any determined Avrami exponents from hot and cold deformation should be comparable. A comparison between cold and hot deformation is summarised in Table 2-10.

It has been shown that the Avrami exponent is affected the grain size of the material but no method for predicting this effect has been given. Therefore, to improve the agreement between the prediction and the experimental results for recrystallisation requires accurate prediction of the Avrami exponent, hence understanding the effect of the grain size distribution on the recrystallisation kinetics is required.

Table 2-10 Comparison of cold and hot deformation to the same strain

	Cold deformation	Hot deformation
Microstructure after deformation	Deformed with little / no recovery	Deformed with potential for dynamic recovery (recrystallisation) depending on strain, strain rate and temperature
Hold at recrystallisation temperature	Potential for recovery during heating to recrystallisation temperature, depending on heating rate, strain and temperature	-
Deformation inhomogeneity	Microbands are seen. Grain boundaries and triple points are generally more deformed than grain interior.	
Recrystallisation nucleation site	Grain boundaries and triple points	
Recrystallisation growth rate and grain size respectively	Faster and finer Based on higher stored energy on deforming to same strain in absence of recovery	Slower and coarser Based on lower stored energy on deforming to same strain (with or without recovery)
Advantages	1) Observation of deformed microstructure without interference of significant dynamic recovery 2) Observation of early stage of recrystallisation nucleation 3) Little barreling effect, i.e. more homogeneous macroscopic strain distribution	1) Replicate the industrial processing route for hot rolled products, i.e. C-Mn steels, HSLA steels etc. 2) Empirically fitted model (Dutta-Sellars) is available.
Disadvantages	Potential for recovery during heating to annealing temperature reducing stored energy	

Chapter 3 Strain induced precipitation in deformed austenite

3.1 Introduction

Nb has always been considered as an important microalloying element for retarding recrystallisation over the last three decades. There are two mechanisms for microalloyed elements retarding recrystallisation, which are solute drag and precipitate pinning [84, 120]. Solute drag effect refers to the retarding force caused by the alloying elements segregating to the migrating boundaries. Precipitate pinning effect is caused by the precipitates forming before / during recrystallisation, which pin the migrating boundaries. If precipitate pinning dominates the retardation mechanism, the thermo-mechanical parameters, i.e. temperature, strain, strain rate are also of great importance to understand the retarding effect. Additionally, under conditions of cold deformation then annealing, the heating rate to the annealing temperature may also affect the precipitation kinetics as this can cause recovery affecting the dislocation structure before precipitation.

The effect of Nb (C, N) strain induced precipitation on recrystallisation mechanism is to retard or even halt the recrystallisation process. The Zener pinning equation has been widely applied to describe the recrystallisation and precipitation interaction for both cold deformed and annealing and hot deformed processes [121- 124]. Some models predict that strain induced precipitates (SIP) either stops or has no influence on the recrystallisation Avrami exponent [68]. Whereas many authors have shown that the Avrami exponents were constant or decreased in the presence of Nb(C,N) SIP for various strains, temperature ranges and Nb concentrations [2, 125- 127]. It is worth noting that whilst the precipitation and recrystallisation kinetics have been studied extensively, the effect of SIP on the recrystallisation mechanisms, i.e. nucleation, growth and Avrami exponent remains unclear. Therefore, a study on the effect of SIP on the recrystallisation Avrami exponent is considered here.

Strain induced precipitation has been observed in both cold deformed and annealed and hot deformed cases [128- 131]. Differences between the strain induced precipitation kinetics in cold and hot deformed cases is expected due to differences in the precipitate nucleation site density and the extent of dynamic recovery. That is, any dislocation density difference between cold and hot deformation leads to precipitation

nucleation site density variation, whilst the extent of dynamic recovery can significantly affect both precipitation nucleation and coarsening. Therefore, precipitation kinetics could be different depending on the deformation temperature (for hot deformation) and the heating profile during annealing (for cold deformation and annealing). However, independent of this it is possible to consider the effect of the actual precipitates size and number density on the recrystallisation Avrami exponent using either hot deformation or cold deformation and annealing situations.

Therefore, to fully understand the effect of strain induced precipitation on the recrystallisation mechanism, the precipitation kinetics in deformed austenite should first be fully understood.

3.2 Strain induced precipitation

There are two types of precipitates observed in deformed austenite; undissolved precipitates (typical size: 100- 300 nm) that are present in the material before deformation (for example formed during casting and retained during reheating in the case of hot deformation, or present in the hot rolled product before cold deformation and annealing) and strain induced precipitates - SIP (size: 5- 25 nm) that form during or after deformation and during the annealing stage, for example Figure 3-1 [132] showing both types of precipitate in a cold deformed then annealed austenitic stainless steel sample with 0.92 wt. % Nb. Strain induced precipitates preferably nucleate and grow on the dislocation networks, and the matrix or undissolved precipitates are randomly distributed, that and their different size mean they can generally be distinguished from each other.

Precipitates can act as recrystallisation nucleation sites, which is called particle stimulated nucleation (PSN), but the minimum precipitate size for PSN is approximately 1μm, which are typically precipitates that form during solidification [1]. It is reported that strain induced precipitates dominate the pinning effect on recrystallisation kinetics due to their fine size and considerably higher number density compared to undissolved precipitates. Therefore, only SIP will be discussed in the following sections.

Davenport et al. demonstrated that strain induced precipitates of Nb(C,N) have a cube-cube relationship with austenite when they form [133]. That is:

$$(100)_{PPT} // (100)_{\gamma}$$
$$[010]_{PPT} // [010]_{\gamma}$$

If the orientation of austenite grains changes after precipitation has occurred, e.g. by grain rotations accompanying deformation or recrystallisation, there would be no specific crystallographic relationship between the Nb(C,N) that had formed in the deformed austenite as there is no crystallographic orientation relationship between recrystallised and deformed austenite.

Strain induced precipitation, compared to matrix precipitation, refers to a phenomenon of precipitation preferentially occurring upon the dislocation networks. When austenite is plastically strained, crystalline defects (mainly dislocations) are introduced into the microstructure. All defects have higher average free energy, then the formation of a nucleus on the defects leads to the release of the free energy, and in return, this leads to a decrease in the activation energy barrier. Additionally, the dislocation network gives a rapid diffusion pathway along the dislocations, i.e. dislocation pipe diffusion that can accelerate precipitation kinetics [6]. Other preferential nucleation sites include excess vacancies, deformation bands, grain boundaries, twin boundaries, stacking faults and inclusions due to their higher free energy.

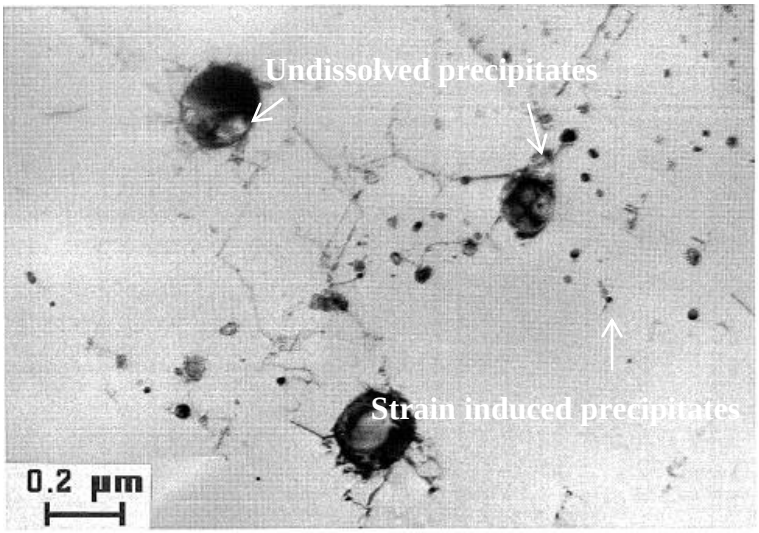

Figure 3-1 TEM image of SIP and undissolved precipitates of NbC in cold deformed and annealed austenitic stainless steel [132]

The precipitation rate can be described by the precipitation starting time, i.e. 5% precipitation. Precipitation – Temperature - Time curves (PTT) have also been widely used, which show the onset and finish of precipitation, under the effect of temperature and time, Figure 3-2 (a) [134]. The onset of precipitation is defined as 5% of the equilibrium precipitation amount, and 95% of equilibrium precipitation is the finish line, which depends on the deformation microstructure and on diffusion rates.

It is well established that a greater strain results in a higher precipitation number density and quicker precipitation behaviour for both hot and cold deformed then annealed samples, Fig 3-2 (b) [135]. It can be seen that the precipitation starting and finishing time decreases with increasing strain for Nb precipitates. This is attributed to the accelerated nucleation rate and growth rate due to the higher dislocation density in the more heavily deformed samples. The precipitation kinetics are accelerated by deformation in two ways. Firstly, dislocation nodes are favoured heterogeneous nucleation sites with a small nucleation barrier, i.e. lower critical free energy for precipitation [136]. Secondly, the accelerated diffusion of Nb along the dislocation pathways increases the diffusion coefficient. Perrard implied that the diffusivity of pipe diffusion should be 2 orders of magnitude faster than bulk diffusion [137]. Palmiere pointed out the activation energy for pipe diffusion is 210 kJ/mol, considerably lower than the 270 kJ/mol of bulk diffusion [138].

Moreover, the distribution of SIP in the deformed austenite is highly localized associated with the formation of localized work-hardened regions in both cold and hot deformed conditions, as shown in Figure 3-3 [8]. In Figure 3-3 (b), the cold deformed and annealed sample clearly shows the strain induced precipitates formed adjacent to the grain boundary region. This will affect recrystallisation due to the non-uniform distribution of both precipitates (acting as pinning points) and dislocation density (affecting the recrystallisation mechanism and driving force) [12].

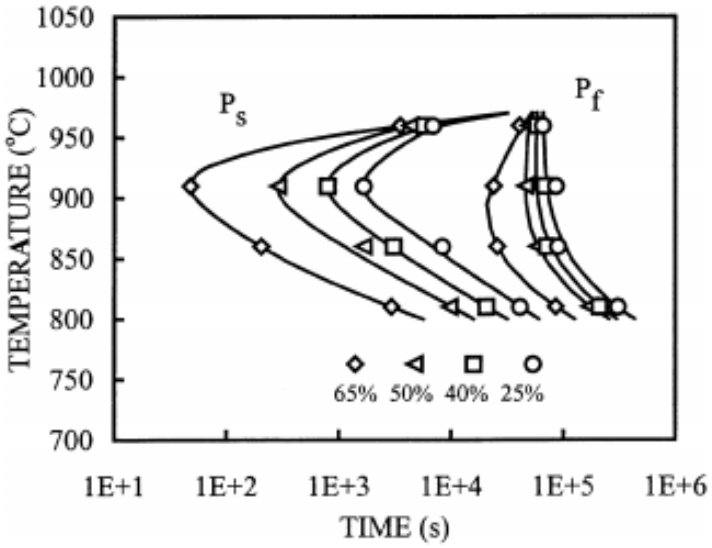

(a)

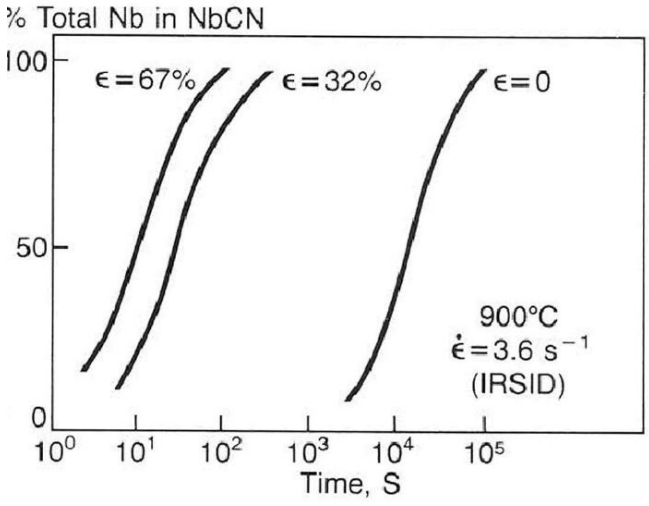

(b)

Figure 3-2 (a) Precipitation-Temperature-Time (PTT) diagram for Nb precipitates in a cold deformed Inconel alloy [132] (b) Precipitation evolution under different strain levels in hot deformed steel containing 0.17C, 0.011N, 0.04Nb [135]

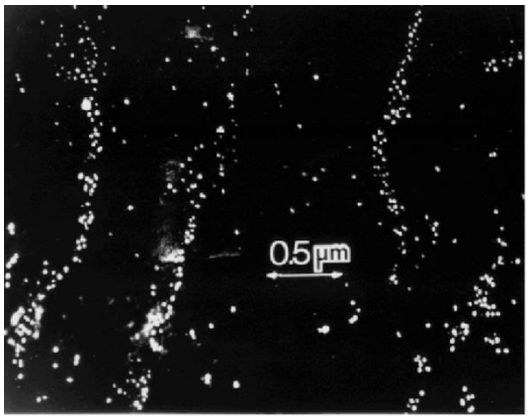

(a)

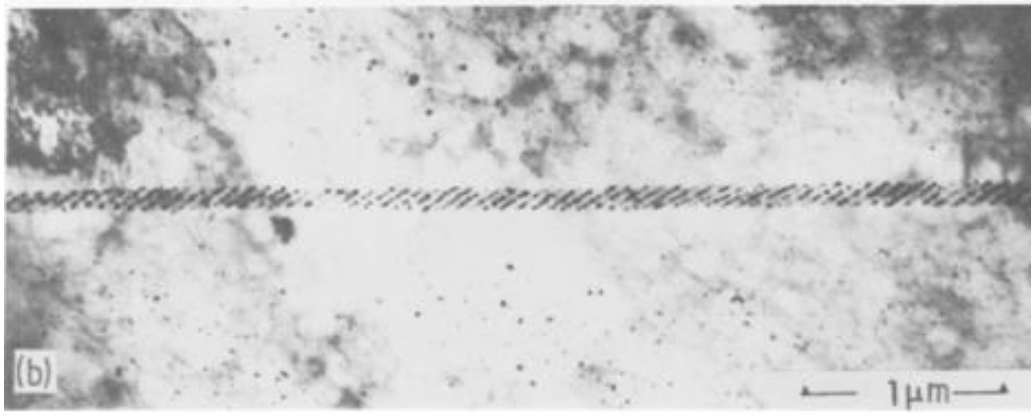

(b)

Figure 3-3 (a) Nb (C, N) SIP formed in deformed austenite for a HSLA steel containing 0.09%C, 0.07%Nb. The sample was deformed at 950 °C, 0.25 strain. Dark field TEM image using (111) NbC reflection [9] (b) NbC strain induced precipitates shown in an austenitic stainless steel with 0.5 wt. % Nb, The sample was deformed to 0.1 strain at room temperature, then annealed at 930 °C for 1800s; the horizontal black line feature in the centre is the grain boundary [139]

3.2.1 Precipitation driving force-solubility product

The driving force for precipitation, ΔG_V is a function of the undercooling and composition, with respect to the solute concentration in the matrix and in the precipitates [124]. It is given as:

$$\Delta G_V = -\frac{RT}{V_m} lnk_s \quad \ldots 42$$

Where R is the universal gas constant, T is the isothermal annealing temperature, V_m is the molar volume of the precipitates and ks is the supersaturation ratio at temperature T, i.e. solubility product.

The solubility product reflects the amount of a compound that is soluble in the matrix. The reaction for NbC can be written as:

$$Nb + C \rightarrow NbC \quad \ldots 43$$

There is a solubility limit for Nb and C at the isothermal annealing temperature, such that the excess of Nb and C atoms will have to form NbC. The higher concentration of Nb and C (i.e. supersaturated), the higher is the driving force for the precipitation process. Also, the precipitation reaction is at equilibrium when the compound concentration is below the equilibrium solubility product. Obviously, the supersaturation ratio is temperature dependent, and for NbC precipitation, ks is given as:

$$\log k_s = \log[Nb][C] = \frac{A}{T} + B \quad \ldots 44$$

Where [Nb] and [C] are the concentrations of Nb and C in solution (in wt. %), A and B are constants and T is temperature. Equations have been developed for different stoichiometry of NbC, NbN and Nb(C, N), examples for NbC are shown in Table 3-1. The most used solubility product is suggested by Irvine. It can be seen from Figure 3-4 that the solubility product varies significantly from different authors. Palmiere has summarised the solubility products for Nb (C,N), and commented that the differences among these products is related to the different techniques used in obtaining them

[140]. Hardness measurement, chemical separation of the precipitates, and thermodynamic calculations have been applied to predict the solubility, and each method has its own limitations. For example, hardness measurements and chemical separation method cannot detect all the precipitates in the matrix, which leads to a higher solubility than expected. Whereas many thermodynamic calculations neglect the effects of other alloying elements. Recently, Sharma et. al. investigated the effect of Mn, Cr, Si and Ni additions on the Nb solubility in austenite and found the effects can be significant even with low concentration, i.e. 1 wt.% [141]. Akben measured the effect of Mn on NbC solubility in HSLA steels and showed that the Nb(C, N) solubility increases with increasing Mn content from 0.42 to 1.9 wt. %, which leads to a decrease in precipitation rate by more than one order of magnitude, Figure 3-5 [142].

The high concentration of Ni in the Fe-30Ni model alloy that can be used to investigate recrystallisation in austenite is likely to affect the solubility of Nb, which will affect the precipitation of Nb(C,N) compared to HSLA steels with similar Nb, C, N levels. The solubility product for Nb in Fe-30Ni model alloy is discussed in the following section.

Table 3-1 Solubility product summary for niobium carbide

References	Solubility product
Irvine [143]	Log[Nb][C]=2.26-6770/T
Palmiere [140]	Log[Nb][C]=2.06-6700/T
Narita [144]	Log[Nb][C]=3.42-7900/T
Smith [145]	Log[Nb][C]=3.7-9100/T
Sharma [141]	$Log[Nb][C]^{0.87}$=2.81-7019.5/T
Lakshmanan [146]	$Log[Nb][C]^{0.87}$=3.4-7920/T

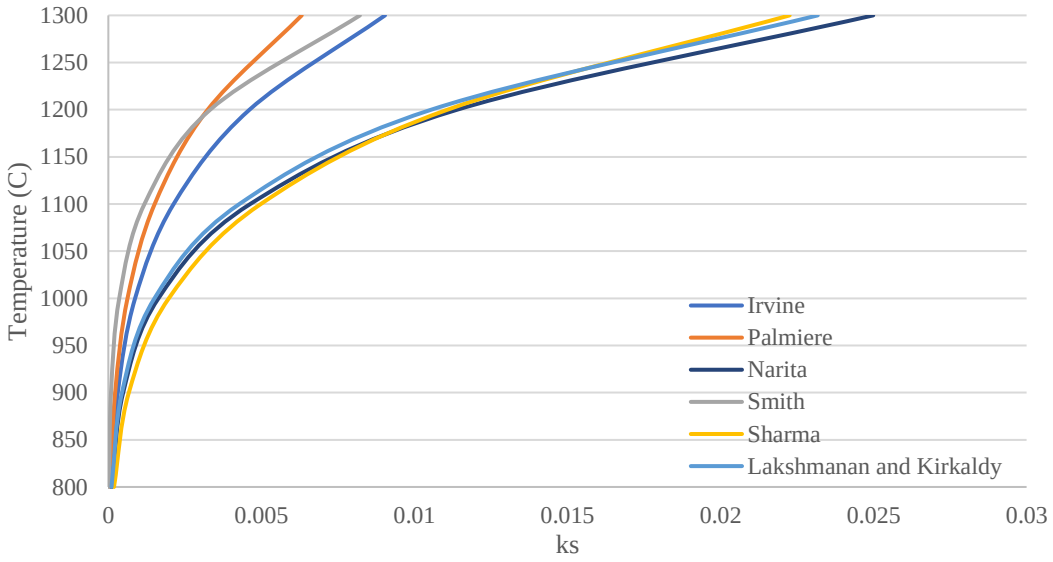

Figure 3-4 Diagram showing NbC solubility products found in the literature (Summarised in Table 3-1)

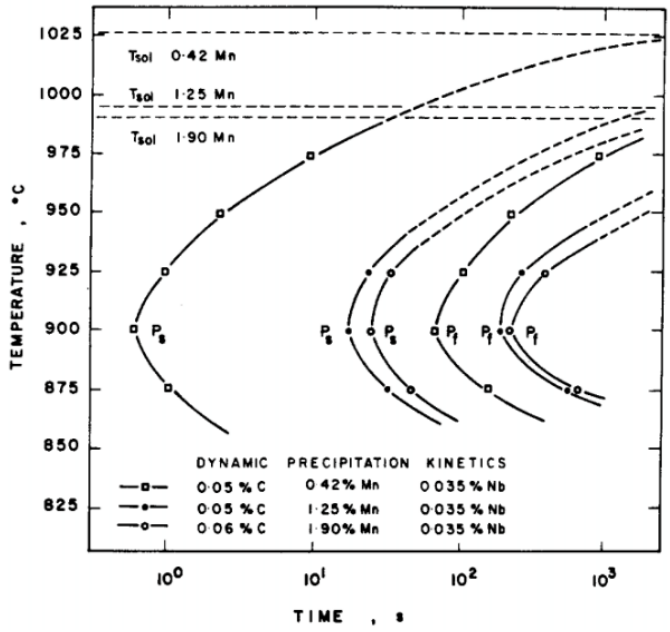

Figure 3-5 Precipitation starting and finishing time for Nb(C, N) for steels containing Mn from 0.42 - 1.9 wt.%. P_s and P_f represents the precipitation starting and finishing time respectively [142]

3.2.1.1 Effect of Ni on the solubility of Nb

Due to a larger γ-phase field in Fe-30Ni compared to in HSLA steels, a greater carbon solubility is expected, which leads to a higher solubility of NbC during reheating. Therefore, it is important in determining the solubility product to take other alloying elements into consideration. Nagarajan et al found the solubility product from Narita (Table 3-1) fitted their results for Fe-36Ni better than other predictions [147].

Thermo-Calc and other databases have been developed to take other alloying elements into consideration. Black has investigated the effect of Ni content on the solubility of NbC, with an example being given in Figure 3-6 for C-Mn steel compared to Fe-30Ni model alloy at 1150 °C [40, 147]. It can be seen that there is a higher solubility of NbC in the Fe-30Ni model alloy, i.e. reduced supersaturation, therefore a higher Nb content would be required to achieve equivalent Nb precipitation kinetics compared to in a conventional HSLA steel. In Black et al.'s work, a high Nb content, i.e. 0.1 wt. %, has been used in the Fe-30Ni alloy to compensate for the higher solubility effect, which is equivalent to 0.04 wt. % Nb in a C-Mn steel. Therefore it is clear that the solubility product produced for C-Mn steels might not be applicable for the Fe-30Ni alloy, therefore software packages such as Thermo-Calc can be used to take into account the effect of Ni on NbC solubility.

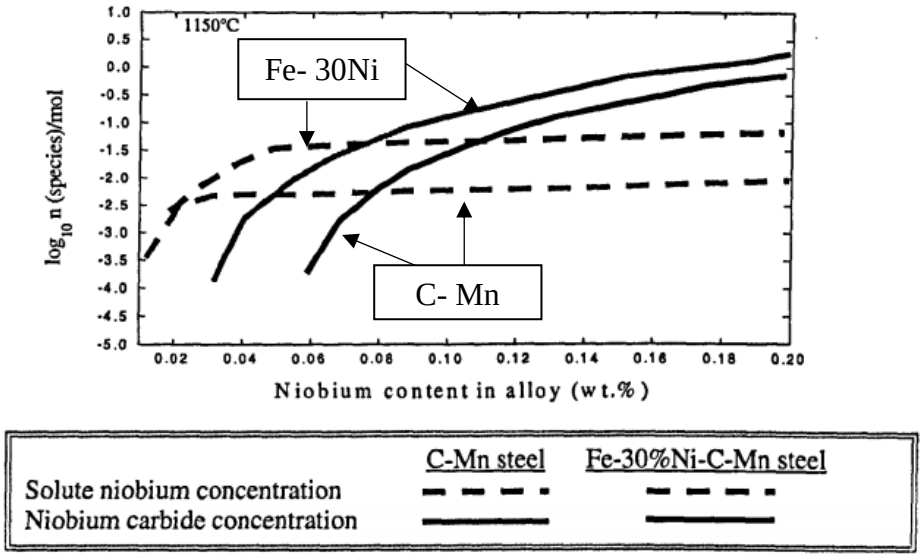

Figure 3-6 Plot determined from Thermo-Calc equilibrium solubility plots for C-Mn steel and Fe-30Ni model alloy. The y-axis shows the equivalent at. % concentration for NbC and solute Nb, while the x-axis shows wt. % niobium in the alloy [40]

3.2.2 Precipitation nucleation

Precipitation nucleation includes the formation of a stable nucleus, and the nucleus growth by diffusion in the austenite microstructure. The activation energy for precipitation nucleation includes an increase in the interfacial energy and the elastic misfit strain energy, whereas the volume free energy and the dislocation core energy (for strain induced precipitation only) decreases with nucleation process. Most studies have neglected the misfit strain energy caused by strain induced precipitates to reduce the complexity [124]. Then the free energy change is given as,

$$\Delta G = A\gamma - V\Delta G_V + \Delta E_d(r) \quad \ldots 45$$

Where γ is the interfacial energy, ΔG_V is the volume free energy, A and V are surface area and volume of the precipitates, r is the precipitate radius, and ΔE_d is the dislocation core energy change within the spherical region with radius r.

γ is the interfacial energy, which is between 0.5 and 0.8 J/m^2.

ΔE_d is given by,

$$\Delta E_d = -0.4Gb^2r \quad \ldots 46$$

Where G is shear modulus, b is burgers vector, r is the radius of the precipitate. Then the equation can be written as,

$$\Delta G = 4\pi r^2\gamma - \frac{4\pi r^3}{3}\Delta G_V - 0.4Gb^2r \quad \ldots 47$$

And the critical radius is calculated as,

$$r_c = \frac{2\gamma}{\Delta G_V} \quad \ldots 48$$

Replacing the radius r with critical radius, the activation energy for strain induced precipitation is then obtained as:

$$\Delta G = \frac{16}{3}\pi\frac{\gamma^3}{\Delta G_V^2} - 0.8Gb^2\frac{\gamma}{\Delta G_V} \quad \ldots 49$$

Many authors have predicted the critical nucleus size based on this approach, and by using the data shown in Table 3-2, the critical strain induced precipitate radius is determined to be approximately 0.5 nm, Figure 3-7. The order of precipitation should be: strain induced precipitation nucleation - grain boundary precipitation nucleation - matrix precipitation nucleation.

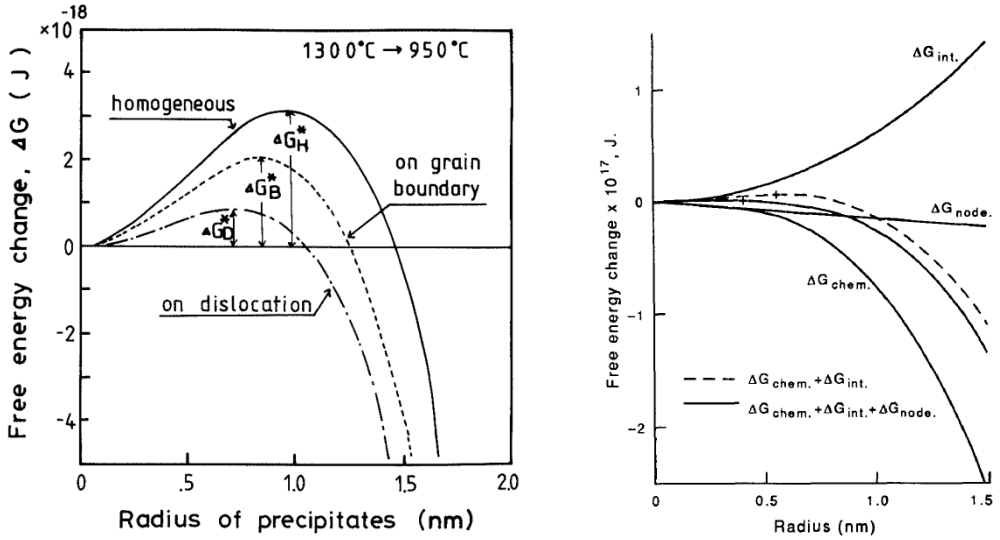

Figure 3-7 Free energy change for precipitation nucleation process calculated by (a) Okaguchi for 0.03 wt. % Nb - 0.02 wt.% Ti and (b) Dutta for 0.03 wt. % Nb [146] [149]

The precipitation nucleation rate is diffusion controlled, which is dependent on ΔG, the free energy of formation of a critical size nucleus, and D, the diffusivity of the solute in the matrix. The steady state nucleation rate is given by [124],

$$\dot{N} = \frac{1}{a^2}[Nb][N_0\exp(-\frac{\Delta G}{kT})][D_0\exp(-\frac{Q}{RT})] \quad \ldots 50$$

Where a is lattice parameter, N_0 is the number of available nucleation sites, D_0 is the diffusion coefficient and Q is the activation energy for solute diffusion. In this case, the diffusion coefficient of Nb will be applied. This is due to the diffusion coefficient of Nb being 5-7 times slower than carbon and nitrogen in the temperature range of

interest, Nb is then the rate-controlling element. [Nb] is the solute concentration, k is the Boltzmann's constant, T is the absolute temperature.

That is, a higher precipitation nucleation rate can be achieved by a lower activation energy for diffusion and a lower critical free energy of forming clusters. The number of available nucleation sites is linked to the dislocation density in the three-dimensional network, which can be calculated by [138]

$$N_0 \approx 0.5\rho^{\frac{3}{2}} \quad \ldots 51$$

3.2.3 Precipitation growth and coarsening

The increase in particle diameter with time during an isothermal hold can be expressed by the diffusion controlled growth theory proposed by Zener:

$$r_t^2 - r_c^2 = 2V_m D(C_{Nb} - C_r)t \quad \ldots 52$$

Where r_c is the mean particle radius at precipitation starting time, r_t is the mean particle radius at time t, C_{Nb} is the bulk concentration, C_r is the local concentration at the precipitate interface, V_m is the molar volume of the precipitate, D is the diffusivity and t is time. Since the diffusivity of the substitutional element Nb is significantly slower than the interstitial element C or N, it is assumed that the growth rate of Nb(C, N) is controlled by Nb. C_0 and C_r can be calculated as [128],

$$C_{Nb} = \frac{C_0 - C_p\frac{4\pi {r_t}^3}{3}}{1-\frac{4\pi {r_t}^3}{3}} \quad \ldots 53$$

$$C_r = C_e \exp(\frac{r_0}{r_t}) \quad \ldots 54$$

Where C_0 is the initial Nb concentration, and $r_0 = \frac{2\gamma V_m}{RT}$.

Precipitation coarsening occurs when the equilibrium precipitation has been reached. Dutta and Palmiere have reported that the strain induced precipitates start to coarsen

at an early stage of precipitation. The precipitation coarsening by Ostwald ripening is given by [150],

$$r_t^3 - r_c^3 = \frac{8V_m D\gamma C_e}{9RT} t \quad \ldots 55$$

The coarsening equation is for bulk diffusion, which shows a $t^{\frac{1}{3}}$ relation. Due to the higher diffusivity along the dislocation networks and grain boundaries, enhanced growth and coarsening has been observed. Zurob reported a dependence of $t^{\frac{1}{5}}$ for precipitation growth and coarsening of Ni-30Fe-0.8Nb with reduction of 10 % - 30 % at room temperature with isothermal holding at 700 °C up to 100 hours [151].

With development of detecting techniques, more and more precipitate data becomes available over a wide range of Nb content, strain and temperature. Most literature work have been focusing on the precipitation kinetics, but the precipitate size evolution is also of great importance because the precipitate pinning force is determined by both precipitation volume fraction, i.e. precipitation kinetics, and the precipitate size at that time. With the same volume fraction, a finer average precipitate size leads to a higher number density and thus, a higher pinning force.

The following section will discuss the effect of each parameter, i.e. temperature, strain level and Nb content, on the SIP growth and coarsening rate, i.e. size evolution. Literature from both cold and hot deformed conditions have been considered, the potential differences in precipitation kinetics attributed to the deformation temperature will be covered in chapter 3.3.

3.2.3.1 Effect of annealing temperature

Firstly, the effect of temperature on precipitate size will be discussed by using data available in the literature. The strain induced precipitate size increases with increasing temperature in both cold deformed and annealed and hot deformed cases and has been observed over a wide range of strain, temperature and Nb content. Stanford observed the precipitates size of NbC in Fe-Mn steel with 0.5 wt. % Nb after 0.07 strain deformed at room temperature and subsequent annealing. It was found that the precipitates size was 5 nm after annealing at 700 °C for 15 minutes, whereas the precipitates were significantly larger, i.e. 30 nm, after annealing at 800 °C for the same amount of time [152].

Kang, Kwon and Hansen observed that the precipitates size increases with increasing temperature (1000 - 850°C) with the same holding time for HSLA steels containing 0.03 - 0.095 wt. % Nb, 0.3 - 0.7 strain [91, 153- 154]. The SIP size is over 20 nm after 300s at 1000 °C compared to 4 nm at 850 °C, 300s. Weiss and Jonas have reported that the average precipitate size increases with temperature for the same strain and isothermal holding time [130]. This agrees with the precipitation growth and coarsening mechanism that the size evolution increases with increasing temperature.

3.2.3.2 Effect of strain

Strain level also plays an important role on strain induced precipitation kinetics. The dislocation network produces preferable nucleation sites for precipitates, and clearly a higher dislocation density, i.e. strain, would lead to a higher precipitation number density, i.e. a finer precipitates size at the same precipitation fraction. However, a higher dislocation density could accelerate diffusivity via pipe diffusion, i.e. faster growth and coarsening rate. Jones claimed that the increased nucleation site number density plays a more significant role on controlling the strain induced precipitate size than the accelerated pipe diffusion. Figure 3-9 shows that the strain induced precipitate size decreases with increasing strain for the same temperature and hold time [155]. The samples containing 0.5 wt. % Nb were either undeformed or deformed to 0.05 (5%) - 0.1 (10%) strain at room temperature prior to annealing at 930 °C for 0.5 hour. It can be seen that the precipitate size decreases with increasing strain, the average precipitates size of NbC in the undeformed sample is 9.3 nm, whereas it is 7.5 nm for

the 0.05 strain (cold deformed sample), 3.5 nm for the 0.1 strain (cold deformed sample). These results strongly support that the SIP size decreases with increasing strain in the absence of recrystallisation during precipitation. Le Bon found in a 0.03 wt. % Nb microalloyed steel that the strain induced precipitates size was comparable at 0.43 and 1.31 strain at 900 °C after 1000s. This was attributed to recrystallisation occurring concurrently with precipitation under these conditions where the moving boundary accelerated the precipitation coarsening rate [121]. Therefore, with increasing strain, the SIP size decreases with increasing strain if there is no interference from moving boundaries, i.e. recrystallisation.

3.2.3.3 Effect of Nb concentration

Thirdly, the effect of Nb content has also been investigated. As discussed in section 3.2, the precipitation driving force, i.e. supersaturation, increases with increasing Nb content. A faster precipitation growth rate is expected for a higher Nb content. Hansen observed the strain induced precipitate size distribution with either 0.031 or 0.095 wt. % Nb within the temperature range of 950- 850 °C at strain 0.9 (hot deformed), 10 - 10000s, Figure 3-10. It can be seen that there is no difference in the SIP size for the different Nb contents between 900- 850 °C where there is little growth exhibited. However at 950 °C, the average strain induced precipitates size increased from 7 to 13 nm when increasing Nb content from 0.031 to 0.09 wt. % at 10000s. Therefore, it suggests that the strain induced precipitates size increases with increasing Nb content because of an increase in growth rate.

No literature has been found on the effect of Nb content on the precipitation kinetics in cold deformed austenitic steels. However, it is not unreasonable to assume that the precipitation growth rate will be accelerated with increasing Nb content based on the diffusion controlled growth theory mentioned in chapter 3.2.3.

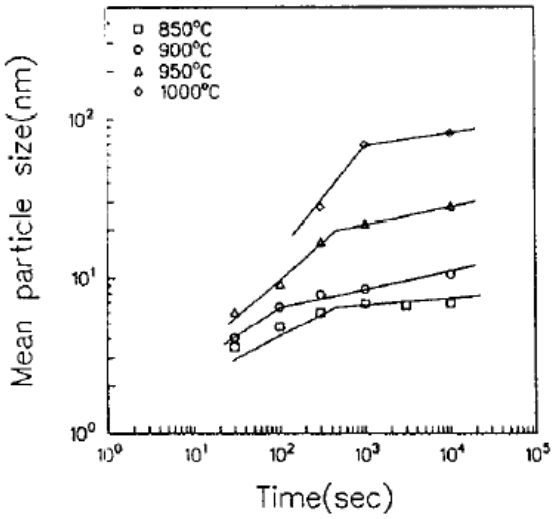

Figure 3-8 Precipitates size evolution in 0.03 wt. % Nb microalloyed steel hot deformed at 0.3 strain then held at various temperatures [153]

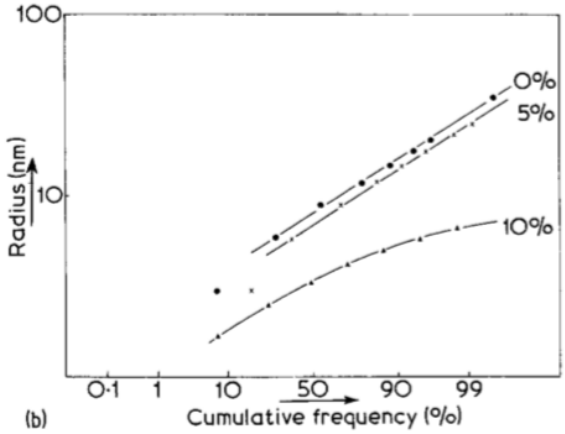

Figure 3-9 Effect of strain on the strain induced precipitate size. The austenitic stainless steel was cold deformed to 0.05 - 0.1 strain then annealed at 930 °C for 0.5 hour [35].

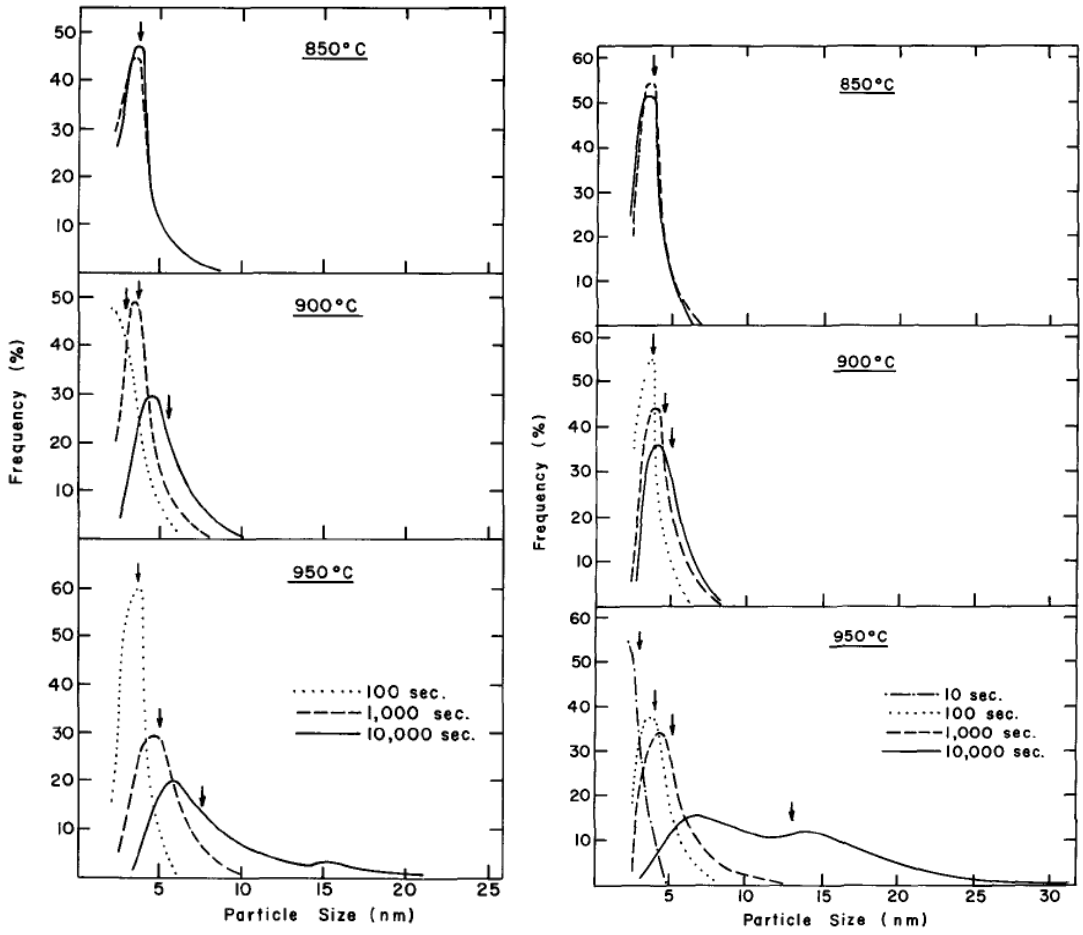

(a) (b)

Figure 3-10 SIP size evolution in HLSA steels with (a) 0.031 wt. % Nb (b) 0.095 wt.% Nb at temperature range 950 - 850 °C, strain 0.9 [91]

3.2.4 Precipitation kinetics

Precipitation kinetics can be described by a JMAK model. Strain induced precipitation is clearly a heterogeneous nucleation process, the heterogeneous nucleation sites include grain boundaries, edges, corners and dislocations. Cahn has summarised the Avrami exponents for heterogeneous nucleation at these sites, Table 3-2. It can be seen that precipitation on grain boundaries is expected to have an Avrami exponent of 1 assuming that precipitation nucleation is site saturated. Similarly, the Avrami exponent for strain induced precipitation nucleated on the dislocation networks, i.e. dislocation nodes and along the dislocation lines, is expected to be low, i.e. 1 or 2 attributed to the nature of the heterogeneous nucleation.

In practice, the Avrami exponent has often been observed to be lower than 1 in both cold deformed and annealed and hot deformed cases. Liu observed the precipitation kinetics in cold deformed Fe-50Ni Inconel alloy, annealing temperature range 810 - 960 °C, strain 0.29 - 1. The Avrami exponents for various conditions were between 0.5 - 1.3 [14]. Wang and Zurob have observed NbC precipitation kinetics in cold deformed Ni-30Fe-0.851 wt. % Nb model alloy. An Avrami exponent value of 0.3 within a strain range of 0.1 - 0.3 has been reported [156]. As for the hot deformed condition, Pereloma stated that the Avrami exponent is between 0.4 - 1.1 for a 0.037 wt.% Nb microalloyed steel after 0.22-0.56 strain and holding between 800 - 900 °C [157]. It has been reported that inhomogeneity in precipitation nucleation and growth leads to a low Avrami exponent, and there does not appear to be any correlation between the reported Avrami values and the strain levels or Nb contents.

Recently, Nagarajan and Palmiere proposed that the precipitation kinetics could be obtained through the precipitation nucleation, growth and coarsening rate [147]. The equation is given by,

$$N = \frac{XV}{\frac{4\pi r_t^3}{3}} \quad \ldots 56$$

Where X is the precipitation fraction, V is the equilibrium volume fraction, N is the number density of the precipitates and r_t is the precipitates size. That is, during the nucleation and growth stage, N and r can be calculated through the nucleation rate and precipitation growth rate. During the coarsening stage, the precipitation fraction is constant, therefore, N is only related to the precipitation coarsening rate. A discrepancy has been reported when using this method to predict the precipitation kinetics for Fe-30Ni-0.38 wt. % Nb, which could be attributed to the faster coarsening kinetics in reality, i.e. pipe diffusion, than bulk diffusion assumed in the prediction [147]. A faster precipitation coarsening rate has also been observed in Nb containing microalloyed steels due to the presence of dislocation networks [124, 148].

To sum up, although the JMAK model has been widely applied to describe precipitation kinetics, a range of Avrami exponents have been reported in the literature attributed to the heterogeneous nucleation of precipitates.

Table 3-2 JMAK model parameters under different heterogeneous nucleation conditions, summarised by Cahn [40]

Nucleation site	Avrami exponent	k
Homogeneous	4	$\frac{\pi}{3} I v^3$
Grain boundary	1	$2 S_{gb} L_{gb}$
An edge on grain boundary	2	$\pi L_{gb} v^2$
A corner on grain boundary	3	$\frac{4}{3} \pi N_c v^3$

Where I is the nucleation rate, v is the growth rate, S_{gb} is area of grain boundary per unit volume, L_{gb} is length of grain boundary edge per unit volume and Nc is density of grain boundary corners.

3.2.5 Cold deformed and annealed and hot deformed precipitation kinetics comparison

As mentioned above, strain induced precipitation occurs in both cold deformed and annealed and hot deformed conditions. Due to the difference in stored energy and the extent of recovery for the two situations (discussed in Chapter 2), the precipitation kinetics can be expected to be different. Nevertheless, the main focus for this chapter is to investigate how strain induced precipitation size and number density affects the recrystallisation Avrami exponent. Any knowledge gained on the interaction between precipitate size, number density and the recrystallisation, i.e. effect on the Avrami exponent will be applicable for both cold and hot deformed situations, although the strain / temperature / Nb content influence on the recrystallisation kinetics will be deformation mode dependent (as discussed in the previous chapter). This statement assumes that the mechanism of interaction is the same between cold and hot deformed samples (i.e. SIP forming on dislocation networks).

Firstly, it has been mentioned that the precipitation starting time decreases with increasing strain, i.e. dislocation density, for both cold deformed and annealed and hot deformed conditions. It has been mentioned in chapter 2.5.2 that the cold and hot

deformed sample for the same strain could have a different stored energy, i.e. dislocation density, attributed to the differing levels of recovery experienced. As a result, the number density of preferential nucleation sites for strain induced precipitation could vary. Black discussed the deformed microstructure in Fe-30Ni model alloy after deformation to 0.25 or 0.5 strain between the temperature range of 900 - 1050 °C [40]. It was found that both microbands and cell-structures/ subgrains were shown at 900 °C and 950 °C, whereas only an equiaxed subgrain structure was seen at 1050 °C due to dynamic recovery at strain 0.5. It was summarised in chapter 2.5 that the Fe-30Ni model alloy cold deformed microstructure contains both microbands and cell structures. This suggests that the dislocation network morphology will be similar for hot and cold deformed material only at temperatures less than 1050 °C based on the statement above, although the number of preferential SIP nucleation sites could vary for the different deformation / annealing temperatures.

Secondly, precipitation kinetics could be different after cold and hot deformation even if the samples have the same stored energy. Dynamic recovery could accelerate the strain induced precipitation kinetics via increasing the local Nb concentration due to migration of dislocations and low angle grain boundaries. A direct observation of Nb segregated to dislocations after hot deformation has been made by Takahashi via atom probe [158]. As a result, the precipitation growth and coarsening could be accelerated during hot deformation. As for cold deformation, the extent of recovery occurred during / after cold deformation and annealing process could be different from during hot deformation, therefore, the extent of Nb segregation adjacent to the dislocation network could also vary, which affects the precipitation kinetics.

There is no direct comparison of the number density of strain induced precipitates between cold and hot deformed samples with the same Nb concentration, strain and (hot deformation and annealing) temperature in the literature. However, the precipitation kinetics in both cold and hot deformed samples have been reported and are summarized below to gain an insight into the NbC precipitation onset time and the growth mechanism for both cold and hot deformed conditions.

3.2.5.1 Cold deformed precipitation kinetics

The precipitation kinetics reported for cold deformed and annealed samples have been found to vary significantly in the literature due to different compositions, strain levels and temperatures being considered. The discussion below summarises the NbC precipitation in austenitic steels.

Kisko observed the strain induced precipitation kinetics in austenitic stainless steel containing 0.05 - 0.45 wt. % Nb. The samples were deformed to a strain of 0.9 at room temperature, the annealing temperature was 1100 °C with a heating rate of 200 °C/s [159]. The precipitates size has been reported to increase with $t^{1/3}$ - $t^{1/6}$ depending on the Nb level. Wang and Zurob measured the precipitation kinetics in a cold deformed Ni-30Fe alloy with 0.85 wt. % Nb, where the strain level was 0.1 - 0.36 and the annealing temperature was 700 °C, Figure 3-11. It was found that 10% equilibrium precipitation is between 20 - 100s depending on the strain level [151]. The precipitates size evolution grew from 2 nm to 10 nm after annealing for 100000s, which follows the relationship of $t^{1/5}$.

From the discussion above the onset of precipitation (5%) could be very early, i.e. within seconds, in the cold deformed then annealed conditions for NbC in austenitic steels. No reports have been found for NbC precipitation kinetics in cold deformed Fe-30Ni model alloy, where the precipitation kinetics will be affected by the different supersaturation of Nb in the material. The precipitation growth and coarsening dependence on time, i.e. $t^{1/5}$, agrees well with the growth and coarsening mechanism along the dislocations (mentioned in 3.2.3).

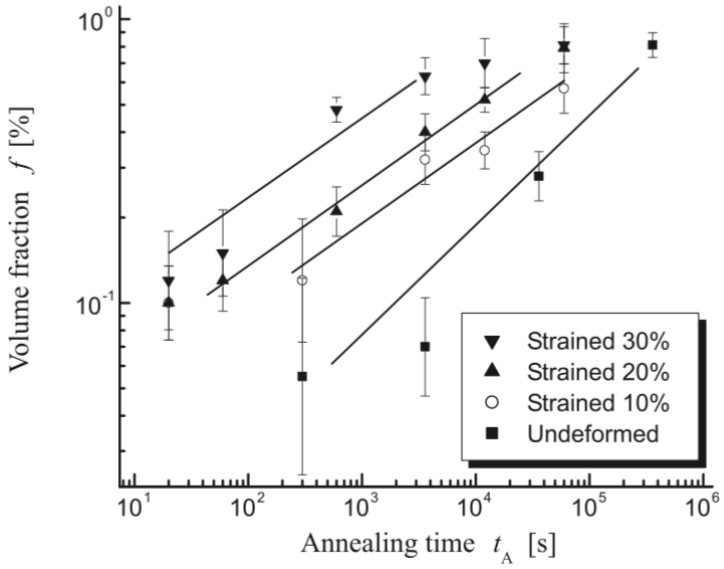

Figure 3-11Precipitation fraction versus time for NbC in a cold deformed Ni-30Fe-0.85Nb model alloy. The annealing temperature was 700 °C [151]

3.2.5.2 Hot deformed precipitation kinetics

The strain induced precipitation starting time has been extensively studied in hot deformed samples over the last three decades due to its importance in controlling recrystallisation during hot rolling.

Table 3-3 summarises the reported time when strain induced precipitates became detectable for various temperatures, strains, strain rate and detecting method. It can be clearly seen that strain induced precipitates have been observed by various groups within the temperature range of 850 - 1000 °C, strain 0.2- 0.7 within 10s of holding at temperature. Palmiere and Janamapa pointed out that the onset time could be as short as 1s for a strain of 0.3 [138]. A comparable precipitation starting time has been reported for hot deformed Fe-30Ni model alloy where Abdollah-Zadeh observed strain induced precipitates at 10s in samples deformed to 0.2 strain with Nb content of 0.02 wt.% [11]. It is not unreasonable to assume that strain induced precipitation occurs at the very early stage of holding at temperature, for example during the onset of recovery and recrystallisation.

To sum up, strain induced precipitation kinetics in both cold deformed and annealed and hot deformed conditions have been reviewed. The reports suggest that the onset of NbC precipitation can be very early in both conditions. However, no literature was found for NbC precipitation in cold deformed then annealed Fe-30Ni model alloy. Therefore, no straightforward comparison could be made in this case. That is, strain induced precipitation kinetics is dependent on the strain level, isothermal annealing temperature and Nb level in both cold and hot deformed samples. As discussed, due to the variation in the stored energy and the extent of recovery, the precipitation kinetics are not directly transferrable between the cold and hot deformed samples (for the same strain and temperature).

Nevertheless, the interaction between precipitates and the moving boundaries, i.e. recrystallisation, is dependent on the precipitates number density and the size distribution. Thus, though the precipitation kinetics is not comparable, the effect of precipitation (at certain size and number density) on the recrystallisation kinetics could be transferred. This will be fully explained in the following section.

Table 3-3 Summary of strain induced precipitation literature

References	Steel chemistry		Deformation conditions			Detection method	Earliest precipitation detection
	%Nb	%C	Temperature, °C	Strain	Strain rate		
[160]	0.16	0.02	1000	0.2	0.5	TEM	1s
[153]	0.03	0.076	850-1000	0.3	10	TEM	3s
[154]	0.042	0.1	900-1000	0.3	10	TEM	10s
[131]	0.033	0.099	950-1000	0.2	10	TEM	10s
[91]	0.031	0.1	850- 950	0.7	2.6	TEM	10s
[91]	0.095	0.11	850- 950	0.7	2.6	TEM	10s
[40]	0.1	0.097	950-1050	0.25	10	TEM	1s
[124]	0.12	0.081	800-1000	0.29	4.2	TEM	0.2s
[138]	0.03	0.1	850-1050	0.1-0.4	10	Softening	1.9s
[161]	0.08	0.1	900	0.44	11	Flow stress	10s
[162]	0.041	0.011	900- 1025	0.2, 0.35	3.6	Softening	10s
[136]	0.05	0.054	900- 950	0.1, 0.25	0.1-0.01	TEM	1s
[130]	0.035	0.05	900-950	0.11-0.75	0.012	TEM	-
[135]	0.04	0.17	900	0.43, 1.31	3.6	TEM	-
[163]	0.031	0.16	800-1100	0.8	-	Hardness	10s
[11]	0.02	0.15	850-1000	0.2-0.9	0.7	TEM	10s
[164]	0.1	0.1	950	0.45	10	TEM	-
[151]	0.085	0.114	700	0.1-0.3	-	STEM	20s

3.3 Interaction between recrystallisation and precipitation

Precipitates interact with recrystallisation in two ways; interactions with dislocations delaying recovery, and stopping grain boundary migration during recrystallisation [136]. The pinning effect of fine particles (d< 0.1μm) is known as Zener drag [1], where the pinning force can be obtained from the precipitate size and number density. If it is assumed that the precipitates are distributed uniformly in the matrix, and Nb(C, N) precipitates are spherical, then the pinning force is given by,

$$F_p = 4r\gamma N_s \quad \ldots 57$$

Where r is the particle radius, γ is the interfacial energy, N_s is the number of particles per unit area.

N_s can be estimated using different models and assumptions, Table 3-4. Recent work has suggested that the subgrain model from Hansen is the most realistic approach for SIP [9]. However, as mentioned, the dispersion of Nb(C,N) is highly localized, Fig 3-12. Thus, the precipitate-pinning force at the preferential recrystallisation nucleation sites will be far higher than the predicted value of Zener drag.

There are three ways in which precipitation interacts with recrystallisation, Table 3-5. It can be seen that there are three stages of interaction behaviour. In stage I, recrystallisation is predicted to complete before any SIP and thus, there is no retardation due to precipitation pinning. The precipitation starting time shifts to the left (shorter time) in the deformed austenite grains compared to undeformed austenite with decreasing temperature. This is due to the greater thermodynamic driving force for precipitation. In stage II, recrystallisation is retarded due to SIP occurring on the deformation substructure during recrystallisation. Then, in stage III, SIP occurs before recrystallisation, and the resulting pinning force will locally halt the recrystallisation process if the pinning force exceeds the recrystallisation driving force.

Jones and Yang have proposed that recrystallisation will be halted once SIP has occurred for cold deformed aluminium alloy [121, 122]. Dutta and Sellars have proposed the same criteria for hot deformed microalloyed steel [124, 148]. That is,

only the onset of precipitation is required to be considered. However, different authors have observed that the presence of SIP during recrystallisation could lead to a 'plateau' or reduction in Avrami exponent instead of a complete halt to recrystallisation.

The following section has considered both cold and hot deformed cases. As mentioned, different deformation conditions could affect the precipitation size and number density, i.e. precipitation kinetics, therefore, the absolute values of pinning force might not be directly comparable between cold and hot deformed conditions for the same strain and isothermal holding temperature. However, the interaction mechanism, i.e. Zener pinning, is applicable in both cases, therefore, whilst the measured SIP data in the cold deformed condition cannot be used to describe/ predict the precipitation kinetics for hot deformation, the evolution of the pinning force and its interaction with recrystallisation, which leads to a change in Avrami exponent is comparable.

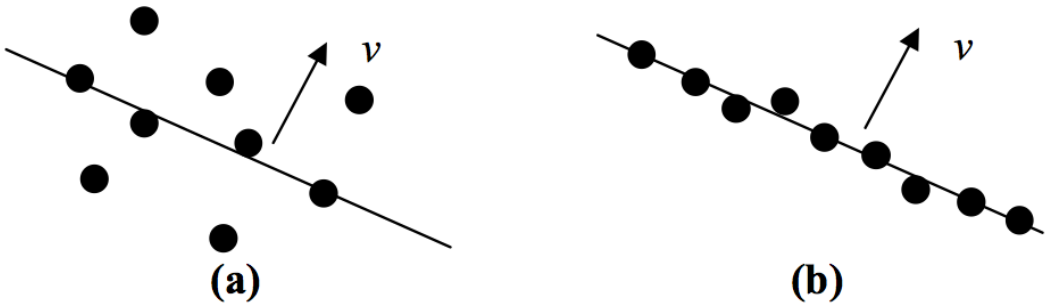

Figure 3-12 Schematic diagram of precipitation pinning effect on boundary migration (a) precipitates randomly distributed in the matrix (b) precipitates heterogeneous nucleated on the deformation substructure

Table 3-4 The models for estimating the precipitate pinning force [9]

Model	Equation	
Rigid boundary	$\boldsymbol{F = \frac{6\gamma f_v}{\pi r}}$	The boundary interacts with particles lying within a distance of ±r of the boundary plane.
Flexible boundary	$\boldsymbol{F = \frac{3\gamma f_v^{\frac{3}{2}}}{\pi r}}$	The boundary interacts with every particle within a single plane until fully pinned
Sub- boundary model	$\boldsymbol{F = \frac{3\gamma f_v}{2\pi r^2}}$	The precipitates are formed on the subgrain boundaries

Table 3-5 The interaction between pinning force, F_p, and the driving force of recrystallisation, F_R [165]

I	$F_R \gg F_p$	Boundary migration is not affected	Dislocations are swept up during recrystallisation, which eliminates the nucleation sites for SIP.
II	$F_R > F_p$	The boundary may move, but at reduced velocity.	The recrystallisation evolution leads to a non-uniform dislocation density, thus, SIP distribution might be heterogeneous.
III	$F_R < F_p$	Boundary migration is halted	Precipitates nucleate on the dislocations pinning the subgrain boundary migration.

3.3.1 Effect of SIP on recrystallisation Avrami exponent

It is clear that the RPTT curve has only considered the effect of SIP on the recrystallisation starting time. In practice, SIP could grow and coarsen during recrystallisation. Therefore, the effect of SIP during recrystallisation also needs to be considered. However, various results with little agreement have been found for the effect of SIP on the recrystallisation Avrami exponent.

3.3.1.1 Cold deformed condition

A reduced Avrami exponent or plateau was reported during annealing of cold deformed samples in a cold rolled Al-0.5 wt. % Zr alloy to a strain of 1, Figure 3-13 [125]. The Avrami exponent was measured to be 1 between 565 - 585 °C, whereas a plateau was observed between 2000 - 4000s at 555 °C, which was attributed by the authors to the presence of strain induced precipitation. Huang investigated the effect of strain induced precipitation on the recrystallisation kinetics of cold deformed aluminium alloy to a strain of 1.6 [126]. A reduced Avrami exponent was observed at 300 °C when SIP occurs during recrystallisation.

However, others have observed that recrystallisation was completely halted by the presence of strain induced precipitation. Jones reported a halt in recrystallisation with the presence of strain induced precipitates for a cold deformed aluminium alloy to a strain of 1.6 between 370 - 410 °C [121]. Yang has investigated the recrystallisation kinetics in Al-0.09 wt. % Sc-0.09 wt. % Zr after cold strain of 2. Recrystallisation was halted once SIP occurred in the matrix between 375 - 325 °C [122]. No literature has been found regarding the SIP and recrystallisation interaction in steels following the cold deformation.

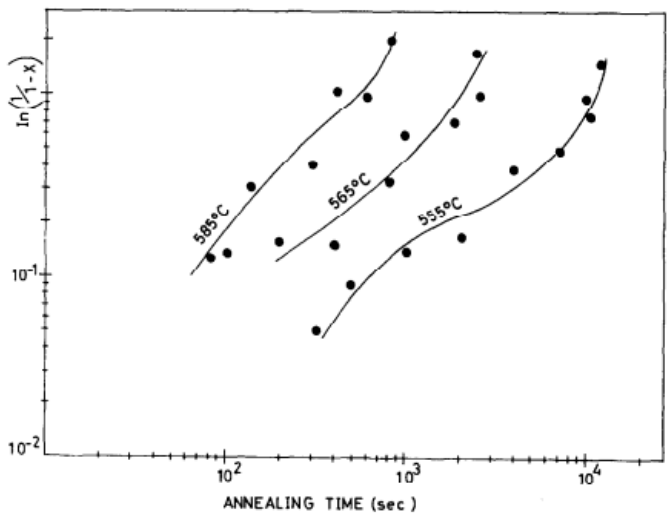

Figure 3-13 log ln (1/1-x) versus log time diagram. The Al-0.5 wt. % Zr samples were annealed at various temperatures after cold rolling to a strain of 1 [125]

3.3.1.2 Hot deformed condition

Similar results have been found in the hot deformed condition. Kang, Medina and Fernandez have reported a plateau recrystallisation behaviour caused by strain induced precipitation at strain 0.3 - 0.35, Nb level 0.03 - 0.045 wt. % and temperature range of 850 - 975 °C [2, 162]. Vervynckt has observed strain induced precipitates retarding recrystallisation at 1000 °C for a 0.16 wt. % Nb steel after 0.2 strain. Figure 3-14 shows the precipitates pinning force with time, it can be seen that the pinning force increases with time during the nucleation and growth stage, and that recrystallisation has halted once the pinning force exceeds the recrystallisation driving force. When the precipitates start coarsening, the pinning force decreases and recrystallisation continued [81]. Therefore, a plateau is shown in the 1000 °C recrystallisation curve during which time the SIP halts recrystallisation.

Le Bon et al reported a delay in the onset of recrystallisation in 0.044 wt. % Nb steel at 900 °C, 0.4 or 1.3 strain [135] and Hansen et al also reported that the strain induced precipitates delayed the onset of recrystallisation and gave a slower recrystallisation growth rate for a Nb content range of 0.031 - 0.095 wt. %, strain 0.7, temperature range of 850 - 950 °C [91]. Whereas there were no plateau shown in both the recrystallisation kinetics.

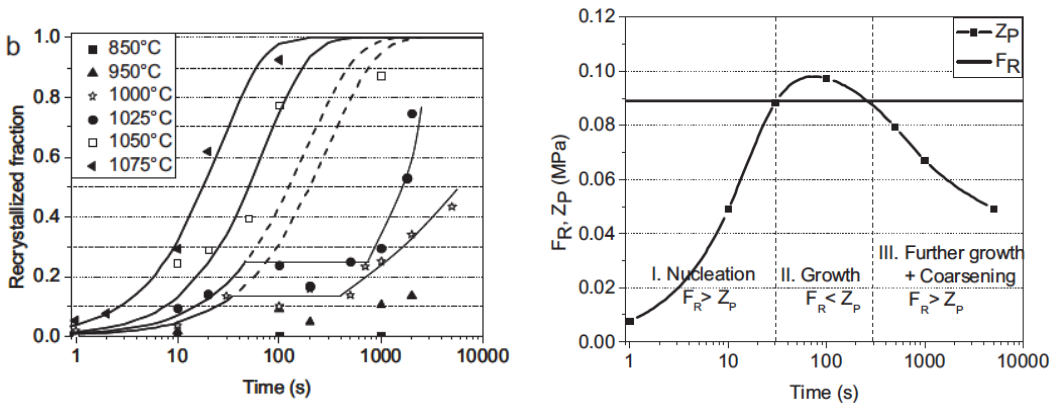

(a) (b)

Figure 3-14 (a) Recrystallisation behaviour of C-Mn-0.16 Nb steel at various temperatures, 0.2 strain (b) pinning force evolution at 1000 °C of C-Mn-0.16Nb steel, 0.2 strain [81]

It can be seen that there are different ways on how SIP changes the recrystallisation Avrami exponent. It is reported that a plateau has been observed in the temperature range of 900 - 1000 °C, strain 0.2 - 0.35, Nb level 0.03 - 0.16 wt.% for hot deformed microalloyed steels. Whilst in cold deformed aluminium alloy, the strain level where the plateau or reduced Avrami exponents was observed is between 1 - 1.6, which is significantly higher. No literature has been found for cold deformed conditions at relatively low strain, i.e. 0.2 - 0.3 strain. As a result, there is a lack of data on how SIP affects the recrystallisation kinetics at low strain levels for cold deformed then annealed samples.

Nevertheless, it has been clearly shown that the onset of precipitation, i.e. precipitation nucleation, is insufficient to describe / predict the interaction between precipitation and recrystallisation for both cold and hot deformed conditions. Therefore, to determine the interaction between recrystallisation and precipitation, knowledge of the amount of precipitation, the precipitation size evolution, i.e. growth and coarsening behaviour, is important.

3.4 Summary

This chapter has reviewed the precipitation nucleation and growth mechanisms, the precipitation kinetics for both cold deformed and annealed and hot deformed conditions. The effects of strain, temperature and Nb content on strain induced precipitation have been explored in detail. It has been shown that precipitation starting time is insufficient as the criteria for defining the interaction between precipitation and recrystallisation. The precipitation growth and coarsening rate are important as, when occurring during recrystallisation, they change the recrystallisation Avrami exponent. Additionally, to predict any plateau time during recrystallisation, a consideration of precipitation coarsening is crucial.

The differences in precipitation kinetics for cold deformed and annealed and hot deformed conditions have been summarised. It is clear that the precipitation kinetics are not comparable between the two situations, even for the same strain and annealing / hold temperature, which will be related to recovery affecting the dislocation density. However, the effect of the precipitates that form (considering their size and number density) on the recrystallisation Avrami exponent, is comparable.

Therefore, to further investigate the effect of precipitation on the recrystallisation rate and mechanism, and hence Avrami exponent, then the precipitation size evolution, i.e. growth and coarsening, needs to be investigated.

Chapter 4 Aims and objectives

It has been identified that there are gaps in current recrystallisation knowledge to predict the effect of grain size distribution on recrystallisation Avrami exponents and in predicting the effect of precipitation size evolution during recrystallisation on the recrystallisation Avrami exponent. The objectives are listed as follows:

- Characterise the recrystallisation kinetics in a Nb-free Fe-30 Ni model alloy after heat treatment to give different initial grain size distributions.

- Determine the Avrami exponents from the recrystallisation kinetics using hardness and optical analysis. Use in-situ EBSD to characterise the progress of recrystallisation, i.e. inhomogeneity, and the role of grain size distribution.

- Relate the Avrami exponent to the grain size distribution in the Fe-30 Ni model steel.

- Compare the effect of the grain size distribution on the Avrami exponent for both cold deformed and annealed and hot deformed conditions and validate the generic applicability of the relationship between Avrami exponent and grain size distribution.

- Compare the recrystallisation kinetics (cold deformed and annealed condition) for Nb-free and Nb-containing Fe-30Ni model alloy to determine conditions where precipitation affects recrystallisation.

- Measure precipitation number density and size distribution using TEM for the Nb-containing Fe-30 Ni model alloy during recrystallisation (cold deformed and annealed condition).

- Link the precipitation kinetics and size evolution to the recrystallisation Avrami exponent to determine the influence of size, number density and precipitate growth / coarsening.

- Compare the precipitation number density and size distribution during recrystallisation for cold deformed and annealed and hot deformed conditions. Validate the generic observations for the influence of precipitate number density and size evolution on recrystallisation and identify the differences between cold deformed and annealed and hot deformed conditions.

Chapter 5 Experimental Procedures

5.1 Introduction

The experimental work has been designed to investigate the effect of initial grain size distributions and Nb additions on recrystallisation kinetics using a model Fe-30 Ni steel. A model Fe-30 Ni steel has been used as it has been shown to give deformation structures similar to those seen in hot rolled HSLA steels but does not undergo an austenite to ferrite transformation, therefore the deformed austenitic microstructures can be retained for room temperature characterisation. Different starting grain size distributions have been generated using different homogenisation heat treatments. Then, cold deformation and annealing tests have been applied followed by microstructural characterisation to determine the recrystallisation kinetics for Fe-30Ni Nb free steels with and without Nb. Then, TEM examination has been carried out to measure the precipitate size distribution and number density. In-situ EBSD has been used to gain a deeper understanding on the microstructure evolution during recrystallisation and the role of initial grain size distribution. A flow chart illustrating the experimental work is shown in Figure 5-1.

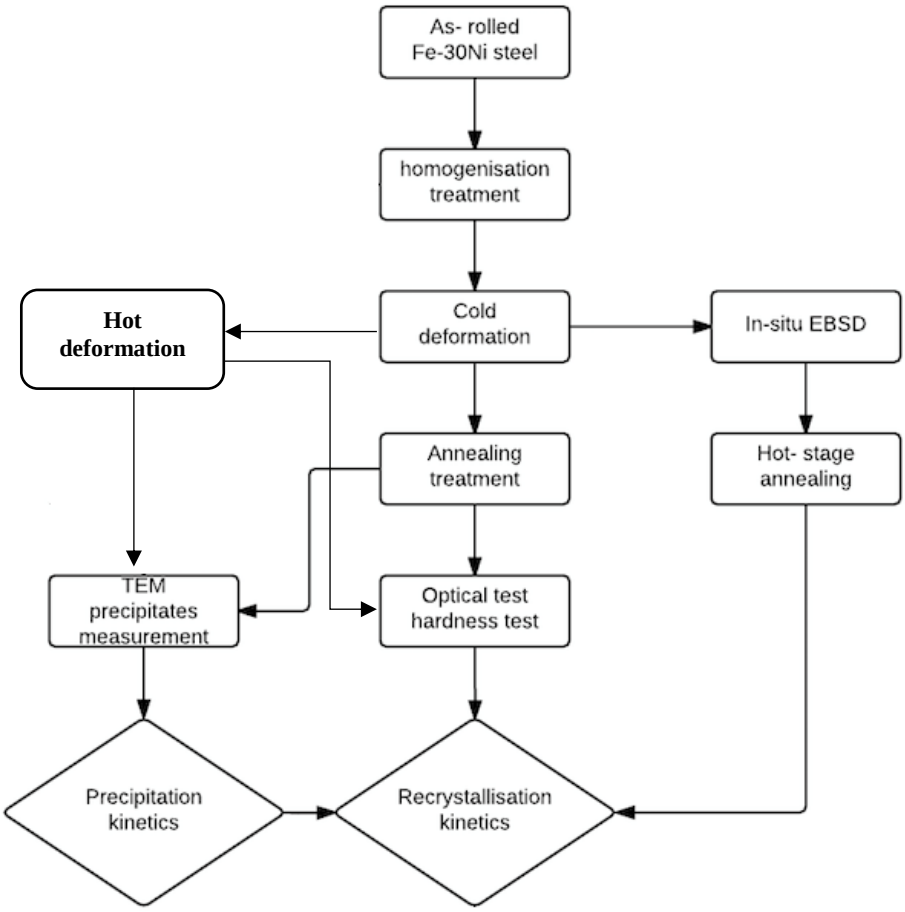

Figure 5-1 Flow chart of recrystallisation and precipitation kinetics investigation

5.2 Materials composition and homogenisation

It has been mentioned in chapter 2.2.2 that the Fe-30Ni has been chosen as the model alloy to study recrystallisation and precipitation in the austenite iron attributed to its austenitic microstructure at room temperature. It is noted that there is an effect of Ni on Nb solubility. Detailed discussions of the model alloy chemistry and its effect on Nb solubility have been included in chapter 2.2.2 and chapter 3.2.1.1.

The materials used in this work are laboratory cast and rolled plates of 20mm thickness, provided by Tata Steel Swinden Technology Centre. Fe-30Ni Nb free model alloy and Fe-30Ni-0.044 wt. % Nb were supplied, whose composition is given in Table 5-1. The as-received as-rolled microstructure for the Fe-30Ni model alloy at the half thickness position is shown in Figure 5-2. The optical image clearly shows deformation bands along the rolling direction with an average spacing of approximately 30 μm. The SEM and EBSD images for the as-rolled microstructure further reveal a bimodal microstructure consisting of recrystallised, equiaxed grains (labelled as A, C in Figure 5-2) and unrecrystallised, elongated grains (labelled as B, D in Figure 5-2). The deformation bands are clearly seen within the elongated grains, and the new recrystallised grains were formed along the deformation bands with an average grain diameter of 20- 30 μm. The average deformation band distance measured by EBSD is 30 ± 2.9 μm, which agrees well with the optical microscopy results.

Kundu observed a similar spacing separation distance in HSLA steel plate, also supplied by Tata Steel STC rolling facility, where the spacing related to pearlite bands related to inter-dendritic chemical segregation during solidification and rolling to give the highly banded appearance [12]. In the Fe-30Ni model alloy in this work the banded structure is due to deformation bands but the spacing is considered to be similar due to the steels having the same casting and rolling schedules. For the Fe-30Ni steel the segregation of alloying elements, such as Mn, is thought to give slightly different deformation behaviour resulting in the banded microstructure.

For the Fe-30Ni with 0.044wt% Nb model alloy, the morphology of NbC and MnS in the as-received microstructure has been investigated using SEM and EDS. Several precipitates have been found and Figure 5-3 (a) shows a NbC precipitate formed within a grain. EDS mapping for Mn, S and Nb has also been carried out and both

MnS and NbC particles have been observed distributed in lines parallel with the rolling direction within a deformation band (for example Figure 5-3 (b)) suggesting that Nb and Mn segregated during solidification giving enriched areas that gave rise to the deformation bands. The MnS particles are generally more than 500 nm in diameter, whilst the NbC precipitates are between 30-100 nm in diameter.

To generate a uniform profile of Nb in the Fe-30 Ni-0.044 wt. % Nb model alloy, i.e. to remove any effect of Nb distributed inhomogeneously from interdendritic segregation on recrystallisation, a homogenisation treatment was carried out.

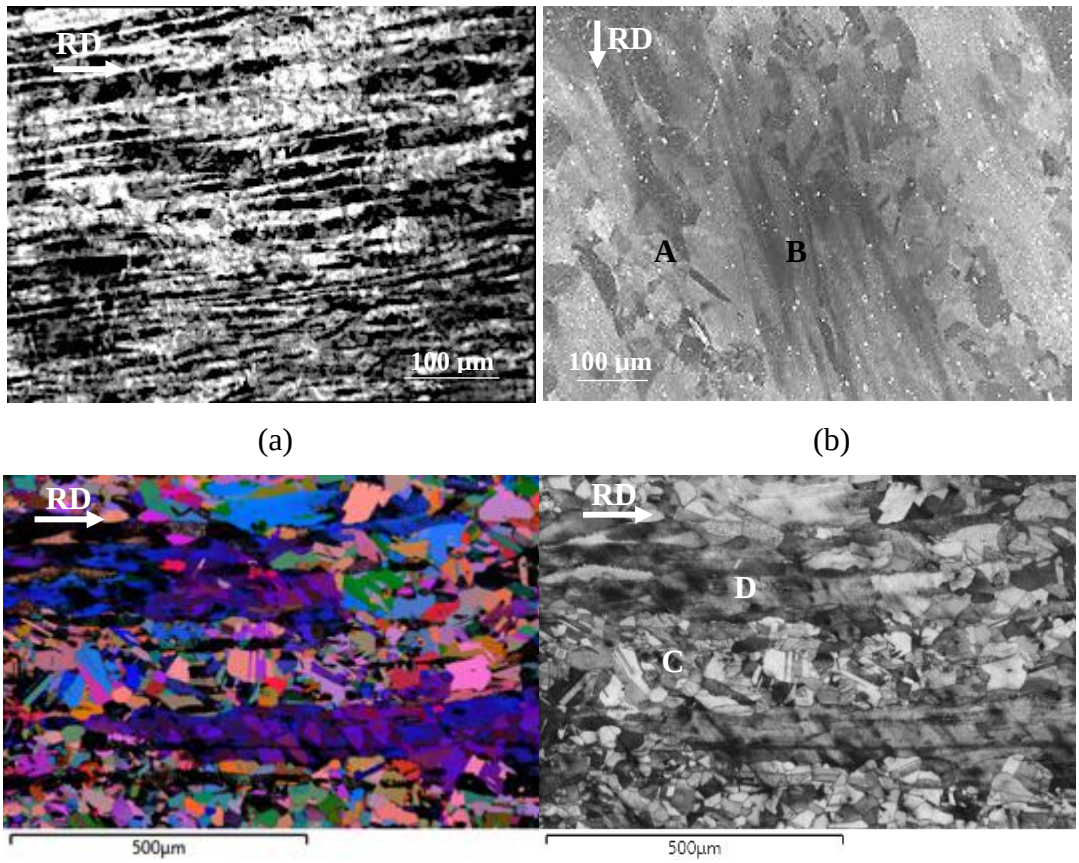

Figure 5-2 As- rolled microstructure for the Fe-30 Ni model alloy by using (a) optical (b) SEM secondary electron (c) EBSD Euler colour (d) EBSD band contrast. Recrystallised, equiaxed grains labelled as A and C and elongated unrecrystallised grains labelled as B and D.

Table 5-1 Material composition, all in wt. %

	C	Si	Mn	S	Cr	Ni	Nb
Nb-free	0.061	0.024	0.52	0.009	0.01	29.95	-
Nb	0.061	0.24	0.53	0.01	0.01	30.01	0.044

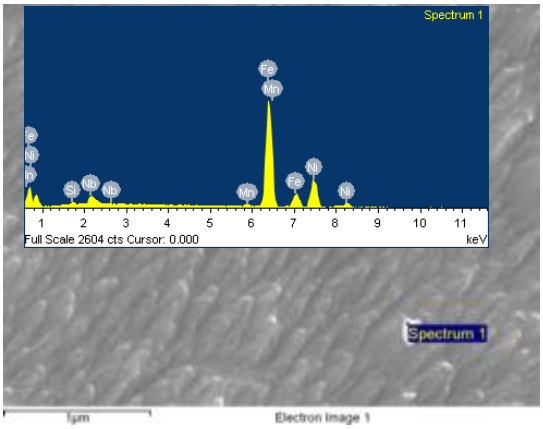

(a)

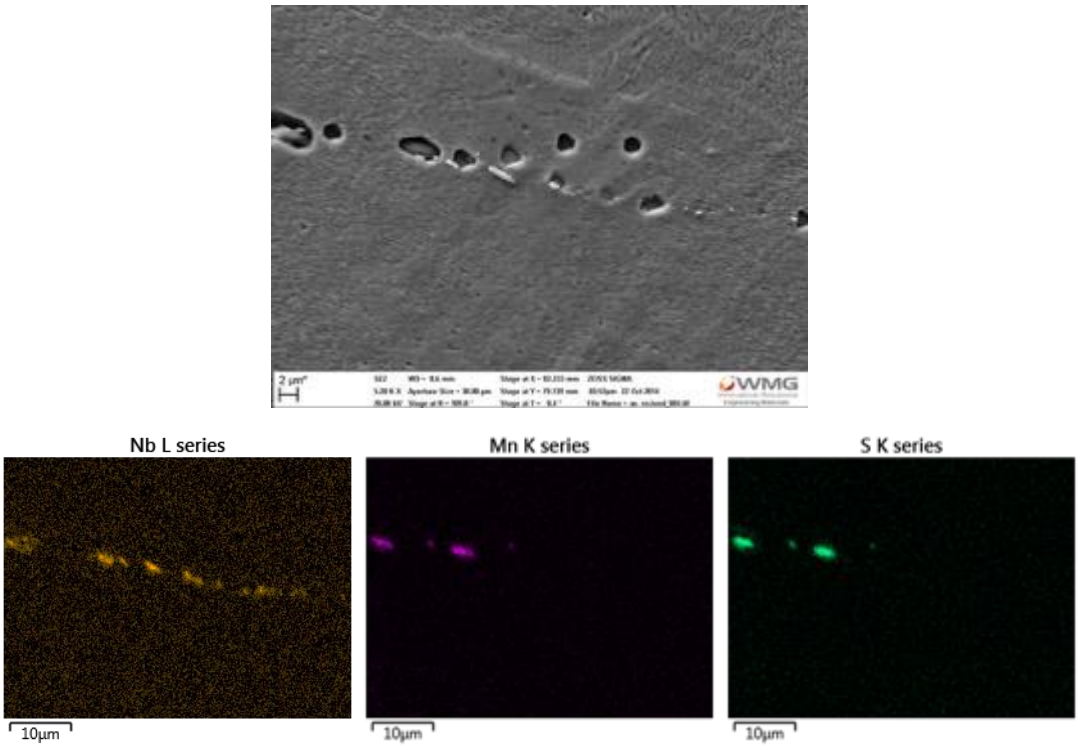

(b)

Figure 5-3 SEM and EDS mapping of MnS, NbC precipitates in the as- rolled microstructure. (a) NbC precipitate shown within a grain (b) MnS and NbC precipitates shown along a deformation band.

Previous work implied that Nb segregation during casting can affect the recrystallisation behaviour [2]. Thus, homogenisation treatments were carried out for the Nb-containing steel in an argon-encapsulated tube, Table 5-2, using samples of 10 diameter × 15mm in length mm. The heat treatment parameters were selected based on the distance between the deformation bands, i.e. the distance between the solute rich and the solute depleted regions. The banding structure was formed due to the segregation of the alloying elements during dendritic solidification [166]. When dendrites solidify, the interdendritic region becomes solute rich due to the higher solubility of liquid. These solute rich and depleted regions were then elongated into a banded structure during rolling, i.e. deformation bands [167].

It was assumed that the Nb segregation distance is the same as the width of the deformation bands, which has been related to the segregation distance observed in the previous study done by Kundu for steel produced using the same casting and rolling parameters [12]. The diffusion distance is therefore half the width of the band, i.e. 15 μm.

Thermo-Calc has been used to calculate the dissolution temperature for precipitates, phase fraction and matrix compositions under equilibrium conditions in the Fe-30Ni-0.044 wt. % Nb model alloy. The version of Thermo-Calc used is 2018a with TCFE9 database. Property diagram mode has been applied to calculate the equilibrium Nb content at various temperatures, also the composition of the material and the temperature range were chosen by using the Thermo-Calc wizard interface, Figure 5-4. The alloying elements used for calculation are shown in Table 5-1. The prediction temperature range is from 1200 to 600 °C, and the equilibrium Nb content and the mole fraction of NbC within the temperature range has been predicted. A microalloyed steel composition with 0.06 wt. % C, 1.5 wt. % Mn, and 0.044 wt. % Nb has also been used to compare the Nb solubility with that in the Fe-30Ni model alloy. The results are shown in Figure 5-5.

It can be seen from Figure 5-5 that the dissolution temperature for NbC in the Fe-30Ni model alloy is 1010 °C compared to over 1090 °C in the microalloyed steel. A higher Nb solubility in Fe-30Ni model alloy has been observed compared to C- 1.5Mn microalloyed steel, as summarised in Table 5-2, which agrees with the literature

mentioned in chapter 3.2.1.1. Therefore, the precipitation kinetics measured in Fe-30Ni model alloy cannot be directly transferred to that in microalloyed steels attributed to the variation in Nb solubility. However, the effect of measured precipitation amounts (size, number density) on the recrystallisation process, and hence Avrami exponent, can be determined.

The equilibrium temperature for 0.044 wt. % Nb and 1.5 wt.% Mn in Fe- 30Ni model alloy has been calculated and summarised in Table 5-3.

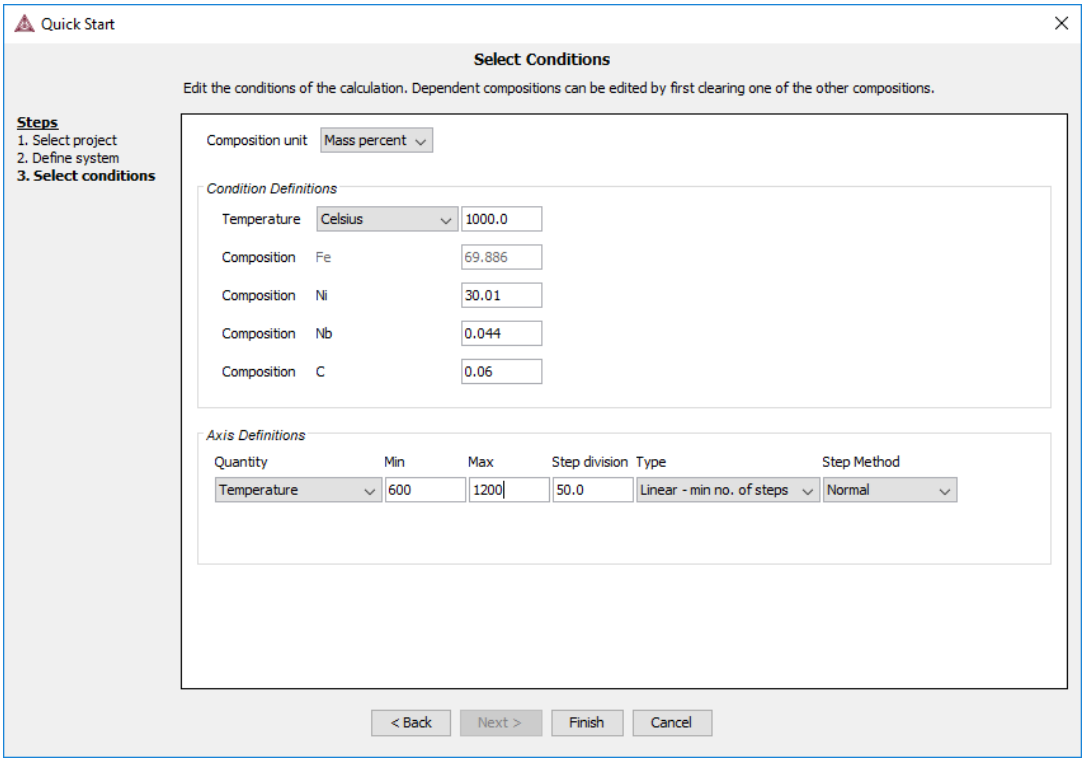

Figure 5-4 Thermo- Calc wizard interface showing the input of composition and the temperature range

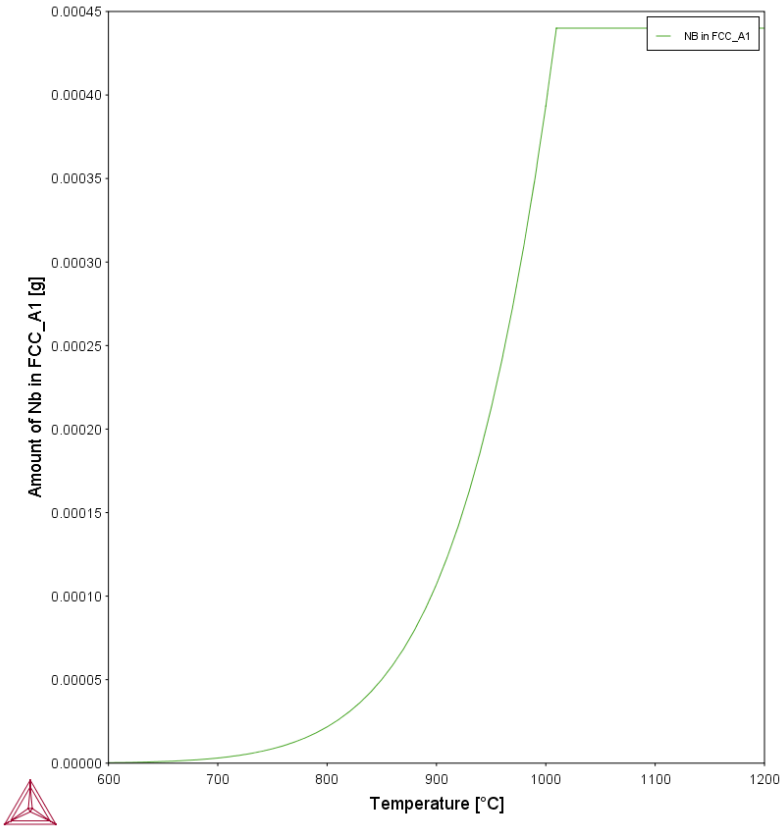
NB in FCC_A1
Amount of Nb in FCC_A1 [g]
0.00045
0.00040
0.00035
0.00030
0.00025
0.00020
0.00015
0.00010
0.00005
0.00000
600
700
800
900
1000
1100
1200
Temperature [°C]

(a)

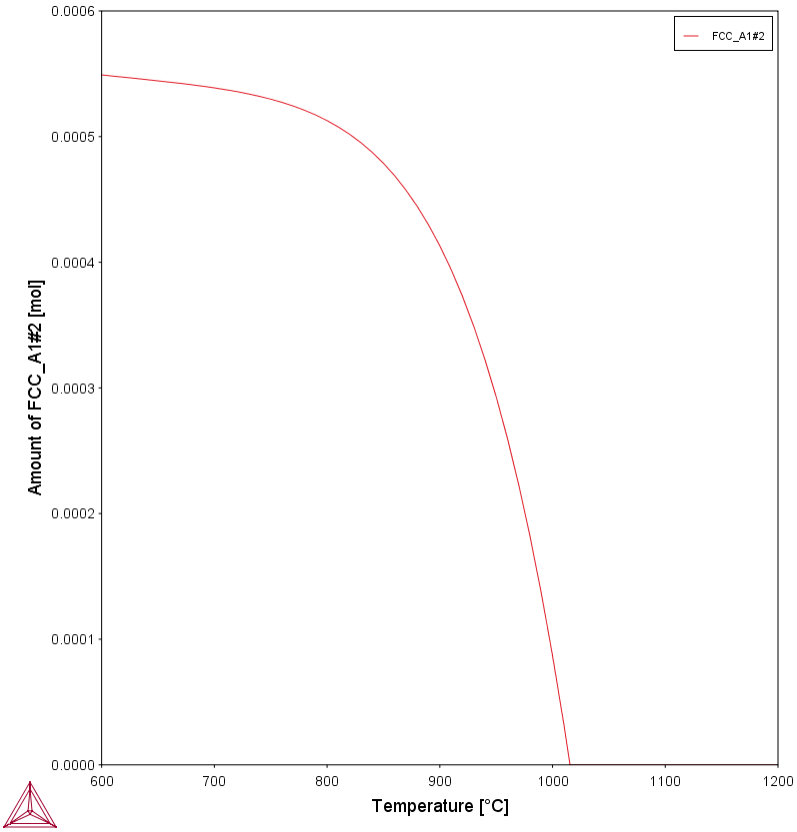
FCC_A1#2
Amount of FCC_A1#2 [mol]
0.0006
0.0005
0.0004
0.0003
0.0002
0.0001
0.0000
600
700
800
900
1000
1100
1200
Temperature [°C]

(b)

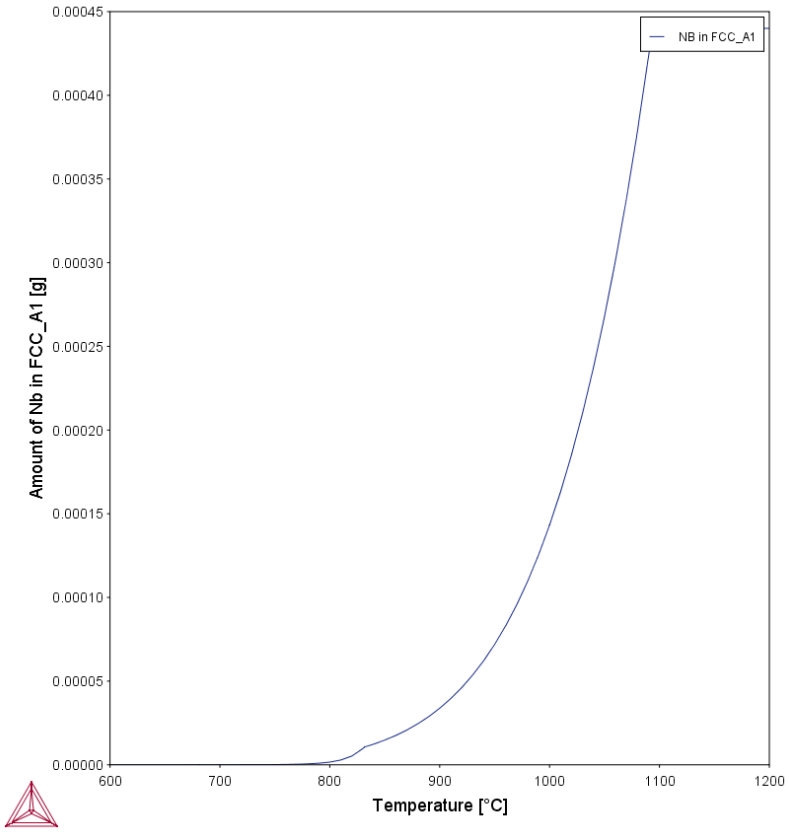

(c)

Figure 5-5 Thermo- Calc calculation result (a) mass fraction of Nb in solution for Fe-30Ni model alloy (b) mole fraction of NbC present (c) mass fraction of Nb in solution for C-1.5Mn microalloyed steel

Table 5-2 Summary of the equilibrium NbC mole fraction in Fe-30Ni model alloy and microalloyed steels calculated by Thermo-Calc

Temperature (°C)	Equilibrium NbC mole fraction	
	Fe-30Ni	C-1.5Mn
950	0.00025	0.00042
900	0.00039	0.00047
850	0.00047	0.0005

Table 5-3 The precipitate stability temperatures calculated by Thermo-Calc

Phase	Temperature (°C)
MnS	1374
Nb(C,N)	1020

It has been mentioned by Cuddy that Nb(C,N) precipitates can remain undissolved after reheating to 70 - 100 °C over the predicted complete dissolution temperatures [168]. Thus, to homogenize the sample, the temperature was set at 1150°C for 4 hours and 1200°C for 2 hours; the heat treatment times were determined using the diffusion equation which is given by,

$$X = \sqrt{Dt} \qquad \ldots 57$$

Where, X is diffusion distance, D is the diffusion coefficient, $D = 1.4 \times 10^{-4}\exp(-\frac{270000}{RT})$ m/s^2 in this case [136], and t is time. The calculated diffusion distances at different temperatures and times are shown in Figure 5-4.

It was found that at the higher temperature, 1200 °C, non-uniform grain growth occurred after 2 hours, Figure 5-5. Therefore, the homogenisation treatment at 1150 °C for 4 hours was chosen for all subsequent testing as a more uniform grain size was generated.

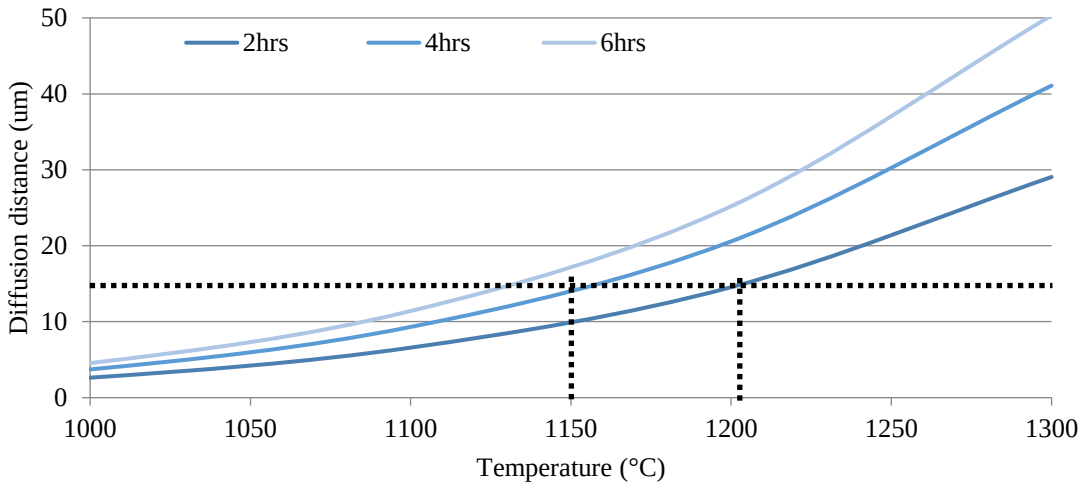

Figure 5-6 Calculated diffusion distances for different reheating time and temperatures.

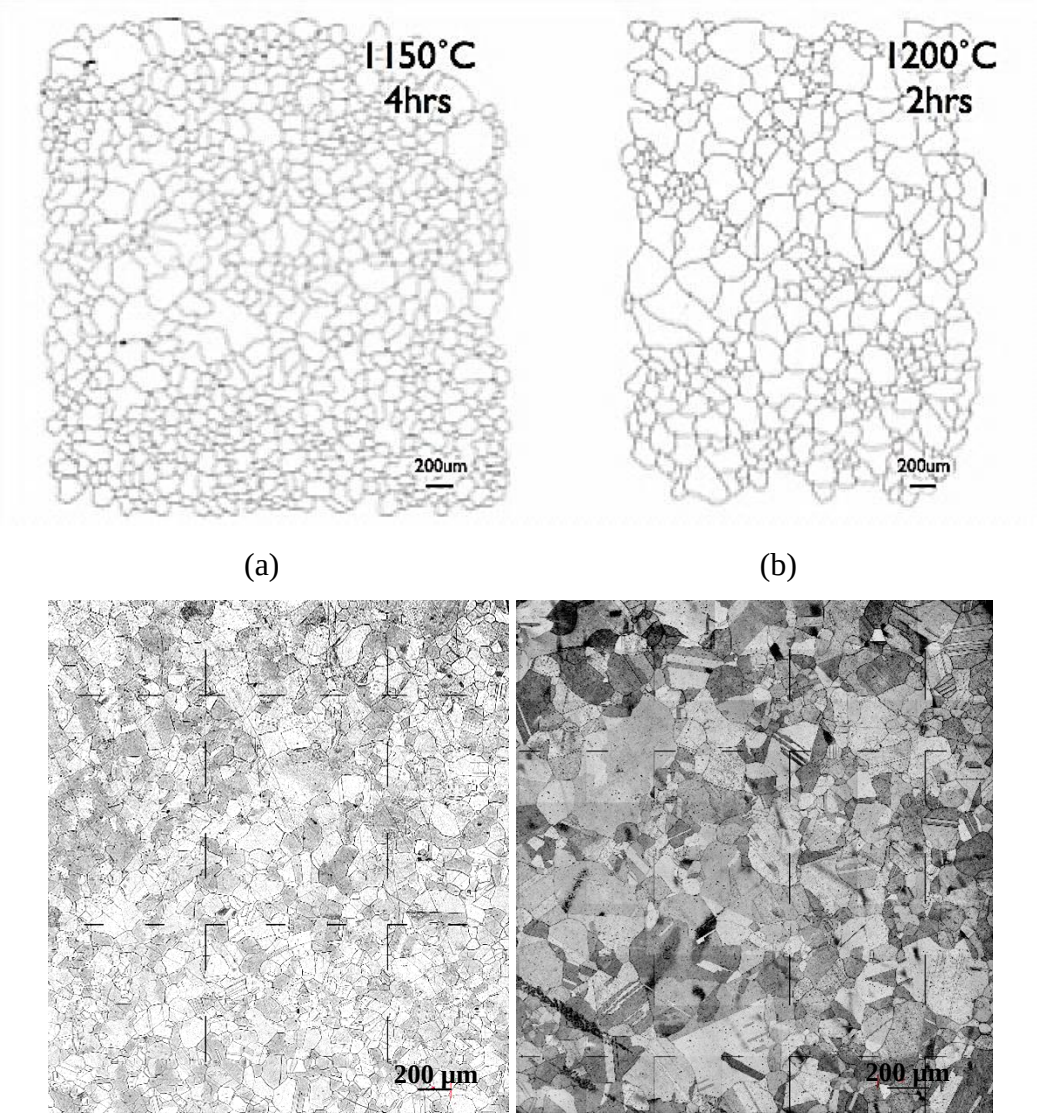

(a) (b)

(c) (d)

Figure 5-7 Grain structures of Fe-30 Ni-0.044 wt.% Nb samples after the solution treatment at 1150°C for 4 hours (a), (c) and 1200°C for 2 hours (b), (d) using traced images (a) and (b) from the optical micrographs (c) and (d).

To confirm that the composition of the model alloys will be uniform the effect of the homogenisation heat treatment on Mn, which is known to segregate during solidification, was considered: the diffusivity in austenite iron is given as, $D = 1.6 \times 10^{-5}\exp(-\frac{261000}{RT})$ m/s^2 [169]. Therefore, during the annealing treatment at 1150 °C for 4 hours the diffusion distance is,

$$X = \sqrt{Dt} = \sqrt{1.6 \times 10^{-5}\exp(-\frac{261000}{RT}) \times 14400} = 52\ \mu m$$

This clearly shows that diffusion of Mn is significantly faster than Nb. That is, the homogenisation is sufficient for both Nb and Mn. However, the homogenisation temperature is considerably lower than the equilibrium stability temperature of MnS. As a result, coarsening of MnS particles is expected. It can be seen that the size of MnS in the as-received material is approximately 0.5 µm, Figure 5-3, which is significantly bigger than the size of Nb(C, N) strain induced precipitates reported in the literature, i.e. 5- 25 nm. The number density of MnS particles is very low (4×10^8/ m^2 with an average size of 0.5 µm) therefore, the presence of MnS will not interfere with the observation of Nb(C, N) in the TEM nor are they expected to affect the recrystallisation kinetics.

Figure 5-8 shows a TEM image of the Nb(C,N) precipitates present in the steel after the homogenisation treatment and the size distribution has been summarised in Figure 5-9. As seen, the mode precipitate size is 15 nm. The precipitates are either partially dissolved precipitates (as the size is smaller than those seen in the as-received material (Figure 6-2) or those that formed during air cooling after homogenisation. The number density measured by TEM is $4.3 \times 10^{18} m^{-3}$. The volume fraction of the undissolved precipitates was calculated as 1.7×10^{-5}, which accounts for 3.5% of the total Nb content in the steel. Therefore, it is not unreasonable to assume the Nb content in solution is 0.044wt. % during subsequent recrystallisation trials, and that these undissolved precipitates will have an insignificant effect on the recrystallisation kinetics.

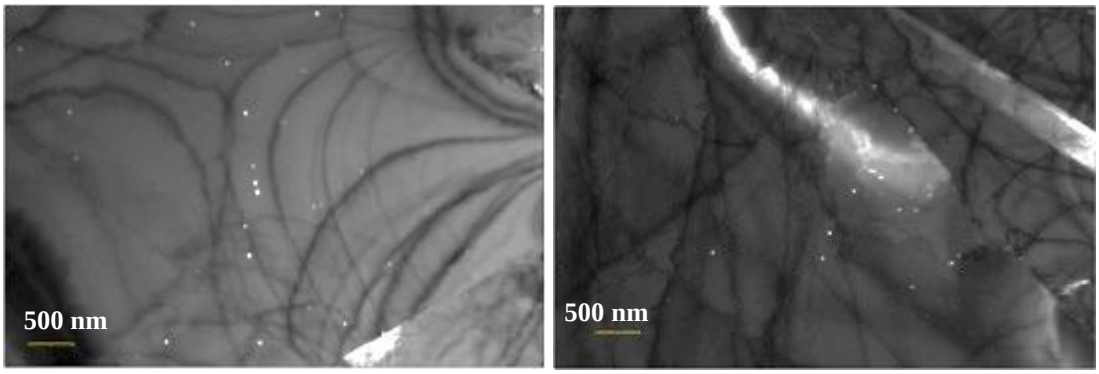

Figure 5-8 TEM images of the residual precipitates after homogenisation treatment

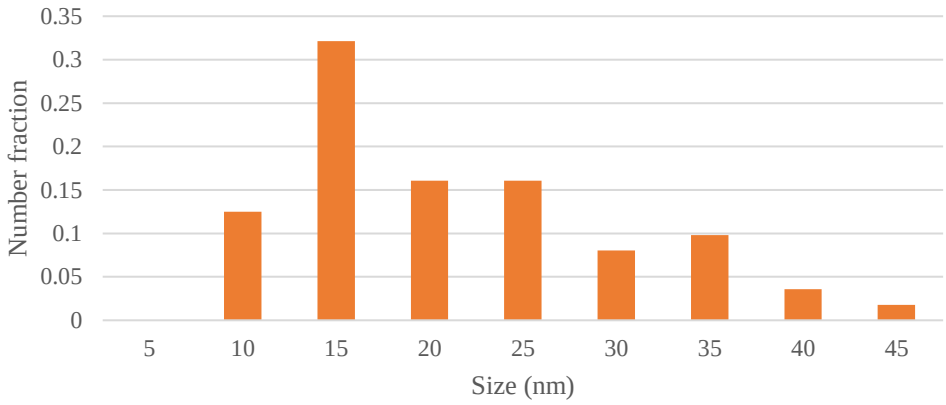

Figure 5-9 Precipitates size distribution in the homogenised Fe-30 Ni-0.044 wt. % Nb sample

Additionally, the Fe-30Ni Nb free steel was heat treated to relieve any residual stress in the sample and to provide different starting grain size distributions for the deformation trials, details in Table 5-4. The homogenised grain size distribution is given in Figure 5-10; a unimodal grain size distribution is seen and a comparable distribution in the Nb free steel has been generated to examine the effect of Nb on recrystallisation in the following tests

Two different starting grain size distributions have been generated to investigate the recrystallisation kinetics in the Fe-30Ni Nb free steel. As mentioned in the literature review (chapter 2.2), microstructures with different grain sizes are reported to have different local stored energy and nuclei density, and hence different recrystallisation rates [39, 64, 170].

Figure 5-11 shows the grain size distributions of the Fe-30Ni Nb free steel after heat treatment at 1300 °C for 5 minutes and 1100 °C for 30 minutes. It can be seen that the 1100 °C- 30 minutes sample gives a mode grain size of 100 µm with a grain size range of 20 - 200 µm, where 80% of grains are between 60 – 140 µm. Whereas the 1300 °C-5 minutes sample gives a mode grain size of 160 µm with a range of 20 - 340 µm, and 80% of grains fall into the region of 80 - 280 µm. The two different grain size distributions will be used to investigate the effect of grain size distribution on the local recrystallisation kinetics and hence the Avrami exponent.

Table 5-4 Homogenisation / heat treatment for different grain size distributions

Temperature (C)	Nb (wt. %)	Time (s)	Grain size range after heat treatment (um)
1150	0.044	14400	20- 340, mode 180
1300	-	300	20- 340, mode 160
1100	-	1800	20- 200, mode 100

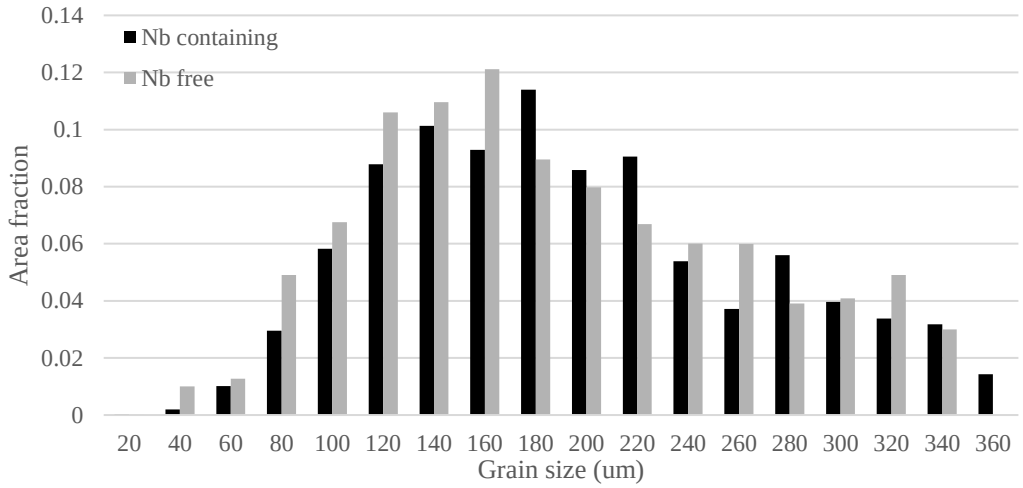

Figure 5-10 Grain size distribution of homogenised samples after 4 hours at 1150 °C for the Nb free and after 5 minutes at 1300 °C for Nb containing steels

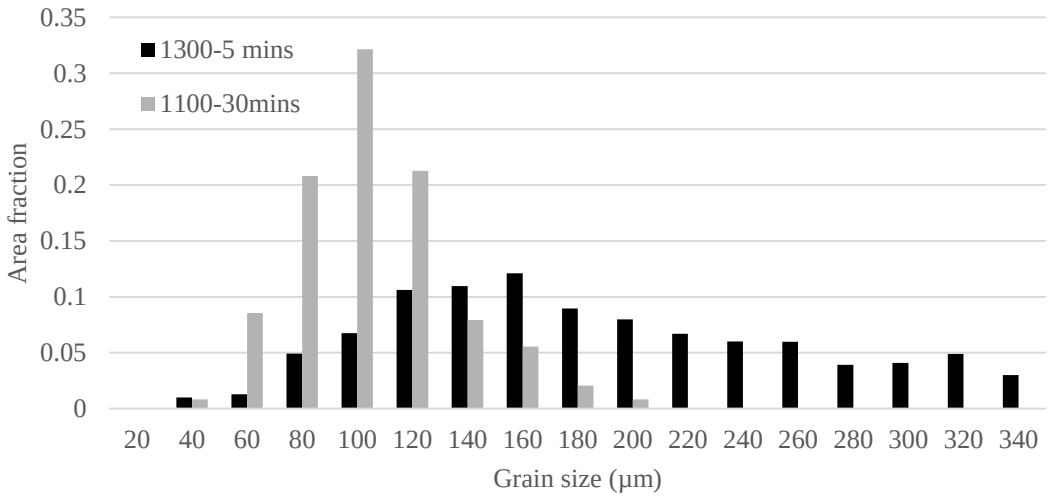

Figure 5-11 Grain size distributions of the Fe-30Ni Nb free model steel after different heat treatments

5.3 Cold deformation and annealing test

The cylindrical specimens were cold deformed to 0.2 or 0.3 strain by uniaxial compression at room temperature on a Instron 3300 series static testing machine before being reheated to 950 °C, 900 °C or 850 °C for various times then quenched into water. Instron testing system is capable of compression tests for 100 kN, with data acquisition rate of 500 Hz and load accuracy of 0.5% of the indicated load. Cold deformation was used as the Gleeble was unavailable for hot deformation for majority of PhD time.

PTFE film was applied as a lubricant to minimize the friction between the anvil and the sample interface. The strain was measured based on the height reduction of the sample after the deformation to take into account machine compliance and elastic strain in the sample. In this case, the flow curve was not corrected for friction or compliance, as the absolute value of flow stress was not required to determine the recrystallisation Avrami exponent. The deformation time was monitored to ensure the strain rate was correct, i.e. deformation time 120s for a strain rate of 0.0025 s^{-1} to a strain of 0.3. The sample dimensions and a schematic diagram of the deformation test are shown in Figure 5-12. Flow stress was not corrected by taking compliance and friction into account, as the absolute value of flow stress was not required to determine the recrystallisation Avrami exponent or kinetics.

Barrelling is known to cause strain inhomogeneity in deformed uniaxial compressed samples due to friction between the anvil and the sample interface. A higher amount of barrelling indicates a higher friction coefficient. An example of the as-deformed sample macro image (sectioned along the compression direction), and the hardness values across the thickness are shown in Figure 5-13. It can be seen that there is little or no barrelling shown in the deformed samples, which indicates that the room temperature deformation was relatively uniform. The macro- hardness profile across the thickness also shows that the hardness was comparably uniform across the thickness, which suggests that the deformation was macroscopically uniformly distributed on a macroscopic scale. The dimensions of the sample, measuring using Vernier calipers has been summarised in Table 5-5.

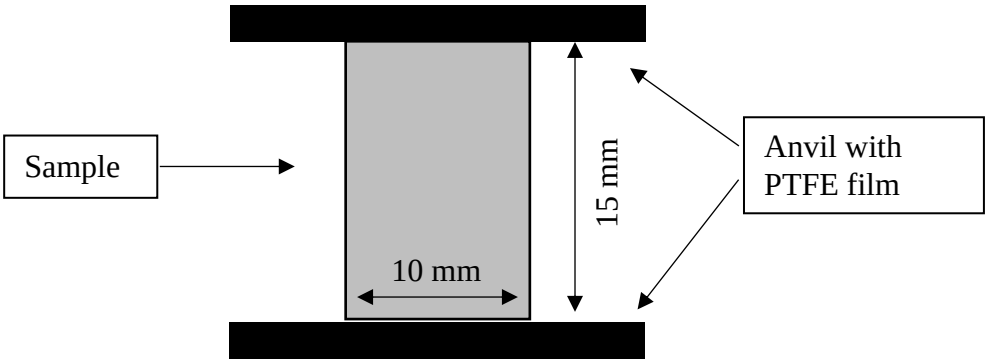

Figure 5-12 Schematic diagram of the deformation test and the sample dimension

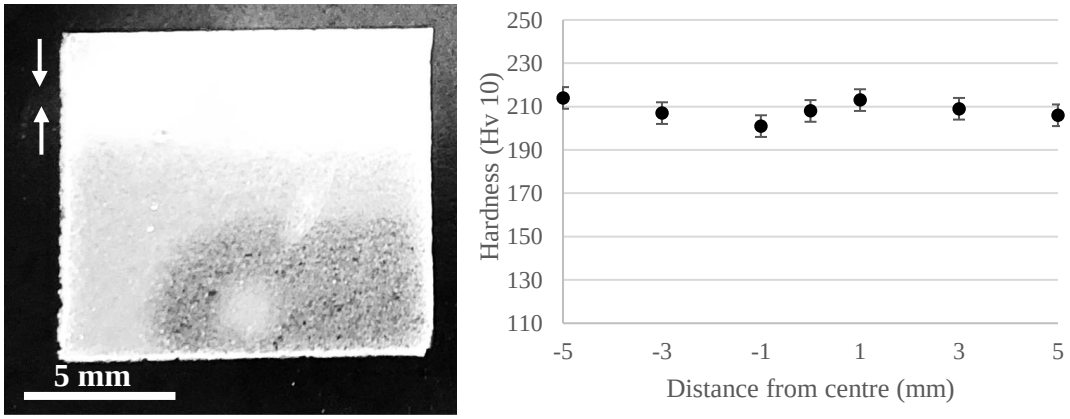

Figure 5-13 Macro image and hardness profile through the thickness (along the compression direction, arrowed) of a sectioned cold deformed sample to 0.3 strain

Table 5-5 Sample dimensions after deformation to 0.3 strain at room temperature

Radius (sample top surface, mm)	11.6
Radius (maximum, mm)	11.6
Height reduction (mm)	3.9

The friction coefficient for the compression test can be determined via measuring the degree of barreling, which is given by [109],

$$m = \frac{\frac{R}{h} \times b}{\frac{4}{\sqrt{3}} - \frac{2b}{3\sqrt{3}}} \quad \ldots 58$$

Where m is the friction coefficient ranging from 0 (perfect sliding) - 1 (sticking friction), h and R are the final height and the theoretical radius respectively. The barreling factor b is given by,

$$b = 4\frac{\Delta R}{R}\frac{h}{\Delta h} \quad \ldots 59$$

Where ΔR is the differences between the maximum radius and the radius of top surface of the sample. Δh is the reduction in height after the compression.

Therefore, the friction coefficient for the cold deformed sample is negligible due to little/ no barreling being observed from the deformed sample.

147 samples have been used to establish the recrystallisation kinetics for the Nb-free and 0.044 wt. % Nb steels at different conditions, Table 5-6. Samples (for cold deformed and annealed tests) of 10× 10× 1 mm were machined from the deformed cylinders, the small size was selected to maximise the heating rate during heat treatment. The samples were put into a pre-heated alumina crucible in the furnace, which had been stabilised at the isothermal temperature. Temperature measurement was by a K type thermocouple (chromel/alumel) placed inside the pre-heated furnace at the crucible location. The schematic diagram of the set up is shown in Figure 5-12. The thermocouple was attached to the crucible, and the sample was placed on top of the thermocouple when the annealing process was taking place.

When the sample was put in place and the furnace door was shut, the crucible temperature was noted to have dropped (typically by approximately 80 °C); it took approximately 30s to heat back to the set temperature. For each sample this time was noted and the isothermal time for recrystallisation was started once the thermocouple reached the set temperature. The samples were taken then out from the furnace and quenched in water.

The microstructure and the hardness evolution during the reheating process have also been studied to ensure no recrystallisation occurred during the reheating stage. This is discussed in chapter 6.4.

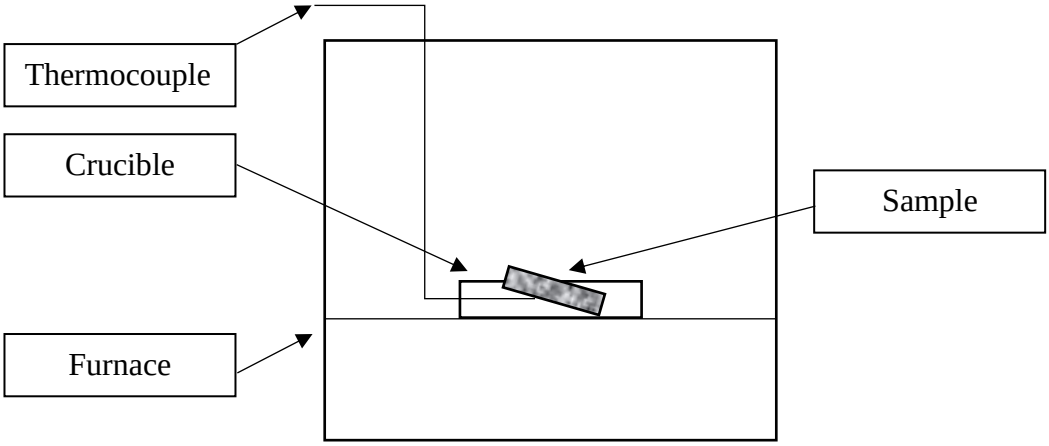

Figure 5-14 Schematic diagram of the temperature measurements during the annealing process for the cold deformed samples

Table 5-6 Cold deformation and annealing test conditions

Temperature	Strain	Starting mode grain size	Nb (wt. %)	Time (s)
850	0.2	100	-	0-240
900	0.2	100	-	0-160
850	0.2	180	-	0- 480
850	0.2	180	0.044	0- 10800
850	0.3	180	-	0- 160
850	0.3	180	0.044	0- 3600
900	0.2	180	-	0- 240
900	0.2	180	0.044	0- 3600
900	0.3	180	-	0- 120
900	0.3	180	0.044	0- 450
950	0.2	180	-	0- 120
950	0.2	180	0.044	0- 480
950	0.3	180	-	0- 90
950	0.3	180	0.044	0- 300

5.4 Hot deformation tests

Stress relaxation tests were carried out using a Gleeble^{TM} HDS thermo-mechanical simulator under uniaxial compression condition. The HDS machine at University of Warwick is shown in Figure 5-15. The Gleeble HDS machine records the load, displacement and temperature data, and is able to deform material to a maximum load of 100 kN. The HDS machine is controlled by Quicksim software written by DSI - the Gleeble manufacturer. The HDS output data are saved as excel files.

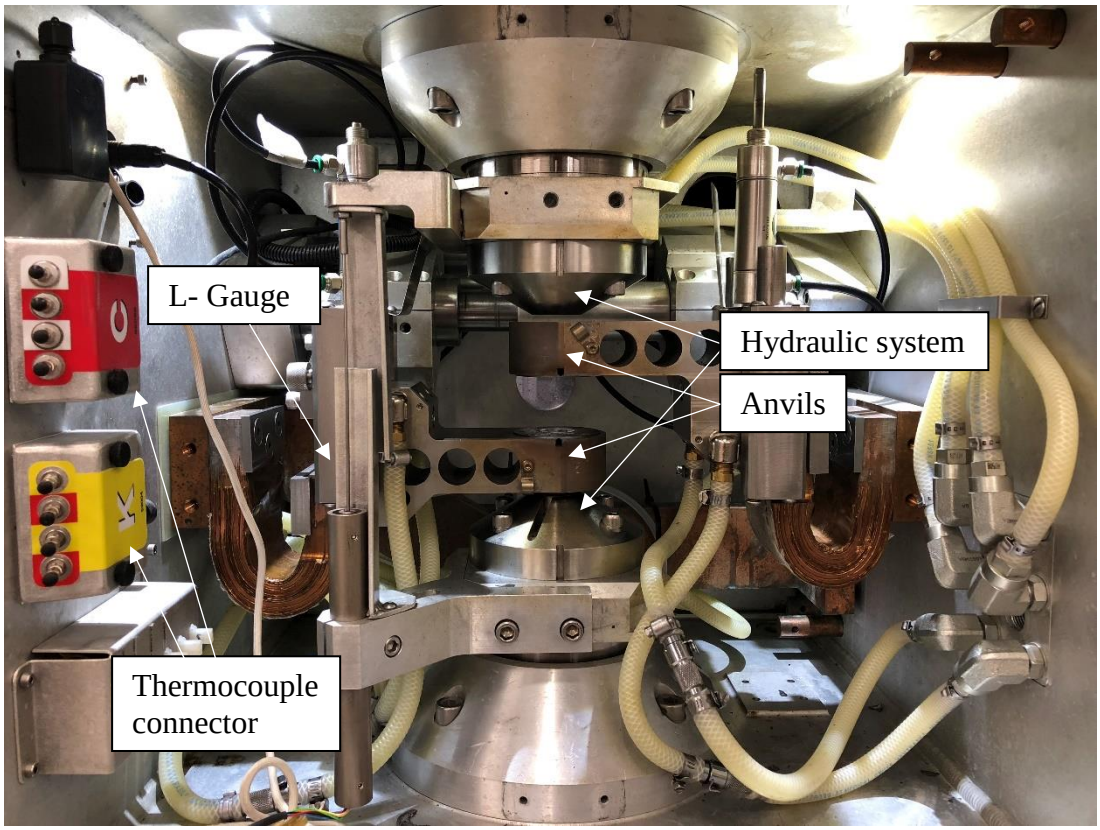

Figure 5-15 Configuration of the Gleeble HDS thermomechanical simulator

Cylindrical specimens (10×15mm in length) were machined for uniaxial compression tests in the Gleeble HDS machine. A schematic diagram of the test specimens is shown in Figure 5-16. K type thermocouples were inserted in a hole drilled to the middle thickness (along the deformation axis) to measure the temperature during testing. Nickel paste and graphite foil were used between the anvil and the samples as lubricants to minimise friction.

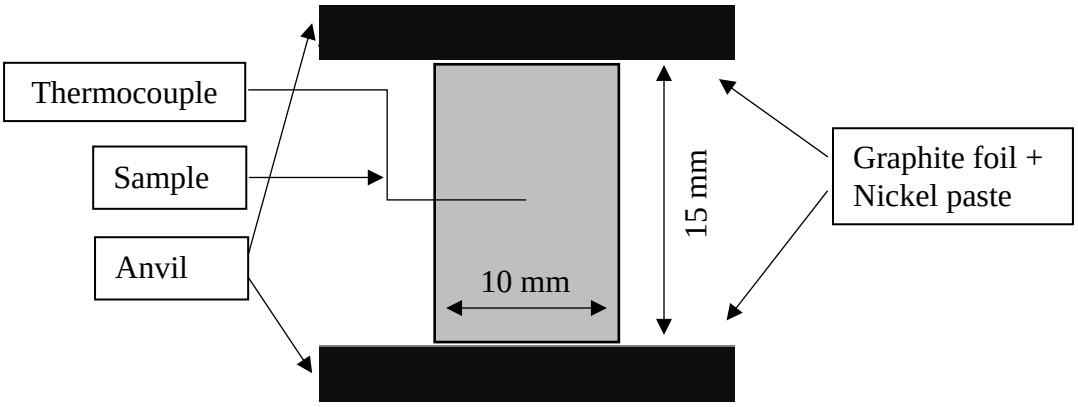

Figure 5-16 Schematic diagram of the deformation test and the sample dimension

Single hit deformation was carried out under different conditions of temperature and strain, as shown in Table 5-7. As samples were homogenised prior to testing, no reheating stage was performed to ensure no change in grain size distribution. For Nb containing model alloy, the as- homogenised samples have shown little undissolved precipitates. During the reheating stage, no precipitation is expected due to faster heating rate (20 °C/s) also the slow precipitation kinetics in the undeformed sample. Figure 5-17 shows a TEM image of an undeformed sample that was reheated and annealed at 950 °C for 120s. Undissovled preicpitates (>15 nm) were still seen, wheresas no evidence of new precipitates (fine in size, <5 nm) were formed during the reheating stage. Samples were deformed at a nominal strain rate of 5 s^{-1}, with the actual strain rate being measured using the experimental recorded data, Figure 5-18. It can be seen that the strain rate was 5 s^{-1} up to 0.3 strain, then decreased until 0.35 strain to avoid overshoot.

It is known that the compliance, friction and the strain rate affect the flow stress value, in this case, the flow stress was not corrected to take the compliance and friction into account. The aim of the hot deformation test was to examine the recrystallisation kinetics, i.e. the Avrami exponent, of the Nb-free and Nb containing model alloy which did not require the absolute flow stress values as the samples were examined by optical metallography or SEM to determine the recrystallisation fraction. The flow stress curves were used to confirm that no dynamic recrystallisation occurring during deformation.

The friction coefficient has been estimated using equation 58 and 59; the measured values have been listed in Table 5-8. The friction coefficient in this case was determined to be 0.28 - 0.35, which is significantly higher than for the cold deformed samples. The hardness values through the sample thickness (along the deformation axis, sample deformed at 950 °C to 0.35 strain and immediately quenched therefore in the absence of recrystallisation) are shown in Figure 5-19, which indicates a macro strain inhomogeneity in the hot deformed samples. This agrees with the literature data discussed in chapter 2.5.4. This clearly shows that the cold deformed samples have a more uniform macroscopic strain distribution compared to the hot deformed sample, attributed to differences in friction. As a result, only the centre region, i.e. 2× 2 mm, has been considered for the following optical analysis.

Table 5-7 Deformation parameters for stress relaxation tests

Strain	Nb level (wt. %)	Mode grain size (μm)	Temperature (°C)	Holding time (s)
0.27	n/a	100	950	5 - 40
0.3	n/a	160	950	760
0.35	n/a	160	950	25 - 300
0.35	0.044	160	950	25 - 300
0.35	0.044	160	850	300 - 3600
0.45	0.044	160	990	5 - 60

Table 5-8 Sample dimension after deformation to various strains at 950 °C

	Strain			
	0.27	0.3	0.35	0.45
Radius (sample top surface, mm)	11	11.1	11.2	11.4
Radius (maximum, mm)	11.4	11.5	11.9	12.2
Height reduction (mm)	3.6	3.9	4.4	5.4

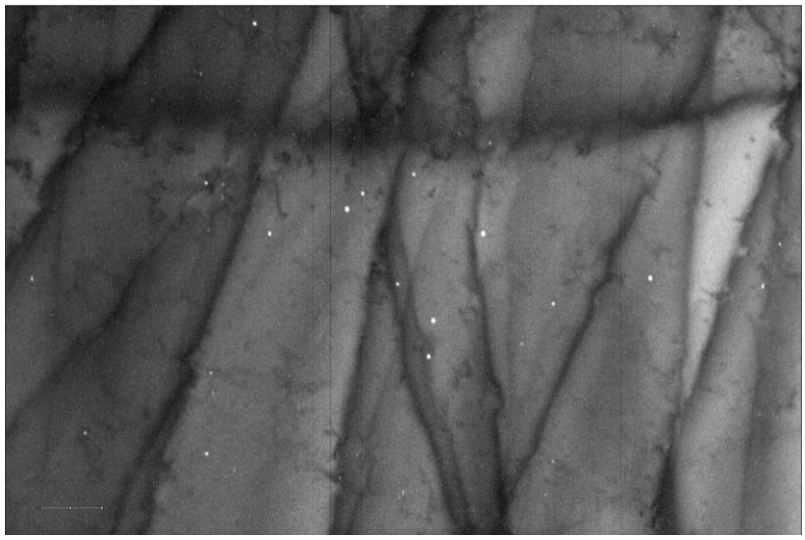

Figure 5-17 TEM image of the homogenised sample reheated to 950 °C, held for 120s then air quenched

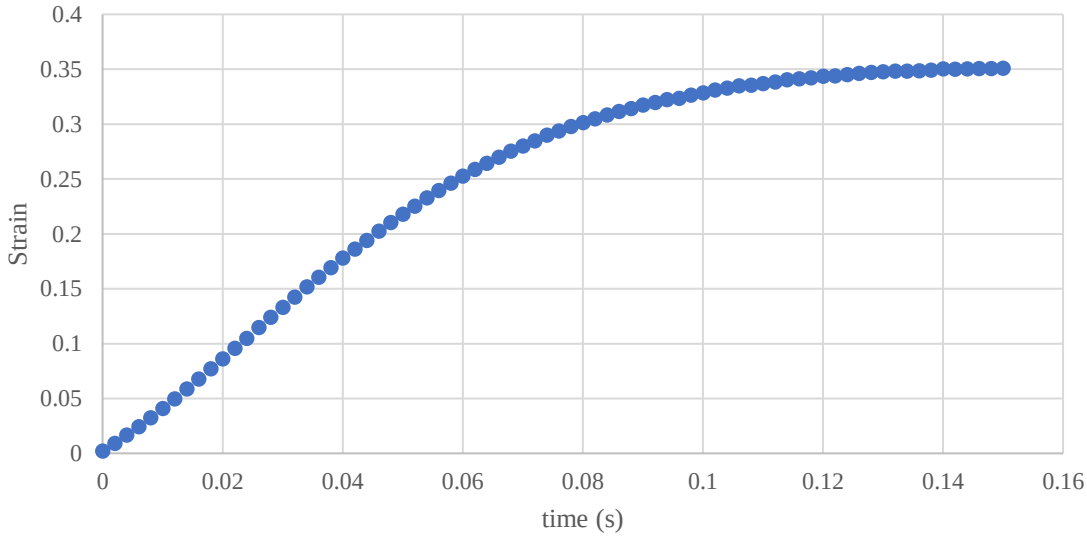

Figure 5-18 An example of the strain versus time data from the hot uniaxial compression from which the strain rate was obtained.

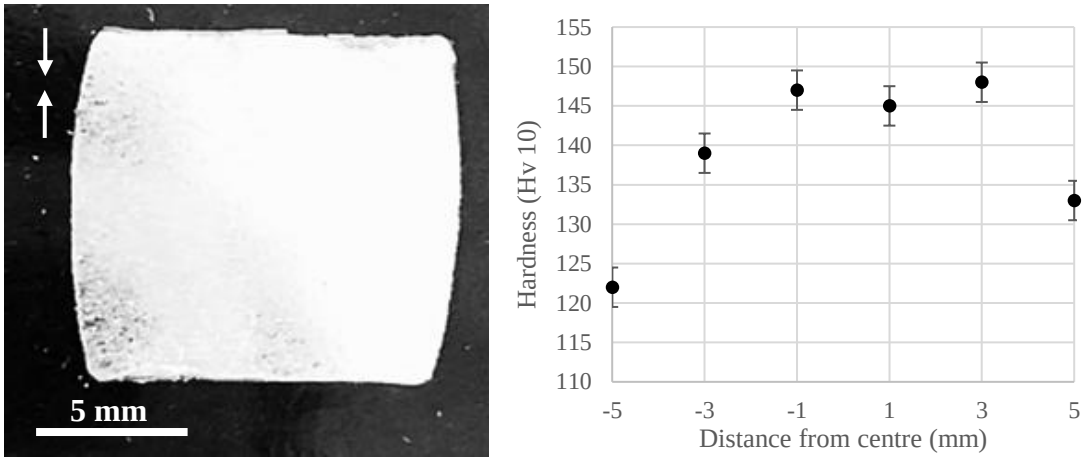

(a) (b)

Figure 5-19 (a) Macro image and (b) hardness profile through the sample (compression direction, arrowed in (a)) of the hot deformed sample to 0.35 strain, 950 °C, strain rate 5 s^{-1}.

5.5 Metallographic examination and hardness tests

The heat-treated and deformed specimens were sectioned on the longitudinal plane. Then the sectioned parts were mounted in Bakelite and ground, polished and etched by Kallings etchant to reveal the austenite grain structures. The sequence of poshining is 9 µm, 3µm, 0.05 µm, the polishing pads were supplied by Buehler. The composition of the etchant is shown in Table 5-8. Polished samples were immersed into the etchant for 1 minute at room temperature before being rinsed and dried for optical analysis.

These samples were examined by Nikon MA200 inverted optical microscopy and the observed grain boundaries were then traced. The grain size was analysed by ImageJ to obtain the grain size distribution. Boundaries were traced by eye and each trace was analysed by the software to obtain the grain size distribution, Figure 5-20. At least 700 grains were analysed to produce the grain size distribution. By comparing the microstructure before and after deformation, recrystallisation, which results in a finer grain size, can be identified. Moreover, measuring and recording each grain size allows a full grain size distribution to be obtained. The distribution can show the fraction of recrystallised grains and indicates the degree of recrystallisation, i.e. full, partial or no recrystallisation, as shown in Figures 5-21 to 5-23. It is worth noting that measuring and counting grain sizes is time consuming due to the large number of

grains needed to give an accurate grain size distribution, which means this approach has practical application limits.

Point counting method has been applied for determining the recrystallisation fraction. The procedure has followed the ASTM E562-02 standard (Standard Test Method for Determining Volume Fraction by Systematic Manual Point Count). An example was given in Figure 5-24. A grid of 15 x 20 squares was overlaid on the microstructure, and the number of crossings in the recrystallised grains was counted; the crossings overlaid on the recrystallised grains are marked). The procedure was repeated for five different optical images per sample, with a total of 1500 points counted for each sample. Then, the recrystallisation fraction was determined as the number of points in the recrystallised grains divided by the total number of points.

It is worth noting that only the central region, i.e. 2 mm away from the cylindrical surface and 3 mm away from the anvil contacting surface have been applied for metallographic examination due to the strain inhomogeneiey for hot deformed samples (based on the hardness measurement shown in Figure 5-19). As for cold deformed and annealed samples,

Macro-hardness testing was carried out using a Wilson VH1150 machine, Hv10 kg load. The hardness was examined on the longitudinal section and 8 indentations were measured on each sample to give an average value. The standard deviation of the hardness measurement has been considered.

Microhardness tests were carried out on a Struers^{TM} DuraScan Micro-hardness tester using an indenting mass of 0.5 kg. The mapping area was 3.5 mm × 7 mm with a step size of 0.25 mm.

Table 5-9 Composition of Kalling's etchant

$CuCl_2$	5 g
Hydrochloric acid	100 ml
Ethanol	100 ml

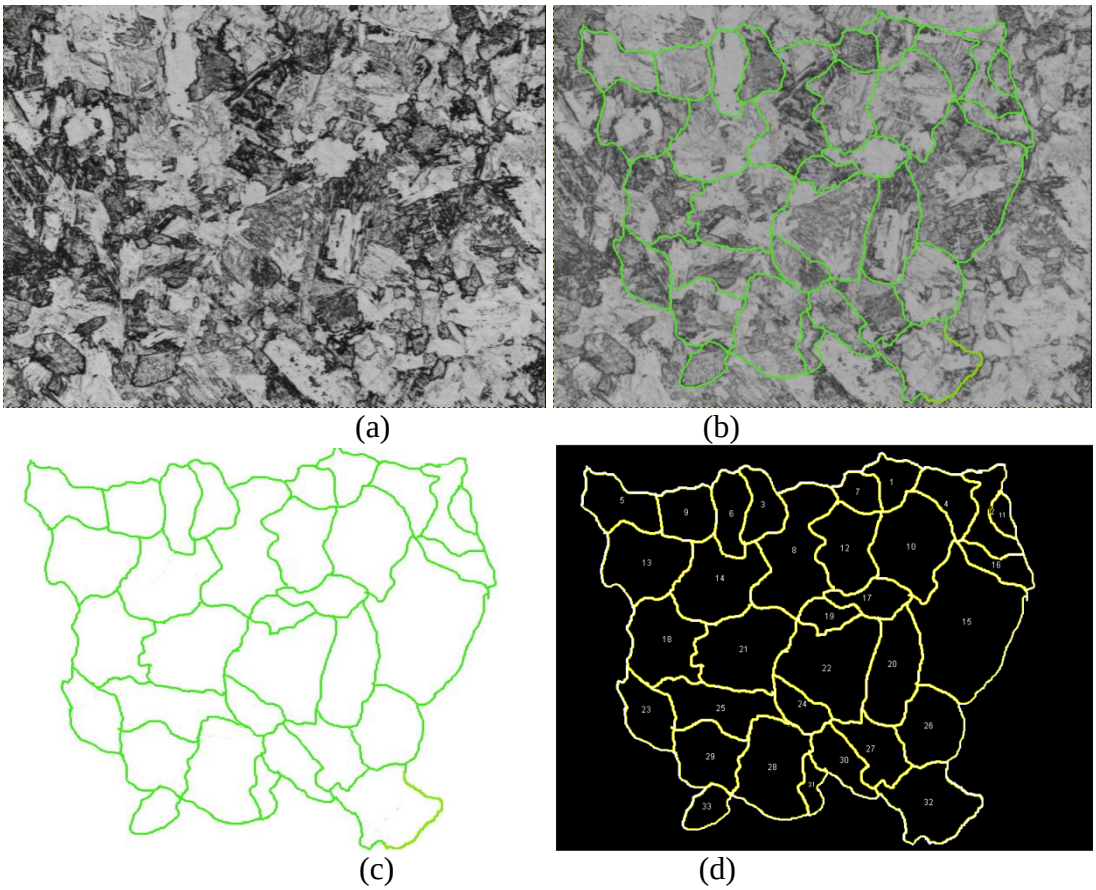

Figure 5-20 Microstructure of a C-Mn steel sample (quenched and tempered before deformation) and grain boundaries trace

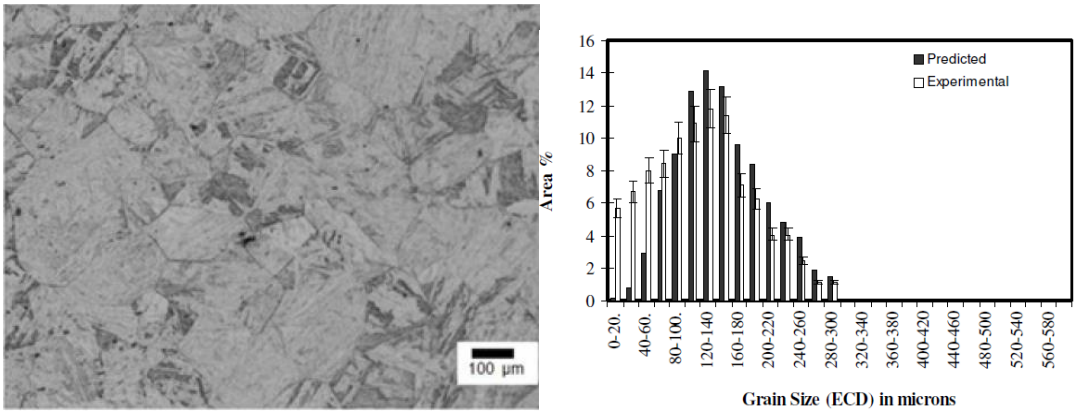

Figure 5-21 Microstructure and grain size distribution of fully recrystallized sample (1075°C, 0.3 strain)

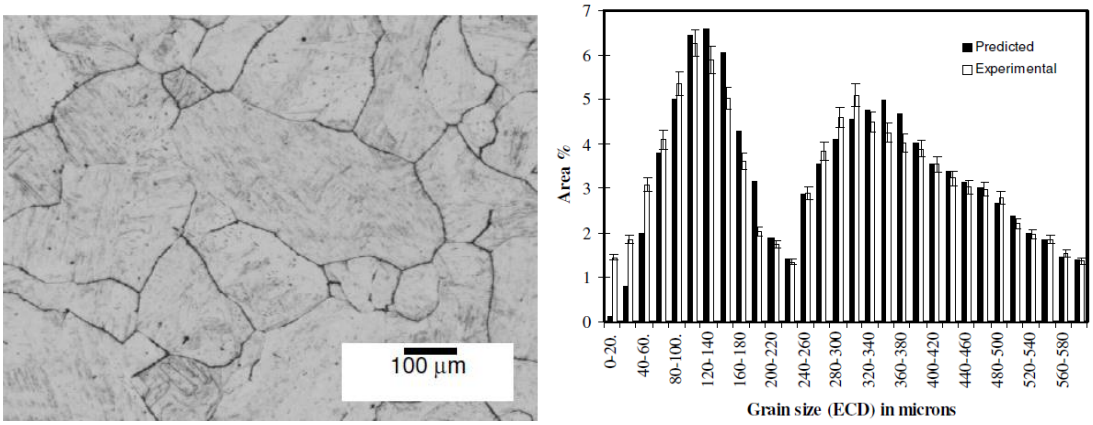

Figure 5-22 Microstructure and grain size distribution of partial recrystallized sample (1025°C, 0.3 strain)

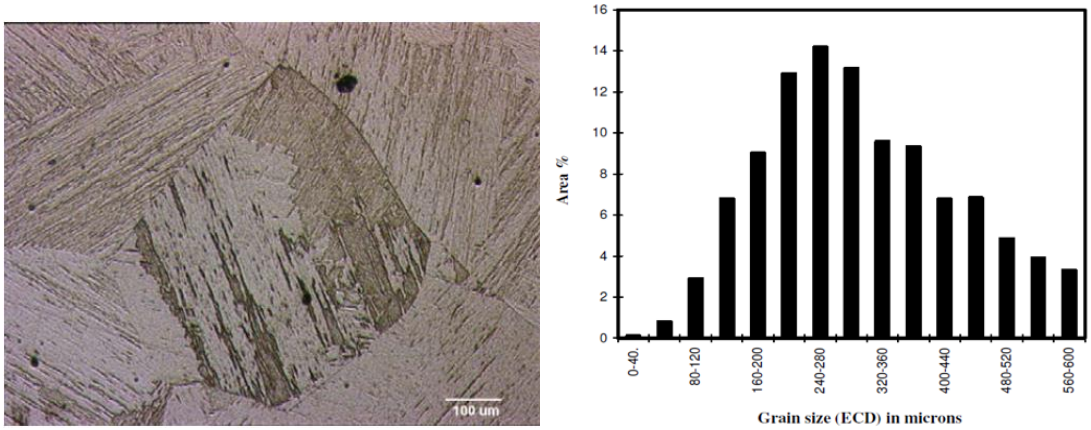

Figure 5-23 Microstructure and grain size distribution of non-recrystallized sample (1225°C, un-deformed)

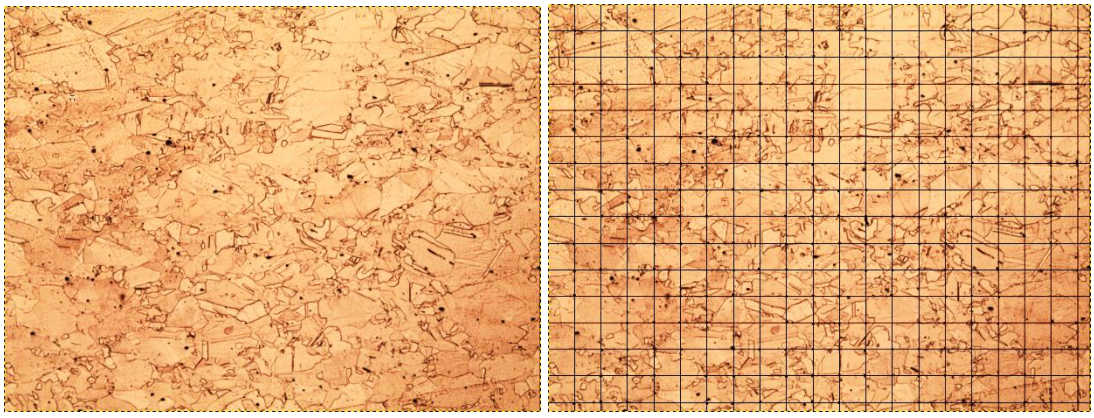

(a) (b)

Figure 5-24 Example of the point counting method used to characterise the recrystallisation fraction of the Fe-30Ni model alloy that has been cold deformed then annealed (sample at 850 °C, 0.3 strain, 1800s shown).

5.6 Scanning electron microscopy

5.6.1 Precipitates characterisation

A Zeiss SIGMA FEG-SEM was used to examine precipitates larger than 100 nm present in the steel (undissolved precipitates in the matrix). The operating voltage was set at 20 kV and an Oxford instrument energy dispersive X-ray spectroscopy (EDS) system with Aztec analysis software was used to characterise the composition of the precipitates. The as received specimen was sectioned along the rolling plane, then grinded, polished by using the method mentioned in chapter 5.4. Then, the specimen was lightly etched by Kallings agent for 30 second prior to SEM imaging.

5.6.2 EBSD study

Samples measuring 3 x 3 mm^2 with a thickness of 1 mm were cut from the transverse cross section of the deformed samples in the central region. The samples were then ground and polished using the same preparation sequence for optical microscopy with an additional step of two hours in a VibroMet 2 Vibratory Polisher (from Buehler) after general polishing to remove any deformation induced during the polishing procedures. Only the central section was selected to ensure the strain was homogeneous.

EBSD mapping was carried out on a square grid with step sizes of 2 - 0.3 µm. The coarse step size has been applied to examine the grain structure and the overall recrystallisation kinetics for both hot and cold deformed samples. Whereas the fine step size was used to reveal the substructure characteristics and the early stage of process in the fine recrystallising grains. The data acquisition was carried out by AZTEC and processing were carried out using the HKL Channel 5 software. Crystallographic texture was represented using the inverse pole figure (IPF).

In order to identify the relationship between the deformed microstructure, recrystallisation nucleation sites and the growth mechanism, in-situ annealing treatments have been carried out in a ZEISS SIGMA FEG-SEM with GATON heating stage. In–situ EBSD was used to observe the microstructure change during the annealing process at elevated temperature. A series of EBSD maps were taken during annealing to examine the effect of grain size distribution on recrystallisation kinetics.

Conventional in-situ EBSD can examine an area of less than 50 x 50 μm^2 due to the limited EBSD scanning speed. As there is no phase transformation in the Fe-30Ni Nb free steel the specimen was cooled down to 500 °C to halt recrystallisation while taking images through EBSD scanning. This provides sufficient time for a bigger area EBSD scan.

The set temperature for in-situ EBSD was 700 °C, the temperature was chosen due to the limitation of the in- situ heating stage. The heating rate was set to be 1°C/s to minimise overshoot at the peak temperature, and the cooling rate was also set to 1 °C/s to allow a controllable cooling process. It takes approximately 2 minutes to reheat and cool for each cycle. Therefore, it is likely that recovery and/or recrystallisation will occur during the reheating and the cooling stage, nevertheless this effect was minimised by choosing a low annealing temperature. It was found that recrystallisation occurred after 5 minutes of annealing at 700 °C, therefore it is not unreasonable to assume that little recrystallisation has occurred during the reheating stage. Additionally, when analysing the in-situ EBSD data, great caution needs to be taken because the recrystallisation fraction at a certain time could be higher than isothermal holding only, however, as EBSD was used to examine the influence of grain size and stored energy, not the rate of recrystallisation, this was not an issue. The mechanism of recrystallisation (nucleation at grain boundaries) was the same in both cases. The sample was deformed to 0.3 strain prior to annealing. The operation conditions for in-situ EBSD are listed in Table 5-10.

Table 5-10 Operating parameters for in-situ EBSD

Operating voltage (kV)	Mapping area (μm^2)	Step size (μm)	Acquisition time (min)	Heating temperature (°C)
20	500 x 350	0.3- 0.7	90	700

5.7 TEM and STEM - strain induced precipitation characterisation

TEM was performed using both JEOL 2000FX and JEOL 2100 transmission electron microscopes operated at 200 kV, STEM was carrired out using FEI Talos at 200 kV. The sample was firstly cut from the bulk specimen as a 1 mm thick plate using a silicon carbide blade and cooling lubricant. Then, the thin plate was glued onto a Gatan disc

grinder to minimize the specimen bend or damage. After that, the plate was ground by silicon carbide paper to a thickness of 150 μm. Then, a Gatan disc punch was used to cut the plate into several disc specimens with a diameter of 3 mm. Electropolishing was carried out by Struers Tenupol-5 twin jet electropolisher. The conditions are shown in Table 5-10. The conditions for the TEM samples examined are listed in the Tables 5-11 and 5-12. CBED (convergent beam diffraction technique) has been used to examine the thickness of the samples. The detailed discussions of the validity and the accuracy of this technique can be found elsewhere [171- 173].

Table 5-11 Twin jet polishing conditions for TEM specimen

Solution	5% perchloric acid, 95% methanol
Flow rate	35/50
Temperature	-30°C to -20°C
Voltage	20V
Sample thickness	150 μm
Time	Automatic

Table 5-12TEM sample conditions for cold deformation

Temperature (C)	Strain	Nb content (wt. %)	Time (s)
950	0.3	0.044	25
950	0.3	0.044	60
950	0.3	0.044	120
900	0.3	0.044	120
900	0.3	0.044	450
850	0.3	0.044	120
850	0.3	0.044	600
850	0.3	0.044	1200
850	0.3	0.044	3000

Table 5-13 TEM sample conditions for hot deformation

Temperature (°C)	Strain	Nb content (wt. %)	Time (s)
950	0.35	0.044	25
950	0.35	0.044	480
950	0.45	0.044	25
850	0.35	0.044	3000

Chapter 6 Microstructure of the as homogenised, heat treated and deformed materials

6.1 Introduction

Knowing the deformed microstructure, including grain size distribution and stored energy distribution is crucial for predicting and understanding the recrystallisation Avrami exponent. Any inhomogeneous nature in the microstructure can lead to inhomogeneous recrystallisation nucleation and growth. It has been widely accepted that the driving force for recrystallisation nucleation is the local stored energy gradient, i.e. strain induced boundary migration. Prior austenite grain boundaries, which provide both high angle grain boundaries (HAGB) and large strain gradients, are the preferred nucleation sites for recrystallisation. In addition, recrystallisation growth is effectively a HAGB migration process, which is also driven by stored energy. Deformation microstructures have been studied previously using EBSD and TEM techniques but there is little information regarding the strain distribution among different grains in one sample.

In this chapter, the deformed Fe-30Ni model alloy is characterised. Particular attention is paid to the cold and hot deformed microstructures with respect to any inhomogeneity in strain distribution and the relationships between strain distribution and grain size. It was discussed in chapter 2 that cold and hot deformed Fe-30Ni samples have comparable deformed microstructures (cells, microbands and subgrains), but the stored energy for the same applied strain level could be different, and this depends on the heating rate to the annealing temperature for cold deformed samples and the strain rate for the hot deformed samples. It was concluded from the literature review in chapter 2 that the effect of grain size distribution on the recrystallisation mechanism should not be affected by whether samples were hot or cold deformed, but the recrystallisation rates would not be comparable.

Therefore, the deformed microstructure and stored energy estimation will be covered in this chapter, but a detailed discussion on the effect of heating rate and strain rate on the stored energy is not included as it is outside the scope of this thesis as the aim for this project is to investigate the effect of the grain size distribution on the

recrystallisation Avrami exponent, which is independent of the strain (and hence stored energy).

6.2 Cold deformed microstructure

The deformed microstructure being described in this section is that of Fe-30Ni Nb free steel and the Fe-30Ni-0.044 Nb steel samples with the mode grain size of 160 μm. The flow stress curve for cold deformation of the Fe-30Ni Nb free steel is shown in Figure 6-1. The hardness value (Hv 10kg) after uniaxial compression is 210 for 0.3 strain, and 180 for 0.2 strain, which compares to an initial hardness of 110 for the homogenised sample. Hardness tests have also been carried out for the Fe-30Ni-0.044 Nb steel and the hardness values at 0.3 and 0.2 strain were the same as for the Fe-30Ni Nb free steel. This suggests that the stored energy for these two steel grades after cold deformation are comparable: this chapter will focus on the Fe-30Ni Nb free steel, and the effect of Nb on recrystallisation Avrami exponent will be discussed later in chapter 8.

Figure 6-2 shows microhardness mapping of the homogenised and the deformed samples. Macroscopically speaking, the variation in hardness shows no clear pattern and therefore suggests that there was no significant macroscopic strain distribution within either the homogenised or the deformed samples, as shown by the macro-hardness measurements. It is worth noting that the step size of the microhardness test is 500 μm, which is larger than the maximum grain size of the homogenised samples. Therefore, it is unlikely to reveal the local strain inhomogeneity so EBSD scanning has been carried out to characterise the strain distribution at a microscopic scale.

Examples of the EBSD mapping of the deformed microstructure of Fe-30Ni Nb free steel and Fe-30Ni-0.044Nb steel at room temperature are given in Figure 6-3. As mentioned in chapter 2.2, local misorientation can be used as an indication of stored energy. This is because local misorientation increases with increasing dislocation density. Large areas (3mm × 3mm) have been examined and two typical examples are shown in Figure 6-3. The local misorientation map of both steel grades clearly shows that the deformation microstructure is inhomogeneous within each individual grain and among different grains at a strain of 0.3. The finer grains appear more deformed

(higher local misorientation) compared to the coarser grains, for example it can be seen that the coarser grains 1 and 2 were deformed considerably less compared to finer grains 3-6.

Additionally, higher local misorientation has been observed at grain boundary regions and triple junctions than the grain interiors, arrows shown in Figure 6-3. That is, the areas adjacent to the grain boundaries and the triple points were more deformed than the interior of the grains, which agrees with the literature for cold deformed microstructures [25, 94]. These heavily deformed regions were reported to promote recrystallisation nucleation, and the initial growth rate is expected to be high around these regions. Additionally, as mentioned in chapter 2.2, the grain size effect on stored energy also needs to be taken into account. The references mentioned above did not discuss any inhomogeneities in strain related to the grain size only with respect to the grain boundary regions. Rehman has mentioned that the recrystallisation kinetics is strongly affected by the stored energy variation among different grains [27]. With a decrease in grain size, the stored energy increases, and as a result, a higher recrystallisation rate is expected for the finer grains. Rollett and Luo also proposed that the local strain distribution affects the recrystallisation rate, and lowers the Avrami exponent of recrystallisation [14, 79]. Therefore, knowledge of the stored energy variation within one grain and across different grains are required to establish a better understanding of recrystallisation kinetics.

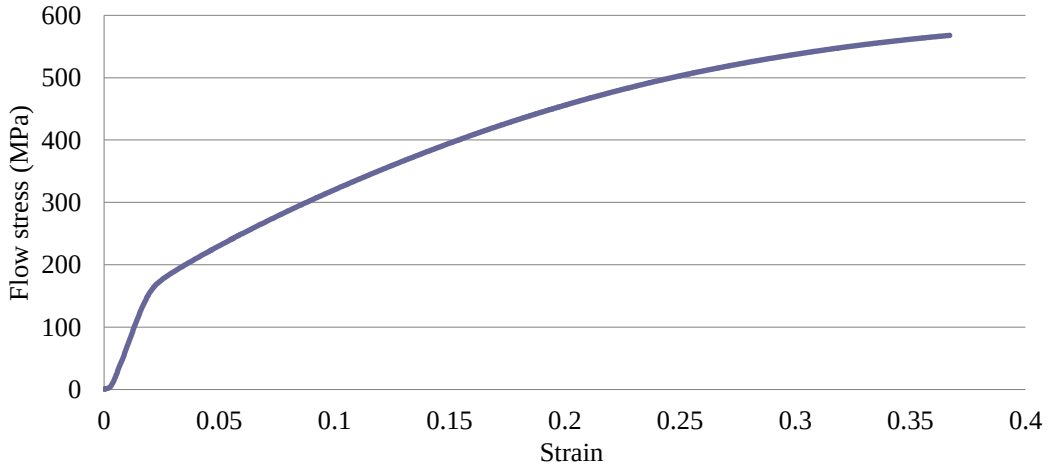

Figure 6-1 Flow stress of Fe-30Ni steel uniaxially compressed at room temperature.

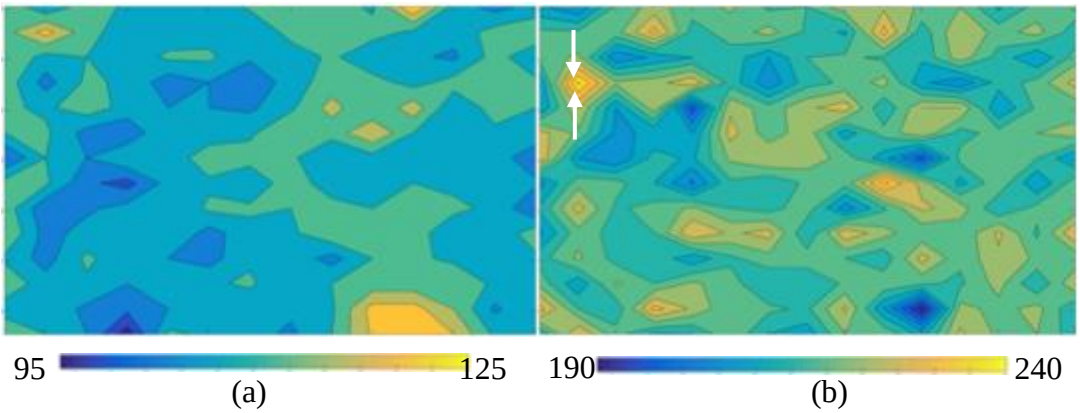

Figure 6-2 Microhardness mapping of Fe-30Ni specimen (a) in the homogenised condition and (b) deformed to 0.3 strain at room temperature, step size 0.5mm. (Examination area 3.5 mm × 7mm). Arrows show the compression direction.

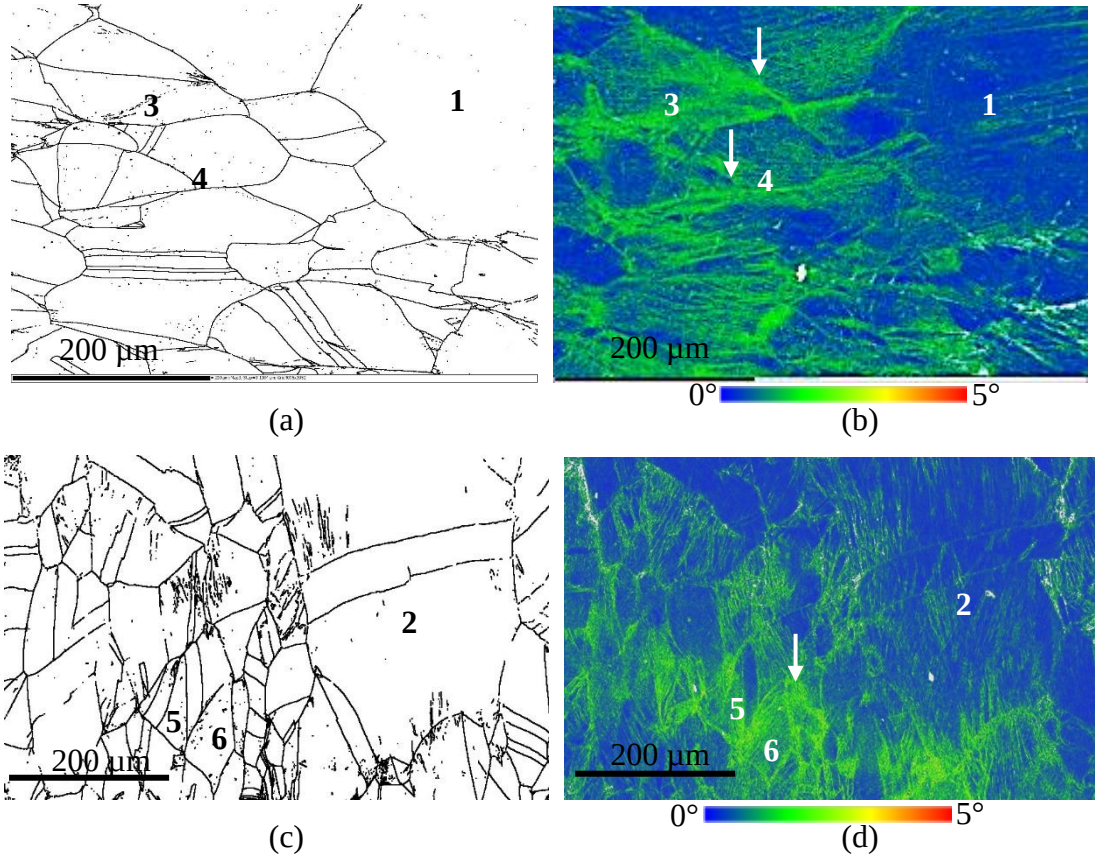

Figure 6-3 (a), (c) High angle grain boundaries (> 10°) and local misorientation (b), (d) EBSD map of samples deformed to 0.3 strain at room temperature, where the local misorientation from 0 to 5 degree is shown in a colour scale. Fe- 30Ni Nb free steel (a), (b) and Fe- 30Ni- 0.044 wt. % Nb (c) (d). The arrows in (b) and (d) indicate higher local misorientation at the grain boundaries, labels 1 and 2 indicate coarser grains with lower local misorientation and labels 3-6 indicate finer grains with higher local misorientation.

6.2.1 Cold deformed microstructure after reheating

Cold deformed Fe-30Ni steel samples were reheated in the preheated furnace (850-950 °C) during the annealing process. Thermocouple readings showed that it took 30 seconds for the sample to reach the set temperature, as described in chapter 5, in which softening (for example static recovery) could occur to reduce the stored energy level. To investigate whether recrystallisation has occurred during the reheating stage, the hardness and microstructure were measured for a sample inserted in the furnace and removed and quenched after 10-30 seconds. It can be seen from Figure 6-4 that the hardness decreases with increasing time and annealing temperature (850 - 950 °C) for holds between 10- 20s. The hardness differences for the different annealing temperatures is less after holding for 30s (HV: 174 - 175), i.e. when the isothermal annealing temperature was reached. The hardness after reheating to the different annealing temperatures is summarised in Table 6-1. It can be seen that there is an approximately 30% hardness reduction compared to the as-deformed hardness value (210 HV for 0.3 strain, 180 HV for 0.2 strain and 110 HV for homogenised and undeformed sample) during the reheating process at both 0.2 and 0.3 strain within the temperature range of 950 - 850 °C. Table 6-1 shows that there is no significant difference in hardness with changing in annealing temperature indicating comparable extent of recovery has occurred during reheating. Thus, the average hardness values for samples held for 30 seconds across the annealing temperature range has been used for both strains to estimate the stored energy. The results indicate that the driving force for recrystallisation at temperatures 850 - 950 °C are comparable, as similar amounts of softening occur during the reheating stage.

The microstructure after reheating and quenching when the sample reached temperature showed no sign of recrystallisation, Figure 6-5. That is, the deformed grains were still elongated for both 0.3 and 0.2 strain, no newly formed recrystallised grains along the grain boundaries and triple points have been observed. This confirms that recrystallisation within the temperature range of 850 - 950 °C, strain 0.3 - 0.2 can be considered as being isothermal. That is, only recovery occurred during the reheating stage. The centre region and the sub-surface region recovered microstructures are shown in Figure 6-6 and indicate uniformity in microstructure (i.e. no recrystallisation is seen in either region).

STEM images of the recovered microstructure are shown in Figure 6-7. The sample was reheated to 950 °C then directly quenched to room temperature. Arrays of subgrains with an average size of approximately 1 µm have been observed, which are similar to the results in the literature mentioned in chapter 2.2 for both cold and hot deformed samples.

In summary only recovery has occurred during the reheating stage, which reduces the overall stored energy and therefore recrystallisation will occur isothermally for the trials carried out.

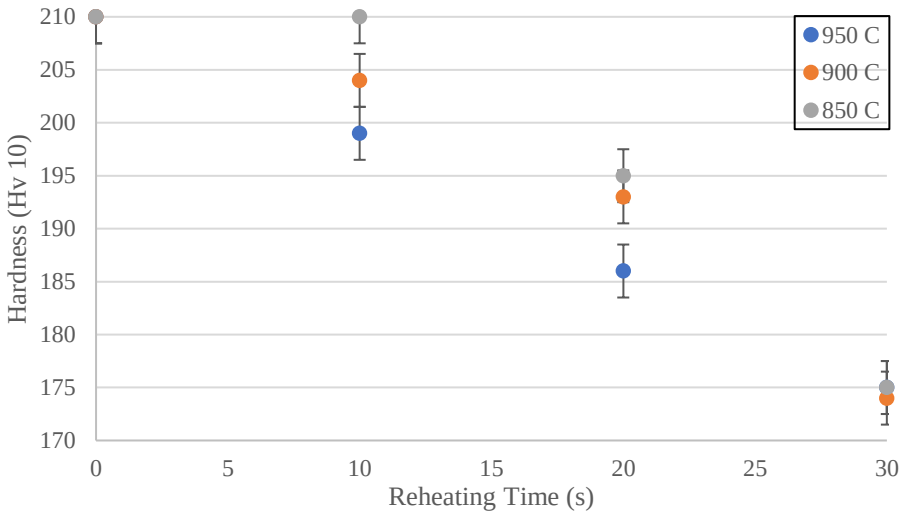

Figure 6-4 Hardness change during reheating for cold deformed samples with 0.3 strain, various target annealing temperatures (850 - 950 °C)

Table 6-1 Summary of hardness values after reheating

Temperature, °C	Strain	Hardness after reheating to the annealing temperature and quenching the sample.
950	0.3	175 ± 3
900	0.3	174 ± 3
850	0.3	175 ± 5
950	0.2	162 ± 1
900	0.2	161 ± 1
850	0.2	158 ± 4

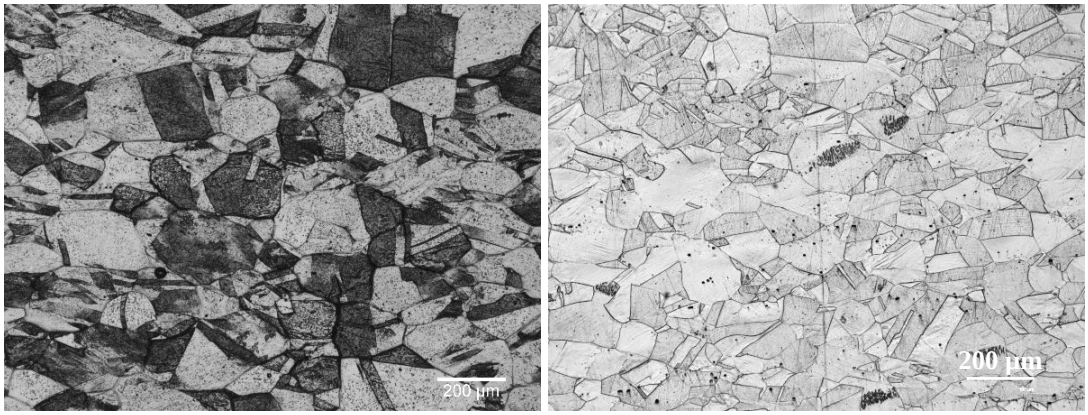

(a) (b)

Figure 6-5 Examples of the reheated and quenched microstructure at 950 °C (a) 0.3 strain and (b) 0.2 strain

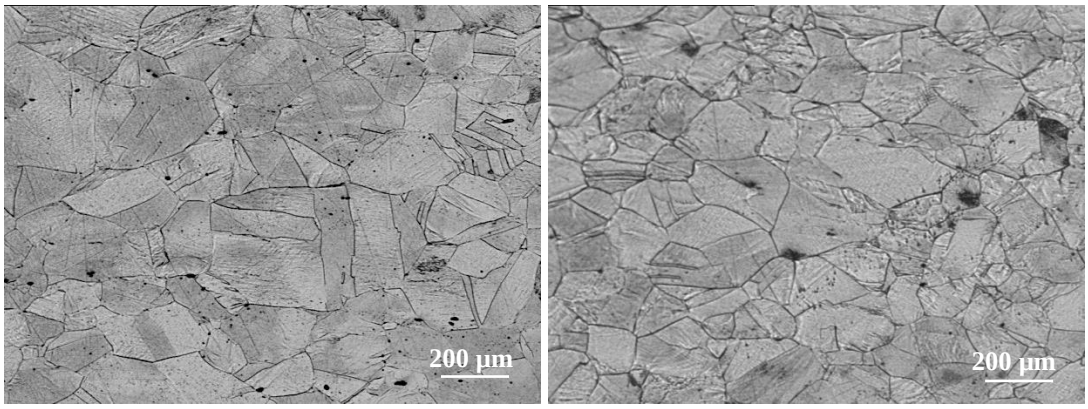

(a) (b)

Figure 6-6 Cold deformed samples at room temperature to 0.3 strain, reheated to 950 °C then quenched: (a) centre region (b) sub-surface region

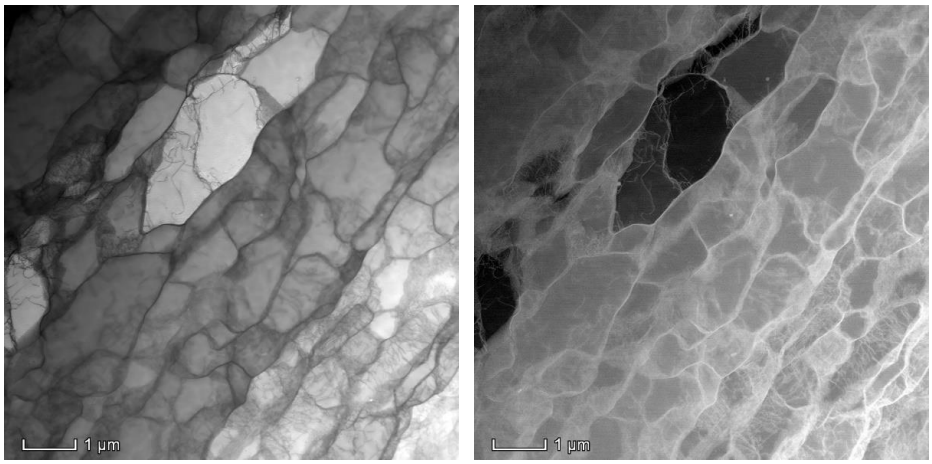

(a) (b)

Figure 6-7 Cold deformed to 0.3 strain and recovered microstructure by STEM at lower and higher magnification (a) (c) bright field (b) (d) HAADF

6.2.2 Effect of reheating stage on precipitation

One of the aims of the project was to investigate the effect of precipitates size and volume fraction, i.e. Zener pinning, on the recrystallisation Avrami exponent. It has been shown in the previous section that recrystallisation occurs during the isothermal annealing stage, therefore, any pinning force change, due to precipitation / precipitate coarsening during the isothermal annealing, could affect the recrystallisation mechanism.

It has been widely acknowledged that the resolution limit for TEM and STEM when observing precipitates in steels is around 2 - 3 nm, whereas the critical radius for strain induced precipitates is around 0.5 nm [68, 122]. As a result, it was not possible to distinguish the very early stage of strain induced precipitation, for example whether this occurred during reheating. STEM images, shown in Figure 6-8, from a sample reheated for 30 seconds to an annealing temperature of 950°C, suggest that there was no strain induced precipitates (or none of a size to be distinguished) observed in the matrix after reheating. It should be noted that despite there being no (observable) precipitates at the onset of recrystallisation it is possible that the precipitation kinetics could be different between a cold deformed and hot deformed sample because of differences in the amount of recovery (static for cold deformed and reheated samples and dynamic for hot deformed samples) affecting the distribution and density of favoured precipitate nucleation sites, as discussed in chapter 3.

Therefore, the absolute values for recrystallisation and precipitation kinetics, i.e. starting time of recrystallisation and precipitation, measured for cold deformed and annealed samples might not be directly comparable to those for hot deformed samples, nevertheless the effect of Zener pinning force evolution, i.e. precipitation size and volume fraction, on the recrystallisation mechanism (Avrami exponent) is expected to be valid.

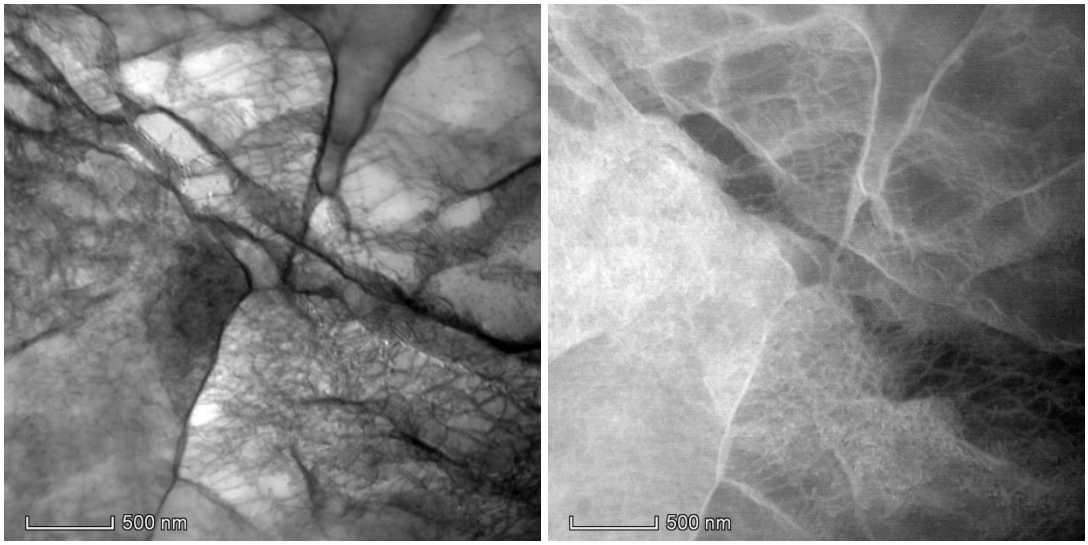

(a) (b)

Figure 6-8 Microstructure of the Fe-30Ni-0.044Nb cold deformed to 0.3 strain, reheated to 950 °C then quenched by STEM (a) bright field (b) HAADF. No precipitates are evident in the microstructure.

6.3 Hot deformed microstructure

In chapter 2.5, it was discussed that the cold and hot deformed microstructures are comparable, but the stored energy for sample deformed at same strain could be different. The flow stress of Fe-30Ni alloy deformed at temperatures of 850 - 950 °C with a strain rate of 5 s^{-1} and quenched at a cooling rate of 80 °C/s after deformation, are given in Figure 6-9. It can be seen that no dynamic recrystallisation has occurred under these conditions as no strain softening is evident. Figure 6-10 shows an EBSD image from the central area of a quenched hot deformed sample where a deformed microstructure with no evidence of recrystallisation can be observed. This further proves that no dynamic recrystallisation occurred during hot deformation. A higher magnification EBSD scan is shown in Figure 6-11. It can be seen that a higher local misorientation occurs around the grain boundary and triple point regions, which is comparable to the cold deformed microstructure discussed earlier, Figure 6-11. This agrees with the literature reports as mentioned in chapter 2.2, i.e. for 316L austenitic steel deformed to 0.29 strain at 900 °C and a Fe-30Ni model alloy deformed to 0.2 strain at 950 °C [10, 35], where the authors reported that the deformed microstructure was inhomogeneous with respect to stored energy. Figure 6-12 (STEM images) showed the hot deformed microstructure consisting of arrays of subgrains, which is also comparable with the cold deformed sample, Figure 6-7. Therefore, these results

show that both cold and hot deformed sample showed comparable deformed microstructures.

As mentioned in chapter 2, the stored energy level after cold deformation is generally higher than after hot deformation to the same strain, which has been attributed to the difference in flow stress, but can also reflect occurrence of dynamic recovery. However, recovery can occur during reheating, which leads to a decrease in stored energy. The hot deformed and quenched samples (deformed at temperatures of 850 - 950 °C, 0.35 strain with a strain rate of 5 s^{-1}), had hardness values of 140- 145 (Hv 10kg) in the central region, which is considerably lower than the hardness of the cold deformed and reheated samples at 0.3 strain. Therefore, for these particular tests the stored energy appears to be different for the cold deformed and annealed and hot deformed samples, also the cold and hot deformed sample recrystallisation kinetics are not directly comparable in every case. This is due to two main reasons: firstly, the recrystallisation driving force for cold deformed samples is dependent on the strain and heating rate, whereas the strain rate and deformation temperature determines the driving force for hot deformation, therefore, an equivalent strain can only be valid at certain strain, strain rate and heating rates; secondly, the recrystallisation growth rate is dependent on the mobility of the grain boundaries, which is dependent on the misorientation between neighbouring grains (i.e. the extent of recovery) [1]. Therefore, the recrystallisation rate could be different between the cold and hot deformed samples.

To sum up, local strain inhomogeneity adjacent to the grain boundary regions is observed in the hot deformed samples and this is comparable to cold deformed and reheated to annealing temperature samples. As a result, the effect of grain size distribution on the recrystallisation mechanism should be comparable between the cold deformed / annealed samples and hot deformed samples, i.e. comparable Avrami exponents.

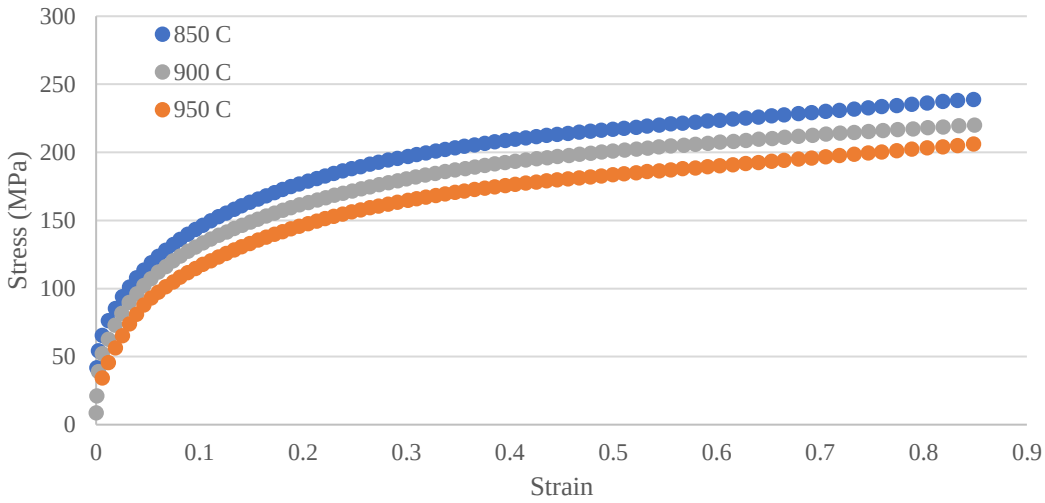

Figure 6-9 Flow stress of Fe-30Ni steel uniaxially compressed at elevated temperature (850- 950 °C).

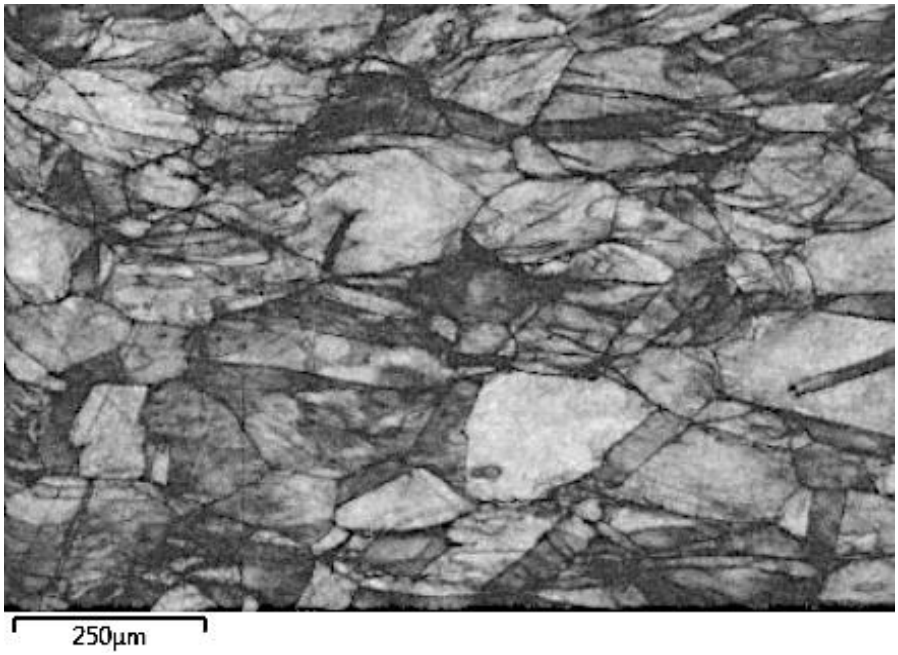

Figure 6-10 Band contrast EBSD image from a central area of a hot deformed sample to 0.3 strain, 950 °C then cooled at the rate of 80 °C/s.

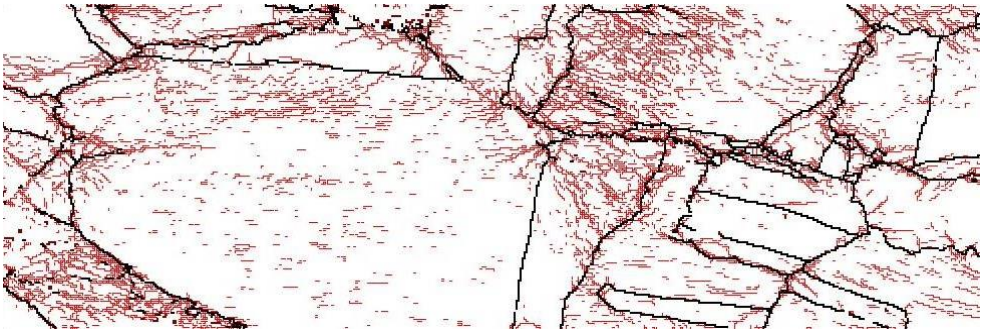

(a)

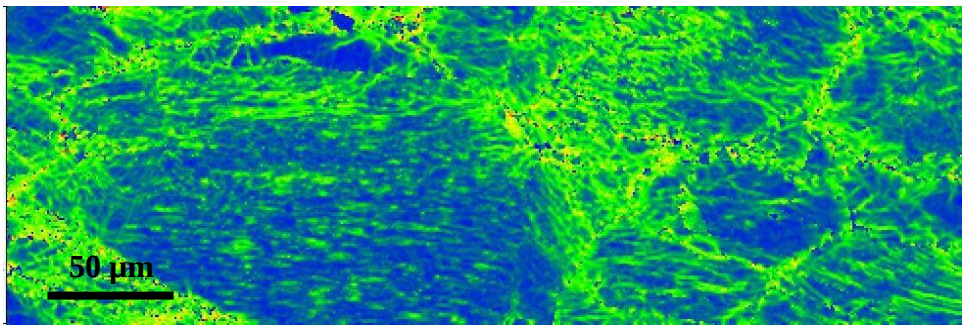

(b)

Figure 6-11 Hot deformed sample at 0.3 strain, 950 °C then air quenched. Recovered microstructure has been observed. EBSD image of (a) grain boundary map, red lines (> 2 degree), black lines (>15 degree), (b) local misorientation map, (0 - 5 degree misorientation shown) and (c) band contrast map

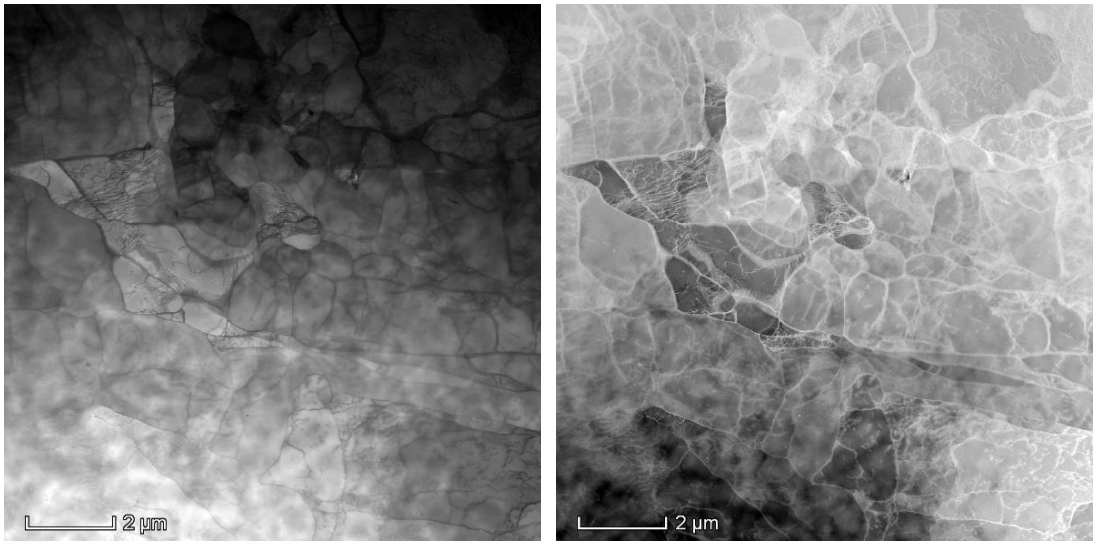

(a) (b)

Figure 6-12 Hot deformed to 0.3 strain and quenched sample showing recovered microstructure by STEM (a) bright field (b) HAADF

It was discussed in chapter 2.5 that the barrelling effect, i.e. strain inhomogeneity, could affect any study of recrystallisation. A macro image and hardness profile from a sectioned hot deformation sample are shown in Figure 5- 17 (b) It can be seen that the hot deformed sample (0.35 strain, 25 seconds hold, 950 °C) shows significant variation in hardness through the sample thickness. Figure 6-13 shows the microstructure from the sample at the centre, quarter thickness and sub-surface locations. A higher recrystallisation fraction, i.e. approximately 30%, is shown in the centre region, whereas no recrystallisation is observed in the sub-surface region. This is due to a higher strain being imparted in the centre region due to barrelling – some temperature variation through thickness may also arise, however hot grips in the Gleeble were used and thermocouple readings showed little thermal gradient. As a result, stress relaxation and double hit deformation tests were considered to be inappropriate to investigate the effect of grain size distribution on recrystallisation mechanisms as the strain inhomogeneity in the hot uniaxial compression deformation tests would affect the Avrami exponent. Where recrystallisation in the hot deformation samples has been considered only the centre region of the sample was investigated.

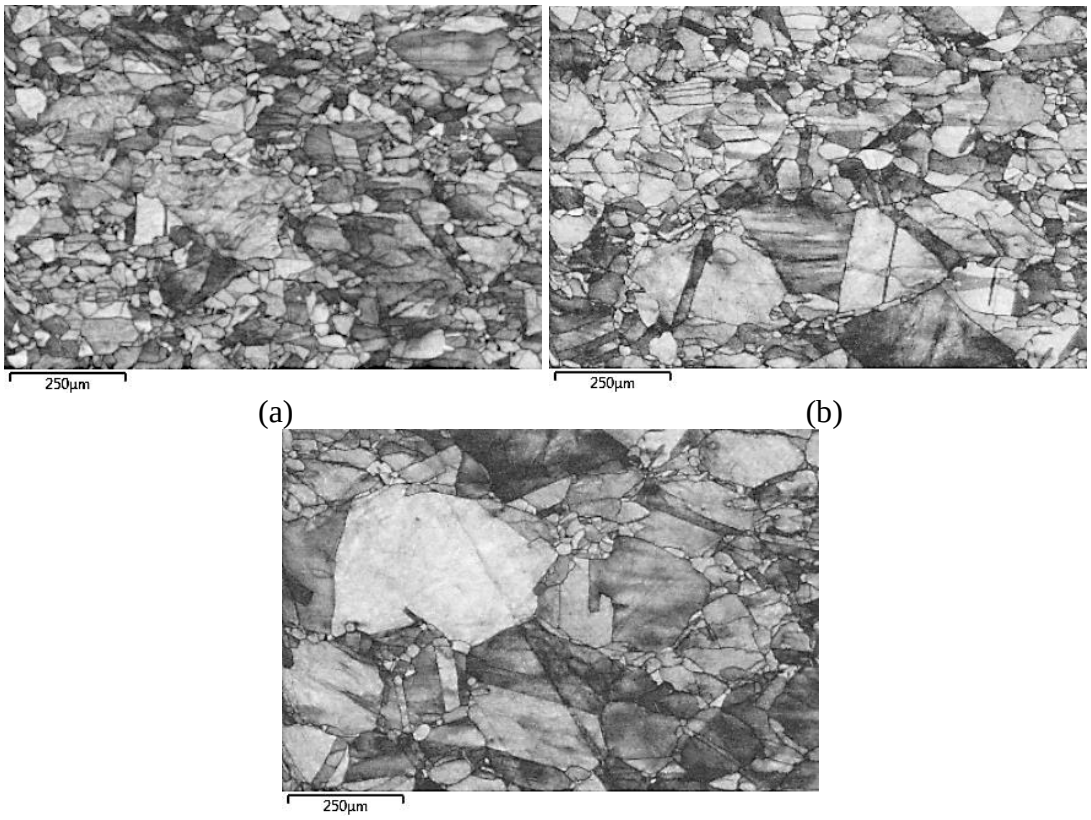

(a) (b)

(c)

Figure 6-13 Hot deformed sample at 950 °C, 0.35 strain 25 s hold: (a) centre region (b) quarter thickness region (c) sub-surface region

6.4 Stored energy estimation

The stored energy can be estimated by the equation below, which was discussed in the literature review (chapter 2.2).

$$\sigma = \sigma_0 + M\alpha Gb\sqrt{\rho} \quad \ldots 60$$

Where M is 3.1, α is 0.15, G = 70 GPa for Fe-30Ni at room temperature, b = 2.59 × 10^{-10}m. Taking $\sigma_y \approx 3\,Hv$ [174], then,

$$\rho = (\frac{3\times\Delta Hv}{M\alpha Gb})^2 \quad \ldots 61$$

Where ΔHv is the increment of hardness values after deformation and reheating.

$$F = \frac{\Delta\rho G\prime b^2}{2} \quad \ldots 62$$

G' represents the shear modulus at elevated temperature, it has been reported that the shear modulus decreases with increasing temperature for iron, and iron-nickel alloys [175- 176]. It has been summarised that the shear modulus in iron-nickel alloy reduces by half at 830 °C compared at 0 °C [175]. Therefore, 35 GPa has been used as the shear modulus at 830 °C in this case.

The dislocation density and the driving force for both strains after cold deformation and reheating has been estimated and is shown in Table 6-4. It can be seen that the driving force is 0.52 MPa for 0.3 strain and 0.36 MPa for 0.2 strain, which are in the range reported in the literature, chapter 2.2.

The stored energy at the centre region of the hot deformed sample after 0.27- 0.45 strain have not been estimated from the hardness measurement. This is because further recovery could occur during the cooling period, therefore the measured hardness values might not reflect the stored energy after hot deformation. Additionally, the hot deformation tests were to examine the effect of grain size distribution on recrystallisation Avrami exponent, the absolute stored energy value is irrelevant in this case.

Table 6-2 Estimation of the dislocation density and the driving force (cold deformed samples), where the hardness increment is the difference between the cold deformed and heated to the annealing temperature sample and initial (homogenized) sample hardness values).

Strain	Hardness increment (HV)	Dislocation density (m^{-2})	Driving force (MPa)
0.3	60	4.5×10^{14}	0.52
0.2	50	3.1×10^{14}	0.36

6.5 Summary

Microscopic inhomogeneity in the strain distribution after both cold and hot deformation has been revealed for both steel grades, where the triple points and grain boundaries have a higher local misorientation due to being more deformed than the grain interior. It was also found that finer grains showed higher local misorientation than coarser grains in the cold deformed samples. The driving force for recrystallisation after cold deformation and reheating to the isothermal holding temperature used for the recrystallisation studies, for both 0.3 and 0.2 strain, has been estimated, and agrees with the literature data [29, 31, 32, 170].

The hardness of the cold deformed samples decreased during reheating, which was attributed to recovery. No recrystallisation occurred during the reheating stage, and it has been confirmed by observing the microstructure after reheating via optical microscope.

The cold deformed and reheated to annealing temperature and hot deformed and quenched samples, both deformed to 0.3 strain, have the different flow stress curves and hardness values, i.e. indicating a different stored energy level. Additionally, both cold and hot deformed samples showed the comparable deformed microstructure (dislocation cells, microbands and subgrains). The Fe-30Ni-0.044Nb steel did not show the presence of any precipitates after cold deformation and reheating to the annealing temperature.

The validity and the comparsion of the cold deformed and the hot deformed tests have been listed in Table 6-3. It can be seen that the stored energy estimation and the macroscopic strain inhomogeneity (flow stress, deformed sample dimension, hardness measurement), are not transferrable between the cold and hot deformed conditions. Nevertheless, the observations of the microscopic strain inhomogeneity were comparable between the cold and hot deformed samples. That is, the grain boundary regions were more deformed than the grain interior, also the finer grains carried a higher stored energy compared to the coarser grains. Therefore, the recrystallisation Avrami exponent will be affected due to the recrystallisation inhomogeneity in both nucleation and growth, which will be discussed in the following chapter 7.

Table 6-3 Comparison of cold deformed and annealed and hot deformed tests

	Tests	Objectives	Transferrable knowledge	Non- transferrable knowledge
1	Flow stress measurement	1. To compare the flow stress between the cold and hot deformed conditions		1. Considerably less dynamic recovery has occurred during the cold deformation compared to the hot deformation. 2. No dynamic recrystallisation has occurred in hot deformation, up to 950°C, 0.8 strain, strain rate $5s^{-1}$.
2	Deformed samples dimension measurement Marcohardness line profile Microhardness mapping	1. Extent of barrelling of cold and hot deformed samples 2. Macroscopic strain inhomogeneity in cold and hot deformed samples (uniaxial compression samples)		1. No barrelling has been seen in the cold deformed samples, whereas significant barrelling has been observed in the hot deformed samples. 2. Marcohardness varied significantly along the sample deformation axis for hot deformed samples attributed to the barrelling, whereas little macrohardness/

		3. Stored energy comparison between the cold and hot deformed samples.		microhardness variation was seen for the cold deformed samples. 3. The stored energy between cold (reheated and quenched) and hot deformed samples could be different.
3	EBSD and TEM deformed microstructure observation	1. Microscopic strain inhomogeneity observation of cold and hot deformed samples 2. Deformed microstructure observation of cold and hot deformed samples	1. Higher stored energy has been observed at grain boundary regions in both cold and hot deformed samples. 2. Microbands have been observed in both cold and hot deformed samples.	
4	Optical observation after reheating Hardness changes during reheating	1. Stored energy/ microstructure change during reheating for the cold deformed samples		1. Only recovery has occurred in this case during reheating. 2. Hardness decreased gradually during reheating, and approximately 35 % of

				hardness (stored energy) has lost during the reheating process.

Chapter 7 Effect of the grain size distribution on recrystallisation mechanism

7.1 Introduction

The chapter focuses on the effect of the grain size distribution on the recrystallisation mechanism. The JMAK model has been used to describe recrystallisation kinetics and mechanism over the last three decades for both cold and hot deformation annealing process, like all models, it includes certain assumptions: a homogeneous distribution of both potential nucleation sites and stored energy are the main assumptions for the JMAK model. Grain size is an important parameter as it strongly affects the stored energy level after deformation, and the grain boundary area, as preferred recrystallisation nucleation sites, is directly related to the grain size. However, as discussed in chapter 2.2.2 and 2.4, one grain size is not sufficient to fully describe the grain size distribution in the matrix, even for a unimodal grain size, and will not account for any inhomogeneity in the microstructure.

The driving force of recrystallisation, i.e. the stored energy, has been shown to be inhomogeneously distributed for both cold and hot deformed samples in Chapter 6, where the grain boundaries and triple points tend to accommodate higher stored energy, and the finer grains show a higher stored energy and a more homogeneous strain distribution than the coarser grains. In addition, finer grains have a higher number of potential recrystallisation nucleation sites per unit area due to their higher grain boundary density compared to the coarser grains. Therefore, the recrystallisation kinetics across the material could vary, including both nucleation and growth of the recrystallising grains. Therefore the effect of grain size distribution on the recrystallisation Avrami exponent, requires further investigation.

It has been acknowledged in the previous chapter that cold and hot deformation samples to the same strain may contain different amounts of stored energy, which is also affected by the strain rate for the hot deformed sample and the heating rate of the cold deformed sample prior to annealing. It was discussed in the literature review (chapter 2.4) that the recystallisation Avrami exponent, is not dependent on the stored energy. To verify that the recrystallisation mechanism, i.e. Avrami exponent, is

independent from the stored energy and the deformation temperature, both cold and hot deformed[1] samples recrystallisation behaviour will be discussed in this chapter.

Additionally, the feasibility of the Sellars approach (described in chapter 2.3) for describing the recrystallisation kinetics for the cold deformed and annealed samples will be investigated, although it is noted that the recrystallisation starting and finishing times obtained from the cold deformed and annealed and hot deformed samples at the same temperature and strain level, i.e. the recrystallisation kinetics, will not be directly comparable as the stored energy values are different. Therefore these recrystallisation starting and finishing times will not be the same as required for industrial hot rolling of HSLA steels. However, it is expected that the effect of recrystallisation inhomogeneity caused by the grain size distribution on the Avrami exponent is still applicable for HSLA steels recystallisation prediction during hot rolling.

The objectives for this chapter are:

1) To determine the recrystallisation kinetics for the model Fe-30Ni Nb free steels and examine the appropriateness of the JMAK model assumptions for this steel.

2) To establish the effect of grain size and grain size distribution on the recrystallisation Avrami exponent value for both cold and hot deformed samples.

3) To modify the JMAK model to take into account grain size distribution effects.

[1] Due to limited availability of the hot deformation thermo-mechanical simulator during this project (due to long term break-down), it was not possible to carry out all tests in the hot deformed condition.

7.2 Microstructure evolution during recrystallisation in the cold deformed samples

The two starting grain size distributions in the Fe-30Ni Nb free steels have been shown in Figure 6-3 (chapter 6.3). As discussed in chapter 2.3, a finer grain size promotes the recrystallisation process. Therefore, the sample with mode grain size of 100 µm is expected to give a faster recrystallisation rate compared to the sample with mode grain size of 160 µm, based on the smaller average grain size and, if each grain size in the range were considered then the recrystallisation rate range for the individual grains is expected to be smaller, due to the narrower grain size range.

The isothermal annealing times at various temperatures has been listed in Table 5-3. The JMAK model has been manually fitted to the experimentally determined recrystallisation fraction – time data by using the double log method. The recrystallisation starting and finishing time is set to be 5% and 85% of recrystallisation respectively.

7.2.1 Optical microstructure observation

It is well recognised that recrystallisation nucleation occurs in the region near the grain boundaries and triple points, due to the local high dislocation density [1]. In addition, in coarse grains, deformation bands can also act as preferred nucleation sites [11]. Figure 7-1 shows optical images of the grain structures after various annealing times at 850 °C after deformation to 0.3 strain, starting mode grain size of 160 µm. Non, partial and fully recrystallised microstructures are shown. Inhomogeneity of recrystallisation nucleation is clearly shown in Figure 7-1 (b) after annealing for 40s, since the grain boundaries have a significantly higher number of recrystallised grains than the matrix interior, as indicated by arrows. This agrees with the literature that the preferred recrystallisation nucleation sites are triple points, twin boundaries and grain boundaries, chapter 2.3. Additionally, it can be seen from Figure 7-1 (c) that both finer and coarser grains have recrystallised nuclei along the grain boundaries, however grains over 200 µm are still shown as being unrecrystallised at 850 °C for 90s, i.e. 50% of recrystallisation. The final micrograph, Figure 7-1 (d) shows the fully recrystallised microstructure. Figures 7-2 and 7-3 showed the microstructure evolution of the mode grain size 160 µm samples at 900 °C and 950 °C after 0.3 strain respectively. Figure 7-4 shows the partially and fully recrystallised microstructure of the mode grain size

160 µm sample on holding at 850 °C after 0.2 strain. As discussed in chapter 2.4.4.3, the recrystallisation rate decreases with decreasing strain. Figure 7-4 (a) clearly shows that recrystallisation nucleation is also heterogeneous at 0.2 strain, with triple points and austenite grain boundaries being the preferred nucleation sites. With decreasing strain, the recrystallisation rate has decreased; for example, more nuclei and a higher recrystallisation fraction is observed for 0.3 strain (Figure 7-1 (a)) than 0.2 strain (Figure 7-4 (a)) after holding for 90s at 850 °C. They all clearly show that the triple points and grain boundaries are the preferential nucleation sites and the coarser grains recrystallised much later compared to the finer grains, as indicated by arrows.

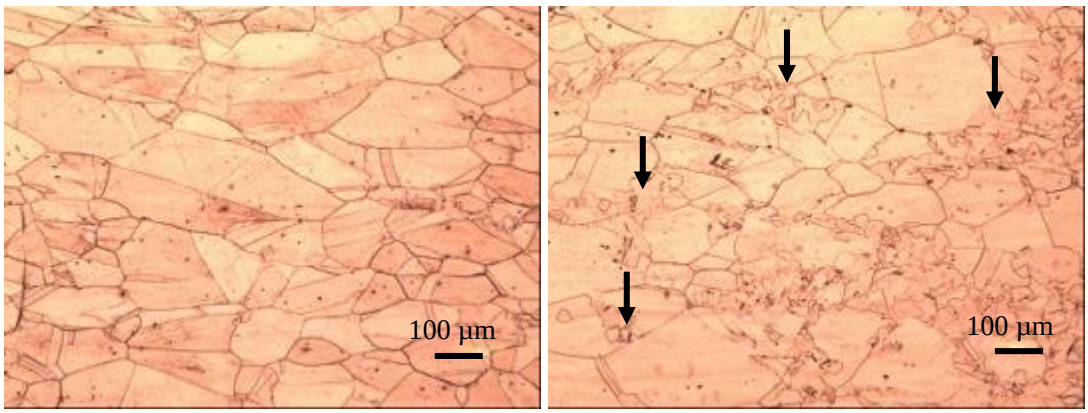

(a) (b)

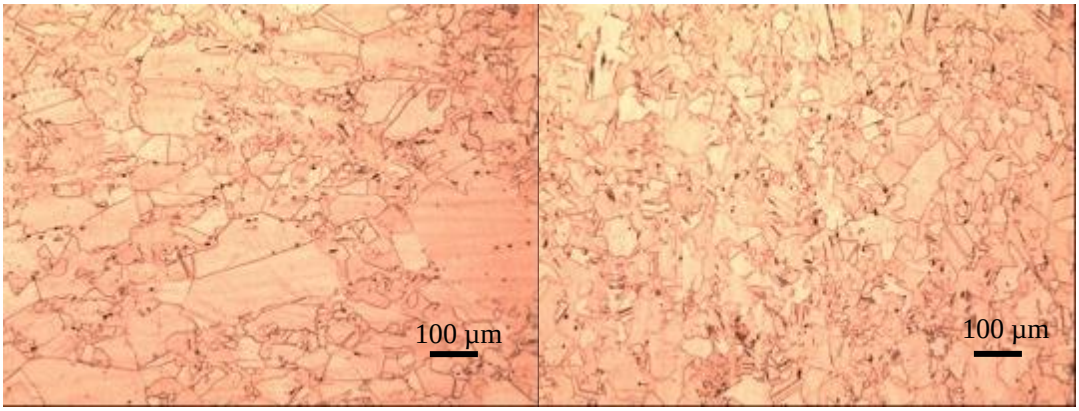

(c) (d)

Figure 7-1 Microstructure evolution at (a) 25s, unrecrystallised; (b) 40s, 20% recrystallised; (c) 90s, 50% recrystallised; and (d) 160s, fully recrystallised at 850°C, 0.3 strain, for the sample with a mode grain size of 160 µm. The arrows in (b) show recrystallisation nuclei preferentially located at grain boundaries and triple points.

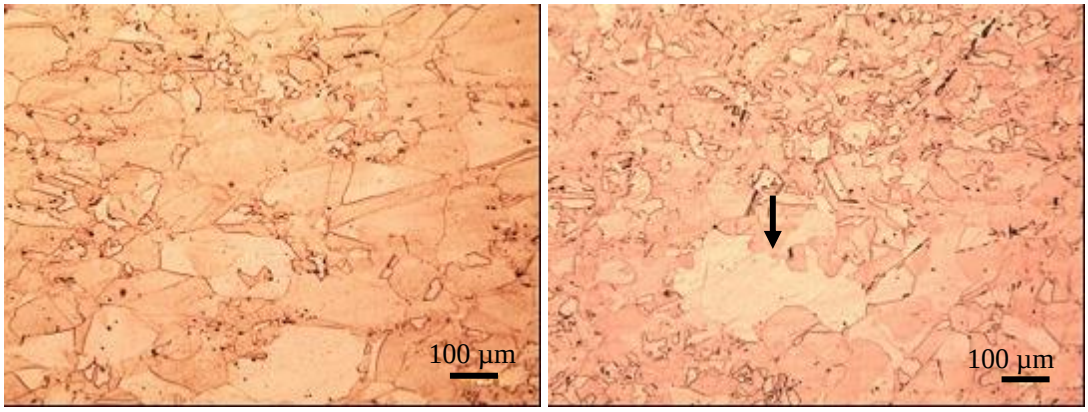

(a) (b)

Figure 7-2 Microstructure evolution at (a) 25s, 35 % recrystallised; (b) 60s, 75% recrystallised at 900 ºC 0.3 strain; with a mode grain size of 160 µm. The arrow indicated a large unrecrystallised grain.

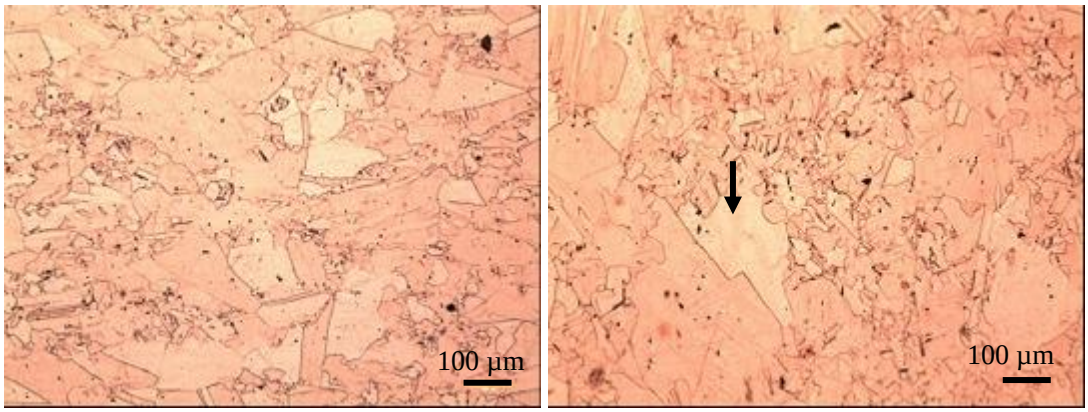

(a) (b)

Figure 7-3 (a) 10s, 30% recrystallised; (b) 25s, 65% recrystallised at 950 °C 0.3 strain, mode grain size of 160 µm. The arrow showed a large unrecrystallised grain

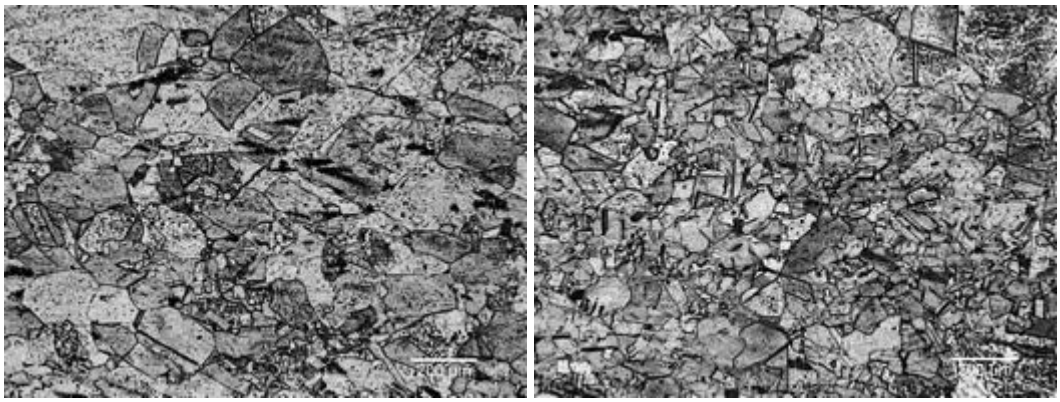

(a) (b)

Figure 7-4 Microstructure evolution at (a) 90s, 18% recrystallised; (b) 480s, 87% recrystallised at 850 ºC, 0.2 strain with a mode grain size of 160 µm.

The recrystallisation evolution with respect to a different starting grain size distribution has also been studied. Figure 7-5 shows the partially (40%) and almost fully recrystallised (87%) microstructure for the mode grain size 100 µm material on holding at 850 °C after 0.2 strain, which has also been compared to the recrystallised microstructures for the initial mode grain size of 160 µm also after 0.2 strain and holding at 850 °C (Figure 7-4). It can be clearly seen that the finer grain size sample was 40% recrystallised at 90s, yet the coarse grain size distribution was only 18 % recrystallised. Thus, the results suggest that recrystallisation rate increases with decreasing initial grain size, which agrees with the literature review, chapter 2.4.4.4.

Additionally, it can be seen that there does not seem to be a significant difference in recrystallisation of the finer and coarser grains as unrecrystallised coarser grains are not apparent in the same way as have been observed for the 160µm mode grain size material (for example Figures 7-2 (b) and 7-3 (b)), which indicates that recrystallisation occurred more evenly over the different grains. Abdollah-Zadeh also observed inhomogeneity in recrystallisation nucleation, occurring more readily at grain boundaries, in a Fe-30Ni model alloy, Figure 7-6 [78]. The figure shows that recrystallised grains nucleate along the grain boundaries, and that impingement between recrystallised grains along the boundary has already occurred at an early stage of recrystallisation. In that work no effect of grain size distribution on recrystallisation kinetics was mentioned.

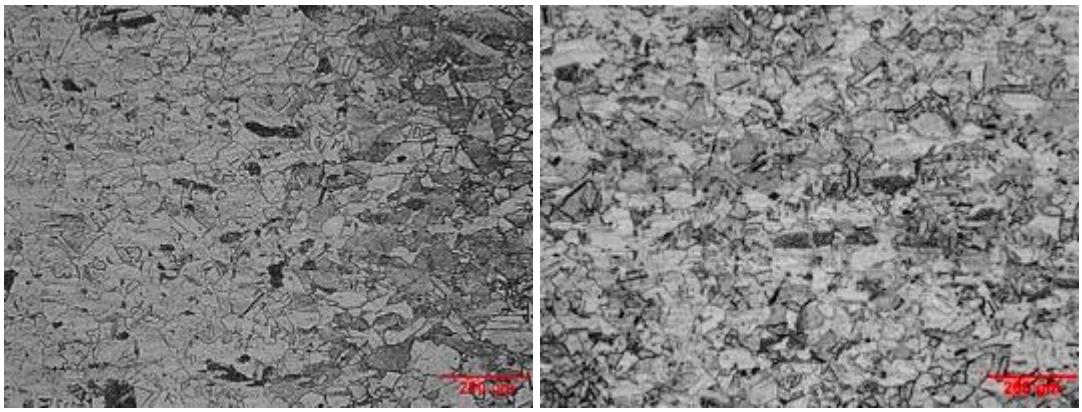

(a) (b)

Figure 7-5 Microstructure evolution at (a) 90s, 40% recrystallised; (b) 160s, 84% recrystallised at 850 ºC, 0.2 strain with a mode grain size of 100 µm

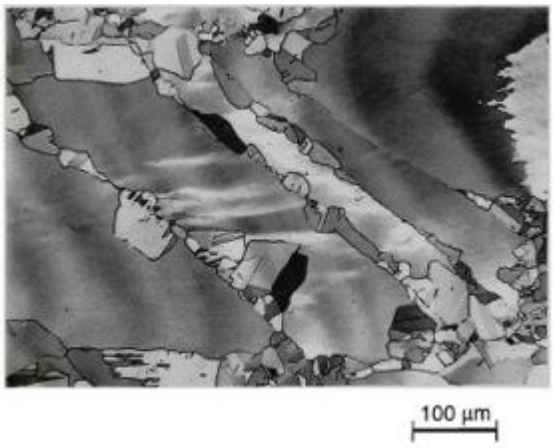

Figure 7-6 The onset of recrystallisation of Fe-30%Ni with initial grain size of 310µm observed at 0.5 strain, 950°C, held for 2s [11]

Grain size distribution evolution during recrystallisation has also been examined to reveal the recrystallisation rate for the different grain size range in the original distribution. For example, if a partially recrystallised grain size distribution shows a comparable grain size distribution to the original distribution for the coarser grain size range, then this indicates that the coarse grains, statistically speaking, have not recrystallised whilst the finer grains have. Figure 7-7 and Figure 7-8 show the grain size distribution evolution for the initial grain size distribution with the mode grain size of 160 µm and the distributions; in Figure 7-7, after holding at 850 °C for 40s (partially recrystallised, 20%) and 160s (fully recrystallised) and, in Figure 7-8, after holding at 900 °C for 25s (partially recrystallised, 35%) and 90s (fully recrystallised). It can be seen in Figure 7-7 that the area fraction of grains in the grain size range over 220 µm at 40s is 24 % compared to 34% in the homogenised condition, yet the area fraction for the finer grain size range, 20-80 µm, has increased significantly from 7 % (homogenised condition) to 41 % (40s during annealing). In addition, the area fraction of the grain size range between 100 – 200 µm has decreased. This suggests that recrystallisation mainly occurs in the grains in the grain size range up to 200 µm, with the coarser grains, i.e. > 200 µm, not recrystallizing in the early stages. The grain size distribution evolution at 900 °C gave a comparable result. It can be seen from Figure 7-8 that grains in the grains size range over 180 µm has only changed from 50% (homogenised condition) to 33%, whereas the grain size range 20-80 µm, has increased significantly from 7 % (homogenised condition) to 34 % (25s during annealing).

Figure 7-9 shows the grain size distribution evolution of samples with the mode grain size of 100 µm after holding at 850 °C for 90s (partially recrystallised, 40%) and 160s (fully recrystallised). It can be seen that the area fraction of the finer grain size, 20 - 80 µm, has increased from 30 % (homogenised condition) to 56 % (90s during annealing), and the coarse grain size range, 120- 200 µm, has decreased accordingly from 37 % (homogenised) to 11% (90s during annealing). Compared to samples with mode grain size of 160 µm, recrystallisation occurred more uniformly at an early stage due to lack of the grains that are larger than 200 µm. This is due to a narrower grain size distribution in the sample with mode grain size of 100 µm. This agrees with the optical image observation that the coarse grains recrystallise at a later stage, as shown in Figure 7-1, 7-2, 7-3, 7-4.

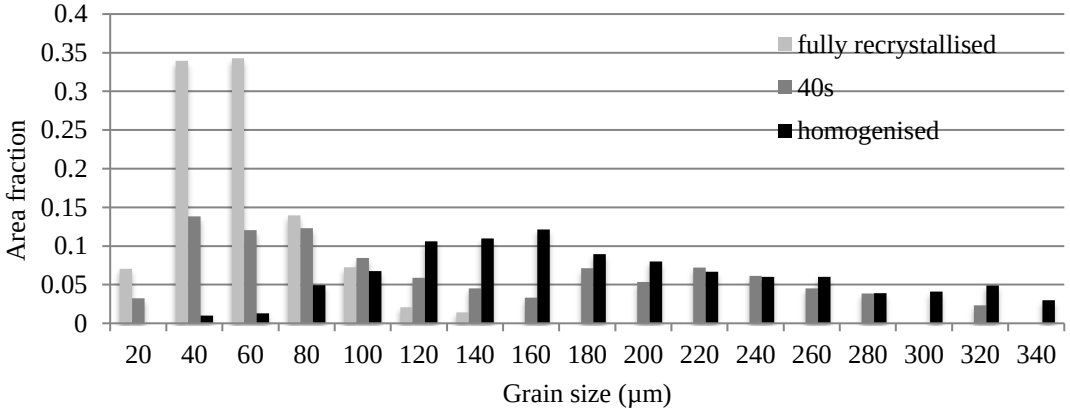

Figure 7-7 Grain size distribution evolution of unrecrystallised (homogenised), 20% recrystallised (40s) and fully recrystallised samples at 850 °C after 0.3 strain for the initial 160 µm mode grain size Fe-30 Ni material.

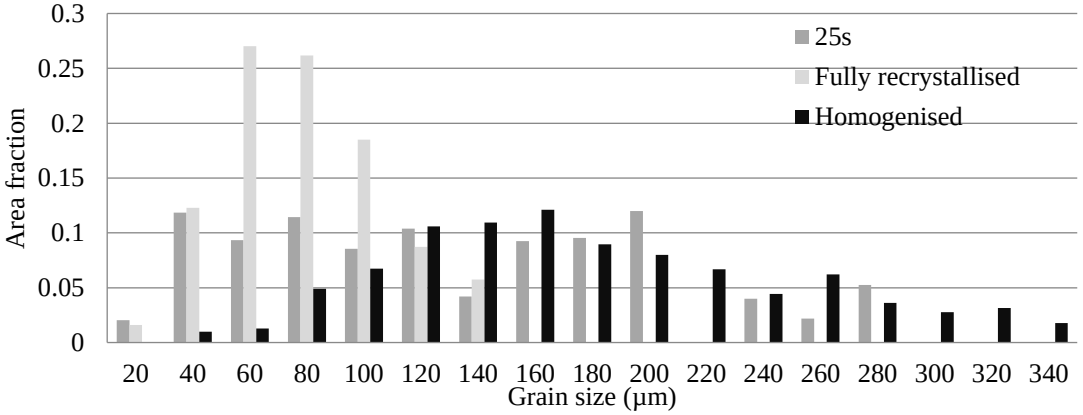

Figure 7-8 Grain size distribution evolution of unrecrystallised (homogenised), 35% recrystallised (25s) and fully recrystallised samples at 900 °C after 0.3 strain for the initial 160 µm mode grain size Fe-30 Ni material.

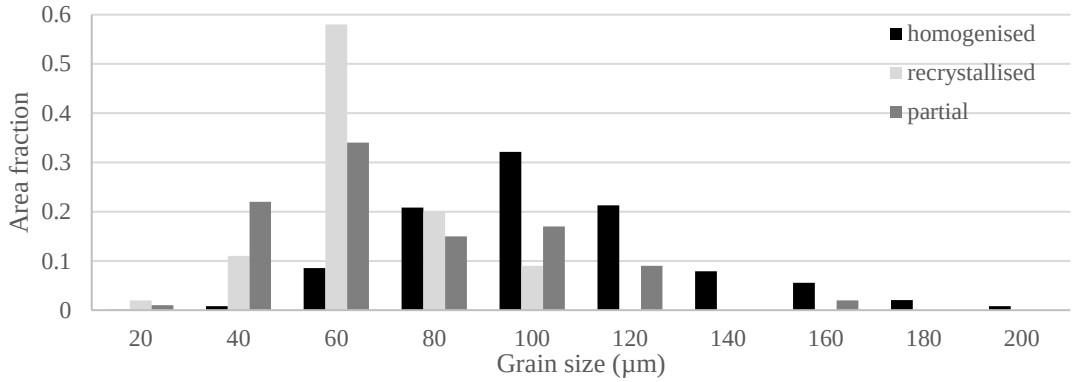

Figure 7-9 Grain size distribution evolution of unrecrystallised (homogenised), 40% recrystallised (90s) and fully recrystallised samples at 850 °C after 0.2 strain for the initial 100 μm mode grain size Fe-30 Ni material.

7.2.2 EBSD and in-situ EBSD microstructure observation

To further investigate the effect of the grain size distribution on recrystallisation evolution, EBSD scanning has also carried out on the Fe-30Ni Nb free steels with mode grain size of 160 μm annealed for 5s at 950 ºC after 0.3 strain to reveal the microstructure at the onset of recrystallisation. In-situ EBSD has been carried out at 700 ºC after 0.3 strain to reveal the microstructure evolution during recrystallisation.

Figure 7-10 shows the sample reheated to 950 °C after 0.3 strain and held for 5s then quenched. The EBSD images show the microstructure at the onset of recrystallisation: Figure 7-10 (b) shows the HAGB (>15 degree) in black and LAGB (>2 degree) in red. More detailed EBSD scanning and TEM examination have been carried out to reveal the recovered/ recrystallisation nuclei microstructures along the grain boundary. The newly formed, i.e. recrystallised, grains are the brighter, finer equiaxed grains in the band contrast image. The identity of these newly formed grains can be further confirmed by their high angle grain boundaries, shown in the grain boundary image. It can be seen that the starting to recrystallise microstructure (0.3 strain, 950 ºC, 5s) consists of both subgrains (surrounded by LAGB) and the recrystallisation nuclei (surrounded by HAGB) along the grain boundary. The subgrain size is around 2-3 μm. Additionally, microbands have also been observed via TEM, Figure 7-11. The microband width is between 0.2 - 1 μm, which agrees well with other research on deformed austenitic microstructures by Black, Cizek, Palmiere and Abdollah- Zadeh [10, 11, 35, 40]. A recrystallised nucleus is shown at the bottom of Figure 7-11.

Therefore, it can be confirmed that these recovered and starting to recrystallise microstructures consist of subgrains formed along the grain boundaries, and their formation and growth consumes the deformed microstructure, i.e. microbands. Additionally, it can be seen that the recrystallised grains nucleate predominantly along the grain boundaries and the triple points. This agrees with the results shown in Figure 7-1, 7-2 and 7-3.

Since misorientation within a grain is caused by the accumulation of dislocations, the local misorientation can be used as a rough measure for the dislocation density distribution [1]. The small subgrains/ recrystallising grains along the prior austenite grain boundaries shown in both band contrast and grain boundary images are also shown in Figure 7-10. The small grains surrounded by LAGB (i.e. misorientation <15 degree) are considered as subgrains, otherwise they are recrystallising grains. It can be seen in Figure 7-10 that both coarse and fine grains have formed recrystallised grains as indicated by arrows. The finer grain region carries more recrystallisation nuclei due to its higher density of prior austenite grain boundaries per unit area. The subgrains are clustered along the grain boundaries indicating that recovery is more pronounced at grain boundaries than in the interior of the grain, therefore the recrystallisation nuclei density is expected to be higher. Similar recovered microstructure has been seen in the fine grain region, the recrystallised grains nucleated along the grain boundaries surrounded by the subgrain microstructure.

The subgrain number density has been determined from EBSD observations of regions with different grain size. The number density of subgrains decreases with increasing grain size, and the number density in the fine grain region is one order of magnitude higher than in the coarse grains, Figure 7-12. This indicates that recrystallisation nucleation is dominated by the grain boundaries and, as a result, the more grain boundary length per unit area, the higher density of recrystallisation nuclei. That is, the combination of the high local stored energy and the high number density of recrystallisation nuclei in the fine grain region, means that recrystallisation nucleation is expected to proceed considerably faster in this area than in the coarse grain region.

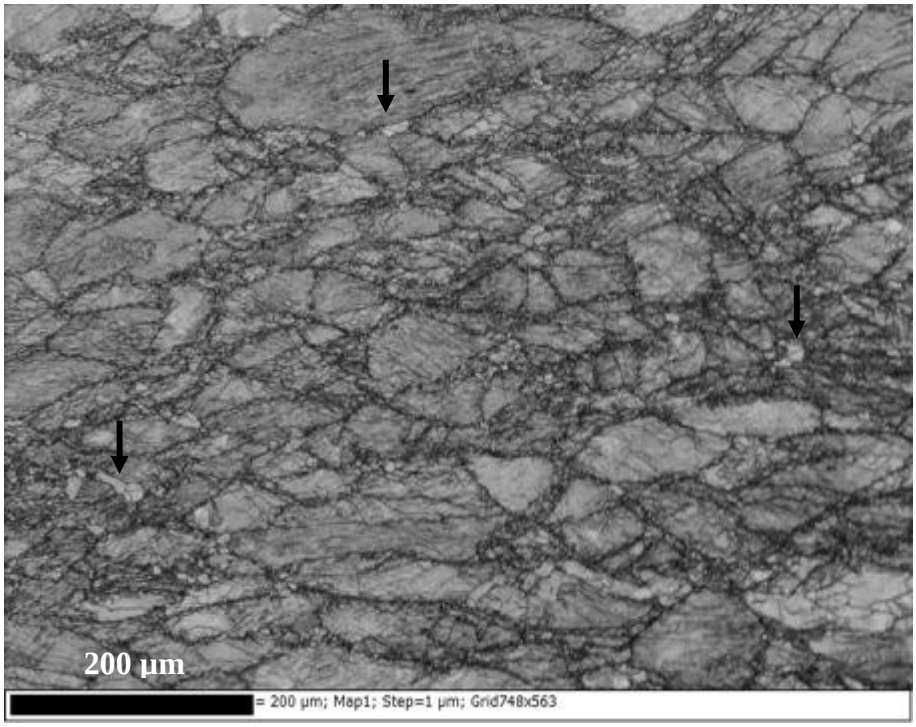

(a)

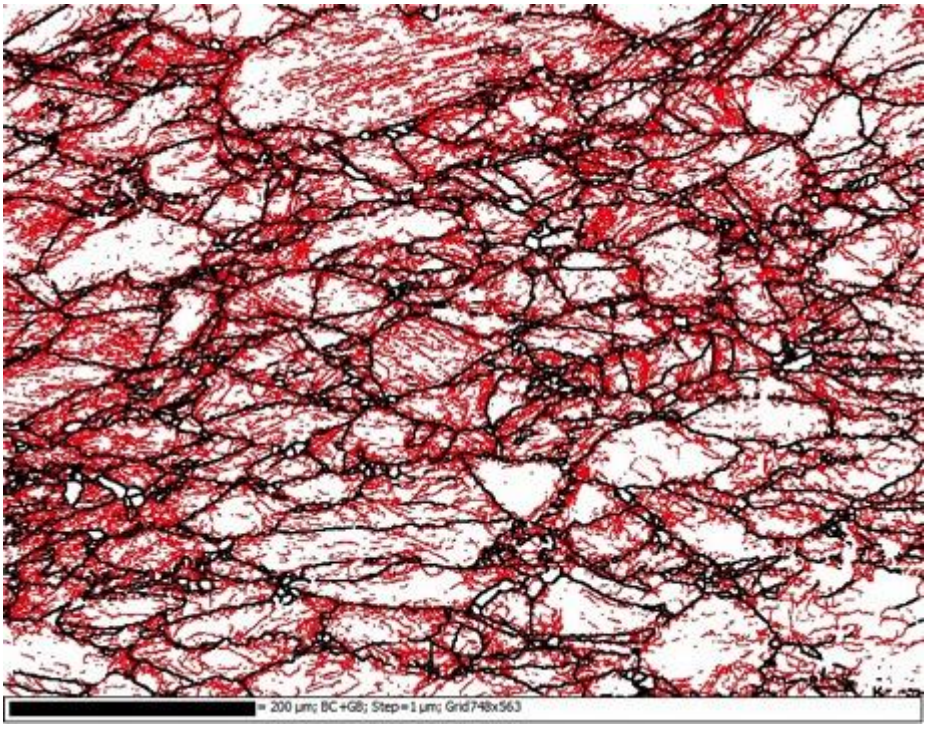

(b)

Figure 7-10 Band contrast (a) and the grain boundary (b) EBSD images for the deformed and recovered microstructure; black: misorientation > 15 degree, red: > 2 degree for the Fe-30Ni Nb free sample deformed to 0.3 and held at 950 °C for 5s.

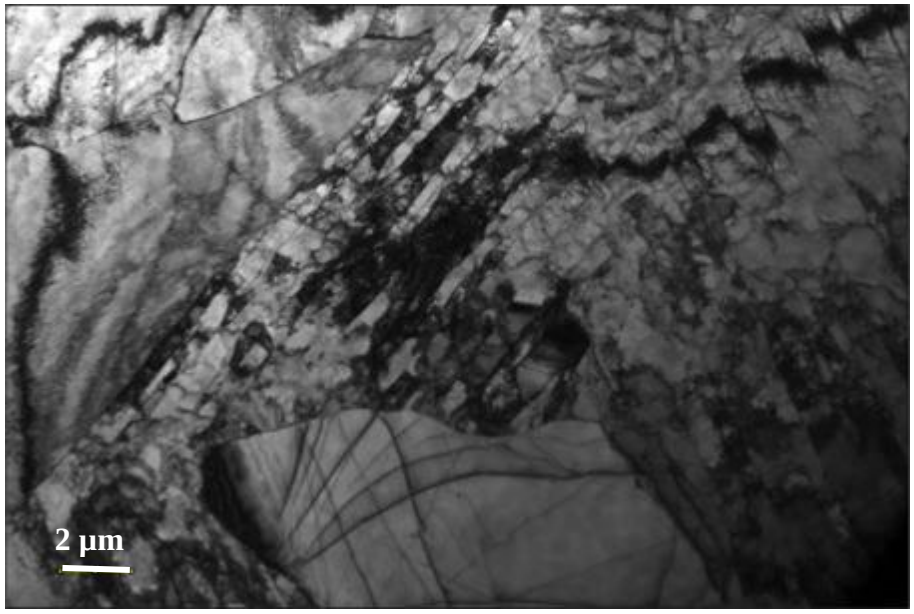

Figure 7-11 Microband microstructure shown in the 950 ºC, 0.3 strain, 5s Fe-30Ni Nb free (deformed and recovered) sample (initial mode grain size of 160 µm)

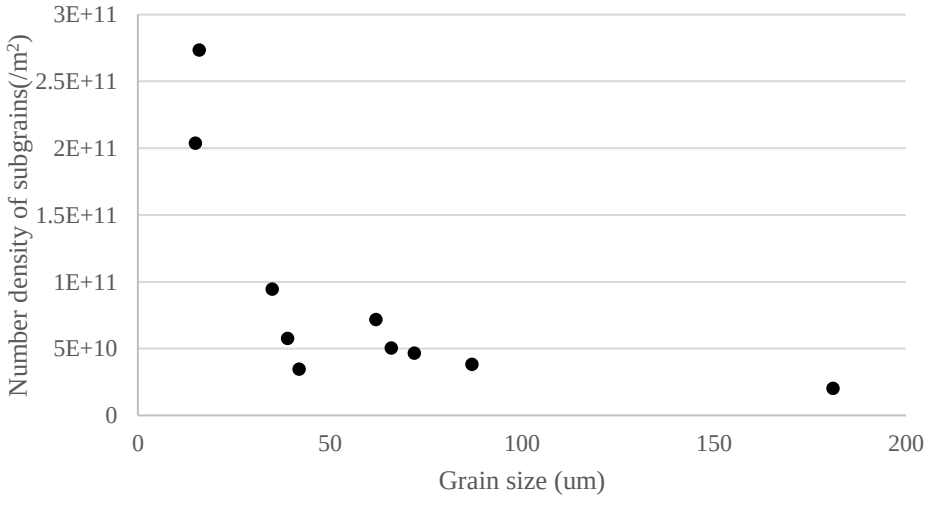

nd

Figure 7-12 Effect of the grain size on the number density of subgrains

In-situ EBSD has also been carried out to reveal the early onset of recrystallisation along the grain boundaries on a sample cold deformed to 0.3 strain and then annealed at 700 ºC. Figure 7-13 shows the early stage recrystallisation along the grain boundary in a fine grain size region. It can be seen from Figure 7-13 that the recrystallisation nuclei are concentrated along the grain boundaries, because these regions have higher stored energy and higher density of preferential nucleation sites, recrystallisation will occur very quickly. It can also be seen from Figure 7-13 (a) that impingement of some

small recrystallizing grains occurs at a very early stage of recrystallisation due to the inhomogeneity of recrystallisation nucleation. Figure 7-13 (b) and (c) suggest that the growth rate of recrystallisation nuclei vary, and impingement occurs throughout the recrystallisation nucleation process. Recrystallisation has already completed in the top left region, whereas recrystallisation proceeded much slower in the bottom right region in Figure 7-13 (f) even though the recrystallised grains formed at the grain boundary at an earlier time. Furthermore, the recrystallising grains impingement could occur locally in the heavily deformed regions even when the overall recrystallisation fraction is still relatively low. Therefore, the assumption in the JMAK model that recrystallisation nuclei are randomly distributed in the matrix is not valid to fully describe the recrystallisation nucleation process. The early impingement of recrystallisation nuclei has been seen due to the heterogeneous nucleation of recrystallisation, which explains why the experimentally determined Avrami exponents are lower than 3 (site saturated nucleation and 3D growth).

Recrystallisation growth has also been examined by in-situ EBSD at 700 °C after 0.3 strain for a sample with initial mode grain size of 160 μm. Local misorientation has been considered as an indication of the local stored energy, and the mis-indexed white pixels in the EBSD maps were assumed to be caused by high levels of deformation. Figure 7-14 shows the local misorientation map of the sample cold deformed at 0.3 strain, then annealed at 700 ºC, mode grain size 160 μm at the onset of recrystallisation and 25 minutes after. The EBSD micrographs reveal that in general, fine grains were more deformed than coarse grains (higher number density of mis-indexed pixels), and these highly deformed regions recrystallised considerably faster. As seen in Figure 7-14 (b), all newly formed grains are located in the highly deformed region shown in Figure 7-14 (a). Thus, the results indicate that higher local strain in the fine grains accelerates the local recrystallisation kinetics. In addition, Figure 7-15 shows the progress of recrystallisation after 25, 40, 60 and 80 minutes at 700 °C for the same region. The fine grain labelled ‘1’ is fully recrystallised and the coarse grain labelled ‘2’ is only 60% recrystallised after 80 minutes, and the recrystallised grains formed in grain 1 are much finer than the grains in grain 2, Figure 7-15 (d). Thus, the results show that more nucleation sites per unit area also lead to faster recrystallisation kinetics of the fine grains.

Several more trials were carried out to confirm the observations made. Figure 7-16 shows an example where there is a fine grain size region located on the left hand side of the micrograph and a much coarser grain can be seen on the right. The coarse grains remain unrecrystallised even when the rest of the area has recrystallised completely. Additionally, the area with the highest stored energy and highest grain boundary length per unit area (i.e. the fine grain area) gives a finer recrystallised grain size.

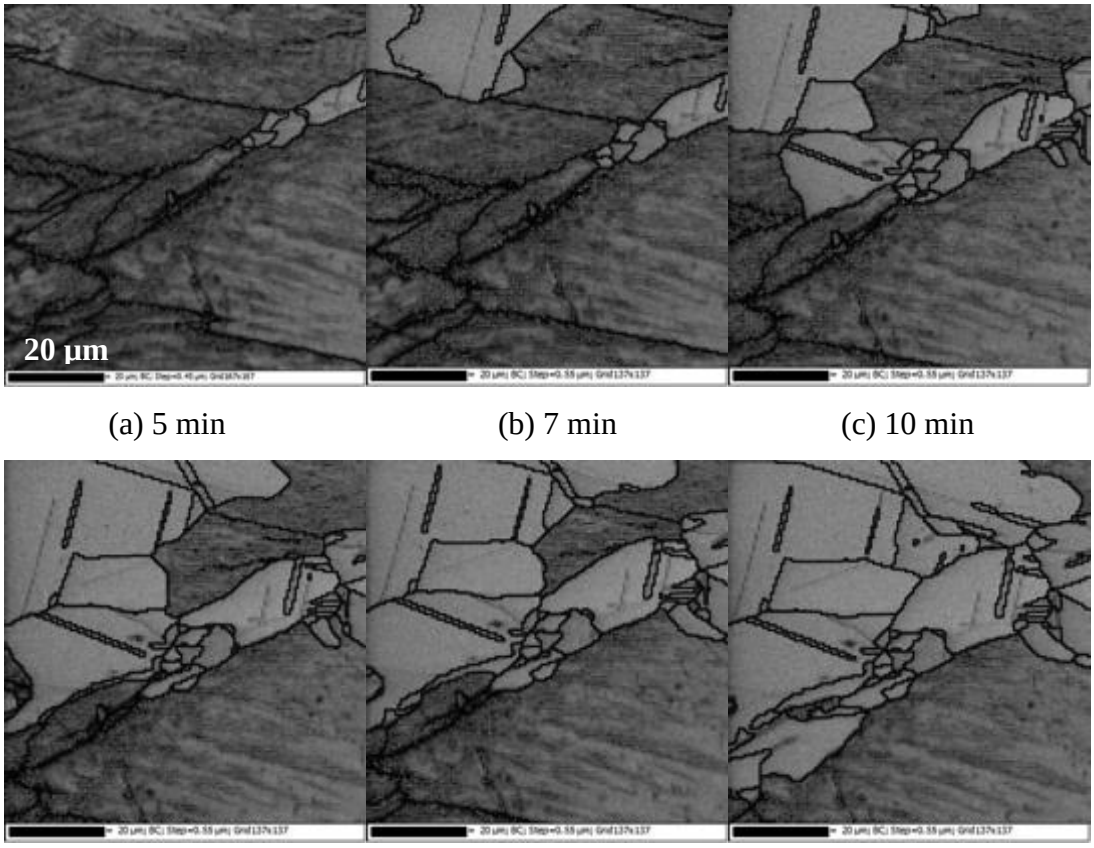

(a) 5 min (b) 7 min (c) 10 min

(d) 13 min (e) 16 min (f) 19 min

Figure 7-13 Band contrast EBSD images showing recrystallised grain impingement at the early stage of recrystallisation, 700 °C, 0.3 strain for a sample with initial mode grain size of 160 µm

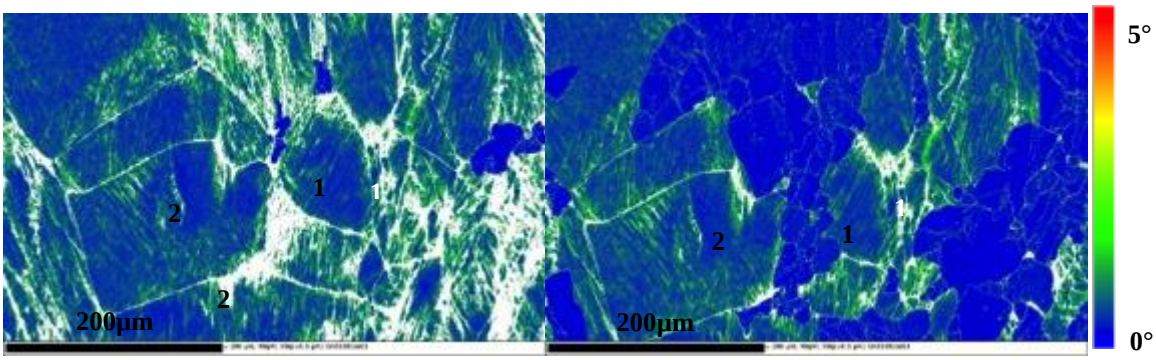

(a) (b)

Figure 7-14 Local misorientation mapping of samples with mode grain size of 160 µm deformed to 0.3 at room temperature, then reheated and held at 700°C for 5 minutes (a), after 25 minutes (b).

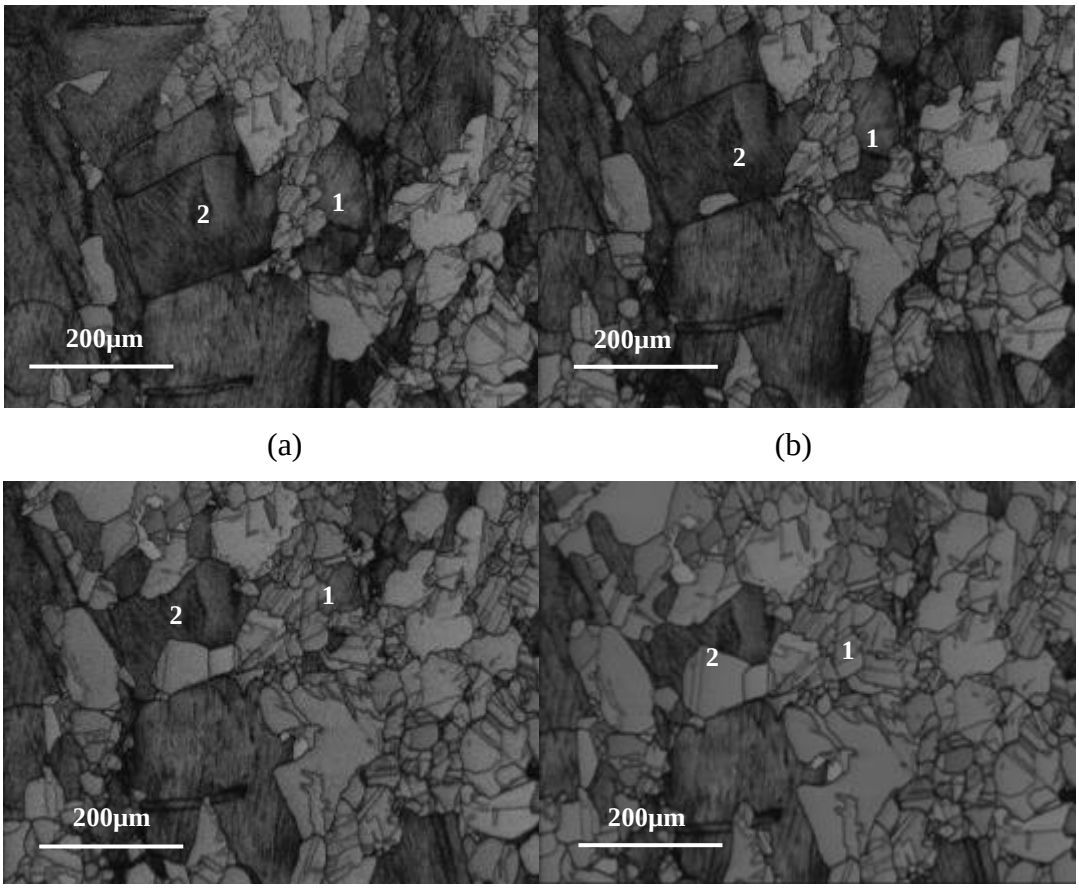

(a) (b)

(c) (d)

Figure 7-15 Band contrast EBSD images for sample with mode grain size of 160 µm deformed to 0.3 strain at room temperature then annealed at 700 °C for 25mins (a) 40mins (b), 60mins (c) and 80mins (d).

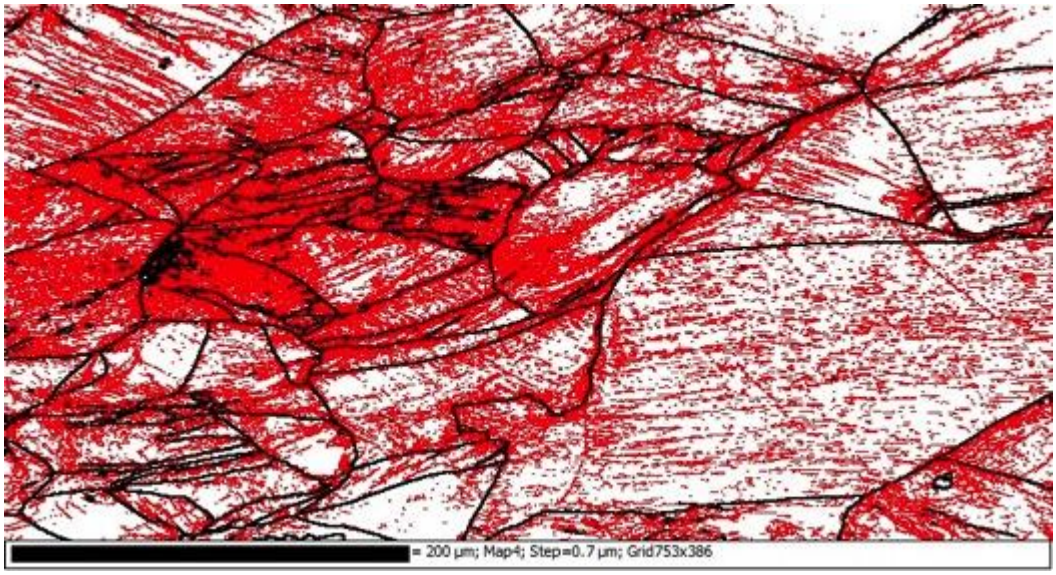

(a)

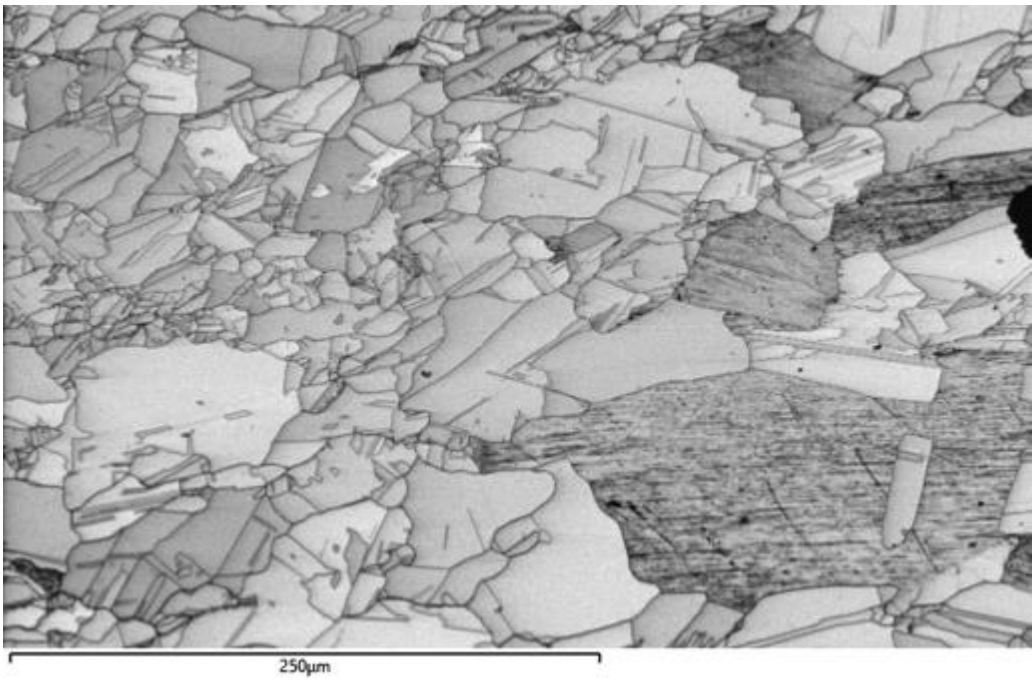

(b)

Figure 7-16 In-situ EBSD image of a sample deformed at 0.3 strain (a) grain boundary image before recrystallisation, black: >15 degrees, red: >2 degrees (b) band contrast image of the same region after 80 minutes at 700 ºC.

Sellars reported that with increasing strain, the recrystallisation rate increases and the final recrystallised grain size is finer [87]. Thus, combining the high local stored energy and high grain boundary length per unit area, the fine grain regions have a higher recrystallisation rate due to a higher density of recrystallisation nuclei. As a result, these heavily deformed regions give a finer recrystallised grain size.

In summary, recrystallisation nucleation is site saturated at 0.3 strain but the nuclei are not randomly distributed. As a result, impingement occurs at an early stage of recrystallisation, which would be expected to lead to a lower Avrami exponent (< 3) than expected based on site saturated nucleation with three-dimensional growth rate. In terms of recrystallisation growth, the in-situ EBSD results revealed that the recrystallisation growth rate is not a constant but decreases with time. This is due to the heavily deformed region having more stored energy and recrystallising first, then the lightly deformed region recrystallising later. The recrystallisation rate in the region with high stored energy is considerably faster than the other regions, therefore, once these regions are consumed, the overall recrystallisation rate decreases.

7.2.2.1 In-situ EBSD surface effect

The microstructure from the surface and the bulk from an in-situ sample (0.3 strain, annealed at 700°C for 80 minutes, 160 μm mode initial grain size) after the annealing treatment has been examined in order to ensure that the surface observations are representative of the bulk behaviour. Figure 7-17 shows the optical microstructure of the surface and the bulk (500 μm beneath the surface, i.e. more than 2 times of the mode grain size of the original material away from the surface) of an in-situ reheated sample. A partially recrystallised microstructure is shown in all four pictures. It can be observed that: firstly, the heterogeneity of recrystallisation is not a surface effect. Both surface and bulk microstructures show that the fine grain regions recrystallised first and the coarse grains are still present. Secondly, the regions that finished recrystallisation first have a recrystallised grain size of a few microns in size in both the surface and bulk micrographs. Therefore, the fine recrystallised grains observed in the heavily deformed region in in-situ EBSD is not a surface effect.

Figure 7-18 shows an EBSD image of the sample deformed at room temperature to 0.3 strain, reheated in the furnace at 950 °C for 160s, then cut and polished to reveal the bulk microstructure. It can be seen that the microstructure consists of regions of fine recrystallised grains and larger grains, which is consistent with the finer regions having been heavily deformed and then recrystallised with a high nucleation density and fast recrystallisation rate. Therefore, the observation of the finer recrystallised grains along the grain boundaries discussed in section 7.2.2 and shown from Figures 7-13 to 7-16 are not surface effects.

7.2.2.2 Texture effect on recrystallisation kinetics

The crystallographic texture of individual grains could affect their level of stored energy after deformation [1]. The stored energy distribution can be revealed by local misorientation mapping and to separate out any texture effect on deformation, the Schmid factor map has been determined. The map plots the maximum Schmid factor for each point. A high value of Schmid factor relates to that grain being in an ‘easy’ orientation to deform for the applied stress, therefore, it might be expected to have more stored energy. Figure 7-19 shows the deformed microstructure. It can be seen that the larger grain 1 carries less stored energy compared to the small grain 2 even though they have comparable Schmid factors, indicating that strain inhomogeneity is influenced more by the grain size variation than any texture variation. It should also be noted that the samples did not have a strong overall texture.

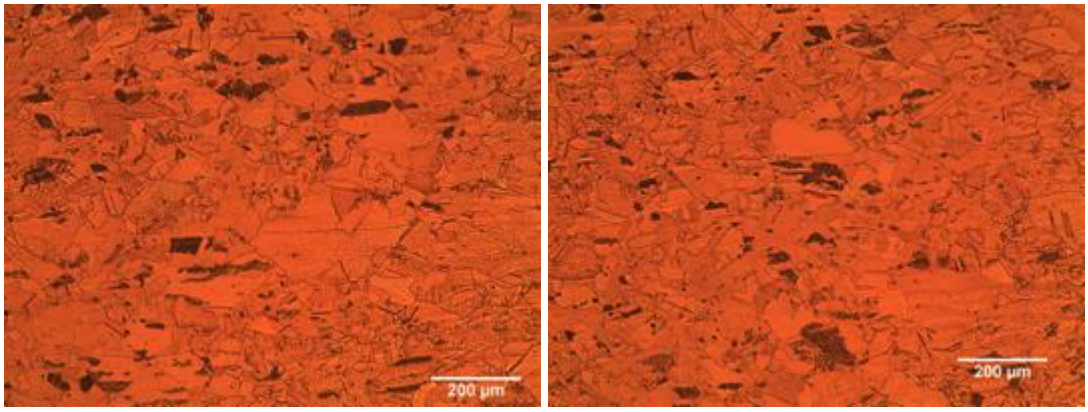

(a) (b)

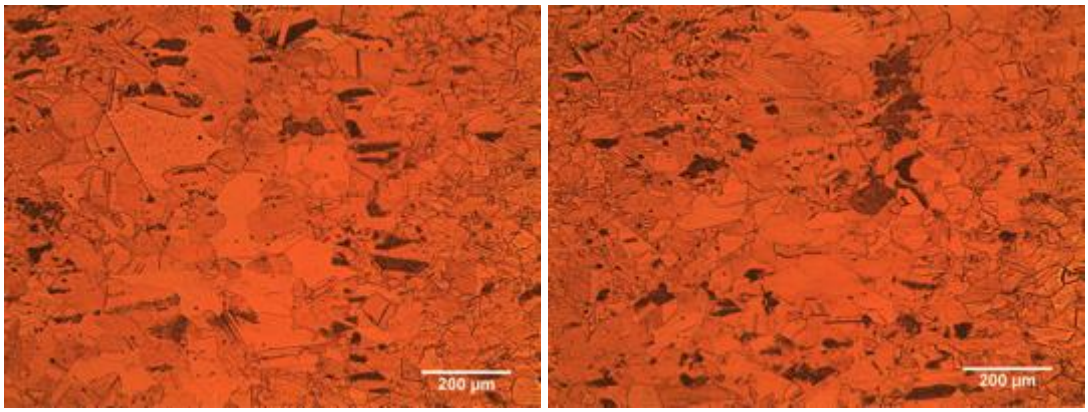

(c) (d)

Figure 7-17 Microstructure comparison between surface (a) (b) and 500 µm under the surface (c) (d) for the in-situ EBSD samples annealed in- situ heating stage at 700 °C for 80 minutes after cold deformed at 0.3 strain, initial grain size 160 µm.

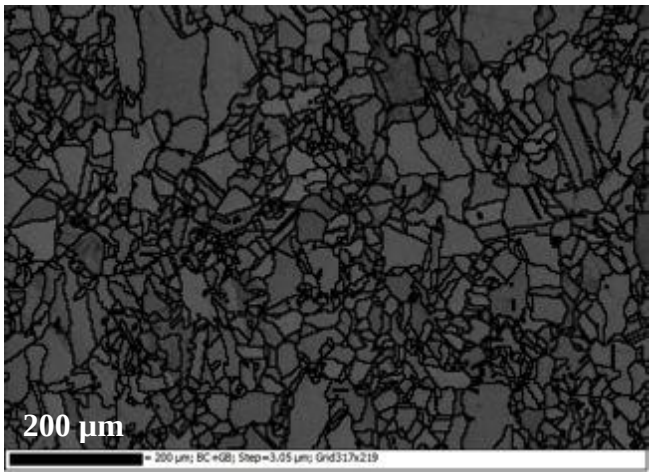

Figure 7-18 EBSD image of a fully recrystallised sample, achieved by reheating in the furnace at 950°C, then cut and polished to reveal the bulk microstructure, black line: grain boundary with misorientation > 15 degrees.

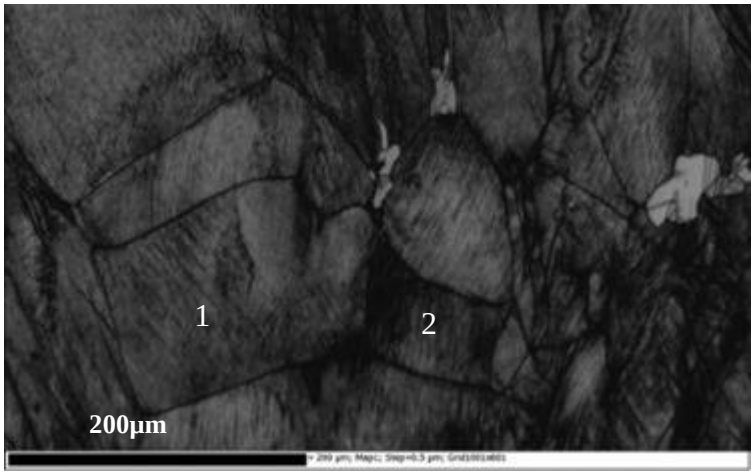

(a)

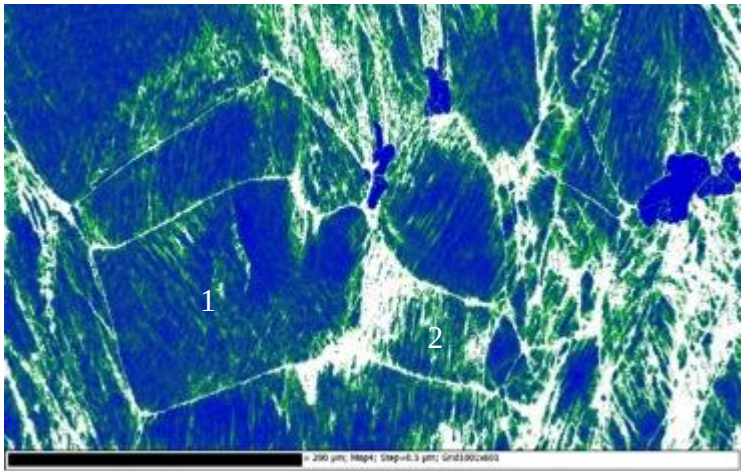

(b)

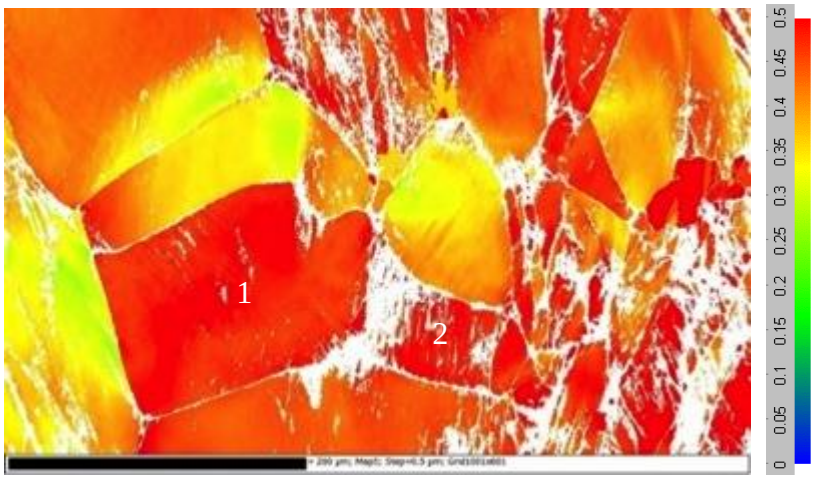

(c)

Figure 7-19 Band contrast (a), local misorientation (b) and Schmid factor (c) of a sample deformed to 0.3 strain at room temperature and annealed at 700 °C for 5 minutes

7.3 Recrystallisation kinetics determination for cold deformed samples

From the microstructure evolution study discussed above, heterogeneity in recrystallisation has been observed. A uniform grain structure, i.e. a tighter grain size distribution, promotes more homogeneous recrystallisation nucleation and growth, as seen for the sample with a 100μm mode grain size compared to the 160μm mode grain size material. It has been shown that the coarser grains recrystallise considerably slower than finer grains under all conditions. This can be attributed to the low stored energy and/ or the low recrystallisation nuclei density compared to the finer grains. To investigate the effect of recrystallisation inhomogeneity with respect to grain size on recrystallisation modelling, the recrystallisation kinetics have been measured and fitted to the JMAK model.

It should be noted results for the samples with the mode grain size of 100 μm at 0.2 strain annealed at 950 °C are not included as recrystallisation completed before 10s, therefore it was not possible to measure the recrystallisation kinetics accurately.

The recrystallisation fraction at different initial grain size distribution, strain, time and temperatures have been summarised in Figure 7-20 based on the microstructural observations of recrystallised fraction and the softening fraction (from hardness measurements). It can be seen that in the temperature range of 950 – 850 °C, for strain between 0.2 – 0.3, then the recrystallisation rate increases with temperature and with strain. It can also be seen that the softening fraction and recrystallisation fraction are not aligned very well. Approximately 30% - 40% of softening occurred before the onset of recrystallisation regardless of the temperature, strain and grain size. This can be attributed to recovery occurring during the reheating process. It agrees with the literature in chapter 2.3 that in cold deformed aluminium, which has a comparable stacking fault energy to Fe- 30Ni model alloy, approximately 40 % recovery occurs prior to recrystallisation. It is worth noting that the softening fraction matches the recrystallised fraction well if the initial softening caused by recovery is excluded.

Figure 7-21 shows the double log normal of recrystallisation fraction versus log normal time for the different temperatures and strains. These plots have been used to obtain the value for Avrami exponent n and the parameter k for the JMAK equation.

Linear plots have been observed for all conditions, which indicates that the recrystallisation nucleation and growth mechanisms have not changed during the recrystallisation process at the different strains and temperatures.

Table 7-1 summaries the JMAK fitting parameters obtained from the double log diagram. It can be seen that the Avrami exponent is independent of temperature and strain within the temperature range of 850 – 950 °C and strain range of 0.2 - 0.3. However, the Avrami exponent is sensitive to the starting mode grain size. The mode grain size of 160 μm samples gave an Avrami exponent of 1.3 on average, and the samples with the mode grain size of 100 μm gave an Avrami exponent of 2.2. Under all conditions, the Avrami exponents are significantly lower than the value of 3 (site saturated with 3D constant growth) or 4 (continuous nucleation with 3D constant growth) proposed in the JMAK model (discussed in chapter 2.4.4 in the literature review).

The use of the softening fraction to determine an Avrami exponent could be one of the reasons lower Avrami exponents than predicted theoretically have been reported, due to the interference from recovery. Therefore, when comparing Avrami exponents from different sets of experiments, the effect of measurement technique needs to be taken into consideration. As recrystallisation kinetics are determined by optical images in this project, recovery is not the cause of the low Avrami exponent in this case.

As discussed in chapter 2.4, a local inhomogeneous strain distribution could lead to the lower Avrami exponents for the coarser grain samples. That is, the grain boundary regions carry more stored energy than the grain interior after deformation, and coarser grains have less grain boundary length per unit area, therefore, the recrystallisation rate difference between the grain interior and the grain boundary region would be more pronounced compared with finer grains, and thus, the Avrami exponent decreases.

The experimentally determined recrystallisation starting and finishing time for the Fe-30Ni Nb free steel cold deformed and annealed samples with mode grain size of 100 μm and 160 μm respectively, at both strains of 0.2 and 0.3 are listed in Table 7-2.

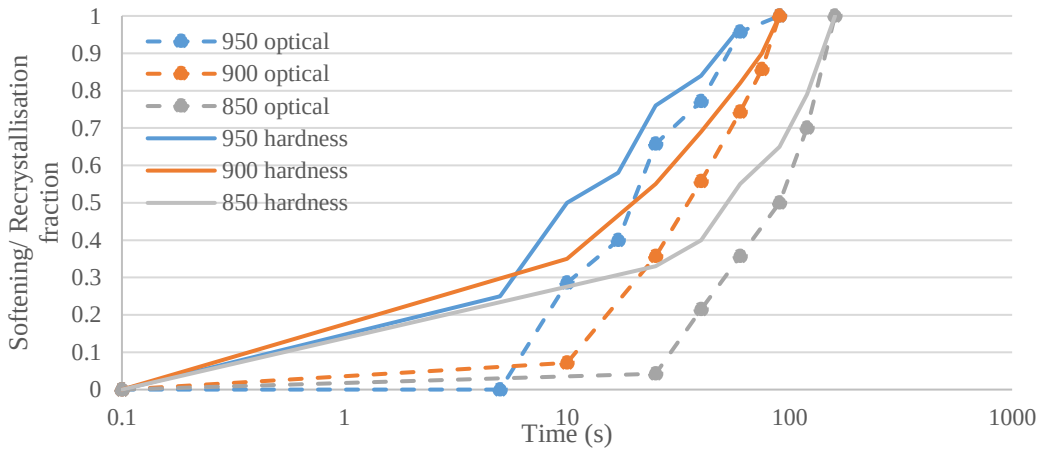

(a)

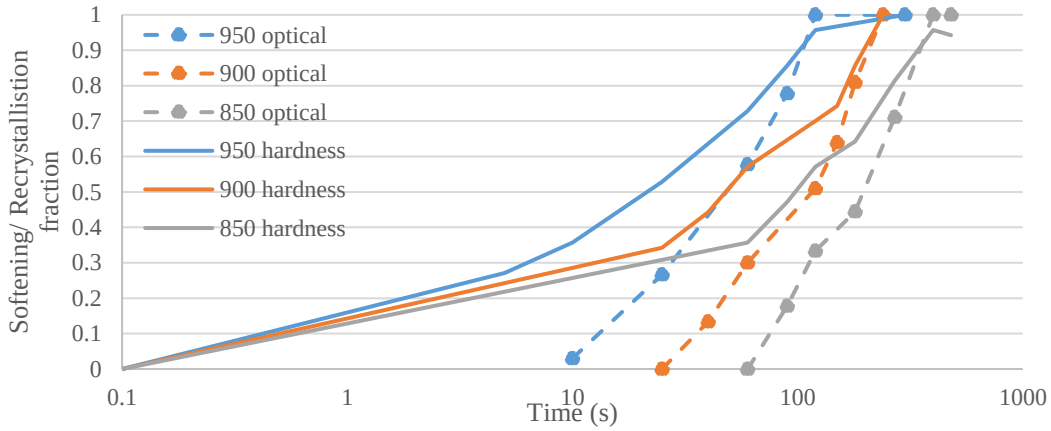

(b)

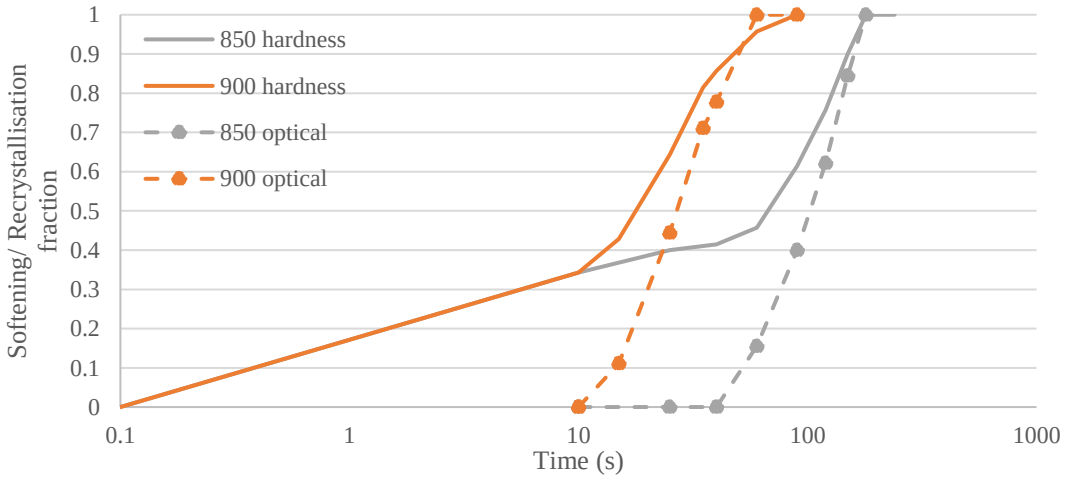

(c)

Figure 7-20 Softening and recrystallisation fraction with temperature for the Fe-30Ni Nb free steel at (a) strain 0.3, mode grain size 160µm (b) strain 0.2, mode grain size 160 µm (c) strain 0.2, mode grain size 100 µm

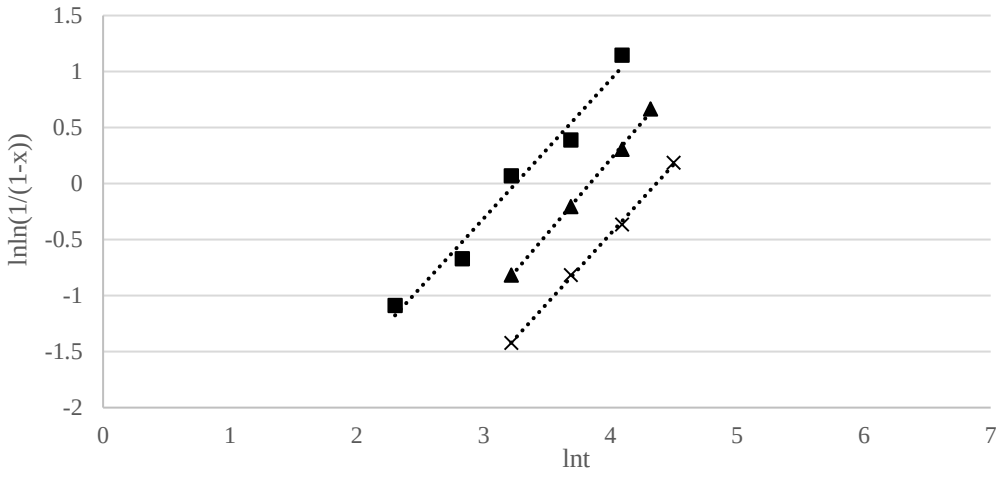

(a)

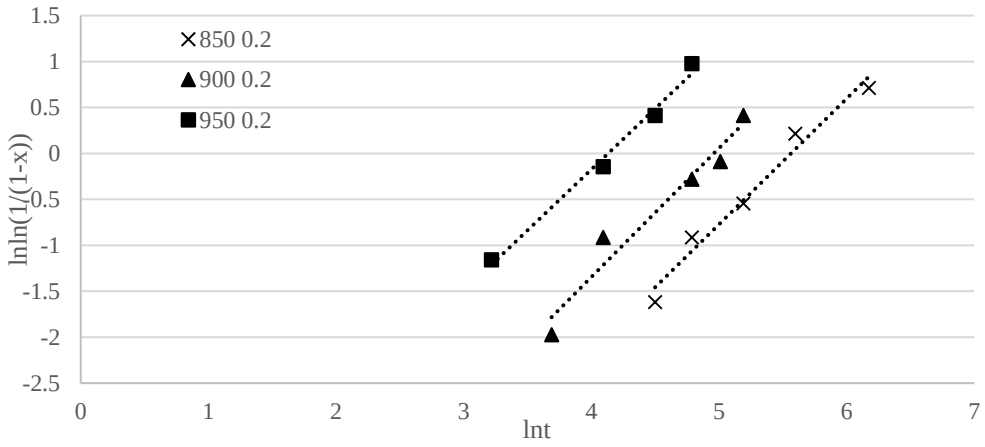

(b)

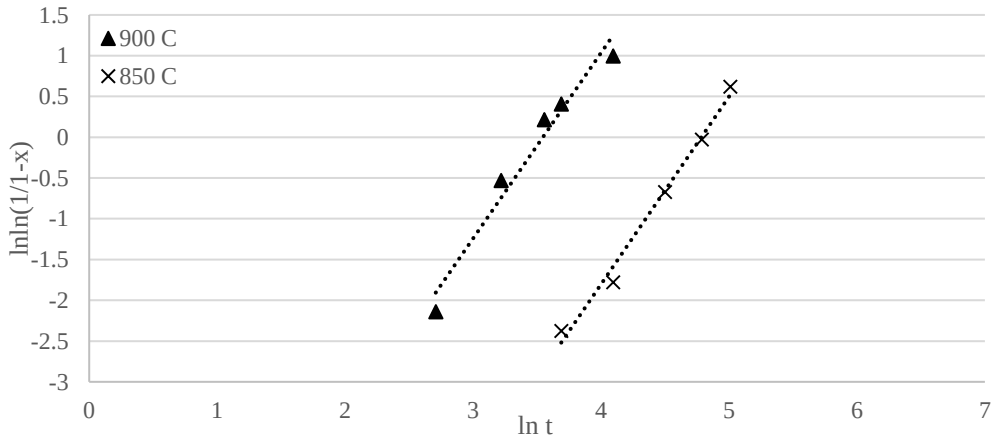

(c)

Figure 7-21 Double log diagram for Fe-30Ni Nb-free steel with mode grain size of 160 µm at (a) 0.3 strain (b) 0.2 strain, and (c) 0.2 strain with mode grain size of 100 µm

Table 7-1 Summary of n and k values under different conditions

Temperature (°C)	Mode grain size (μm)	Strain	Experimental n value	Experimental k value
950	160	0.3	1.2	0.0178
900	160	0.3	1.3	0.006
850	160	0.3	1.4	0.0013
950	160	0.2	1.3	0.006
900	160	0.2	1.4	0.001
850	160	0.2	1.3	0.0005
900	100	0.2	2.3	0.0062
850	100	0.2	2.3	0.0012

Table 7-2 Experimentally determined recrystallisation starting and finishing time

Temperature (°C)	Strain	Mode grain size (μm)	Recrystallisation starting time (s)	Recrystallisation finishing time (s)
950	0.3	160	2.2	43.4
900	0.3	160	5	75.2
850	0.3	160	13.4	171.6
950	0.2	160	5.8	111
900	0.2	160	16.7	226.3
850	0.2	160	29.8	416.8
900	0.2	100	9.4	45.9
850	0.2	100	32.9	158

7.4 Recrystallisation modelling for cold deformed samples

It has been mentioned in Chapter 2.4 that the Sellars approach for recrystallisation modelling has been widely applied for hot deformed samples. In this work it has been shown that the difference between the cold and hot deformed samples in the Fe-30Ni model alloy is the stored energy level, which, for the same applied strain, is dependent on the strain rate (i.e. dynamic recovery during hot deformation) and the reheating rate (static recovery following cold deformation). For both cold deformed and annealed and hot deformed samples the recrystallisation mechanism is the same, therefore, the Sellars approach for describing the recrystallisation kinetics of the cold deformed and annealed sample has been investigated in this section.

As discussed in Chapter 6, no recrystallisation was observed in the cold deformed reheated to the annealing temperature and directly quenched samples at 950 - 850 °C, 0.3 - 0.2 strain, although recovery occurs. All samples were reheated in the same muffle furnace following the same procedures therefore only one heating rate was applied which should mean the amount of recovery, and hence stored energy, will be the same after reheating for the same initial strain and annealing temperature, and there should be no effect on recrystallisation Avrami exponent.

When considering using the Sellars approach, an accurate recrystallisation activation energy for Fe-30Ni steel is required (as mentioned in chapter 2.4.4) and the strain exponent needs to be considered (to account for the potential effect of recovery in Fe-30Ni). In the previous section it has been shown that there is an effect of grain size distribution on the Avrami exponent, this has been further investigated to determine if a predicted value can be used, rather than having to determine a value to give a good fit to experimental data.

7.4.1 Effect of temperature on recrystallisation kinetics

It has been pointed out in the literature review (chapter 2.4.4.2) that the recrystallisation activation energy varies for different materials. Fe-30Ni steel has been used in this project and its recrystallisation activation energy is different from C-Mn steels, and is a required input for recrystallisation modelling. The time for 50% recrystallisation follows an Arrhenius equation,

$$t_{50\%} = A \exp(\frac{Q}{RT})$$

Then, the recrystallisation activation energy can be obtained from a plot of $lnt_{50\%}$ against 1/T. Figure 7-22 shows the Arrhenius plot, i.e. a plot of ln ($t_{0.05}$) as a function of 1/T for Fe-30Ni at 0.3 strain and 0.2 strain. It can be seen that the recrystallisation activation energy is 186 kJ/mol at 0.2 strain and 199 kJ/mol at 0.3 strain. As mentioned in the literature review (chapter 2.4), the recrystallisation activation energy is expected to be independent of strain. Therefore, the difference between the values determined for 0.2 and 0.3 strain is considered as experimental error / material variability. The average recrystallisation activation energy in this case is 192 kJ/ mol. Abdollah-Zadeh measured the recrystallisation activation energy for a hot deformed Fe-30Ni model alloy within the strain range 0.2 - 0.5 and temperature range 850 - 1000 ºC, and reported a value of 192 kJ/mol [176], which agrees well with the experiemental value determined in this work. The activation energy is considerably lower than that reported for C-Mn steels (300 kJ/mol). This can be atttributed to the formation of annealing twins leads to a lower activation energy of recrystallisation.

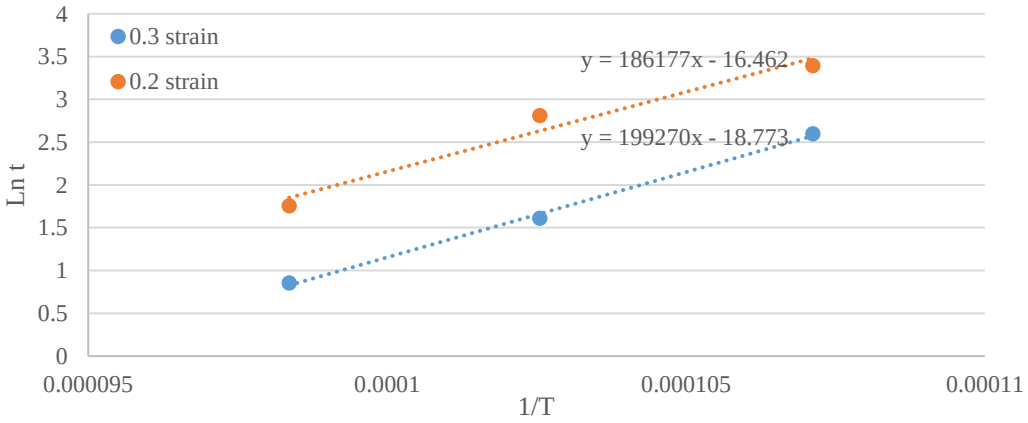

Figure 7-22 Plot of $lnt_{0.5}$ against 1/T at 0.3 and 0.2 strain

7.4.2 Effect of strain on recrystallisation kinetics

In this project, samples were deformed at room temperature, then annealed at elevated temperature. Therefore, the relationship between strain and the stored energy could be different compared to the industrial situation during TMCR where deformation occurs during hot rolling at high temperatures. In addition, it has been mentioned in the literature (chapter 2.4) that the relationship between strain and stored energy is

dependent on the material properties. That is, materials with a different stacking fault energy could have different amounts of stored energy after experiencing the same strain. There is no available literature for the strain exponent in the Sellars approach appropriate for cold deformed Fe-30Ni model alloy. Figure 7-23 shows the relationship between the experimentally determined time of 50 % recrystallisation and the strain level. Due to only two strains having been measured in this project, there is insufficient data to determine a strain exponent for the Fe- 30Ni cold deformed and annealed tests.

However, using the available data set, the results suggest that the strain exponent is between 2 and 3. Therefore, it is not unreasonable to adopt a strain exponent of 2.5 for this work, i.e. an average value between 2 - 3. The strain exponent used for hot deformed C- Mn steel is 4, which is considerably higher than Fe- 30Ni under the cold deformed and annealed condition. It suggests that recrystallisation for hot deformed C- Mn steels is more sensitive to strain than cold deformed and annealed Fe- 30Ni.

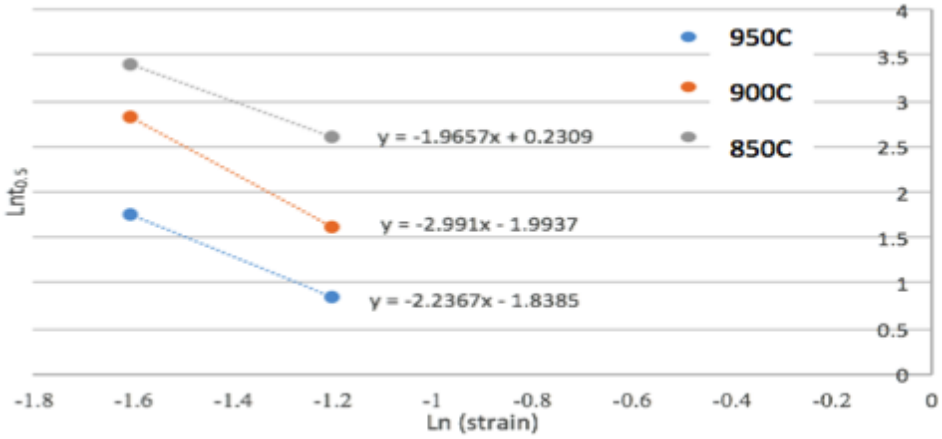

Figure 7-23 Plot of $lnt_{0.5}$ against ln (strain) at 950°C – 850°C, 0.2 – 0.3 strain

7.4.3 Effect of grain size distribution on recrystallisation kinetics

To determine how a grain size distribution can affect the recrystallisation kinetics, and hence the Avrami exponent, it was assumed that each grain separately follows the JMAK model in which site saturation and three dimensional constant growth rate occurs, giving an n value of 3. The overall recrystallised fraction was determined as the sum of the recrystallised fractions for each grain size. The initial grain size

distributions used are shown in Fig 5-9. Then, the recrystallisation kinetics for each grain class can then be calculated as,

$$X_n = 1 - \exp\left(\ln(0.95)\left(\frac{t}{R_{sn}}\right)^3\right) \quad \ldots 63$$

Where, X_n is the recrystallised fraction for each grain class at time t and R_{sn} is the recrystallisation starting time for each grain size class, which can be predicted by the Sellars approach, which will be covered in the following chapter.

Then, the overall recrystallisation fraction will be,

$$X = A_{20}X_{20} + A_{40}X_{40} + \cdots = \sum_{n=20}^{360} A_n\left[1 - \exp\left(\ln(0.95)\left(\frac{t}{R_{sn}}\right)^3\right)\right] \quad \ldots 64$$

Where A_n is the area fraction of each grain size class and n represents the grain size class, e.g. 20 represents grains in the size range 0-20 µm.

The individual grain size class consideration provides a quantitative description of the grain size distribution effect on the recrystallisation kinetics, with the Avrami exponent being related to the grain size distribution, such that it can be predicted for a given grain size distribution. To give an estimation of the Avrami exponent for different grain size distributions, a simplified derivation has been developed.

The cumulative area fractions for the different grain size distributions considered in this work are given in Figure 7-24. It can be seen that the 1300 ºC - 5mins sample, i.e. mode grain size 160 µm, gives a flatter slope compared to the 1100 ºC - 30mins sample, i.e. mode grain size 100 µm, due to its wider grain size distribution. $D_{0.9}$ and $D_{0.1}$ are the grain size at the 90% and 10% cumulative area fraction respectively, and are listed in Table 7-3. This clearly shows that the sample with mode grain size of 100 µm has a much tighter distribution as the grain size at the 90% of the cumulative area fraction is 140 µm compared to 260 µm for the sample with mode grain size of 160 µm.

Assuming each grain size class recrystallises individually, then the recrystallisation curve should roughly follow the cumulative area fraction curve; that is, the slope of the cumulative area fraction determines the Avrami exponent.
The Avrami exponent is measured by the experiment as,

$$n = \frac{lnln\left(\frac{1}{1-X}\right)}{\ln(t)} \quad \ldots 65$$

Where X is the recrystallisation fraction at time t.

The recrystallisation time for 10% and 90% are approximately equal to the recrystallisation starting time for $D_{0.1}$ and $D_{0.9}$ assuming each grain size class recrystallise individually.

Therefore, the Avrami exponent can be estimated as,

$$n = \frac{lnln\left(\frac{1}{1-0.9}\right) - lnln\left(\frac{1}{1-0.1}\right)}{\ln(t_{0.9}) - \ln(t_{0.1})} \quad \ldots 66$$

As recrystallisation starting time is proportional to the square of grain size,
Then the equation is given as,

$$n = \frac{3}{\ln(\frac{D_{0.9}}{D_{0.1}})^2} \quad \ldots 67$$

Where $D_{0.9}$ and $D_{0.1}$ are the grain size at the 90% and 10% cumulative area fraction respectively.

A summary of the predicted and experimental values of the overall Avrami exponents for the material is shown in Table 7-4. It can be seen that the experimental Avrami exponents have been predicted well for the samples with mode grain size of 160μm. An under-estimation has been seen for the samples with mode grain size of 100 μm (1.9 rather than 2.2-2.3), although the approach shows the correct trend in Avrami exponent. This is because the grain size determines the potential nucleation site

number per unit area and also the strain inhomogeneity. With decreasing strain, the strain distribution tends to be more homogeneous across different grains, then as a result, the Avrami exponent could be higher than predicted. A schematic diagram of the overall recrystallised fraction predicted using the classic JMAK model and taking into account the separate grain size classes in the grain size distribution is shown in Figure 7-25. It can be seen that the Avrami exponent decreases considerably compared to the classic JMAK model, which also affects the recrystallisation starting and finishing time prediction (discussed in the following section).

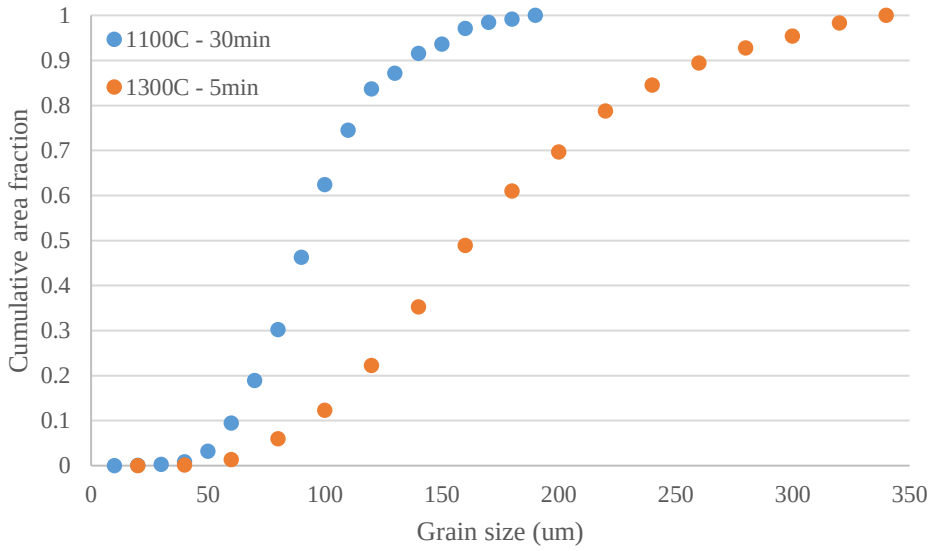

Figure 7-24 Cumulative area fraction for the two different grain size distributions, generated using two different heat treatments, considered in this work.

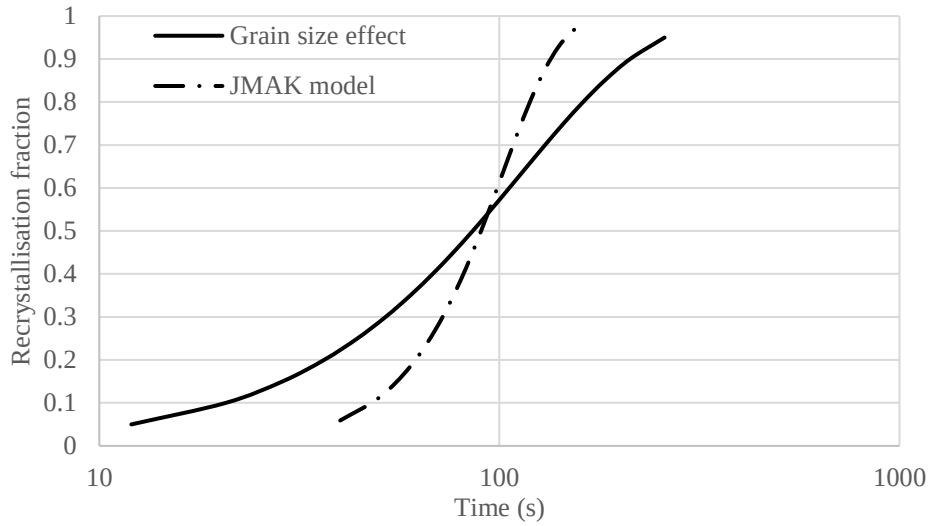

Figure 7-25 Schematic diagram of recrystallisation kinetics of Fe-30 Ni Nb free predicted by JMAK classic model (n=3) and the grain size effect model

Table 7-3 $D_{0.1}$ and $D_{0.9}$ for two different starting grain size distribution

Sample	$D_{0.9}$ (um)	$D_{0.1}$ (um)
1100 - 30mins	140	60
1300- 5mins	260	80

Table 7-4 Summary of Avrami exponent predictions by individual grain size class consideration

Temperature (C)	Grain size range (um)	Strain	Predicted value	Experimental value
950	20-340	0.3	1.3	1.2
900	20-340	0.3	1.3	1.3
850	20-340	0.3	1.3	1.4
950	20-340	0.2	1.3	1.3
900	20-340	0.2	1.3	1.4
850	20-340	0.2	1.3	1.3
900	20-200	0.2	1.9	2.2
850	20-200	0.2	1.9	2.3

7.4.4 Sellars approach for recrystallisation in cold deformed and annealed Fe- 30Ni

As mentioned, the strain exponent, recrystallisation activation energy and the Avrami exponent have to be determined for the material examined, grain size distribution and deformation mode (hot or cold). The constant A in the Sellars approach affects the recrystallisation starting time prediction significantly, and is been empirically fitted, hence a range of values are reported in the literature. Therefore, a new constant of 1.5×10^{-14} has been determined to fit the experimental data for Fe- 30Ni Nb free steels in this work. The proposed model is given as,

$$R_s = 1.5 \times 10^{-14} d_0^2 \varepsilon^{-2.5} \exp\left(\frac{195000}{RT}\right) \quad \ldots 68$$

$$X = 1 - \exp(\ln(0.95)(\frac{t}{R_{0.05}})^n) \quad \ldots 69$$

Where $n = \frac{3}{\ln(\frac{D_{0.9}}{D_{0.1}})^2}$.

It can be seen that the value of constant A in the modified model differs from the Sellars approach used for hot deformation such as the Dutta-Sellars model [68]. This is because the Dutta-Sellars model was developed to fit the experimental data for hot deformation of C-Mn steels and microalloyed steels. Whereas in this case, the model has been fitted for cold deformation and annealing of Fe-30Ni Nb free steels. The recrystallisation activation energy is considerably different between the two materials, therefore, the constant A, as a fitting parameter is different. In addition, the relationship between the strain applied (cold or hot) and the recrystallisation starting time will be different due to differing levels of recovery, which also leads to a different constant A value. Therefore, the proposed model constants are only applicable for the Fe-30Ni model alloy in the cold deformed then annealed condition. However, the effect of grain size distribution on the Avrami exponent, is applicable for both cold and hot deformed conditions, which will be discussed in the following section.

The predicted and experimental results for recrystallised fraction are shown in Figure 7-26. It can be clearly seen that a good agreement has been obtained for samples with the different starting grain size distributions, strain range 0.2 – 0.3 and temperature range 850 – 950 ºC with the new model, with the exception for the 850 °C at 0.2 strain samples. The Avrami exponents have been predicted well by the grain size distribution giving good agreement to the experimental data. The discrepancy with the experimental data for recrystallisation prediction for 850 °C at 0.2 strain may be due to the prolonged time before onset of recrystallisation available for recovery i.e. more stored energy has been consumed during the reheating/ holding time compared to other conditions, and as a result, the onset of recrystallisation has been delayed accordingly.

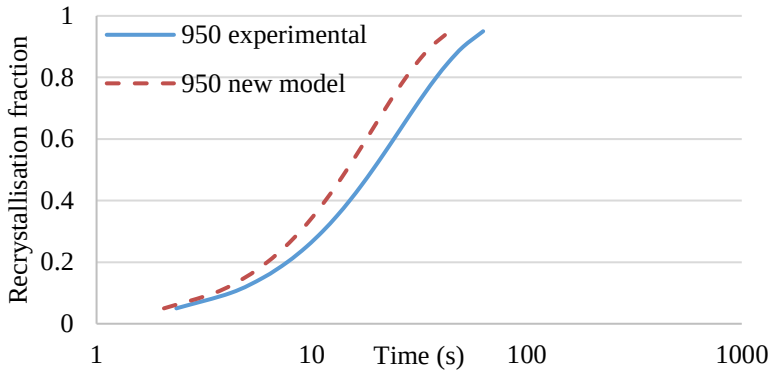
950 experimental
950 new model
Recrystallisation fraction
1
0.8
0.6
0.4
0.2
0
1
10
Time (s)
100
1000

(a)

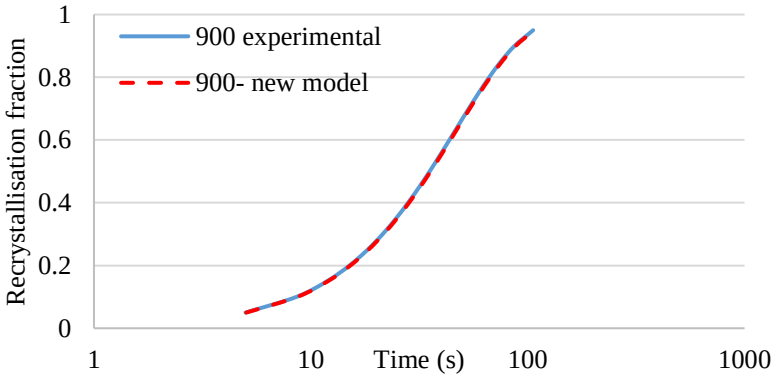
900 experimental
900- new model
Recrystallisation fraction
1
0.8
0.6
0.4
0.2
0
1
10
Time (s)
100
1000

(b)

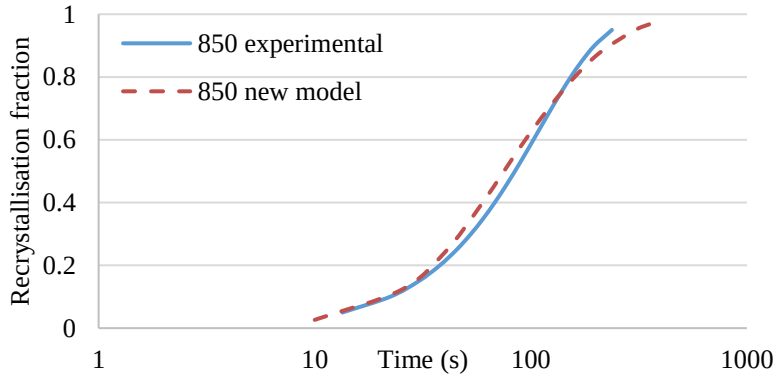
850 experimental
850 new model
Recrystallisation fraction
1
0.8
0.6
0.4
0.2
0
1
10
Time (s)
100
1000

(c)

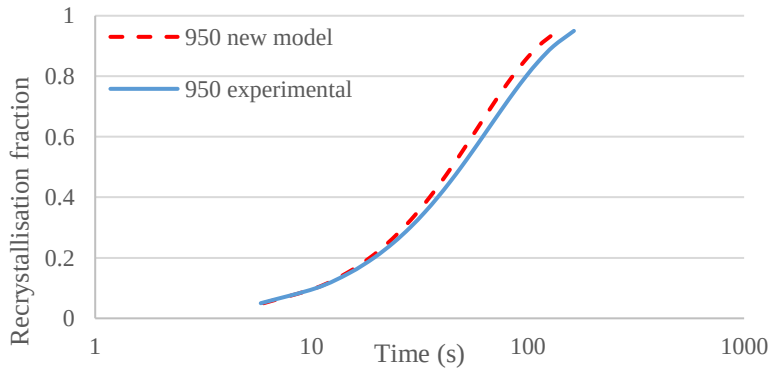
950 new model
950 experimental
Recrystallisation fraction
1
0.8
0.6
0.4
0.2
0
1
10
Time (s)
100
1000

(d)

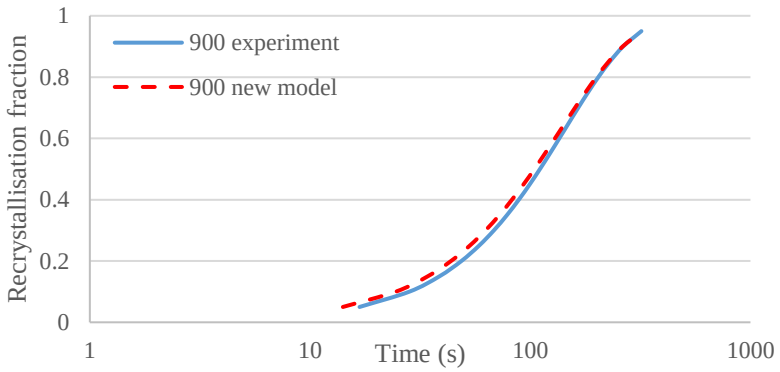
900 experiment
900 new model
Recrystallisation fraction
1
0.8
0.6
0.4
0.2
0
1
10
100
1000
Time (s)

(e)

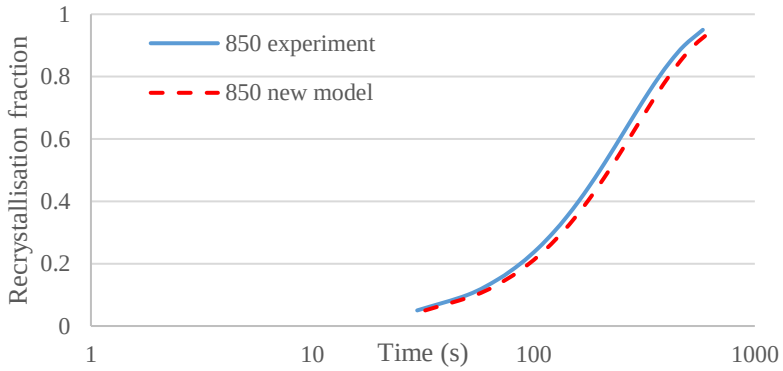
850 experiment
850 new model
Recrystallisation fraction
1
0.8
0.6
0.4
0.2
0
1
10
100
1000
Time (s)

(f)

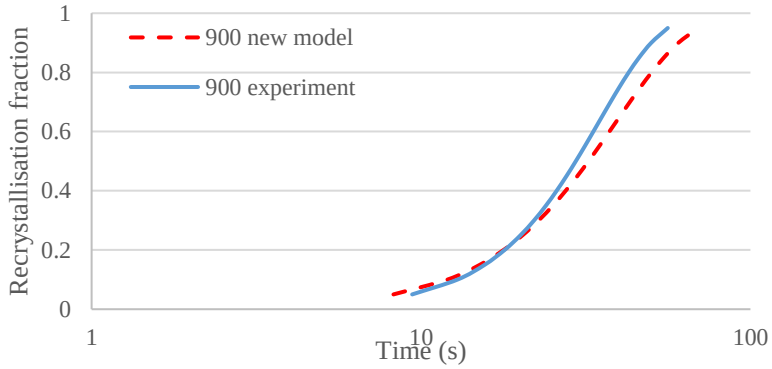
900 new model
900 experiment
Recrystallisation fraction
1
0.8
0.6
0.4
0.2
0
1
10
100
Time (s)

(g)

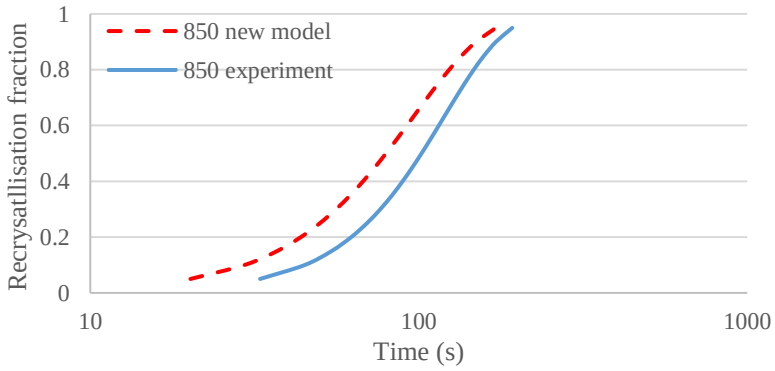
850 new model
850 experiment
Recrysatllisation fraction
1
0.8
0.6
0.4
0.2
0
10
100
1000
Time (s)

(h)

Figure 7-26 Predicted (modified model taking into account the grain size distribution) and measured recrystallisation fraction with time comparison (a) 950°C, 0.3 strain, grain size range 20- 340µm (b) 900°C, 0.3 strain, grain size range 20- 340µm (c) 850°C, 0.3 strain, grain size range 20- 340µm, grain size range 20- 340µm (d) 950°C, 0.2 strain, grain size range 20- 340µm (e) 900°C, 0.2 strain, grain size range 20- 340µm (f) 850°C, 0.2 strain, grain size range 20- 340µm (g) 900°C, 0.2 strain, grain size range 20- 200µm (h) 850°C, 0.2 strain, grain size range 20- 200µm

7.5 Recrystallised microstructure and grain size distribution of the cold deformed and annealed samples

The recrystallised microstructure is crucial for the final mechanical properties. A uniform microstructure with fine and equiaxed grains is desired. It can be seen in Figure 7-27 (a) that the grain boundaries and triple points are generally more deformed than the interior of the grains as the subgrain boundaries are more concentrated in these regions, as discussed in chapter 6. Then, when these regions recrystallised, the recrystallised grain size is fine. In addition, Figure 7-27 (b) shows an 80% recrystallised microstructure, and a mixed size of recrystallised grains can be seen. Clusters of the fine sized recrystallised grains can be clearly seen along the grain boundary region, Figure 7-27 (c), which is attributed to its high localised stored energy and greater number of potential nucleation sites. However, the recrystallised grain sizes vary within grains. The finer initial grains give a more uniform recrystallised structure than the coarser grains. That is, in a region with a finer initial grain size, a higher nuclei density gives more recrystallised grains, therefore, the recrystallised grain size distribution is narrower. It has already been seen that the recrystallised grain size distribution is independent of temperature within the temperature range of 850-900 °C at 0.3 strain, Figure 7-7 and 7-8.

Donadille has investigated the recrystallised grain size for cold deformed austenitic stainless steel with an initial grain size of 100μm [177]. It was found that the Sellars equation 40 for predicting the grain size is applicable to the cold deformed and annealed samples in the strain range of 0.5 - 2.3, temperature range 1000 - 850 °C with a strain exponent of -1 (same as the original Sellars model proposed for hot deformation). An example of the relationship between the strain and the average recrystallised grain size for cold deformed and annealed austenitic stainless steel is shown in Figure 7-28. Therefore, the Sellars equation has been applied for the cold deformed Fe-30Ni alloy to describe the recrystallised grain size. As mentioned in chapter 2.6, D' values were given as 0.35, 0.6 and 0.8. By using the Sellars equation (equation 40 and 41), the predicted mode recrystallised grain size distribution is calculated, and poor agreements have been observed, Figure 7-29. This is due to lack of consideration of difference of both nucleation site density and strain levels in each individual grain size class.

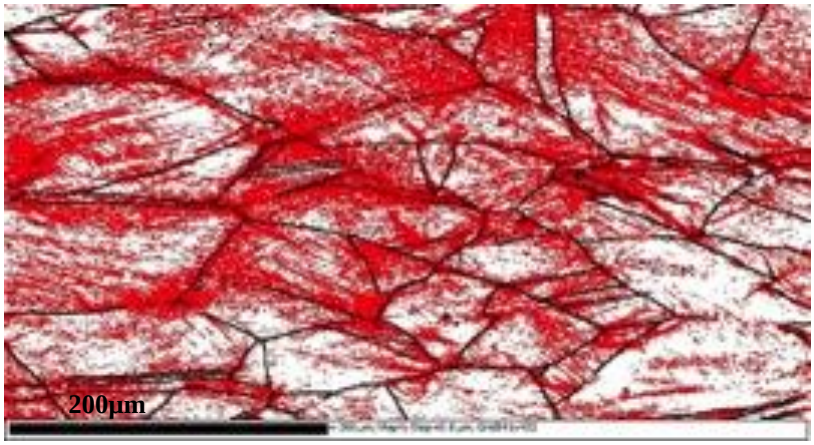

(a)

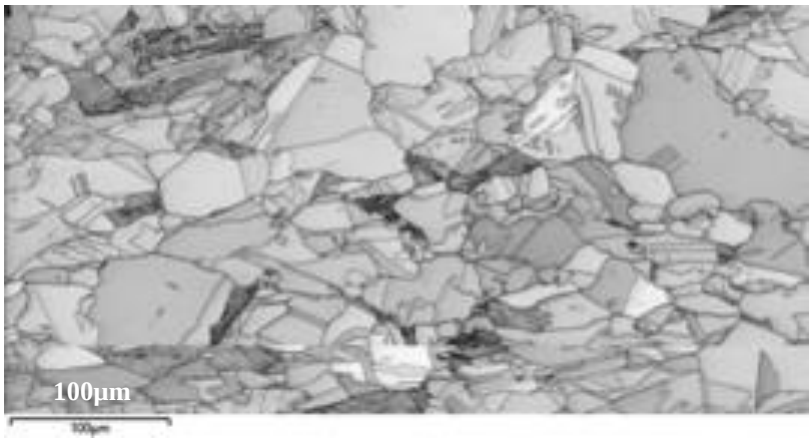

(b)

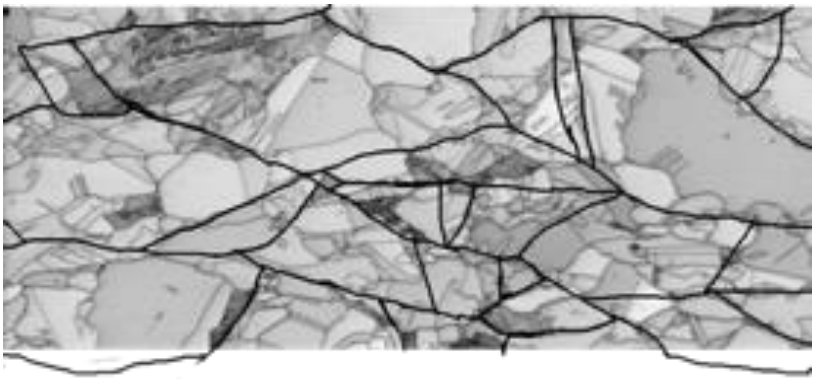

(c)

Figure 7-27 EBSD image of (a) deformed microstructure, black boundaries: > 15 degrees, red boundaries: > 2 degrees (b) 80% recrystallised microstructure (c) Hand drawn initial grain boundaries overlaid with the recrystallised microstructure

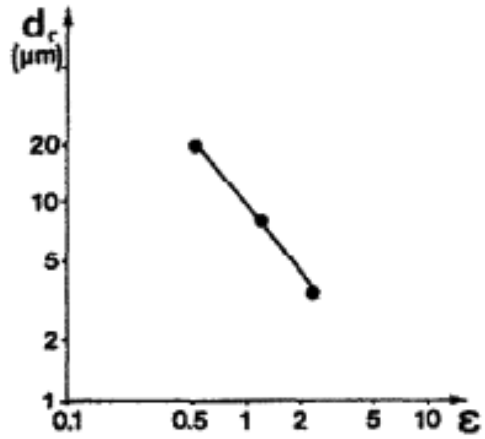

Figure 7-28 Effect of strain on the average recrystallised grain size of cold deformed austenitic stainless steel isothermally annealed at 900 °C [177]

The final recrystallised grain size distribution prediction has also applied the model proposed by Kaonda [178]. The model extended the Sellars equation (equations 40 and 41) to predict the recrystallised grain size distribution by applying the equation onto each individual grain size class for both cold and hot deformed samples. D' has been fitted to the first 5% of the grain size class, the mode grain size and the largest grain size class for different starting grain size, Table 7-5. The equation of Kaonda's model is given by,

$$D_{rex} = D' D_0 \varepsilon^{-1} \quad \ldots 70$$

Table 7-5 D' values for different starting mode grain sizes from Kaonda's approach

Mode grain size (μm)	D' (5%)	D' (mode)	D' (max)
160	0.15	0.18	0.18
100	0.2	0.15	0.15

The comparison between the predicted and the experimental recrystallised grain size distribution is shown in Figure 7-30. It can be seen that the predicted grain size distribution gives the same range as the experimentally determined ones. The recrystallised mode grain size for samples with initial mode grain size of 160 μm has been over predicted for 0.3. Whereas recrystallised mode grain size has been predicted well for the 0.2 strain with the mode grain size of 160 μm also the samples with mode grain size of 100 μm. The discrepancy at 0.3 strain could attributed to the experimental error in this case.

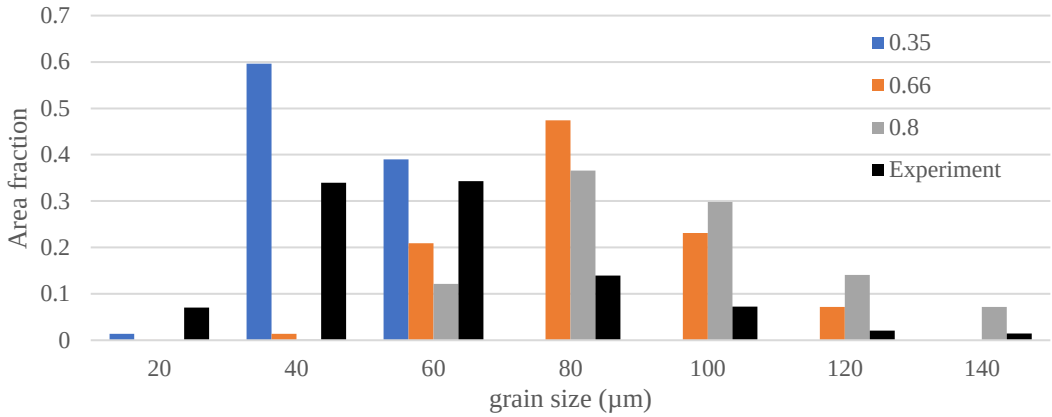

(a) Recrystallised grain size distribution at 0.3 strain, starting mode grain size of 160 μm, using Sellars model with various D'

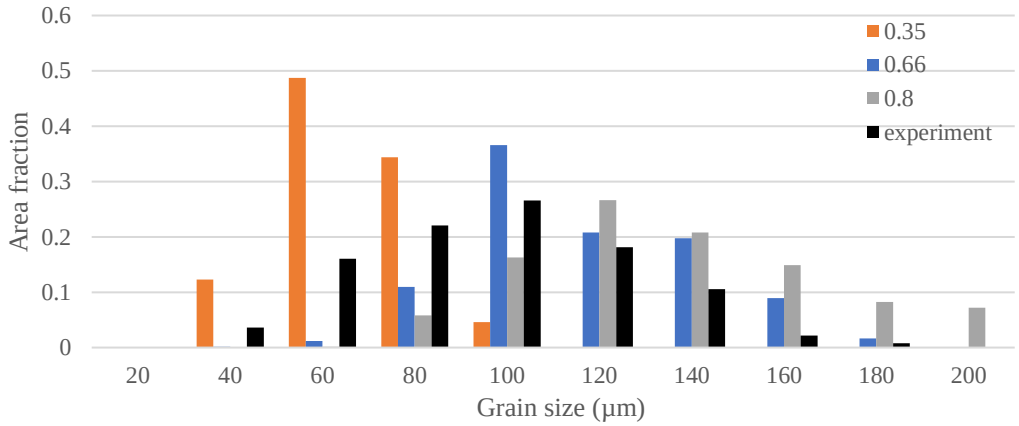

(b) Recrystallised grain size distribution at 0.2 strain, starting mode grain size of 160 μm, using Sellars model with various D'

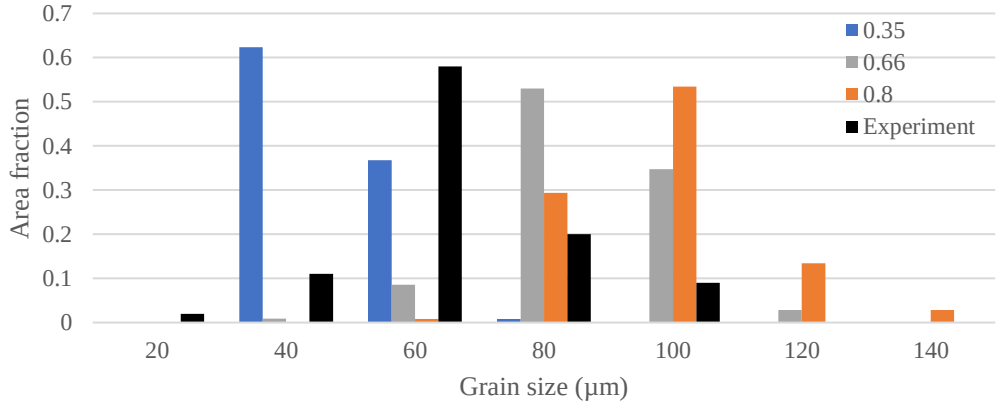

(c) Recrystallised grain size distribution at 0.2 strain, starting mode grain size of 100 μm, using Sellars model with various D'

Figure 7-29 Prediction and experimental results for Fe-30Ni Nb free steel at different starting grain size distribution and strain levels by Sellars model with various D'

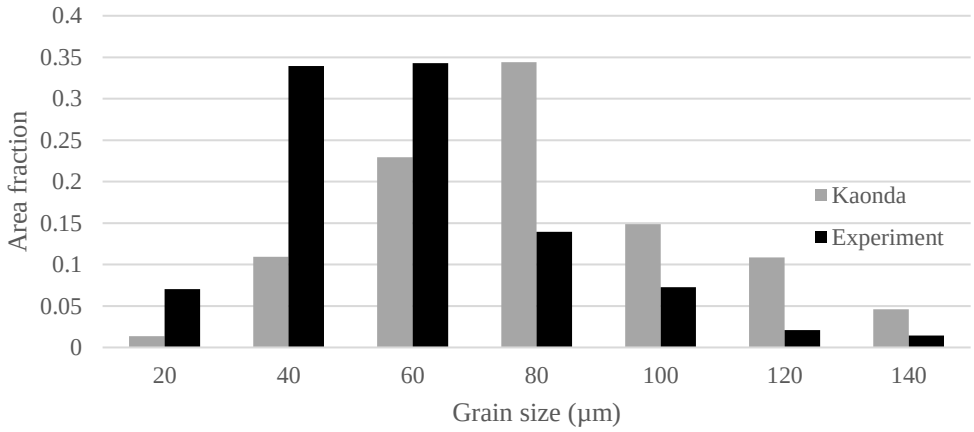

(a) Recrystallised grain size distribution at 0.3 strain, starting mode grain size of 160 μm, using Kaonda's approach

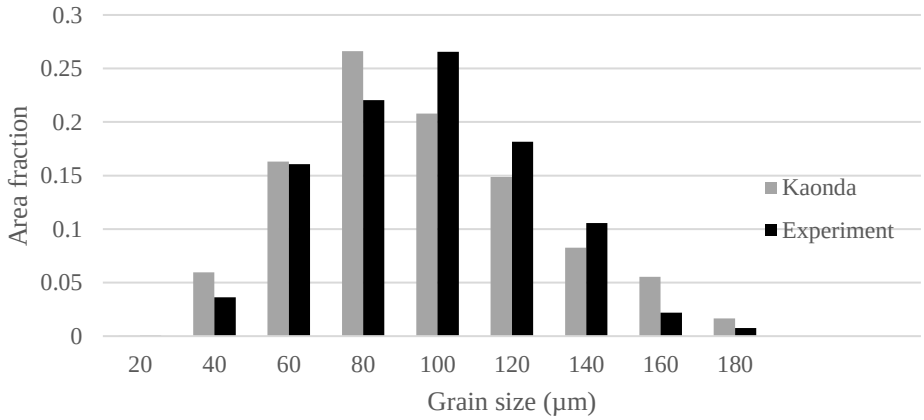

(b) Recrystallised grain size distribution at 0.2 strain, starting mode grain size of 160 μm, using Kaonda's approach

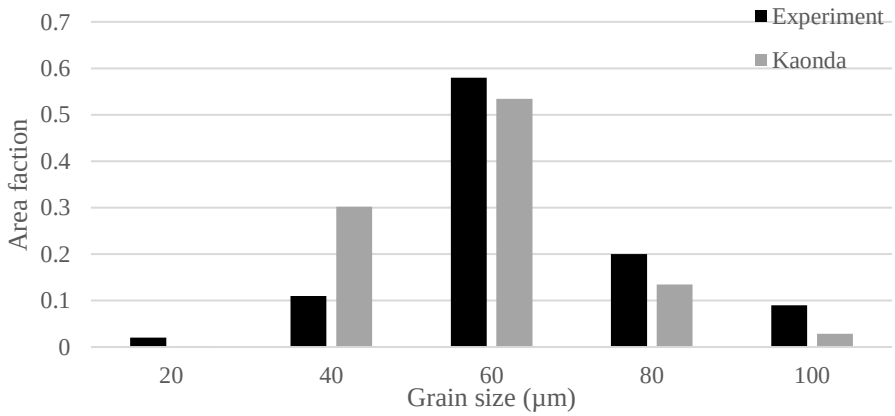

(c) Recrystallised grain size distribution at 0.2 strain, starting mode grain size of 100 μm, using Kaonda's approach

Figure 7-30 Prediction and experimental results for Fe-30Ni Nb free steel at different starting grain size distribution and strain levels by Kaonda's approach

7.6 Hot and cold deformed samples recrystallisation comparison

It has been mentioned in chapter 2.5 that cold and hot deformation leads to a comparable deformed microstructures (cells, microbands and subgrains), which has been further verified by the experiment al results shown in chapter 6. The difference in stored energy between the cold deformed / reheated and hot deformed sampels is expected to affect the recrystallisation starting and finishing time, but should have no effect on the recrystallisation Avrami exponent. In this section a limited number of tests have been carried out on the Fe-30Ni Nb free steel with different initial grain size distributions to confirm that the effect of grain size distribution on the recrystallisation Avrami exponent under hot deformed conditions is the same as for cold deformation and annealing.

It was shown that the no dynamic recrystallisation occurs during hot deformation from observation of the hot deformed and immediately quenched samples after deformation at 950 and 850 °C in Chapter 6. Observation of the partially recrystallised microstructure from samples hot deformed to 0.3 strain and then held for varying times at 950°C showed that recrystallisation nucleation occurs in the region near the grain boundaries and triple points, attributed to the local high dislocation density [9]. Figure 7-31 shows an optical image of the partially, i.e. 27%, recrystallised grain structure after 760s at 950 °C after hot deformation to 0.3 strain, starting mode grain size of 160 μm. It can be clearly seen that the coarser grains were only partially recrystallised, i.e. as arrowed, though the recrystallising grains have formed along the grain boundary regions. In contrast the cold deformed and annealed sample after 0.3 strain was fully recrystallised after 60s at 950 °C with the same initial grain size distribution. This suggests that the hot deformed sample shows slower recrystallisation kinetics compared to the cold deformed sample at 0.3 strain, which is attributed to lower stored energy. The sluggish recrystallisation kinetics is as expected for the coarser grains in this case. Therefore, the coarse grains could take significantly longer times to reach full recrystallisation, for example even after 760s the recrystallisation fraction was only 27%. Hence, a higher strain of 0.35 was used in the hot deformed case for the samples with a mode grain size of 160 μm to investigate the recrystallisation mechanism to ensure complete recrystallisation within a reasonable hold time after deformation. As discussed previously the recrystallisation mechanism, and hence

Avrami exponent, is independent of the strain, therefore any effect of grain size distribution should still be evident.

Figure 7-32 shows optical images of the grain structures after various times at 950 °C after hot deformation to 0.35 strain, starting mode grain size of 160 µm. It can be seen that the recrystallisation nucleation occurs primarily at grain boundaries and triple points under the hot deformation conditions, Figure 7- 32 (a). Additionally, slow recrystallisation kinetics is also clearly seen for coarser grains in Figure 7-32 (c) after annealing for 120s; for example one grain over 200 µm remaining unrecrystallised after 81% of recrystallisation, whereas most fine grains have recrystallised. The final micrograph, Figure 7-32 (d) shows the fully recrystallised microstructure.

The grain size distribution evolution during recrystallisation for the hot deformed samples shows a comparable trend with the cold deformed samples (discussed in chapter 2.6), Figure 7-33. The area fraction of the grains over 200 µm has not changed between the as-deformed and 25s condition, whereas the area fraction of the finer grains, i.e. 20 - 100 µm has increased drastically from 13 % to 43 %. This strongly suggests that recrystallisation occurred faster in the finer grains, whereas the coarser grains recrystallised at the latter stage. Additionally, it can be seen that the mode recrystallised grain size for the samples deformed at 950 °C to 0.35 strain is coarser than the cold deformed sample at 0.3 strain, which could be due to the lower stored energy after hot deformation (even at the higher strain) in this case due to dynamic recovery.

Figure 7-34 shows optical images of recrystallisation evolution after hot deformation to 0.27 strain at 950 °C, initial mode grain size of 100 µm. It can be seen from Figure 7-34 that after 5s, 17% has recrystallised; after 10s, 58% has recrystallised; after 15s, 70% has recrystallised and after 40s there is fully recrystallisation. It can be seen that there does not seem to be a significant difference in recrystallisation rates for the finer and coarser grains as unrecrystallised coarser grains are not apparent in the same way as have been observed for the 160µm mode grain size material, i.e. Figures 7-34 (b) which indicates that recrystallisation occurred more evenly over the different grain sizes, as was seen for the cold deformed and annealed samples.

The recrystallisation kinetics after hot deformation are shown in Figure 7-35 and 7-36. The JMAK model has been fitted using the approach described in chapter 7.3. The sample with a mode grain size of 160 μm gave an Avrami exponent of 1, whilst the sample with a mode grain size of 100 μm gave a value of 1.8, which is in the same range as obtained from the cold deformed samples (Table 7-3). The slight difference in the values between the cold and hot deformed conditions may be due to the some macroscopic strain inhomogeneity (due to sample barrelling) in the hot deformed sample compared to the cold deformed condition (as discussed in the literature review chapter 2.5).

It can be seen from Figures 7-35 and 7-36 that the recrystallisation kinetics, i.e. the recrystallisation starting and finishing time, is considerably slower for the hot deformed conditions, which is consistent with the hot deformed samples having a lower stored energy due to dynamic recovery as suggested by the coarser recrystallised grain size discussed above. Therefore, the absolute values for R_s and R_f and the recrystallisation kinetics cannot be compared between hot deformation and cold deformed and annealed samples (which is not the focus of this project), but the effect of the grain size distribution on the recrystallisation mechanism, and hence Avrami exponent, is the same in both cases.

In summary, recrystallisation inhomogeneity caused by the grain size distribution has also been observed under hot deformed conditions at 950 °C, strain 0.27 - 0.35, where the coarser grains recrystallise at a later stage compared to the finer grains. This agrees well with the observations made for the cold deformed then annealed samples. The Avrami exponents measured for hot deformation were in the same range as observed in the cold deformed samples, confirming that the recrystallisation mechanism is the same and that the grain size distribution has a direct effect on the Avrami exponent.

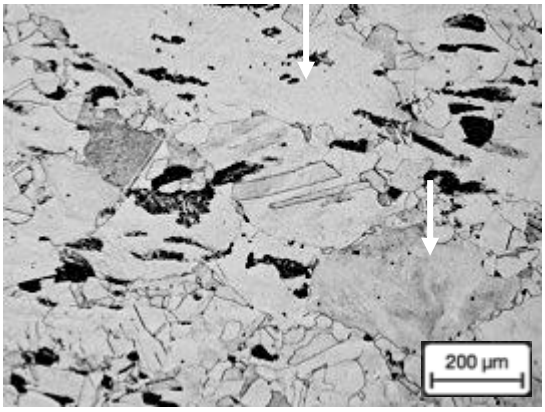

Figure 7-31 Microstructure after holding for 760 s after hot deformation at 950 ºC, 0.3 strain with a mode grain size of 160 µm showing 27% recrystallised. Coarse undrecrystallised grain arrowed.

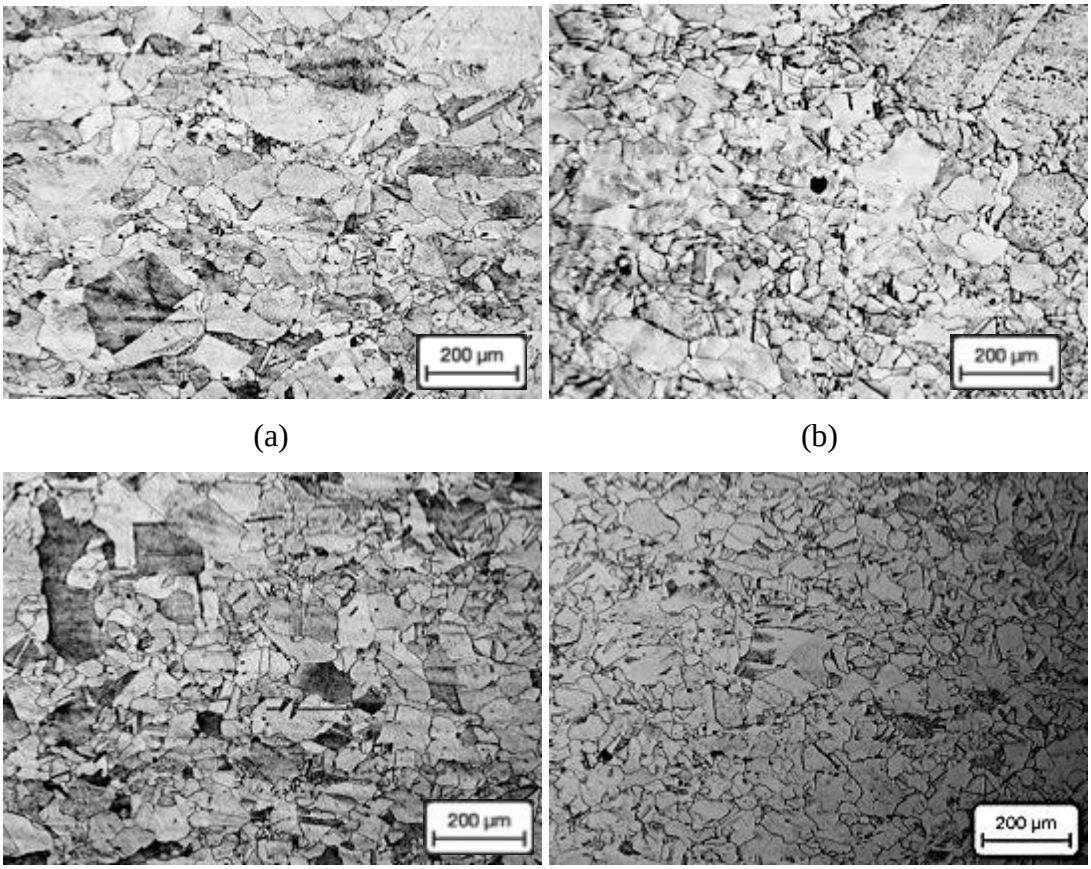

Figure 7-32 Microstructure evolution at (a) 25s, 28 % recrystallised; (b) 60s, 61% recrystallised (c) 120s, 81% recrystallised (d) 300s, fully recrystallised at 950 ºC, 0.35 strain with a mode grain size of 160 µm

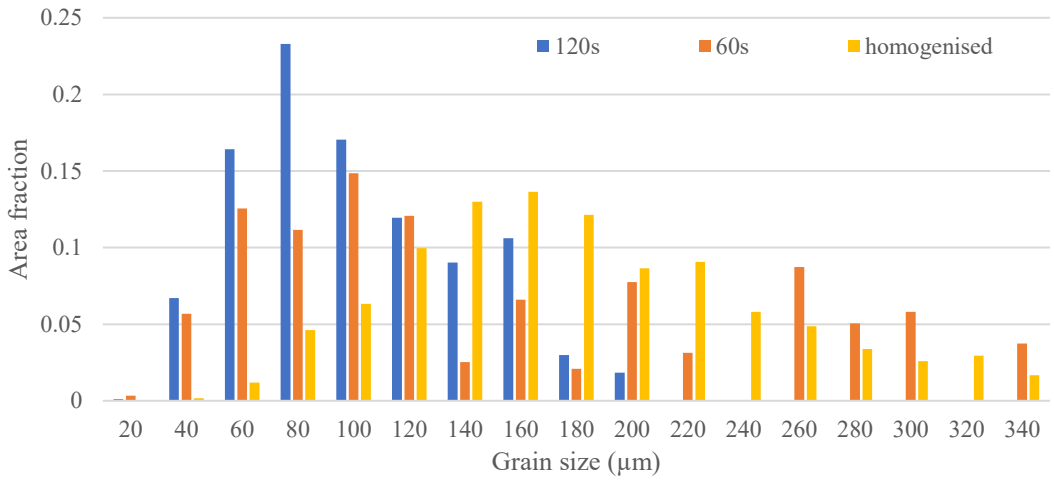

Figure 7-33Grain size distribution evolution of unrecrystallised (homogenised), 61% recrystallised (60s), 81% recrystallised (120s) samples at 950 °C after 0.35 strain for the 160 µm mode grain size Fe-30 Ni material.

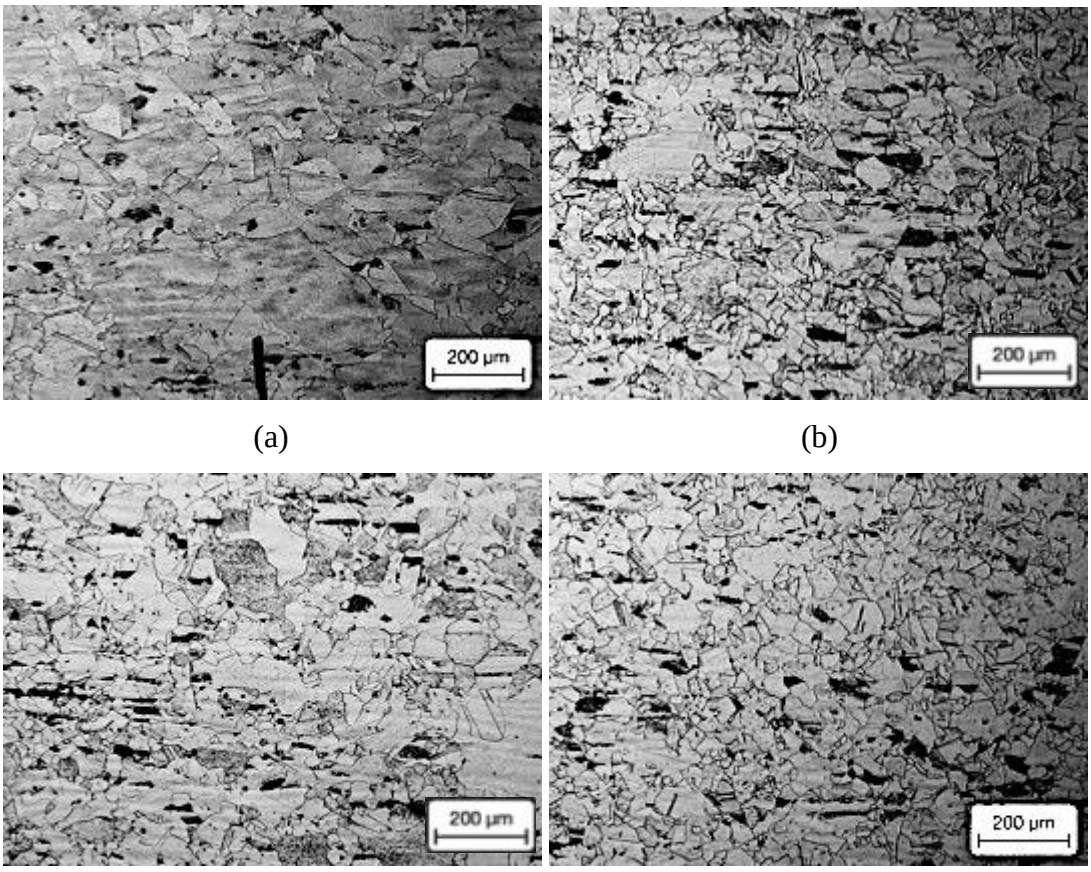

(a) (b)

(c) (d)

Figure 7-34 Microstructure evolution at (a) 5s, 17% recrystallised; (b) 10s, 58% recrystallised (c) 15s, 70% recrystallised (d) 40s, fully recrystallised at 950 ºC, 0.27 strain with a mode grain size of 100 µm

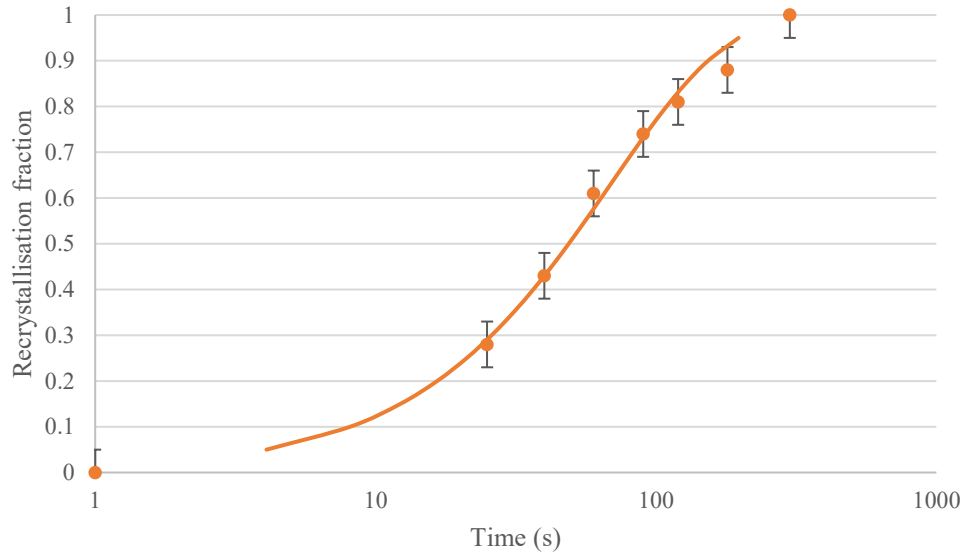

(a)

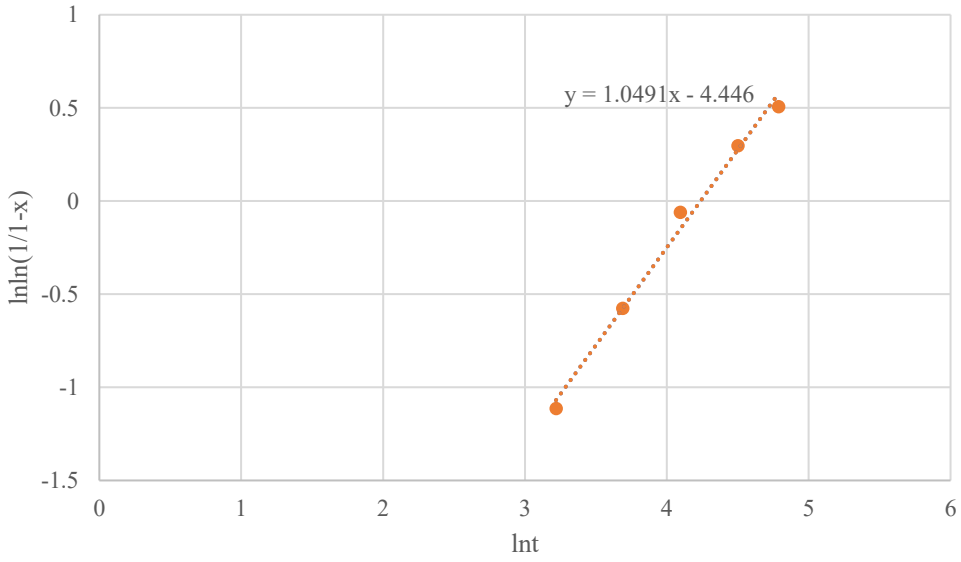

(b)

Figure 7-35 (a) Recrystallisation fraction versus time (b) lnln(1/1-x) versus lnt of sample deformed at 950 °C, 0.35 strain, $5s^{-1}$, with a mode grain size of 160 μm.

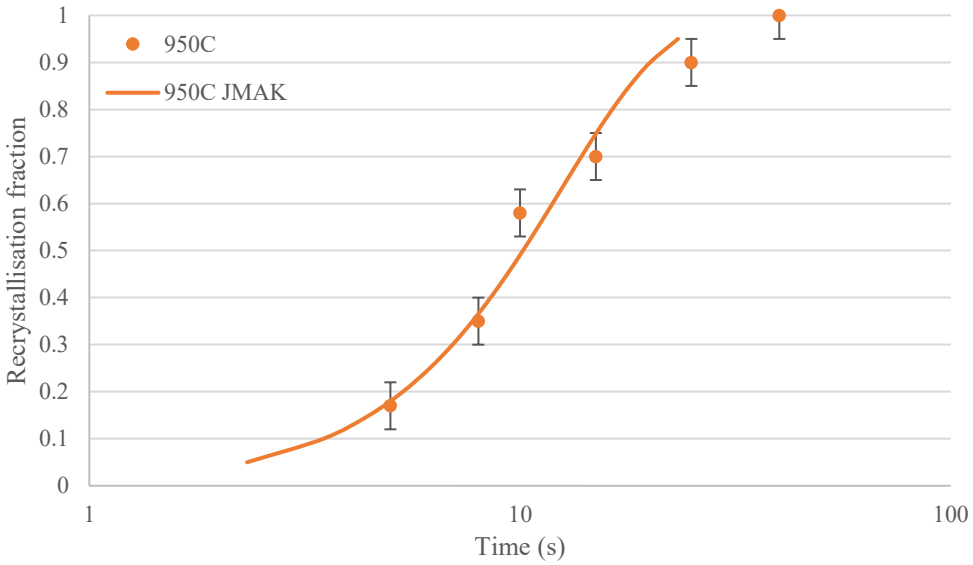

(a)

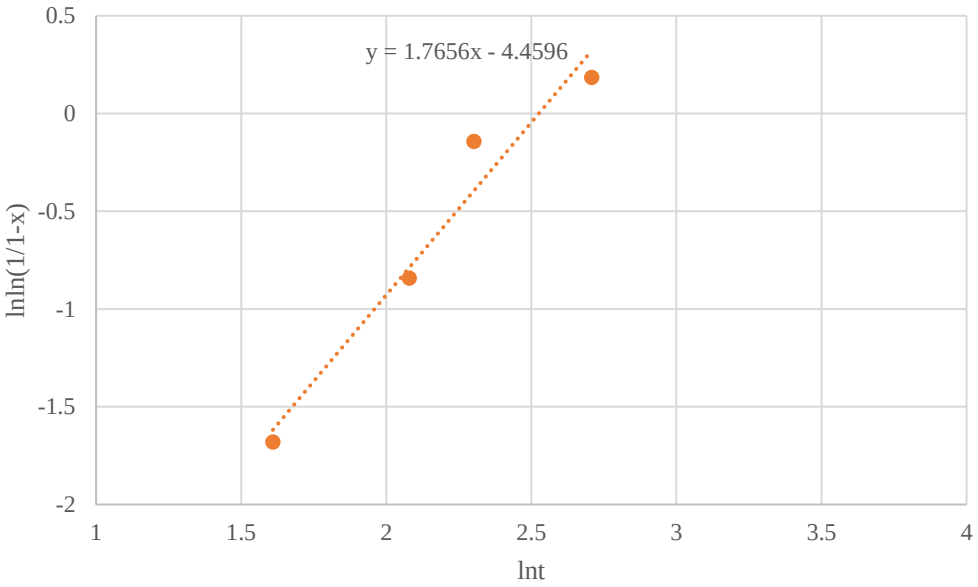

(b)

Figure 7-36 (a) Recrystallisation fraction versus time (b) lnln(1/1-x) versus lnt of sample deformed at 950 °C, 0.27 strain, $10s^{-1}$, with a mode grain size of 100 μm.

7.6.2 Case study: Model application for hot deformation of HSLA steels

To validate the proposed Avrami exponent prediction model a HSLA steel with 0.044 wt. % Nb was considered. Before testing the steel was reheated to 1225˚C for 1 hour to represent a commercial reheat procedure followed by quenching (to preserve the prior austenite grain size). The reheated samples were then deformed at 1050°C to 0.3 strain (strain rate of 10 s^{-1})and held for 1000s then quenched. Then the samples were tempered at 500˚C for 5 minutes, which is a heat treatment designed to enhance prior austenite grain boundaries. Metallographic examination was carried out to generate the grain size distribution of the homogenised sample, which showed a fully martensitic microstructure after quenching and tempering, Fig 7-37 (a). A uniform grain size distribution is seen, Fig 7-37 (b), within the range of 25- 425 µm with 56 % of grains (by area) within the range of 25- 225 µm and a mode grain size of 225µm. The recrystallisation fraction was measured using the stress relaxation method after deformation at Tata Steel STC. The optical images observed at the central region and the anvil contacting region did not show any differences, i.e. there is reasonable strain homogeneity, Figure 7-38. Thus, the recrystallisation fraction measured by stress relaxation method has been used to determine the recrystallisation rate. The details of calculating the recrystallisation fraction from the stress relaxation data is shown in Appendix 3.

The grain size at 10 % of the cumulative area fraction is 150 µm, and 325 µm for 90%. Therefore, the predicted Avrami exponent for the initial grain size distribution is given as,

$$n = \frac{3}{\ln(\frac{D_{0.9}}{D_{0.1}})^2} = \frac{3}{\ln(\frac{325}{150})^2} = 1.9$$

The recrystallisation kinetics and the Avrami exponent measurement for the HSLA steels is shown in Figure 7-39. It can be seen that the Avrami exponent has been determined to be 1.9, which agrees with the prediction.

Therefore, the effect of grain size distribution on the recrystallisation mechanism and Avrami exponent, and the proposed model to predict the Avrami exponent from the grain size distribution, is not only applicable for Fe-30Ni under the cold deformed and annealed condition, but also applicable for HSLA steels in the hot deformed condition.

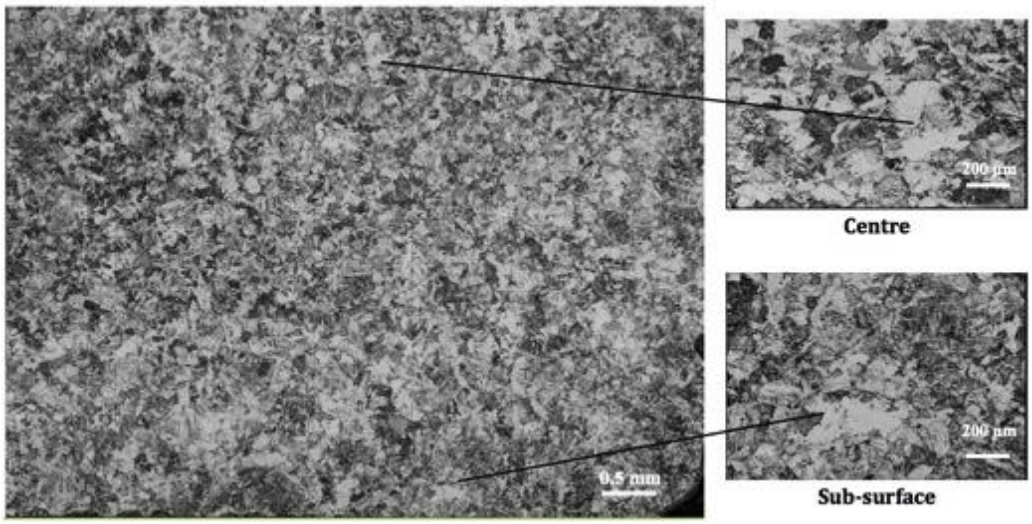

(a)

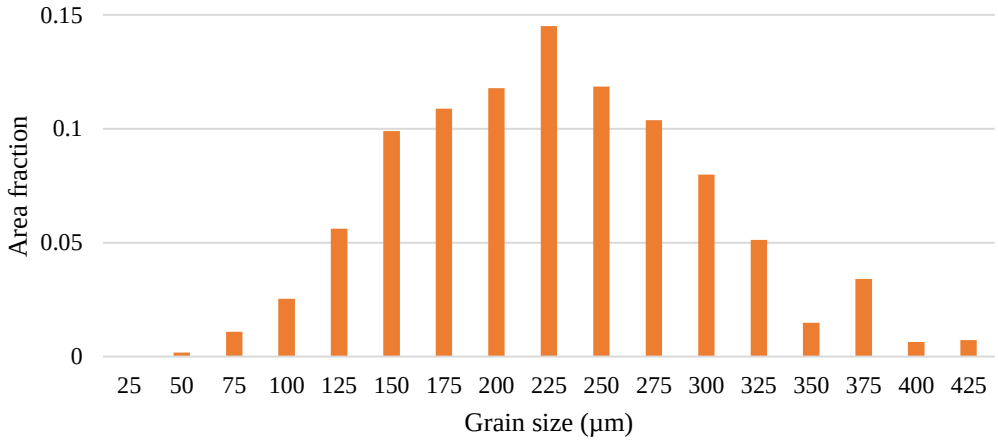

(b)

Figure 7-37 (a) optical image and (b) grain size distribution of the homogenised, reheated, quenched and tempered sample

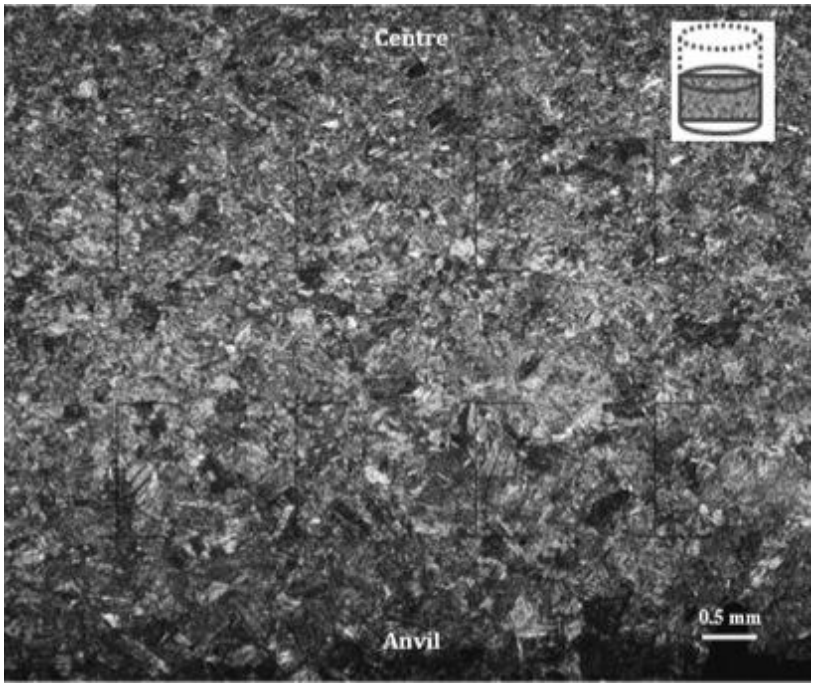

(a)

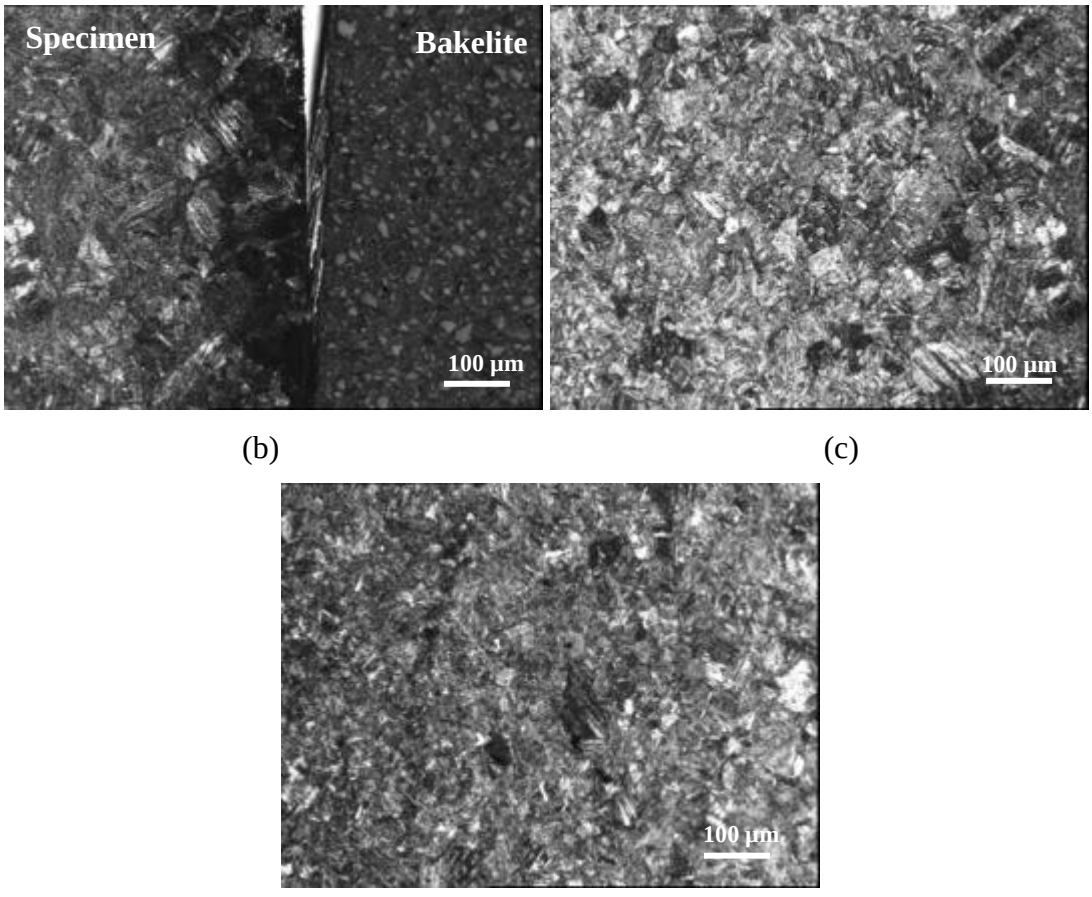

(b) (c)

(d)

Figure 7-38 Microstructure of HSLA steel samples after recrystallisation:.(a) Overall view (b) sub-surface, (c) quarter-thickness and (d) mid-thickness

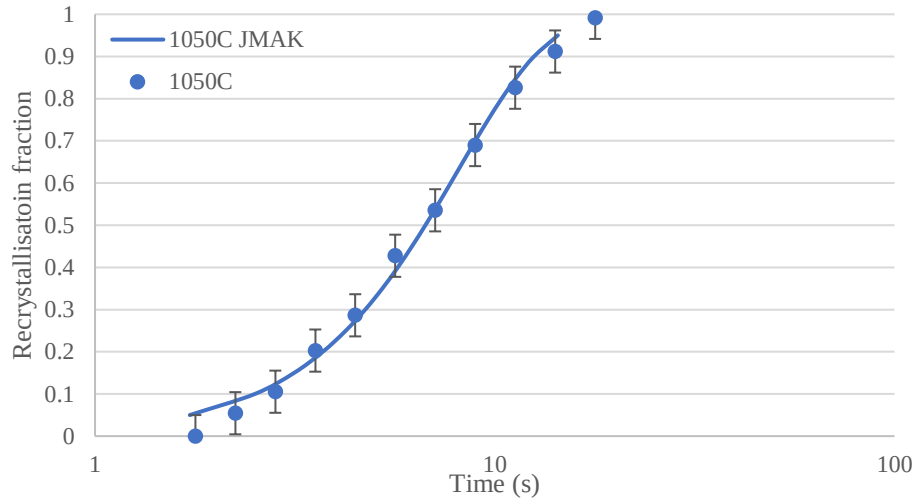

(a)

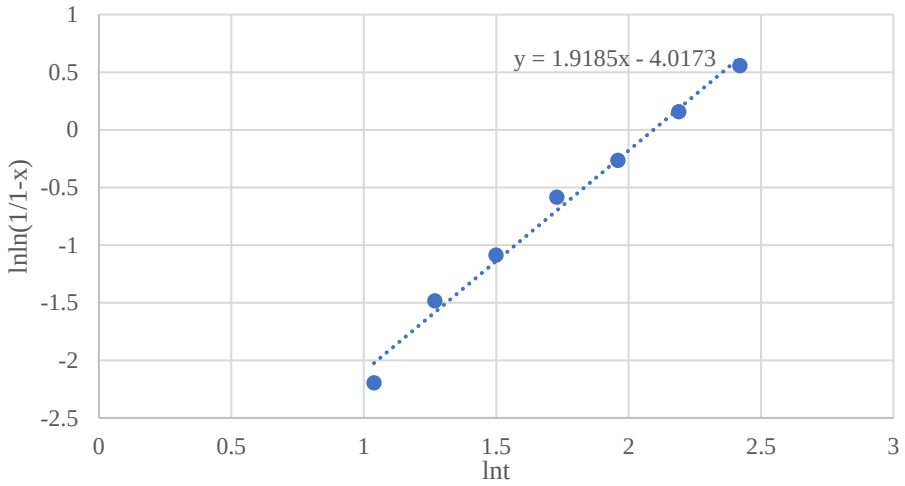

(b)

Figure 7-39 (a) Recrystallisation fraction versus time (b) lnln(1/1-x) versus lnt of sample deformed at 1050 °C, 0.3 strain, $10s^{-1}$ for HSLA steel

7.7 Summary

Inhomogeneity in recrystallisation nucleation and growth has been observed using optical microscopy and EBSD scanning showing that recrystallisation nuclei are not randomly distributed. As a result, impingement of recrystallised grains along the grain boundary occurs at an early stage of recrystallisation leading to a lower Avrami exponent. Additionally, the recrystallisation growth rate decreases with time. That is, the heavily deformed regions have more stored energy and thus recrystallise first, then the lightly deformed region recrystallises later. The recrystallisation rate of the region with high stored energy is considerably faster than the rest. Furthermore, it has been observed that the finer grains recrystallise faster than the coarser grains due to both the higher stored energy and higher density of potential nucleation sites.

It has been found that the grain size distribution influences recrystallisation with a lower Avrami exponent being seen for a larger mode and wider grain size distribution. The Avrami exponent can be predicted from the grain size distribution, with a simple approach considering the grain size at the 10% and 90% cumulative area fraction giving good predictions. The Avrami exponent prediction, developed using data for cold deformed and annealed Fe-30Ni samples has also been applied to hot deformed Fe-30Ni and a HSLA steel and good agreement has been seen.

The validity of the Sellars approach for describing the cold deformed Fe-30Ni model alloy has been investigated. The proposed equation has been applied successfully to describe the recrystallisation kinetics of the samples deformed at room temperature between 0.3 - 0.2 strain, annealing temperature 950- 850 °C. It is, however, worth noting that the predicted recrystallisation starting and finishing times, i.e. the proposed model for cold deformed Fe- 30Ni model alloy, cannot be directly transferred to the hot deformed condition due to the variation in the stored energy between the two conditions. Faster recrystallisation kinetics are observed for the cold deformed then annealed samples at same strain in this case.

The validity of the recrystallised grain size distribution modelling by Kaonda's approach has also been examined. The recrystallised mode grain size has been slightly overestimated after 0.3 strain for the sample with an initial mode grain size of 160 μm.

Whereas good agreements have been observed after 0.2 strain, for the samples with mode grain sizes of 160 and 100 μm.

The validity and comparison of the cold deformed and annealed tests and hot deformed tests have been listed in Table 7-6. It can be seen that recrystallisaiton inhomogeneity in nucleation and growth have been observed in both cold and hot deformed samples via both optical and EBSD. Additionally, the measured recrystallisation Avrami exponents were comparable between the cold and hot deformed samples, which validated the proposed Avrami exponent model to take grain size distritbution into consideration. Nevertheless, it is worth noting that the recrystallisation starting and finshing time also the recrystallised grain size distribution are not comparable/ transferrable between the cold and hot deformed conditions attributed to the difference in the stored energy.

Table 7-6 Comparison of cold deformed and annealed and hot deformed tests

	Tests	Objectives	Transferrable knowledge	Non- transferrable knowledge
1	Optical observation of recrystallisation In- situ EBSD observation of recrystallisation	1. Recrystallisation nucleation and growth inhomogeneity for cold and hot deformed samples 2. The grain size distribution evolution during recrystallisation for cold and hot deformed samples	1. Recrystallisation nucleation occurs along the grain boundary regions, and the recrystallisation growth is faster in the finer grains for both cold and hot deformed conditions,.	
2	Recrystallisation kinetics determination	1. Avrami exponent for cold and hot deformed samples 2. Recrystallisation starting and finishing time for cold and hot deformed samples	1. Recrystallisation Avrami exponent is strongly affected by the grain size distribution for both cold and hot deformed samples. Comparable Avrami exponent has been reported from samples with comparable	1. The recrystallisation starting and finishing time for cold deformed and annealed samples are faster compared to the hot deformed samples at same strain.

			2. A tigher grain size distribution gives a higher recrystallisation Avrami exponent	
3	Recrystallised grain size measurement	1. Recrystallised grain size for cold and hot deformed samples		1. Cold deformed and annealed samples gave a finer recrystallised grain size at 0.3 strain than the hot deformed samples annealed after 0.35 strain. This could be due to a higher stored energy for the cold deformed samples.

Chapter 8 Effect of Nb on the recrystallisation kinetics

8.1 Introduction

It was shown in chapter 7 that the grain size distribution plays an important role in determining the recrystallisation kinetics. The individual grain size class consideration predicted the Avrami exponent well.

In this chapter, the recrystallisation behaviour of a homogenised (to remove Nb segregation) Fe-30Ni-0.044 wt. % Nb model alloy has been used to investigate the effect of Nb on the recrystallisation kinetics, in particular the Avrami exponent. The grain size distribution is shown in Figure 8-1. To determine the recrystallisation kinetics 0.3 - 0.2 cold strain, and 0.45 - 0.35 hot strain was applied followed by annealing / holding at 950 - 850 °C for different times; the microstructural evolution and the grain size distribution of non, partially and fully recrystallised samples during recrystallisation were characterised, along with the strain induced precipitates and their size evolution.

The cold deformed and annealed samples have been used to investigate the role of the strain induced precipitates on the recrystallisation rate, in particular the Avrami exponent, from which a model for the Avrami exponent is proposed. The hot deformation tests were carried out to compare the recrystallisation and precipitation kinetics with cold deformed samples. It is noted that the absolute values of recrystallisation starting and finishing time, and the precipitation kinetics are not expected to be equivalent between the two conditions or to those for microalloyed steels due to the difference in the Nb solubility and stored energy (as discussed in the literature review and previous chapters). In terms of Nb solubility it can be seen that the predicted Nb solubility in the Fe-30Ni model alloy used is considerably higher compared to in a C-Mn microalloyed steel, Figure 8-2, meaning that the precipitation kinetics measured in Fe-30Ni cannot be directly transferred to describe the Nb precipitation kinetics in microalloyed steels. Nevertheless, the interaction between precipitation, in terms of the number and size of precipitates, and recrystallisation and its effect on the recrystallisation Avrami exponent can be considered to be generic.

The starting grain size distributions, after homogenisation, for the Fe-30Ni Nb free and 0.044wt. % Nb steels are shown in Figure 8- 1. It can be seen that the mode grain size for the Nb containing steel is 180 µm, and the grain size range is between 20-360 µm. The grain size distribution of the Nb free steel is also shown in Figure 8-1 for comparison and has a starting grain size of 160 µm, with grain size range of 20-340 µm. Therefore, the starting grain size distributions are comparable for these two steels which will eliminate the effect of grain size distribution on the recrystallisation kinetics.

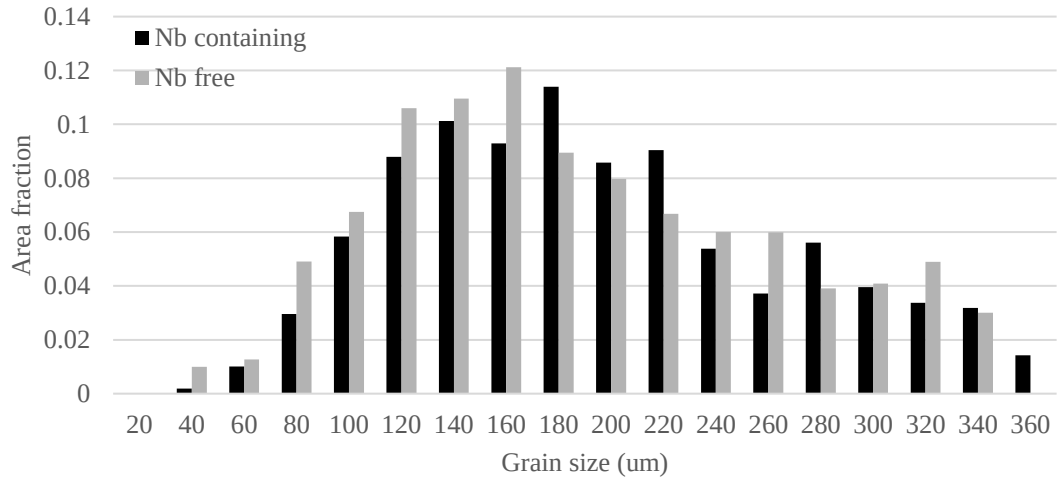

Figure 8-1 Starting grain size distribution of Fe-30Ni Nb free and 0.044wt. % Nb

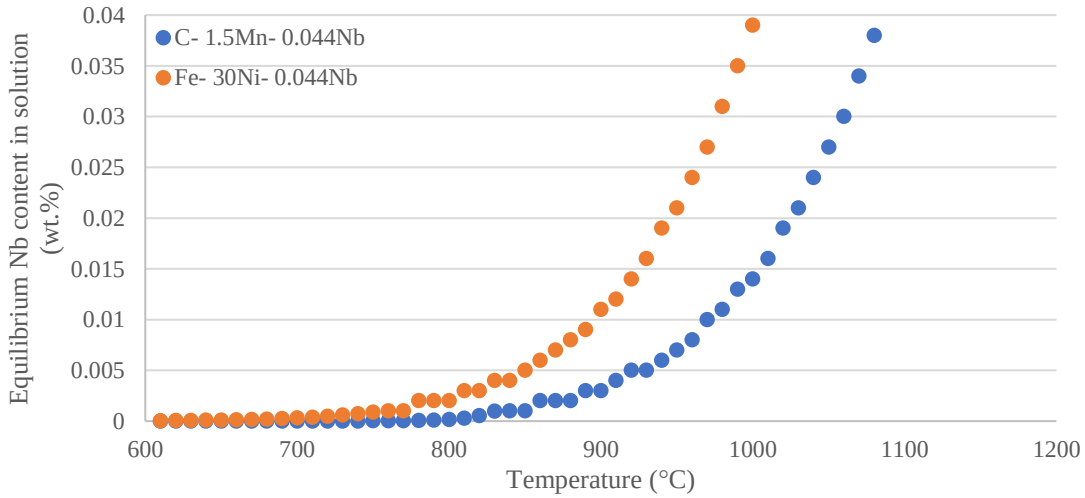

Figure 8-2 The Nb solubility in Fe-30Ni and C-Mn steel calculated by Thermo- Calc

8.2 Cold deformed conditions

8.2.1 Softening behaviour of the Fe-30Ni-0.044wt. % Nb steel

The softening behaviour has been monitored for the Fe-30Ni-0.044 wt. % Nb steel by measuring the hardness after different annealing times. Hardness change during recrystallisation in the absence of precipitation is determined by competition between the elimination of the deformed substructures and grain refinement [11, 153]. It has been reported in chapter 3.2 that strain induced precipitation can occur during recovery and recrystallisation, which leads to the retardation in softening as well as a potential increment in hardness from the precipitates. Therefore, a slower softening rate would be expected for the Nb containing model alloy compared to the Nb free alloy under the same conditions. It has been mentioned in chapter 6 that SIP was not detected in the cold deformed sample heated to the annealing temperature and then immediately quenched, which indicates that precipitation hardening is not expected during reheating.

Analysis of the hardness changes for precipitation has been carried out, this requires an assessment of how much effect precipitation may have on the hardness value. The precipitation hardening equation, i.e. Ashby-Orowan equation, is given as,

$$\Delta\sigma_y = \frac{0.13Gb}{\lambda}\ln\frac{r}{b} \quad \ldots 71$$

Where G is the shear modulus, b is the burgers vector, λ is the precipitates interspacing, r is the precipitates radius.

Assuming the strain induced precipitates are spherical and uniformly distributed in the matrix, and taking $\Delta\sigma_y = 3Hv$, the relationship between the precipitate size and the hardness increment caused by precipitation hardening at various interspacing, i.e. number density, can be estimated, Figure 8- 3. The precipitates interspacing, i.e. 50-200 nm, has been chosen based on literature results [47, 148, 160] and the TEM observations, which will be discussed in the following section. The relationship between number density and interspacing can be estimated by using the equation:

$$N = \frac{1}{\lambda^3} \quad \ldots 72$$

The standard deviations for the hardness measurement on the cold deformed and annealed samples were between 3 and 5, as discussed in chapter 6. Therefore, if the hardness value at a later time is higher than the previous data points by over 5, it suggests that the strain induced precipitation has occurred.

If there is no softening occurring, by using hardness measurement the size and number density of strain induced precipitates that are expected to show an increase in hardness (i.e. increment above 5) can be determined, Table 8-1; for example when the size is greater than approximately 2 nm at 200 nm spacing with a number density of 1.2×10^{20} m^{-3}, i.e. 0.09 % of the equilibrium precipitation.

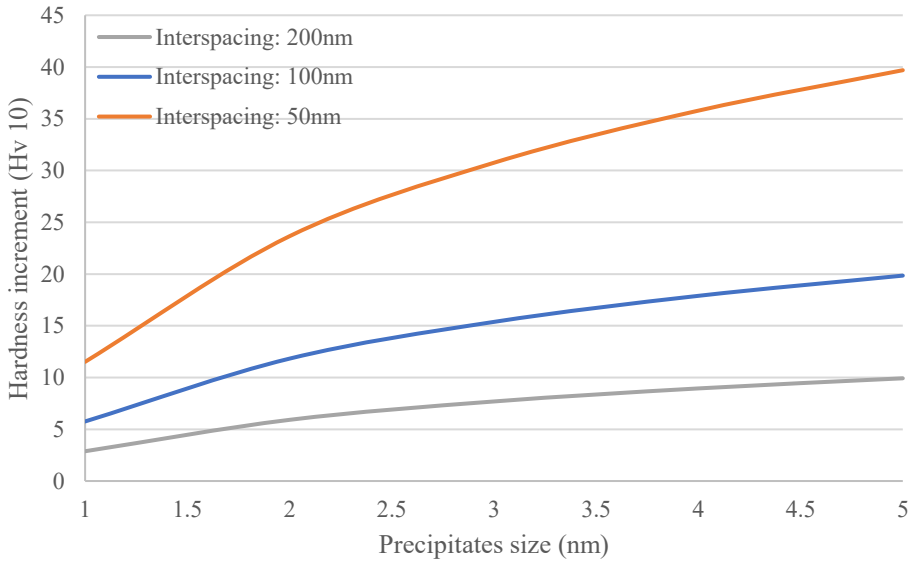

Figure 8-3 Predicted hardness increment caused by strain induced precipitation with various interspacing and size

Table 8-1 Summary of the precipitation hardening prediction

Ppt interspacing (nm)	Ppt number density ($/m^3$)	Ppt size at hardness increment of 5	Ppt fraction
200	1.2×10^{20}	2	0.09 %
100	1×10^{21}	1	0.09 %
50	8×10^{21}	-	-

However, using macroscopic hardness measurement as an indication of precipitation requires great caution, especially at low Nb content and low strain levels. This is due

to interference from the softening mechanisms during precipitation, i.e. recovery and recrystallisation. That is, the hardness measurement might not reflect the presence of strain induced preicpitates when softening occurs simultaneously. Therefore, the threshold for the hardness measurement to detect strain induced precipitation could be significantly higher due to recovery.

The absolute hardness values of Nb free and Nb containing model alloy are shown in Figure 8-4. It can be seen that no significant precipitation hardening has been observed (hardness increment >5) at temperatures 950 - 850 ºC, 0.3 strain. It is worth noting that the hardness values decrease at a much slower rate for the Nb-containing model alloy compared to the Nb free alloy at 900 ºC, which suggested a slower recovery process attributed to either/ both solute drag or/ and precipitation.

No significant precipitation hardening is suggested before recrystallisation within the temperature range of 950 – 850 °C at 0.2 and 0.3 strain, as the initial softening due to recovery is similar between the two steels (with and without Nb additions). It also should be noted that the hardness change is insufficient to determine the extent of precipitation as very fine or widely dispersed precipitates are not expected to give rise to a significant hardness increase. Therefore, from the softening curves, it is not possible to distinguish whether the delay in the onset of recrystallisation is due to the solute drag effect or also precipitation pinning from very fine / dispersed precipitates.

As a result, hardness measurement is insufficient to determine whether strain induced precipitates are present in this case. TEM observation for strain induced precipitates have therefore been used to investigate the precipitation kinetics, which will be discussed in section 8.2.3. The softening behaviour discussion below is to investigate the softening / recrystallisation kinetics in the Nb containing model alloy.

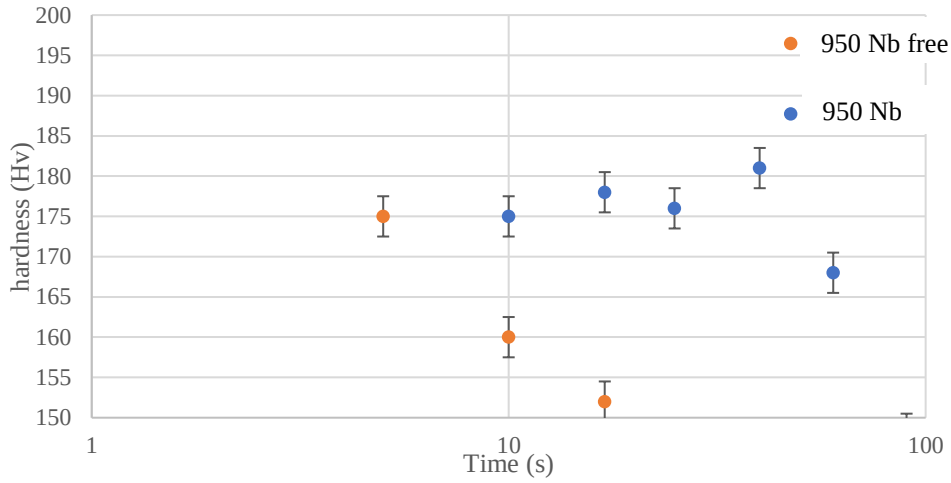

(a)

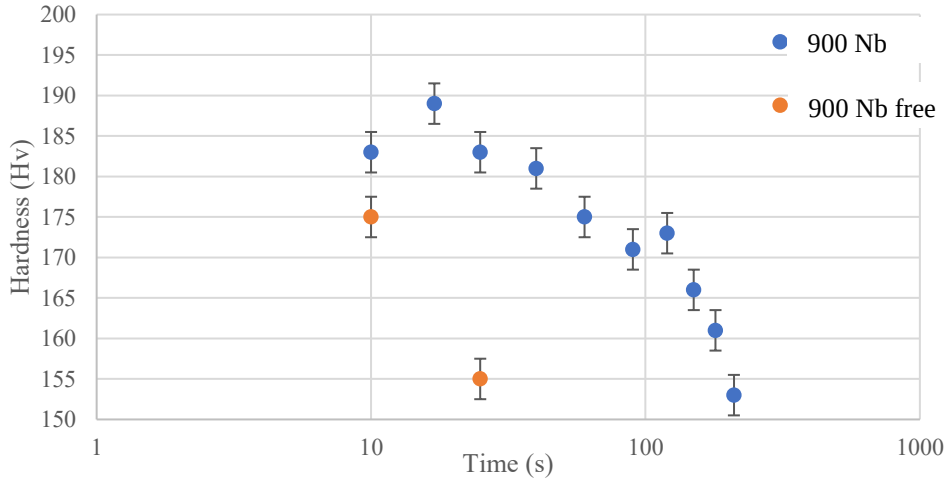

(b)

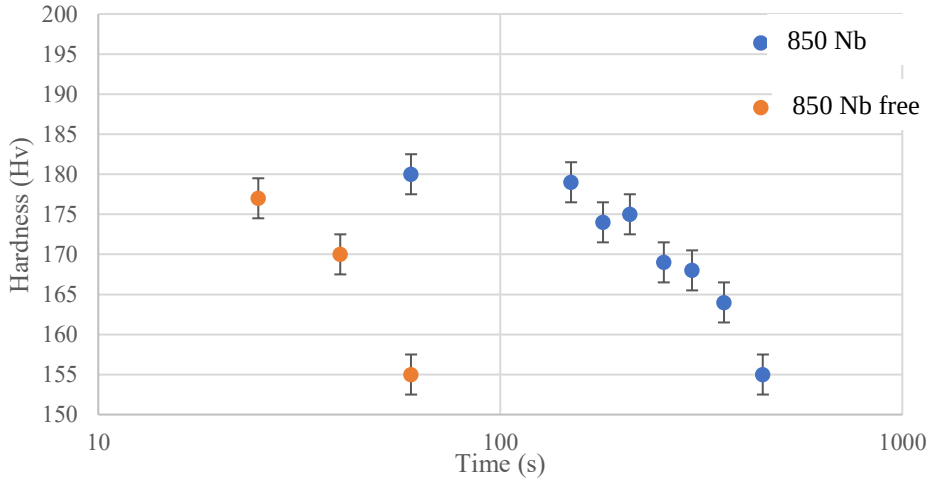

(c)

Figure 8-4 The hardness values for the 0.044 wt. % Nb and Nb free samples after 0.3 cold strain and annealing at different temperatures

The softening curves for both 0.3 and 0.2 strain (cold deformed) are shown in Figure 8-5. It can be seen that a significant fraction of hardness decrease occurs during the first 10 seconds of annealing under all conditions (where measured), which is expected to be due to recovery during reheating, as was observed for the Fe-30Ni Nb free samples, discussed in section 7.3. The softening curves for the Fe-30Ni-0.044 wt. % Nb samples then show a plateau region after the initial softening due to recovery before the onset of recrystallisation, which was not seen for the Nb free steel, indicating that the recrystallisation nucleation process has been delayed by the Nb addition.

From Figures 8-5 it can be seen that the slopes of the softening curves after the plateau region (i.e. the softening associated with recrystallisation) are comparable between the Nb containing and Nb free samples at 950 °C, 0.3 strain and 950 – 850 °C at 0.2 strain. This indicates that any precipitation hardening has not affected the softening curve. Whereas a sluggish onset of the softening curve can be observed at 900 °C at 0.3 strain (i.e. lower slope initially), and a decrease in softening rate (overall lower slope) is shown at 850 °C at 0.3 strain for the Nb containing steel. The decreased softening rate indicates that the Avrami exponent has been affected by the Nb addition; optical metallography was carried out to confirm the decreased recrystallisation rate and is discussed in section 8.2.2. Therefore, from the softening curve comparisons it is suggested that the Nb addition has delayed the onset of recrystallisation under the conditions mentioned above and had an effect on the recrystallisation rate under some conditions (higher strain and lower temperature in the range examined). The results also indicate that the recrystallisation rate was decreased rather than halted completely due to the presence of SIP for the steel and conditions examined.

It is unclear exactly why the Nb containing model alloy shows a variation in the Avrami exponent with changing temperature. Therefore, further examination of the effect of SIP on the recrystallisation kinetics was carried out.

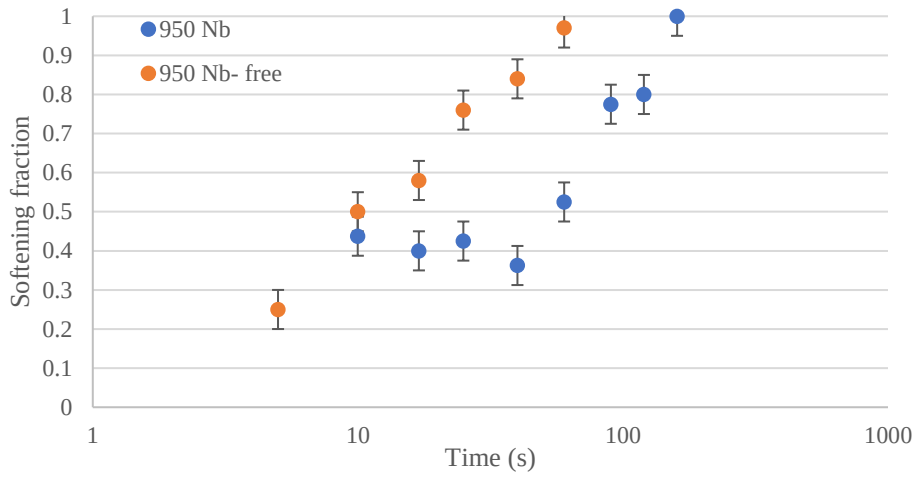
950 Nb
950 Nb- free
Softening fraction
Time (s)
0
0.1
0.2
0.3
0.4
0.5
0.6
0.7
0.8
0.9
1
1
10
100
1000

(a)

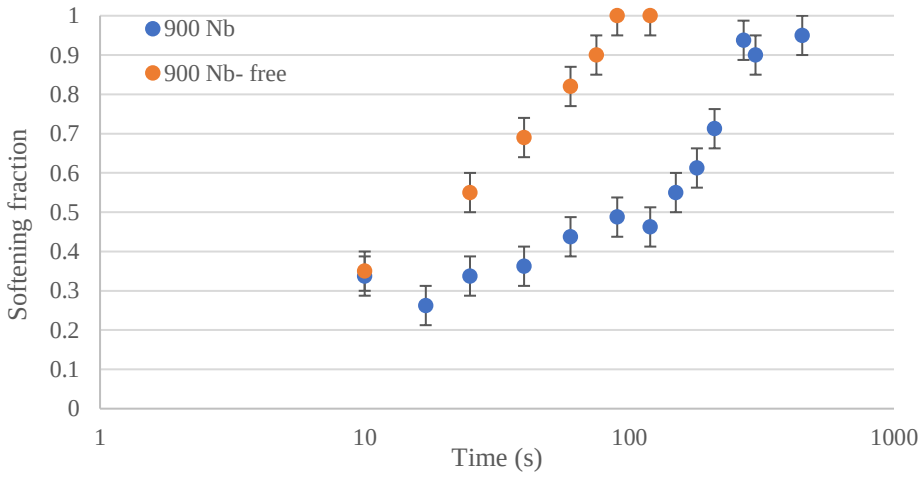
900 Nb
900 Nb- free
Softening fraction
Time (s)
0
0.1
0.2
0.3
0.4
0.5
0.6
0.7
0.8
0.9
1
1
10
100
1000

(b)

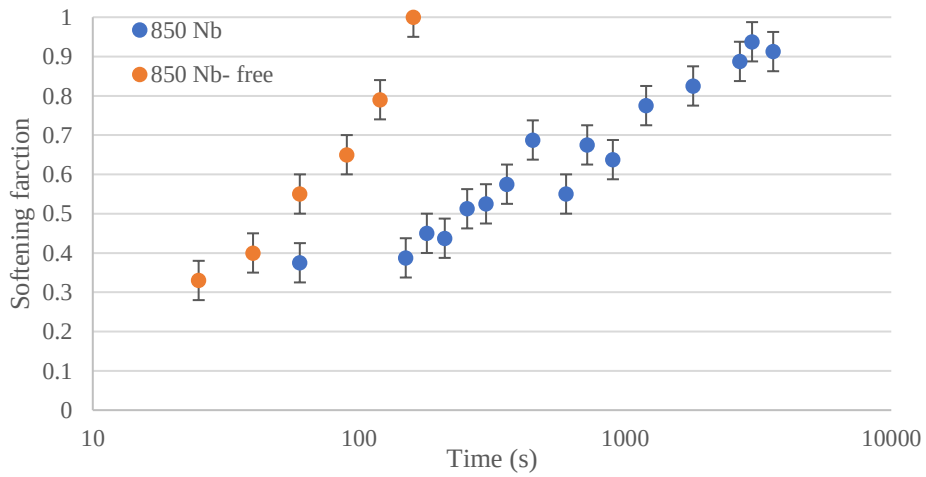
850 Nb
850 Nb- free
Softening farction
Time (s)
0
0.1
0.2
0.3
0.4
0.5
0.6
0.7
0.8
0.9
1
10
100
1000
10000

(c)

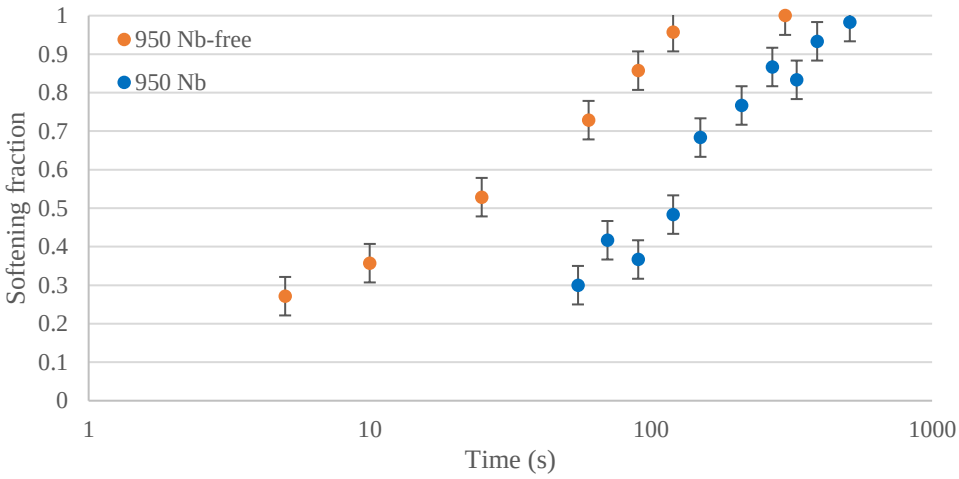

(d)

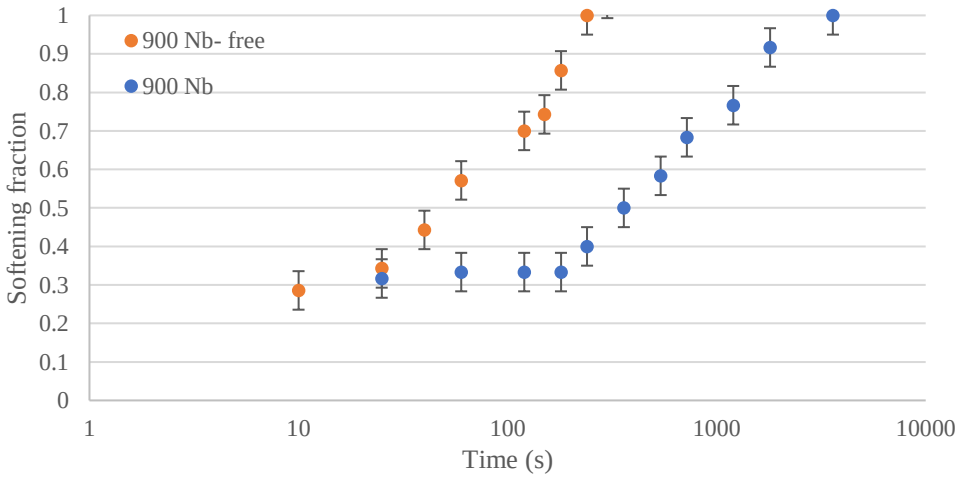

(e)

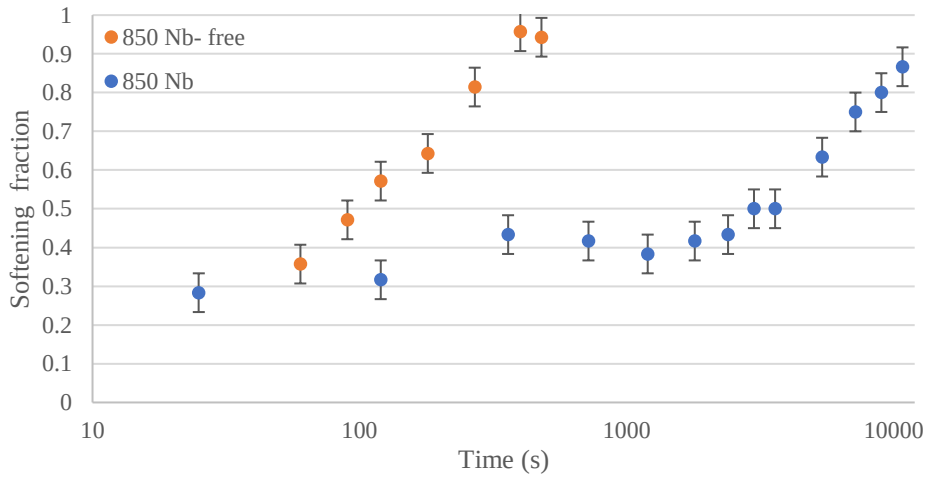

(f)

Figure 8-5 Softening behaviour of 0.044 wt. % Nb and Nb free samples after 0.3 cold strain (a) (b) (c); 0.2 cold strain (d) (e) (f)

8.2.2 Recrystallisation kinetics of Fe-30Ni-0.044wt. % Nb steel

To determine the recrystallisation kinetics for the Fe-30Ni-0.044 wt. % Nb alloy, determination of the recrystallisation fraction was carried out by the point counting method, as discussed in chapter 5.4. The resulting data points have been fitted with a JMAK model via the double log method, which has been discussed in the literature review in section 2.4.3. The use of recrystallised fraction from optical images to determine the Avrami exponent avoids any concerns that precipitate strengthening may have affected the softening curves presented earlier to ensure that the suggestions that SIP has affected the recrystallisation rate for 850°C, 0.3 strain is correct. The recrystallisation evolution for the Fe-30Ni-0.044 wt. % Nb steel within the temperature range of 950 - 850 °C at strains of 0.3 and 0.2 are shown in Figures 8-6, 8-7 and 8-8. Figure 8-6 (a) shows the deformed, elongated grain microstructure at 950 °C, 0.3 strain at 25s. Figure 8-6 (b) (c) (d) show a mix of recrystallised grains and deformed grains in samples heat treated at 40s and 120s, and a fine, equiaxed grain morphology observed at 160s. Figure 8-6 (c) shows a region where the coarser grains recrystallise slower compared to the finer grains, as indicated by the unrecrystallised coarse grain that is arrowed, similar to what was observed for the Nb free steel, discussed in section 7.2.1.

Figures 8-7 and 8-8 show the partially recrystallised microstructures at 0.3 strain and 0.2 strain after annealing at 900 and 850 °C respectively. It clearly shows that recrystallisation proceeded under these conditions. The recrystallisation curves of the Fe- 30Ni-0.044 wt. % Nb steels under these conditions are shown in Figure 8-9, and the recrystallisation starting and finishing times are listed in Table 8-2. The experimental results show that 85 % recrystallisation has completed within the temperature range of 950- 850 °C for the annealing times used showing that precipitation does not halt recrystallisation. Recrystallisation also proceeded after 0.2 strain, 950- 850 ºC. A delay in recrystallisation starting time caused by the Nb addition (compared to measurements for the Nb free condition, Table 7-1, 7-2) has also been observed under these conditions. It suggests that the Nb addition causes an order of magnitude delay in time of the onset of recrystallisation.

Table 8-3 summarises the predicted (based on the approach discussed in chapter 7.5 taking the grain size distribution into consideration) and the measured Avrami

exponents for the Nb containing steel. It can be seen that the Avrami exponent predictions fit well with the experimental data except for the condition of 850 °C, 0.3 strain where the Avrami exponent is lower than predicted. This suggests that the presence of Nb (either acting via solute drag or SIP) has no effect on the Avrami exponents (although it affects recrystallisation nucleation as evidenced by the delay in the recrystallisation start temperature) except for the condition of 850 °C, 0.3 strain. Therefore the role of Nb appears different at this condition.

Whilst there have been many reports in the literature on Nb affecting the recrystallistion kinetics through the formation of SIP in both cold deformed and annealed and hot deformed samples there is limited information on the conditions (precipitate size and number density) where the Avrami exponent is affected. Therefore TEM characterisation of strain induced precipitates has been carried out to examine the precipitation kinetics of NbC with respect to time and temperature for the 0.3 strain samples where a change in Avrami exponent has been observed.

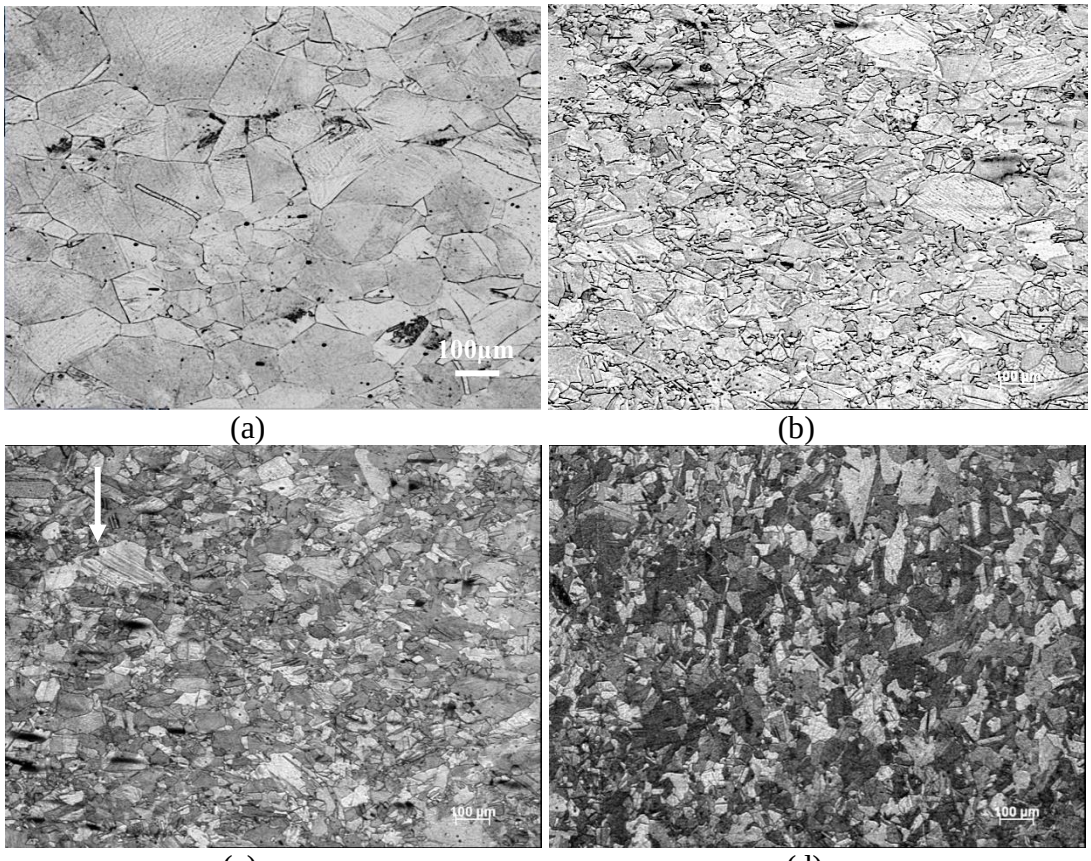

Figure 8-6 Microstructure evolution during recrystallisation of Fe-30Ni- 0.044 wt. % Nb at 0.3 strain, 950 °C (a) 25s, elongated grains are seen (b) 40s (c) 120s (d) 160s

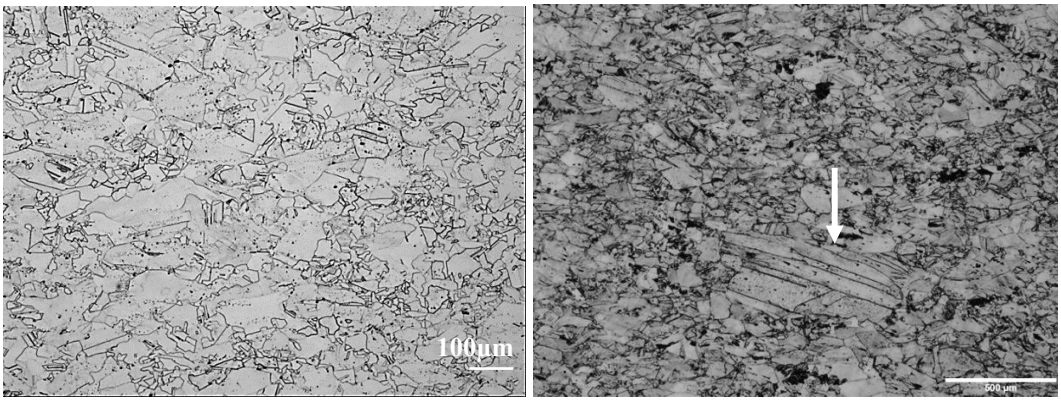

(a) (b)

Figure 8-7 Microstructure evolution during recrystallisation of Fe-30Ni- 0.044 wt. % Nb at 0.3 strain (a) 210s at 900 °C, (b) 450s at 850 °C

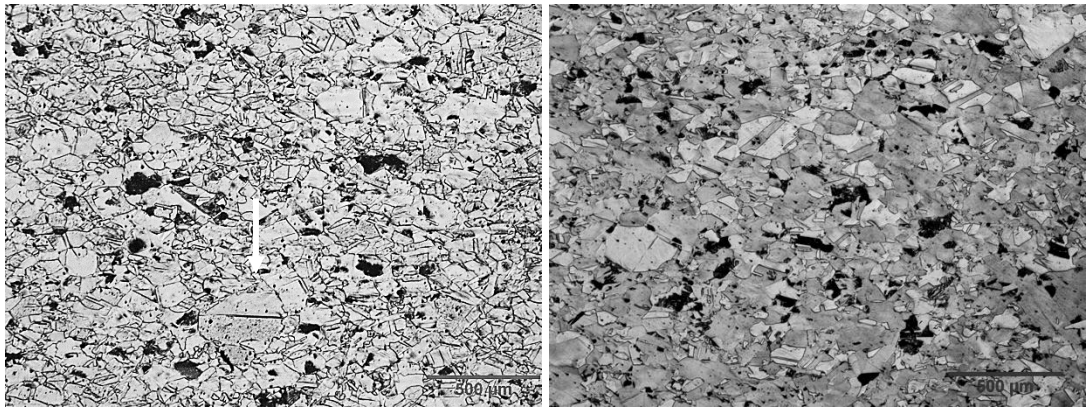

(a) (b)

Figure 8-8 Microstructure evolution during recrystallisation of Fe-30Ni- 0.044 wt. % Nb at 0.2 strain (a) 720s at 900 °C, (b) 5400s at 850 °C

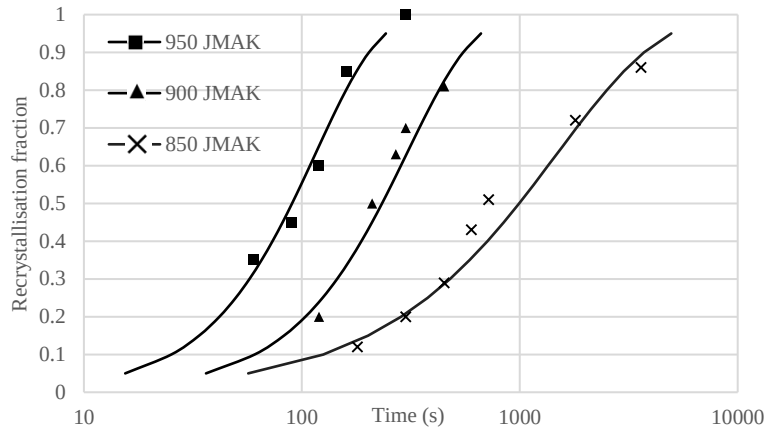

(a)

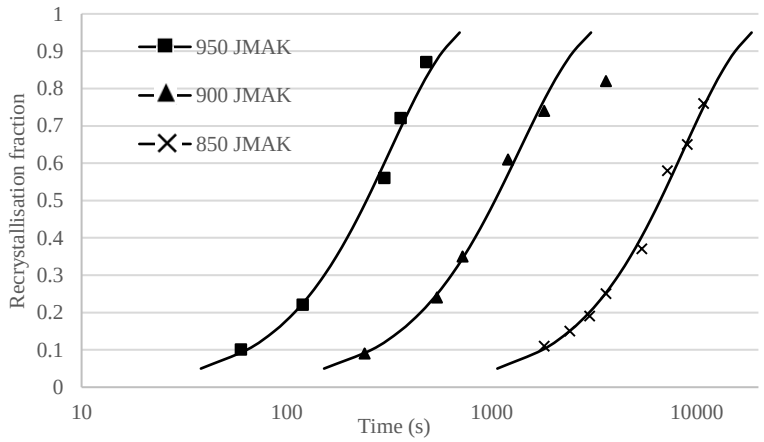

(b)

Figure 8-9 Recrystallisation kinetics of Fe-30Ni -0.044wt% Nb at (a) 0.3 strain (b) 0.2 strain

Table 8-2 Summary of the JMAK fitted recrystallisation starting and finishing time based on the experimental data

Temperature (°C)	Strain	Experimental R_s (s)	Experimental R_f (s)
950	0.3	15	178
900	0.3	36	479
850	0.3	57	3000
950	0.2	38	503
900	0.2	152	2179
850	0.2	1066	13441

Table 8-3 Summary of Avrami exponents under different conditions

Temperature (°C)	Nb content (wt. %)	Strain	Predicted n value	Experimental n value
950	0 (Nb free steel)	0.3	1.3	1.2
950	0.044	0.3	1.4	1.4
900	0 (Nb free steel)	0.3	1.3	1.3
900	0.044	0.3	1.4	1.4
850	0 (Nb free steel)	0.3	1.3	1.4
850	0.044	0.3	1.4	0.9
950	0 (Nb free steel)	0.2	1.3	1.3
950	0.044	0.2	1.4	1.4
900	0 (Nb free steel)	0.2	1.3	1.4
900	0.044	0.2	1.4	1.3
850	0 (Nb free steel)	0.2	1.3	1.3
850	0.044	0.2	1.4	1.4

8.2.3 NbC precipitates characterisation

TEM thin foil examination has been performed to investigate the NbC precipitation behaviour after cold deformation at 0.3 and 0.2 strain and annealing via conventional and scanning transmission electron microscopy. The strain induced precipitates have been observed at 850 °C, 0.3 strain in Figure 8-10; 900 °C, 0.3 strain in Figure 8-11; 950 °C, 0.3 strain in Figure 8-12. EDS mapping has been carried out on these samples to confirm that the observed precipitates are NbC, Figure 8-13. Strain induced precipitation has been observed at the early stage of recrystallisation within the temperature range of 850- 950 °C, 0.3 strain. At 950 °C, the strain induced precipitates could be seen at 25s, (less than 10% of recrystallisation). SIP was observed for the 20% recrystallisation at 900°C, 120s sample and in the sample with less than 10% recrystallisation at 850°C, 120s. In terms of 0.2 strain, SIP was seen in the sample with 22 % of recrystallisation at 950°C, 120s.

It can be seen from these images that the SIPs are distributed in a localised fashion on the subgrain/ dislocation structures. This is due to the strain induced precipitation nucleation sites being mainly on the austenite subgrain boundaries. Figure 8-14 shows the recovered microstructure prior to recrystallisation for the sample after holding at

950 °C for 25s. The dislocation network can also be seen within each individual subgrain. The size of the subgrains is approximately 1-2 μm in diameter, which agrees well with the EBSD results for the recovered microstructure of the Nb free alloys (shown in Figure 7-11). It is worth noting that the diameter of these cell-like structures is approximately 0.1 μm in diameter, which is significantly smaller than the critical recrystallisation nucleus size stated in the literature and observed in this work. Therefore, it is suggested that the strain induced precipitates in this case have formed when the subgrains / dislocations cells were still very small, i.e. at the very early stage of recovery, prior to recrystallisation. It has been mention in section 8.2 that the interspacing for strain induced precipitates is between 50 – 200 nm, which agrees well with the experimental results, i.e. precipitation aligning in cell like structures of 100 nm diameter. Whilst the SIP have been observed to form during recovery they are very small (therefore have not caused any increment in hardness) and have not affected the extent of recovery (as did not change the degree of softening due to recovery). This agrees well with the literature that strain induced precipitation occurs at the very early stage of annealing in the cold deformed and annealed conditions.

The strain induced precipitate size distributions observed in the temperature range 950 - 850 °C after 0.3 strain have been summarised in Figure 8-15 and Table 8-4. The average precipitate size formed at higher temperature is much larger than at lower temperatures for the same holding time. It can be seen that the precipitate size increases significantly during the holding time from 25s to 120s for the recrystallisation temperature of 950 °C. The average strain induced precipitate size increased from 3 nm after 25s to 10 nm at 120s. Whereas, the average precipitate size was 5.2 nm at 900 °C and 4.3 nm at 850 °C for 120s, showing little coarsening with time, with growth being slow at 850 °C, that is, the average strain induced precipitate size only increased from 4 nm to 6 nm after holding at 850 °C for 3000s.

The precipitates size evolution at 0.3 strain within the temperature range of 950 - 850 °C is shown in Figure 8-16. It can be seen that the precipitation growth and coarsening rate increases with increasing temperature. The growth and coarsening rate were significantly slower at 850 °C, 0.3 strain than at 950 °C. The time dependence exponents were between 0.7 - 0.1 in this case. It can be seen that the extrapolated value

after reheating, i.e. 0s at isothermal holding, is between 0.4 - 2 nm, which is below the TEM detection limit for strain induced precipitates. This further indicates that there was little precipitation, i.e. very fine precipitate size, occurring during reheating. The number density shown in Table 8-6 also indicated the early onset of coarsening at the higher temperature, which could be attributed to the accelerated pipe diffusion [146]. In order to understand the precipitation coarsening more accurately, better understanding of the diffusion mechanisms during recrystallisation is required, which was not in the scope of the present study.

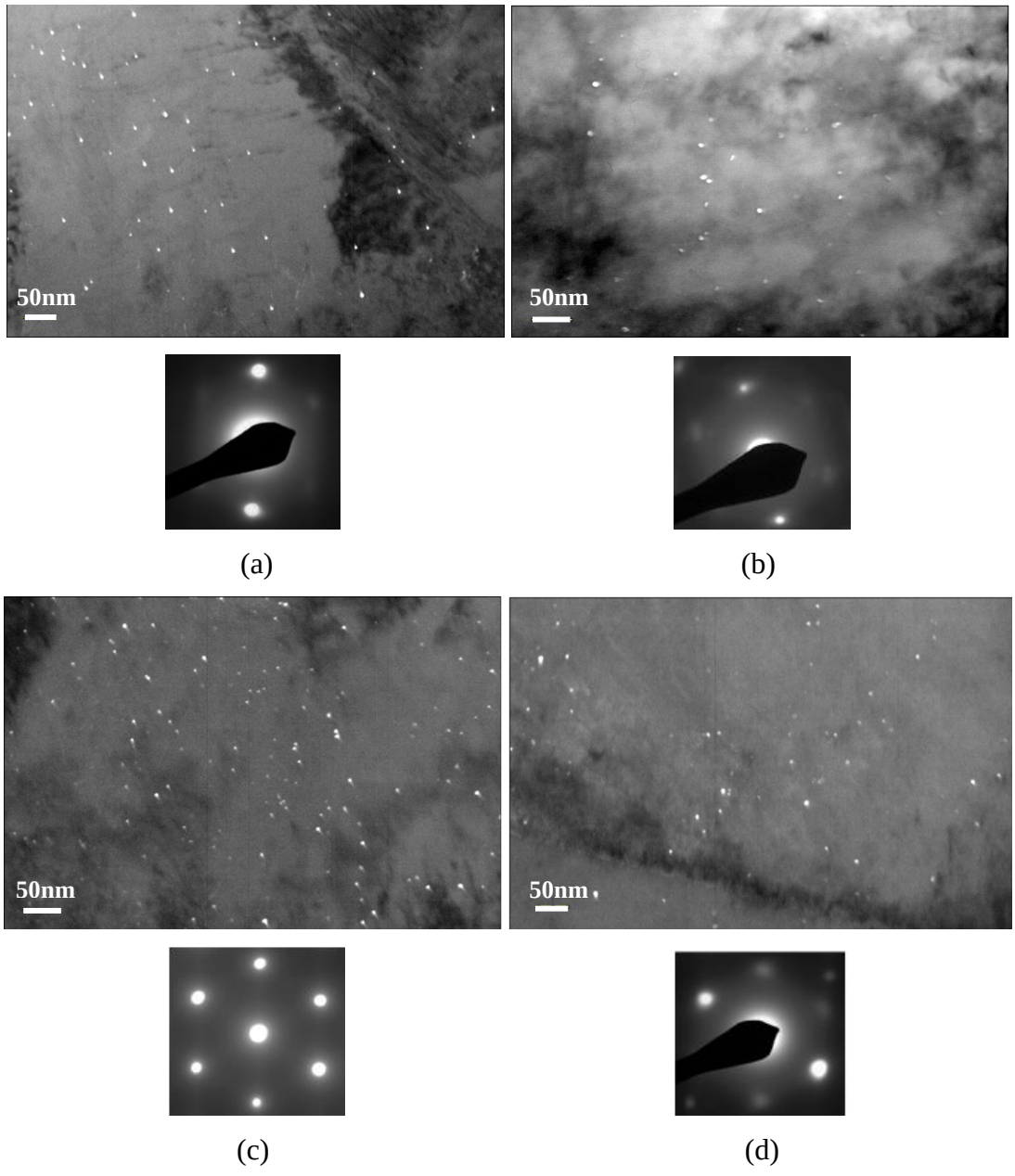

Figure 8-10 TEM dark field micrographs showing SIP in specimens deformed to 0.3 strain at room temperature and held at 850°C for (a) 120s (b) 600s (c) 1200s and (d) 3000s

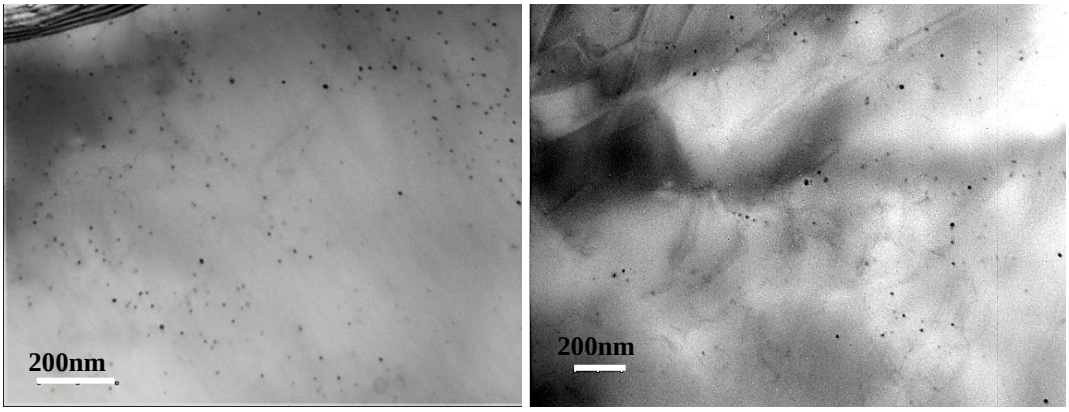

(a) (b)

Figure 8-11 TEM bright field micrograph showing SIP in specimens deformed to 0.3 strain at room temperature and held at 900°C for (a) 120s and for (b) 450s

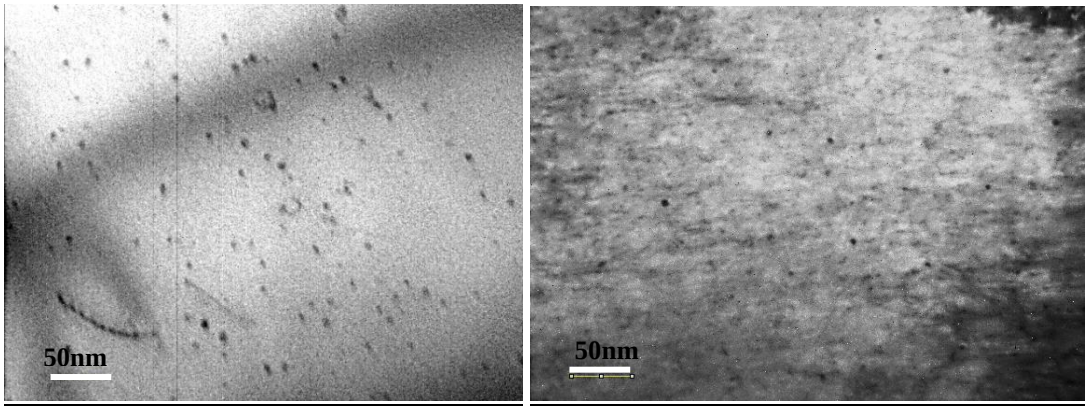

(a) (b)

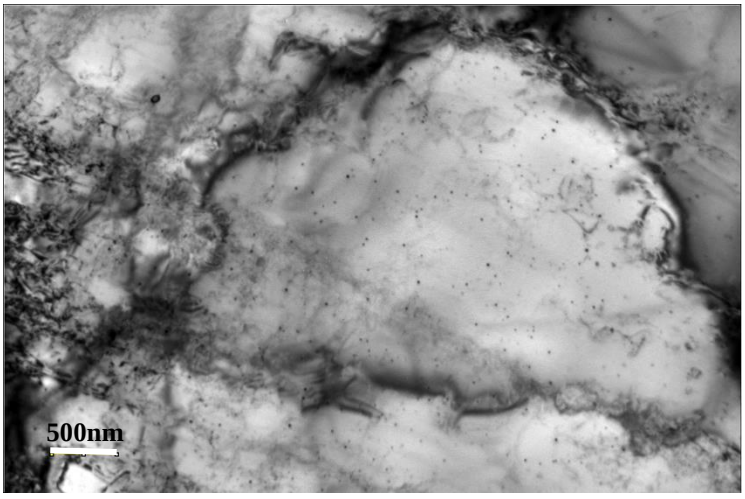

(c)

Figure 8-12 TEM bright field micrographs showing SIP in specimens deformed to 0.3 strain at room temperature and held at 950C for (a) 25s, (b) 60s and (c) 120s

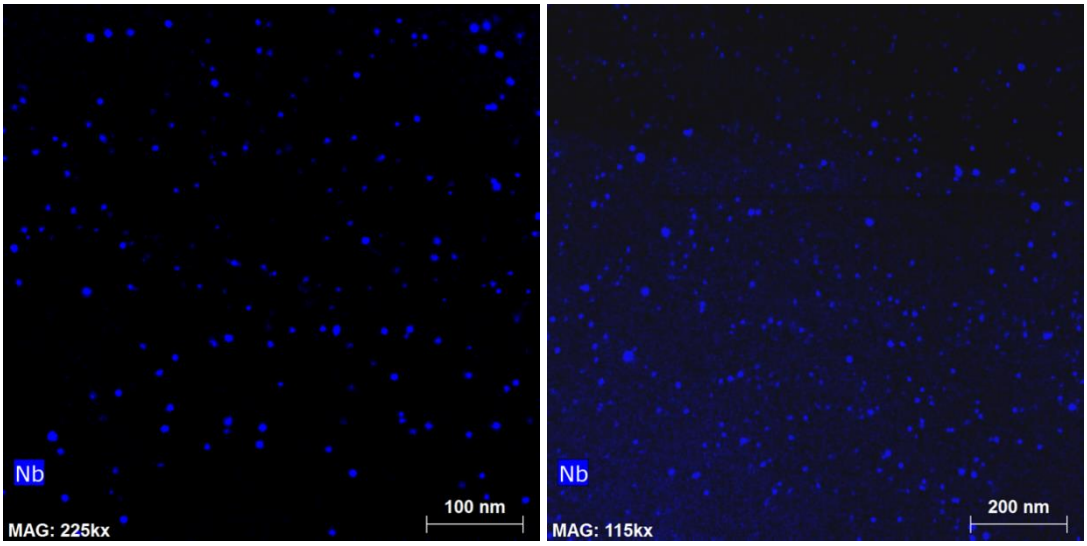

(a) (b)

Figure 8-13 EDX mapping of the specimens deformed at 0.3 strain, and annealed at 900 °C, 120s (a) and at 850 °C, 120s (b) showing the precipitates to be Nb rich.

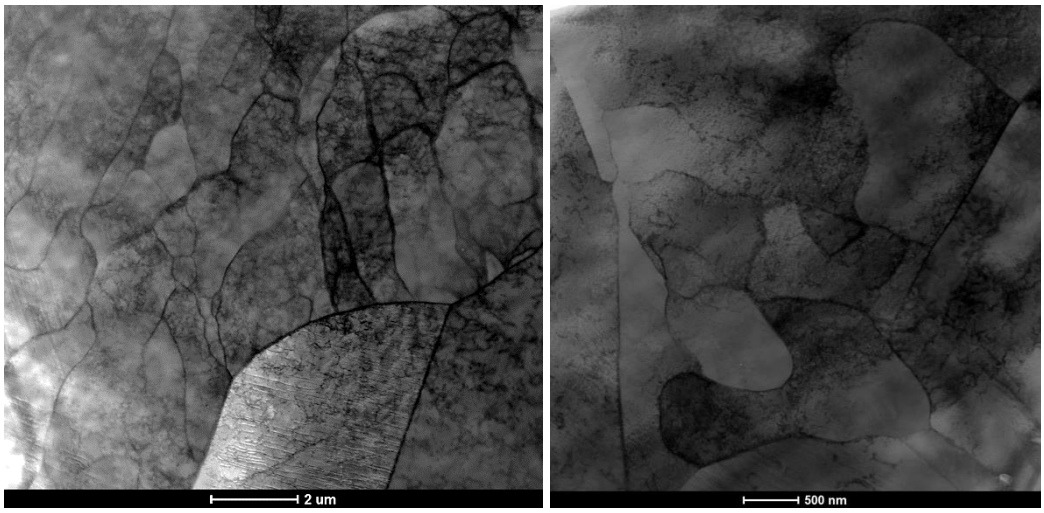

(a) (b)

Figure 8-14 Recovered microstructure in the Nb-microalloyed steel at 950°C, 0.3 strain, 25s. (a) lower magnification (b) higher magnification

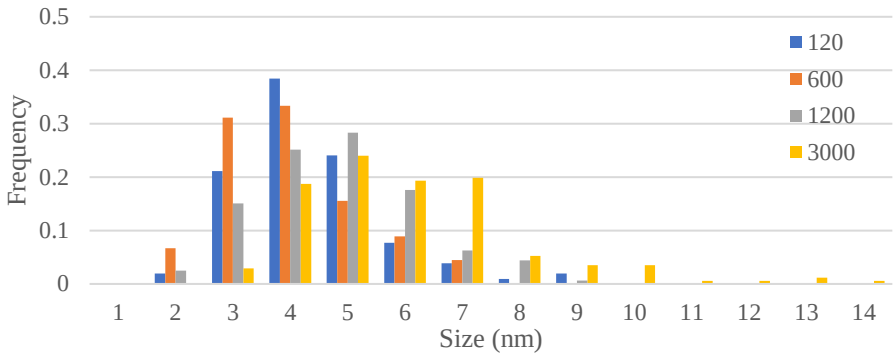

(a)

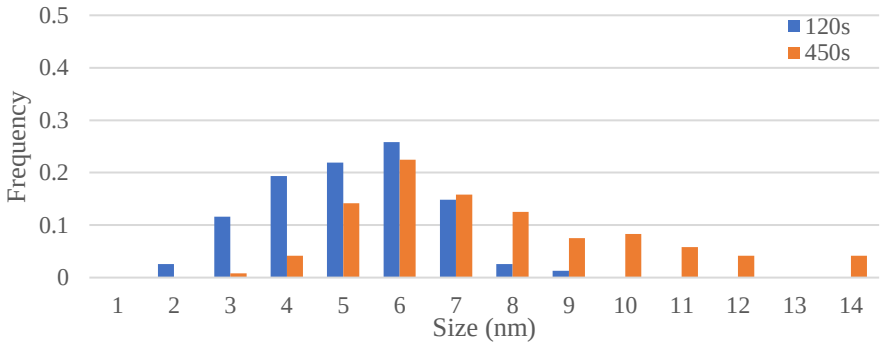

(b)

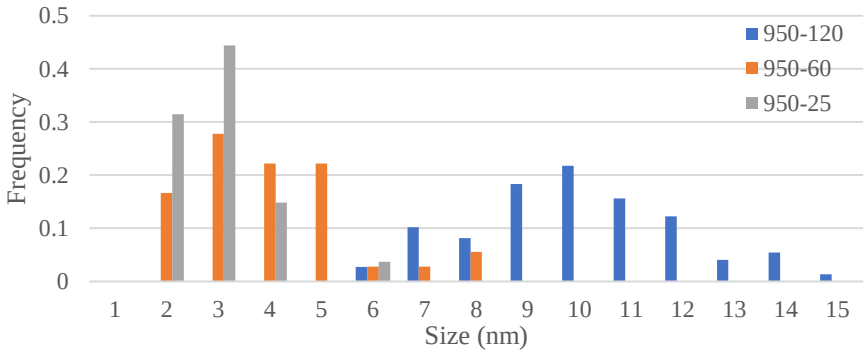

(c)

Figure 8-15 Strain induced precipitation size evolution after 0.3 strain at (a) 850 °C (b) 900 °C and (c) 950 °C

Table 8-4 Mean particle size for samples annealed at 950 - 850 °C after a cold deformation of 0.3 strain

Test temperature (°C)	Holding time (s)	No. of precipitates counted	Mean diameter (nm)	Standard deviation (nm)	95% Confidence limit (nm)
850	120	312	4.4	1.3	4.4± 0.2
	600	303	4.1	1.2	4.1± 0.3
	1200	327	4.8	1.4	4.8± 0.2
	3000	309	6.1	2	6.1± 0.3
900	120	351	5.9	1.5	5.9± 0.2
	450	306	8.5	2.5	8.5± 0.4
950	25	270	3.5	1.3	3.5± 0.3
	60	301	4.6	1.3	4.6± 0.4
	120	317	10.4	1.5	10.4± 0.2

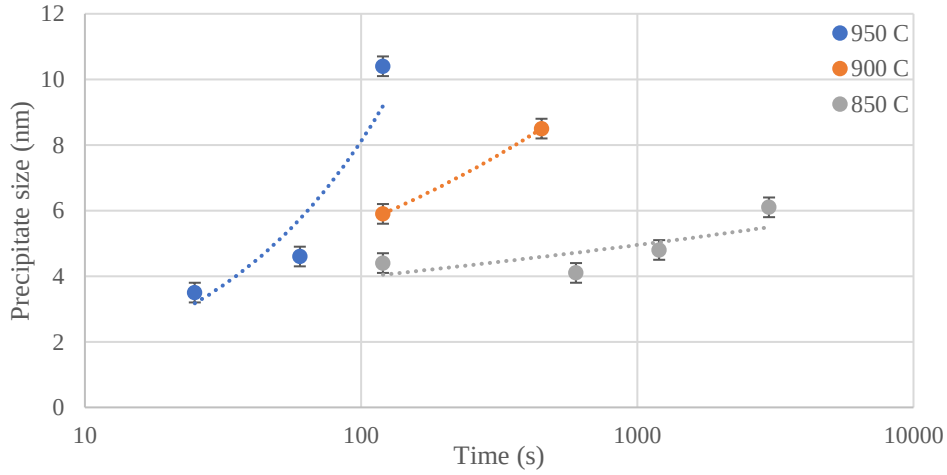

Figure 8-16 The experimental values of the strain induced precipitation size evolution

The number density of strain induced precipitates at 0.3 strain within the temperature range of 950 - 850 °C has been summarised in Table 8-5. The TEM foil thickness was measured via CBED technique, as discussed in chapter 5.6. It can be seen that the precipitate number density at 950 °C decreased from 3.15×10^{21} m^{-3} to 0.55×10^{21} m^{-3}. Whereas the precipitates at 850 °C showed no sign of significant coarsening as the number density did not change systematically, being in the range 1.34×10^{21} m^{-3} to 3.63×10^{21} m^{-3}. Therefore, combining the precipitate size distribution and the number density evolution, it can be confirmed that strain induced precipitation coarsening occurred at both 950 °C and 900 °C during recrystallisation, yet little coarsening has been observed at 850 °C during recrystallisation.

The results suggests that both Nb solute atoms and Nb (C, N) precipitates are present in the matrix at the early stage of recrystallisation within the temperature range of 950 - 850 °C. The results also show that coarsening, i.e. a decrease in number density, started when the precipitates reached approximately 4.6 – 4.8 nm in size. That is, it shows that the strain induced precipitation coarsening occurs before reaching equilibrium fraction.

Table 8-5 Number density of Nb(C, N) strain induced precipitates at 0.3 strain annealed at temperature 950- 850 °C for various times

Temperature (°C)	Time (s)	Size (nm)	Number density ($\times 10^{21}$/ m^3)	Volume fraction	Equilibrium percentage
950	25	3.5	3.15	0.000095	33 %
	60	4.6	2.24	0.000197	68 %
	120	10.4	0.55	0.00027	100%
900	120	5.9	1.05	0.00011	26 %
	450	8.5	0.8	0.00026	63 %
850	120	4.4	1.34	0.000059	12 %
	600	4.1	2.28	0.000078	16 %
	1200	4.8	3.63	0.00021	44 %
	3000	6.1	2.85	0.00033	69 %

8.2.4 Effect of Nb on recrystallisation kinetics

It has been shown above that the strain induced precipitates were present prior to the onset of recrystallisation. Therefore, the delay of onset of recrystallisation could be caused by both solute drag and precipitation pinning.

It has been well recognised that the presence of precipitates during and after deformation reduces the grain boundary migration rate [135, 138, 163, 179, 180]. Additionally, grain boundary migration accelerates the precipitation growth rate as the Nb solute atoms segregate to grain boundaries to lower interfacial energy [9] and dislocation networks and moving boundaries accelerate the coarsening rate of precipitation by pipe diffusion [181]. To account for the effect of precipitates pinning on recrystallisation kinetics, the pinning force has been calculated. Zener pinning has been discussed in chapter 3.5, and from the results presented in this chapter, it can be seen that the strain induced precipitates were heterogeneous nucleated on the dislocation nodes and/or the subgrain boundaries. Therefore, to estimate the pinning force, an assumption is made that all strain induced precipitates lie on the subgrain boundaries. Then, the pinning force is given as [91],

$$F_p = \frac{3\gamma f \bar{l}}{2\pi r^2} \quad \ldots 73$$

Where γ is the interfacial energy, f is the volume fraction of the strain induced precipitates, r is the radius of the strain induced precipitates and $\bar{l}$ is the subgrain boundary intercept, which is 0.5×10^{-7} m in this case, taken as the average value measured from Figures 8-10 to 8-14.

The reason that the presence of precipitation does not correlate to a cessation in recrystallisation could be due to an insufficient pinning force by the strain-induced precipitates within the temperature range 950 - 850 ºC and Nb level of 0.044 wt.%. If the strain induced precipitation occurs before the onset of recrystallisation, then the retardation of recrystallisation could be reflected by the increasing recrystallisation activation energy. Nevertheless, if strain induced precipitation nucleation and growth occur during recrystallisation, then the recrystallisation could be halted or continue at a decreased rate, and the Avrami exponent would decrease as a consequence.

The estimated local pinning force is shown in Table 8-6 for the samples after 0.3 strain. It can be seen that the local pinning force at 950 °C is 0.28 MPa compared to 0.1 MPa at 850 °C at the onset of recrystallisation, and the pinning force decreases dramatically at 950 °C, 120s to 0.14 MPa. The pinning force at 950 °C was insufficient to stop recrystallisation, but delayed the onset of recrystallisation, as seen in figure 8-4 (a). At 900 °C, the strain induced precipitates are also already present at the onset of recrystallisation, i.e. 120s, 20% of recrystallisation, leading to a sluggish onset of recrystallisation. However at 850 °C, the pinning force increased with increasing time attributed to the slow precipitation growth rate at 850 °C up to 3000s. That is, the recrystallisation rate decreased with time at 850 °C, which led to a decrease in Avrami exponent. The relationship between the pinning force and the softening rate is shown in Figure 8-17. Decreasing recrystallisation rate caused by the increasing pinning force has been clearly shown at 850 °C, 0.3 strain. Also the delay in the onset of recrystallisation attributed to the initial presence of precipitation pinning and solute drag at 950 °C, 0.3 strain is shown.

As a result, the pinning force at 5% precipitation is likely to exceed the recrystallisation driving force due to the high number density of precipitates, and the pinning force is expected to remain high due to there being sufficient Nb in solution and a fine precipitates size to give growth rather than coarsening. Whereas at low Nb and strain level, i.e. 0.044 wt.% Nb and 0.3 strain in this case, the coarsening of precipitates occurs considerably faster than at higher strain levels, therefore the pinning force might not be sufficient to halt recrystallisation but slow down the recrystallisation kinetics. Additionally, if precipitates growth and coarsening continues during recrystallisation, the Avrami exponent would also be affected due to the changes in net driving force of recrystallisation. If coarsening occurs quickly enough, the Avrami exponent would be the same as the Nb free case and then recrystallisation rate is unaffected due to the drastic decrease in the initial pinning force. Therefore, the growth and coarsening mechanism of precipitates also need to be taken into consideration.

That is, the recrystallisation rate was decreased significantly at 1200s at 850 °C, 0.3 strain, and the measured pinning force at this point is 0.26 MPa. Additionally, no obvious change in Avrami exponent has been observed at 950 - 900 °C even though

the strain induced precipitates presented during recrystallisation. This is due to the low pinning force during recrystallisation at these two conditions, i.e. 0.1 - 0.14 MPa.

Therefore, it can be seen that the strain induced precipitates can slow down the recrystallisation kinetics when the pinning force is not sufficient to halt recrystallisation completely. In this case, the effective pinning force to slow down the recrystallisation is 0.26 MPa, approximately half of the driving force of recrystallisation. Additionally, it is worth noting that both number density and precipitate size are crucial to affect the recrystallisation kinetics. The effective pinning force to retard recrystallisation is strongly dependent on the stored energy level. The pinning force mentioned above therefore could be different for different strain levels, also different deformation temperatures, i.e. cold an hot deformation.

Additionally, it has been mentioned that both Nb atoms and NbC exist in the matrix before and during recrystallisation. Therefore, the effect of solute drag also needs to be considered. As mentioned in chapter 2.4.4.5, solute drag can be estimated by the SRP parameter, which was developed when strain induced precipitates do not present in the matrix.

Zurob's approach for modelling the solute drag effect has been considered in this case. Zurob mentioned that the boundary mobility is affected by the Nb content level in solution [83], which is given as (see discussion in chapter 2.4.4.5),

$$M(t) = (\frac{1}{M_{pure}} + \alpha C_{Nb})^{-1} \quad \ldots 74$$

Where,

$$\alpha = \frac{\beta N_v (kT)^2}{E_b D} (\sinh\left(\frac{E_b}{kT}\right) - \frac{E_b}{kT}) \quad \ldots 75$$

$$M_{pure} = \frac{0.192}{T} \exp(\frac{-20837.14}{T}) \quad \ldots 76$$

In the equation, β is the grain boundary width (1 nm), N_v is the number of atoms per unit volume, k is the Boltzmann constant, E_b is the solute boundary binding energy (19.3 kJ/ mol), D is the bulk diffusivity of Nb in austenite (1.4×10^{-4}exp(-270000/RT)) and T is the temperature. These values are summarised by Dutta and Zurob [83, 124].

The recrystallisation growth rate G = MP, where M is the mobility and P is the net driving force of recrystallisation. Therefore the recrystallisation kinetics, as discussed in chapter 2.4, can be linked to the decreased mobility through solute drag.

Table 8-6 Number density of Nb(C, N) strain induced precipitates at 0.3 strain annealed at temperature 950 - 850 °C for various time

Temperature (°C)	Time (s)	Size (nm)	Number density ($\times 10^{21}$/ m^3)	Local pinning force (MPa)
950	25	3.5	3.15	0.28
	60	4.6	2.24	0.26
	120	10.4	0.55	0.14
900	120	5.9	1.05	0.12
	450	8.5	0.8	0.13
850	120	4.4	1.34	0.1
	600	4.1	2.28	0.16
	1200	4.8	3.63	0.3
	3000	6.1	2.85	0.3

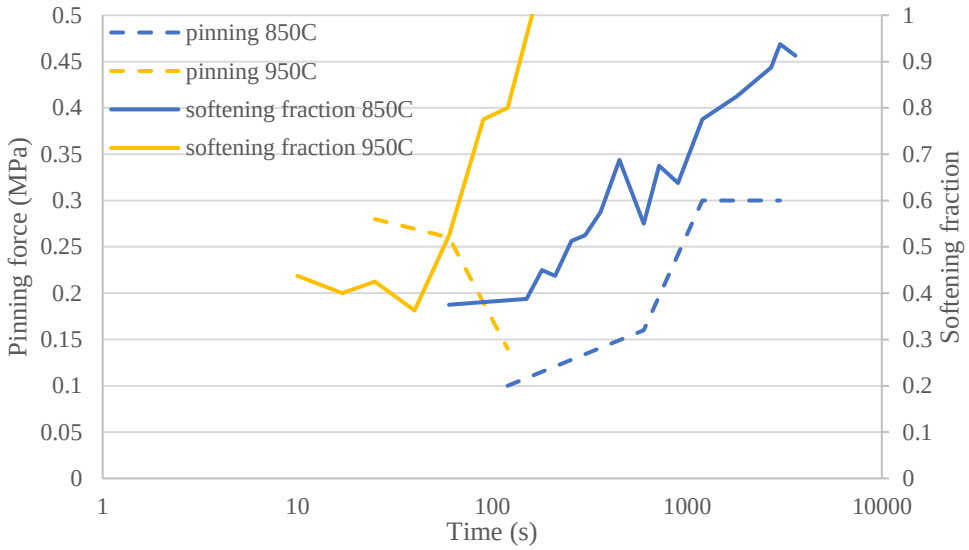

Figure 8-17 Pinning force and softening fraction comparison for samples deformed at 0.3 then annealed at 950 °C and 850 °C

It has been shown in Table 8-7 that approximately 80% of Nb atoms are still in solution at 20% of recrystallisation at 950 - 850 °C, 0.3 strain. Therefore, it is not unreasonable to assume that at least 80% of Nb is still in solution at the onset of recrystallisation. Then the mobility of the grain boundary at each temperature can be calculated. The predicted delayed recrystallisation starting time caused by solute drag has been calculated. It is worth noting that no strain induced precipitation pinning has been taken into account in this calculation. The effect of material composition and the grain size distribution has been taken into consideration by using the recrystallisation activation energy of 195 kJ/mol, strain exponent of -2.5 and the constant A value of 1.5×10^{-14} has been applied to calculate the recrystallisation starting time, as discussed in chapter 7. The results have been summarised in Table 8-7.

It can be seen that the proposed model shows reasonable good agreement with the results using Zurob's approach for the effect of solute drag on recrystallisation kinetics. However, when strain induced precipitation occurs, the solute drag term has to be applied with caution. The reasons are explained as follows.

Firstly, it has been mentioned in the literature that the solute drag force is dependent on the boundary migration rate [83]. The empirical model proposed by Jonas and

Yamamoto was fitted when no precipitates were present and the boundary migration rate is significantly slower when strain induced precipitates are present.

Secondly, the solute drag effect is also affected by the solute concentration along the moving boundary and in the matrix, also the diffusivity of the solutes in and near the grain boundary [82, 83]. When precipitation occurs, the Nb level in the matrix decreases leading to a decreased solute drag effect. Also, strain induced precipitates could either grow / dissolve or coarsen at the recrystallisation interface, i.e. the moving grain boundary, due to its higher Nb level and the increased diffusivity [181]. Therefore, the concentration along the grain boundary and in the matrix is expected to be different when precipitates are present and growing / coarsening along the grain boundary.

In this case, only one Nb content level, i.e. 0.044 wt. %, has been used, and it has been shown to give a reasonable agreement with the Zurob's approach. However, it is not possible to discuss the validity of the solute drag term across a wide range of Nb concentration. Therefore, further investigation is required to examine the solute drag term.

Table 8-7 Effect of solute drag on boundary mobility and recrystallisation kinetics by using Zurob's approach

Temperature (°C)	M (predicted)	k (predicted)	Predicted retardation time by solute drag (s)	Actual retardation time (s)
950	1.1×10^{-12}	0.0048	6	12.8
900	0.4×10^{-12}	0.0012	18.4	31
850	0.1×10^{-12}	0.0002	93.2	42.6

Additionally, it has been mentioned in the previous section that the onset of recrystallisation has been further delayed due to the presence of strain induced precipitates. Therefore, a term has been added in the model Rs equation to take into account of the precipitation pinning. It was shown in chapter 2.4 that,

$$R_s = \left(\frac{\ln(0.95)}{k}\right)^{\frac{1}{n}}$$

Where, k= $-\frac{\pi N G^n}{3}$, G = MP. It can be seen that the recrystallisation starting time is then proportional to the driving force of recrystallisation, P.

Additionally, n value is related to the recrystallisation rate, the decrease in growth rate with time can be written as [1],

$$G(t) = At^m \quad \ldots 77$$

Then the value m can be calculated as,

$$m = \frac{\ln G}{\ln t} = \frac{\ln(F_{rex} - F_P)}{\ln t} \quad \ldots 78$$

Also, the solute drag term has been modified to fit the values predicted by Zurob's approach. Therefore, the modified model is given as,

$$n = \frac{3}{\ln(\frac{D_{0.9}}{D_{0.1}})^2} + \frac{\ln(F_{rex} - F_p)}{\ln t} \quad \ldots 79$$

Where F_{rex} is the recrystallisation driving force and F_p is the precipitation pinning force at the onset of recrystallisation, D is the initial grain size, ε is the strain. The Avrami exponent prediction is based on the individual grain size class approach, in this case, the change of recrystallisation growth rate with time has also been taken into account.

Assuming the pinning force is 0.25 MPa at the onset of recrystallisation at 950 °C and 900 °C, and the pinning force is 0.1 MPa at 850 °C, which is based on the observation of the precipitation kinetics discussed earlier. The driving force has been measured in chapter 6, which is 0.53 MPa. Then, the prediction by the modified recrystallisation starting time and the n value is shown in Table 8-8.

It can be seen in Table 8-8 that the predicted recrystallisation starting time and the Avrami exponents have significantly improved relative to the measured values.

Although the recrystallisation starting time at 850 °C is still over-predicted. This could be attributed to an overprediction in solute drag also the experimental error in estimating the strain induced precipitation pinning force.

Additionally, the proposed model is only applicable for the low Nb content (<0.044 wt. %) and strain level (<0.3). This is because recrystallisation will be halted if the precipitates pinning force exceeds the recrystallisation driving force.

Table 8-8 The recrystallisation starting time and Avrami exponent predicted

Temperature (°C)	Measured R_s (s)	Predicted R_s (s)	Measured n value	Predicted n value
950	15	12.6	1.4	1.5
900	36	38	1.3	1.3
850	57	85.9	0.9	1

8.3 Hot deformed conditions

8.3.1 Recrystallisation kinetics of Fe-30Ni- 0.044 wt.% Nb steel

The recrystallisation kinetics of Fe-30Ni-0.044 wt. % Nb has been studied in the hot deformed condition to validate the proposed theory for the effect of strain induced precipitation on recrystallisation kinetics. The samples were deformed to 0.45 - 0.35 strain at 950- 850 °C at a strain rate of 5 s^{-1}. Optical micrographic examination has been carried out to establish the recrystallisation kinetics of the model alloy, TEM was used to measure the strain induced precipitates size evolution. It has been mentioned in Chapter 7 that the hot deformed samples (0.3 strain) showed a considerably slower recrystallisation rate compared to the cold deformed samples attributed to the lower stored energy. Therefore, higher strains have been applied to examine the recrystallisation Avrami exponent after hot deformation.

The optical images after hot deformation at 950 °C, 0.35 strain are shown in Figure 8-18. It can be seen that the preferential recrystallisation nucleation sites are triple points and grain boundaries, as arrowed. The onset of recrystallisation has been delayed due to the Nb addition compared to the hot deformed Nb free model alloy. Coarser grains, i.e. > 200 µm, have been observed to have a slower recrystallisation rate, Figure 8-18

(c), which agrees with the previous observation for cold deformed and annealed Nb free and Nb containing alloys, and also the hot deformed Nb free alloy. Therefore, the same effect of grain size distribution on the recrystallisation kinetics is expected in this case. The recrystallisation curve for the Fe-30Ni-0.044 wt. % Nb steels at 950 °C, 0.35 strain is shown in Figure 8-19. A delay in recrystallisation starting time caused by the Nb addition (compared to measurements for the Nb free condition, chapter 7.5) has also been observed under these conditions. The recrystallisation starting time is 12s, and it finishes at 205s, which is slower than for the Nb free steel (R_s: 4s and R_f: 127s). The Avrami exponent is measured to be 1.2, which is in the same range as the Nb free model alloy under the same conditions.

Figure 8-20 shows the optical images after hot deformation at 0.45 strain, 950 °C. Considerably faster recrystallisation kinetics has been observed compared to the 0.35 strain condition, which can be attributed to a higher stored energy. The coarser grains, i.e. > 200 µm, have been observed recrystallising at a slower rate, as seen in Figure 8-20 (a) and (b), which agrees well with the other conditions (both cold and hot deformed). The Avrami exponent has been measured to be 1.2 in this condition, Figure 8-21 which agrees with the hot deformed condition at 0.35 strain and the cold deformed condition at 0.3 - 0.2 strain at 950 °C.

Figure 8-22 shows optical images of the hot deformed samples at 850°C, 0.35 strain. A slugglish onset of recrystallisation and a decreased Avrami exponent has been observed. It can be seen from Figure 8-22 (b) that the recrystallising grains were formed along the grain boundaries at 1500 s, but the growth rate is considerably slower compared to the samples held at the higher temperature, i.e. 950°C. The Avrami exponent was measured to be 0.8 over the recrystallisation range observed, Figure 8-23.

Decreased Avrami exponents due to the presence of strain induced precipitates has been reported by other authors under hot deformation condition. Llanos reported that the Avrami exponents decreased from 1 to 0.8 within the range of 1100 - 950 °C for 0.11 wt. % Nb microalloyed steels at 0.3 strain [181]. Kang reported that the Avrami exponent decreased from 1.1 to 0.6 for 0.03 wt. % Nb microalloyed steels within the

temperature range of 1050 - 850 °C at 0.3 strain [153]. Abdollah-Zadeh has reported that the recrystallisation Avrami exponent changed in a Fe-30%Ni-0.02wt% Nb alloy from 1.5 at 900 – 1000 °C to 0.9 at 850°C after 0.2 strain due to the presence of strain induced precipitation (SIP) Figure 8-23 [11].

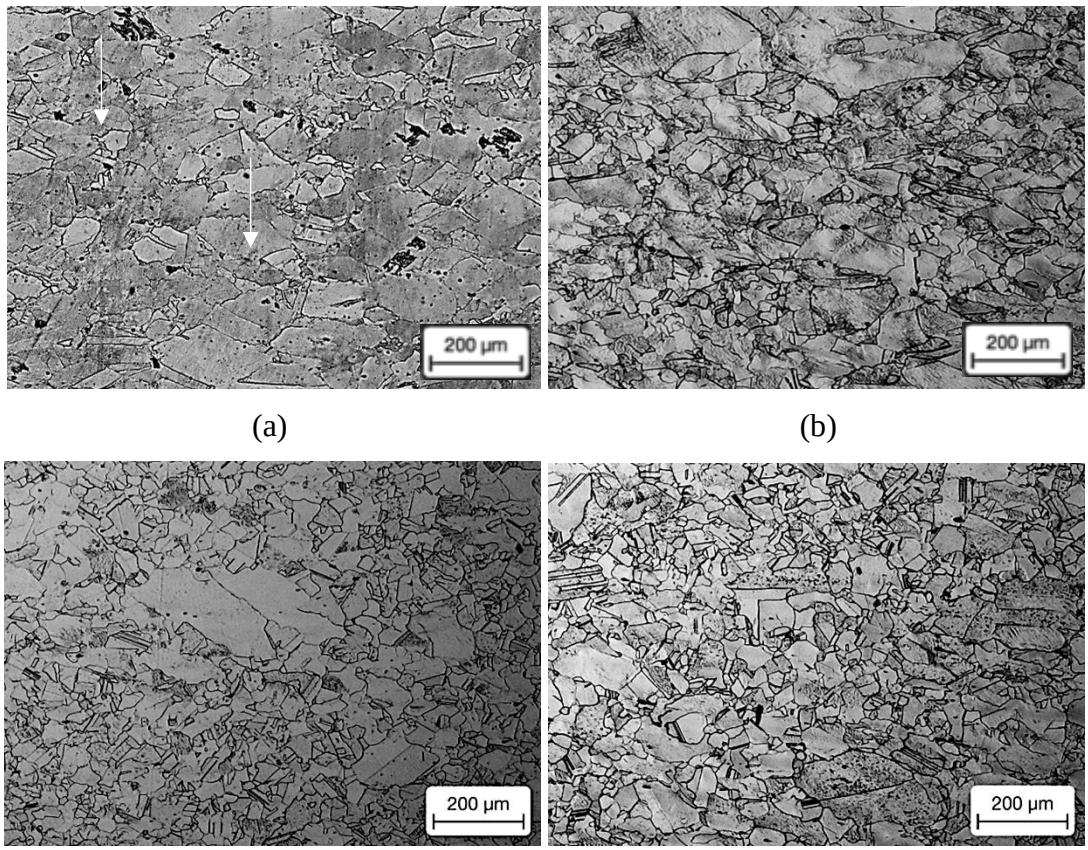

(a) (b)

(c) (d)

Figure 8-18 Microstructure evolution of hot deformed samples Fe-30Ni with 0.044wt% Nb at 950 °C, 0.35 strain for (a) 25s (b) 60s (c) 120s (d) 300s

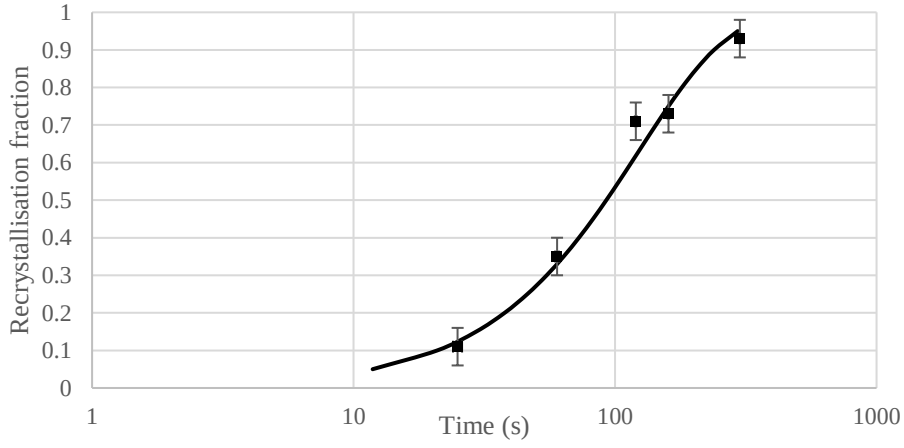

Figure 8-19 Recrystallisation kinetics of Fe-30Ni with 0.044wt% Nb deformed at 950 °C, 0.35 strain

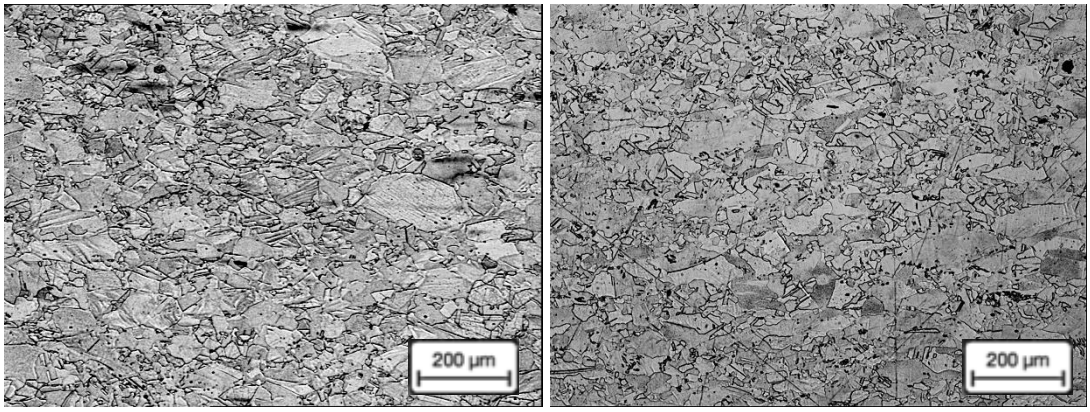

(a) (b)

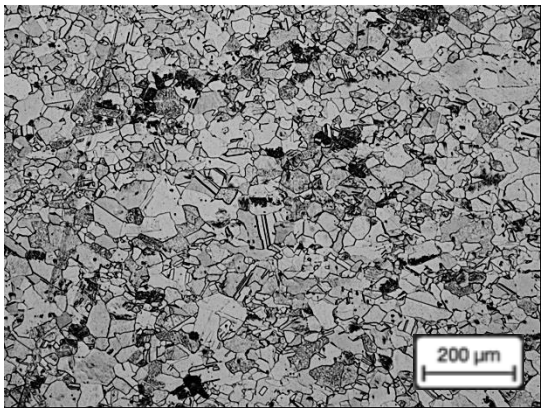

(c)

Figure 8-20 Microstructure evolution of hot deformed samples at 950 °C, 0.45 strain for (a) 25s (b) 40s (c) 60s

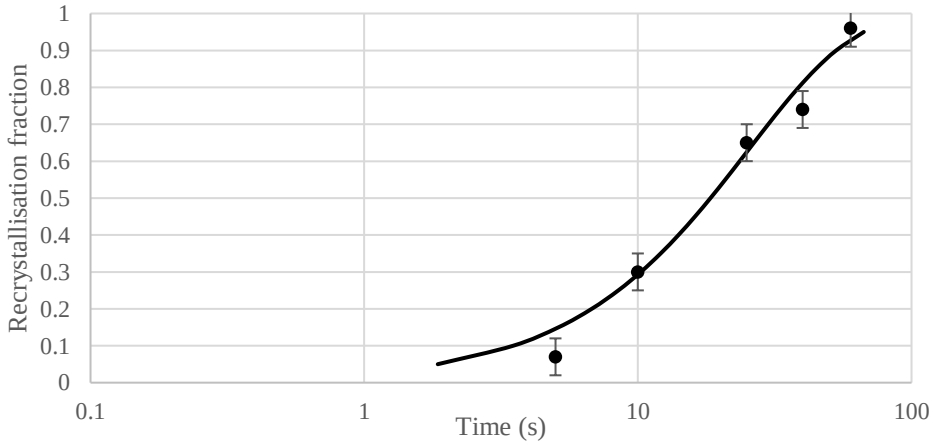

Figure 8-21 Recrystallisation kinetics of Fe-30Ni with 0.044wt% Nb deformed at 950 °C, 0.45 strain

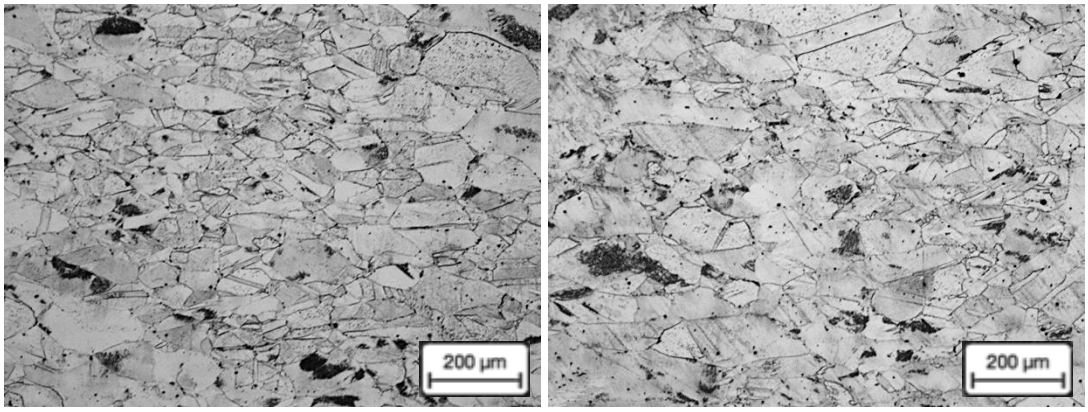

(a) (b)

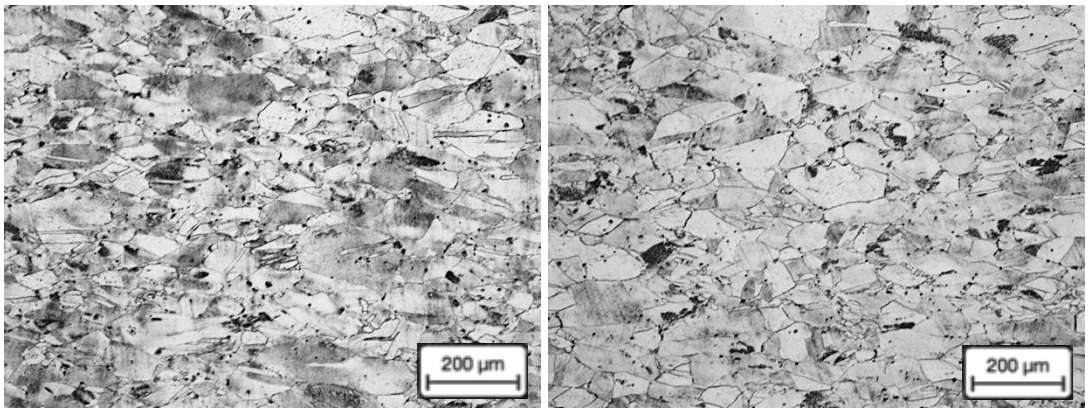

(c) (d)

Figure 8-22 Microstructure evolution of hot deformed samples Fe-30Ni with 0.044wt% Nb deformed at 850 °C, 0.45 strain (a) 900s, (b) 1500s (c) 2400s (d) 3600s

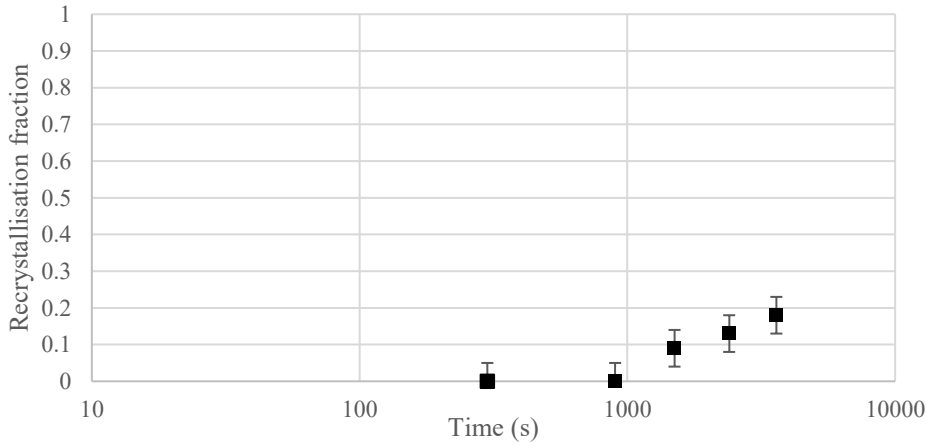

Figure 8-23 Recrystallisation kinetics of Fe-30Ni with 0.044wt% Nb deformed at 850 °C, 0.35 strain

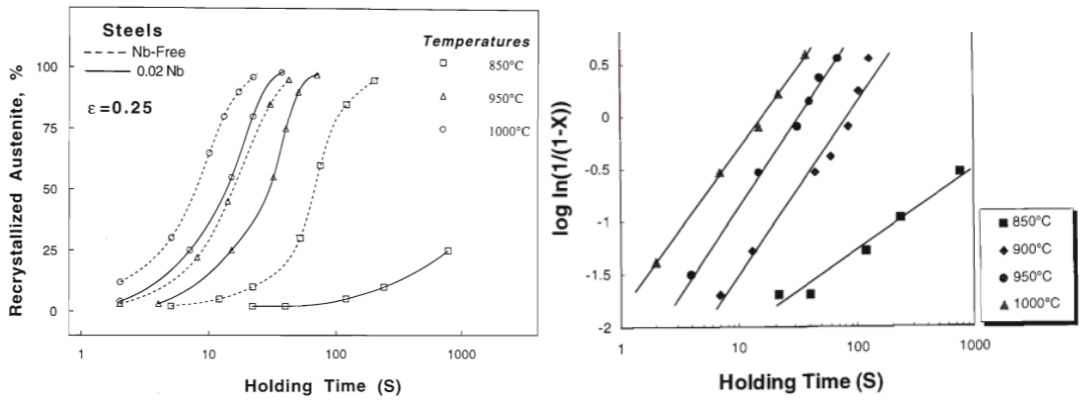

(a) (b)

Figure 8-24 The recrystallisation evolution of Fe-30Ni- 0.02wt% Nb or Nb-free with initial grain size of 310 μm, at 0.25 strain and various temperatures. [11]

In summary it has been shown that the absolute recrystallisation starting and finishing time for the Nb containing model alloy after hot deformation are not comparable to the cold deformed samples, which is attributed to the differences in stored energy and also potentially the precipitation kinetics. However, the cold and hot deformed samples showed comparable Avrami exponents under the conditions when it is proposed that SIP did or did not affect the recrystallisation rate. Further analysis on the precipitation kinetics and its effect on recrystallisation kinetics, i.e. Avrami exponent, in the hot deformed condition is given below.

8.3.2 NbC precipitation characterisation

To determine whether it is the presence of SIP that changes the recrystallisation Avrami exponents, TEM examination has been carried out. As mentioned in Chapter 6, both microbands and equiaxed subgrains have been seen in the hot deformed samples, which is comparable to the cold deformed and reheated microstructure. Therefore, in both cold and hot deformed samples, the preferential strain induced precipitation nucleation sites are microbands and subgrain boundaries.

Strain induced precipitates have been seen in the hot deformed samples at 950 - 850 °C, 0.35 - 0.45 strain. The distribution of precipitates showed a cell-like structure, which agreed well with the literature, also the observations from the cold deformed and annealed samples. Figure 8-24 shows the recovered sub-grain microstructure at 950°C, 0.35 strain, 25s where it can be seen that the strain induced precipitates were

formed in the deformed matrix. After further holding at temperature the SIP coarsen and the distribution is easier to see, for example Figure 8-25 clearly shows a cell structure of strain induced precipitates after annealing of 300s. Similar features have also been observed by other authors: Davenport has reported that the strain induced precipitates distributed in a cell-like manner, suggesting the strain induced precipitation occurs on subgrain boundaries in hot deformed samples [133]. Kwon also suggest that the strain induced precipitates were in localised arrays [154]. Palmiere observed that the Nb(C,N) were heterogeneously nucleated on the microbands [138].

The strain induced precipitates size distribution was measured for the hot deformed samples. The average SIP size at 25s after 0.35 strain is significantly larger than seen for the cold deformed and annealed samples: the hot deformed samples (0.35 strain) gave an average SIP size of 12 nm compared to 3.5 nm in the cold deformed samples (0.3 strain, isothermally holding at 950 ºC for 25s). Additionally, the number density of SIP in the hot deformed samples (0.35 strain) was one order of magnitude smaller compared to the cold deformed samples (0.3 strain). The SIP size increased to 28 nm at 300s annealing after hot deformation at 950°C, which suggests considerably faster precipitation growth and coarsening kinetics than seen for the cold deformed samples where a maximum average size of 10.4 nm was seen at 950°C. For the hot deformed samples at 0.45 strain, the size distribution, Figure 8-29, showed that the average size is 12 nm after 25s, which is considerably larger than the cold deformed sample annealed at the same temperature, after a lower strain (0.3). Additionally, the SIP size of the hot deformed sample at 850 °C, 0.35 strain, 3000s is shown in Figure 8-30. It can be seen that the average size is 8 nm, which is considerably finer compared to the samples annealed at 950 ºC.

The average size, number density and calculated pinning force for the hot deformed samples have been summarised in Table 8-9. It can be seen that the pinning force is significantly smaller compared to the cold deformed samples. It is suggested that this is due to there being a higher dislocation density present in the cold deformed sample at the onset of precipitation, which leads to an increase in the number density and a decrease in SIP size (as summarised in Chapter 3). Dynamic recovery occurring during

hot deformation could accelerate the strain induced precipitation growth and coarsening significantly by enhancing diffusivity.

Similar precipitates size has been observed by other authors at similar strain levels: Dutta mentioned that strain induced precipitates grow to 10 - 15 nm in diameter within 100 seconds at 900 °C, 0.2 strain for a 0.03 wt.% Nb microalloyed steel [148] and attributed this high diffusivity to pipe diffusion via dislocation networks. Davenport et al. have also observed an accelerated precipitation coarsening rate (compared to the bulk diffusion coarsening predictions) for 0.07 wt. % Nb steels, 0.25 strain, where the strain induced precipitate size reached 9 nm after 100 seconds [133]. However, little coarsening was observed at high strains: Hansen studied precipitate size evolution at 0.7 strain for 0.031 - 0.095 wt. % Nb containing steels where the average precipitate size only increased from 4.5 nm to 5.5 nm after 10000 seconds at 900 °C [91]. Additionally, Le Bon observed that the strain induced precipitate size is 4.5- 4.8 nm after 1000 seconds at 900 ºC, strain 1.31, Nb level 0.04 wt.% [135]. Jonas pointed out that static recrystallisation increases the growth and coarsening rate of precipitates due to the higher diffusivity and Nb level at the moving boundary front [130]. In the work presented here there is no direct observation that the precipitates were coarsening significantly at the moving boundary front. Nevertheless, both mechanisms suggest a considerably higher diffusivity compared to bulk diffusion of Nb.

Abdollah-Zadeh measured the NbC SIP size in Fe-30Ni-0.02 wt.% Nb after hot deformed to 0.25 strain then held between 22 - 780s at 850 °C, Figure 8-31. It can be seen that the average SIP size is 5.6 nm at 22s, then increased only slightly in size to 450s. Therefore, it suggests that the strain induced precipitates could have a prolonged pinning period at 850 °C. Based on the similar conditions used in this literature and the current experiment, it is not unreasonable to expect a similar SIP size and slow precipitation growing and coarsening rate at 850 °C for the Fe-30Ni- 0.044 wt.% Nb steel.

8.3.3 Effect of NbC on recrystallisation kinetics

It has been mentioned in the earlier section on the cold deformed then annealed samples that the effect of precipitation on the recrystallsation kinetics is strongly linked to the precipitates size. That is, if the SIP average size is well above the critical size for coarsening when recrystallisation occurs such that the pinning force is reducing with continued time, then the Avrami exponent will not be affected due to the low / reducing pinning force. Whereas, if there are some SIP still nucleating and/or growing during recrystallisation, then the Avrami exponent will be affected and have a lower value as the recrystallisation rate is reduced. In the hot deformed samples at 950°C, the Avrami exponent between Nb free and Nb containing model alloys is comparable since the SIP were already large (12 nm) and coarsening when recrystallisation occurred, hence there was a reducing pinning force. However, a lower Avrami exponent is seen at 850°C for the Nb containing model alloy due to the slow precipitation kinetics such that precipitates are expected to be small and still growing based on the literature and the experimental observation, which leads to a higher pinning force. Additionally, it is worth noting that the pinning force is less than for the cold deformed samples, but as the stored energy is also less in the hot deformed condition, therefore a lower pinning force is required to retard recrystallisation.

These observations are in agreement with those reported in the literature: Hansen has reported that the retarding force is strongly affected by the precipitate size, for example in microalloyed steels with Nb levels of 0.031 - 0.095 wt. % and strain level 0.7, it was reported that there was no recrystallisation occurring at 850°C with no precipitation coarsening observed up to 10000 s, whereas the precipitates were found to coarsen from 4 nm to 8 nm in diameter at 950 °C, at 10000s and also recrystallisation was completed. Jonas has also observed a strong relationship between the precipitate size and the retardation of recrystallisation for a 0.074 wt. % Nb steel, at 815 - 930°C and 0.25 strain. The precipitate size at which recrystallisation commenced (i.e. pinning force was no longer sufficient to stop recrystallisation) was 8.6 - 9 nm for both temperatures [9]. Therefore, the presence of strain induced precipitates can stop or slow (if a sufficient pinning force is generated) recrystallisation however, if sufficient coarsening of the strain induced precipitates occurs then the pinning force decreases and recrystallisation is no longer retarded.

Therefore, the results confirm that recrystallisation can proceed even in the presence of SIP in the hot deformed condition and the recrystallisation Avrami exponent is not affected by the SIP at 950°C due to its fast coarsening kinetics at this temperature. However, the precipitation nucleation and growth rate is considerably slower at a lower temperature (850°C), therefore, the pinning force could increase during recrystallisation, as a result, the recrystallisation Avrami exponent decreases, which agrees well with the observation in the cold deformed then annealed samples.

The observations under the hot deformed condition further validate the mechanism by which SIP affects the recrystallisation kinetics observed for cold deformed and annealed samples. The absolute precipitation kinetics and recrystallisation kinetics are not directly transferable between the two approaches due to the different extent of stored energy and recovery. Neither can the data measured in either cases be used to determine the HSLA steels precipitation / recrystallisation kinetics. Nevertheless, all the data clearly demonstrate that the recrystallisation Avrami exponent is dependent on the strain induced precipitation kinetics, i.e. nucleation and growth rate such that under conditions when SIP are still nucleating and growing during recrystallisation (rather than coarsening), then the recrystallisation Avrami exponent is decreased compared to the same material without the presence of SIP.

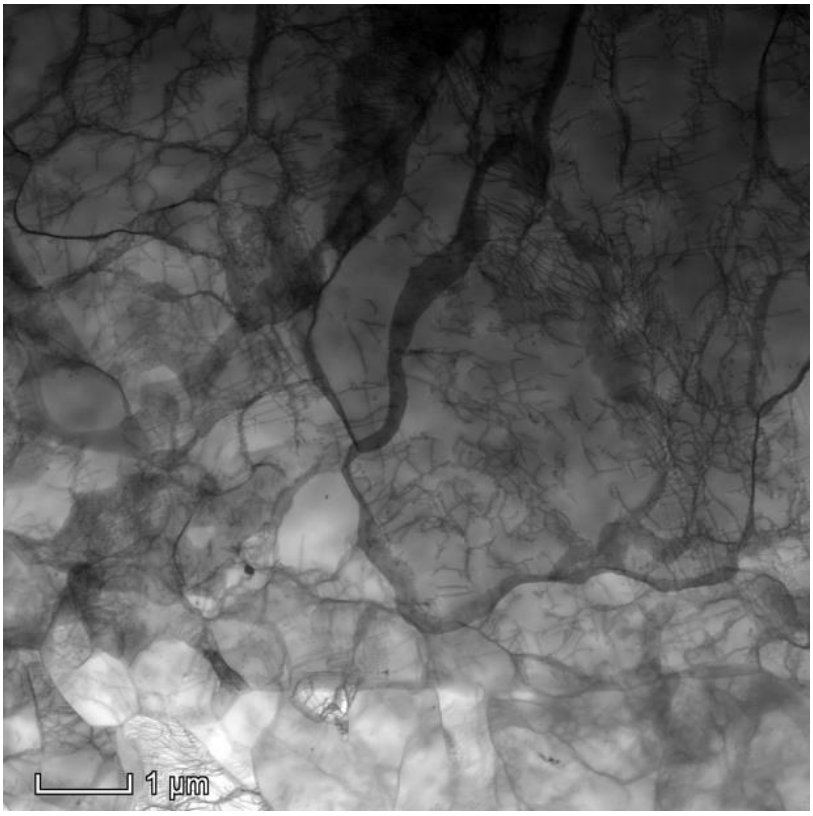

(a)

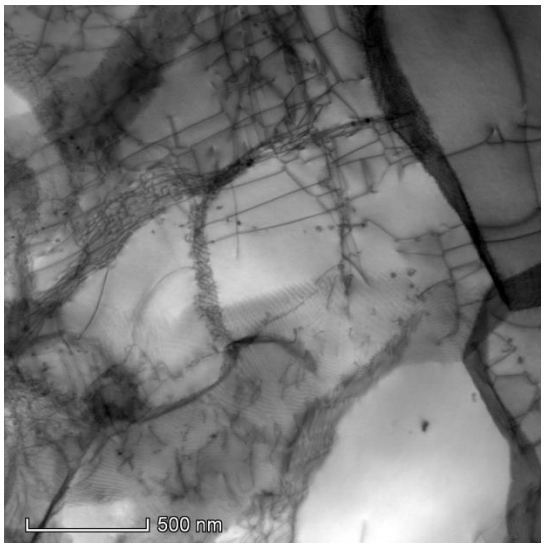

(b) (c)

Figure 8-25 SIP shown in the hot deformed samples at 950 °C, 0.35 strain, held for 25s (a) low magnification STEM showing the subgrain structure (b) high magnification STEM showing subgrains and SIP (c) high magnification HAADF

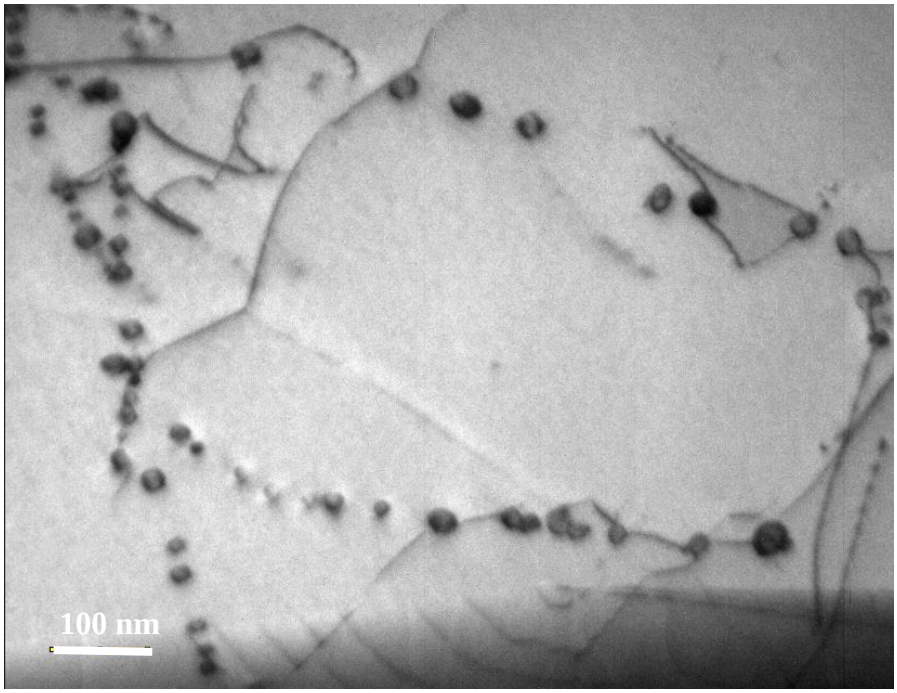

Figure 8-26 SIP shown in the hot deformed samples at 950 °C, 0.35 strain, held for 300s

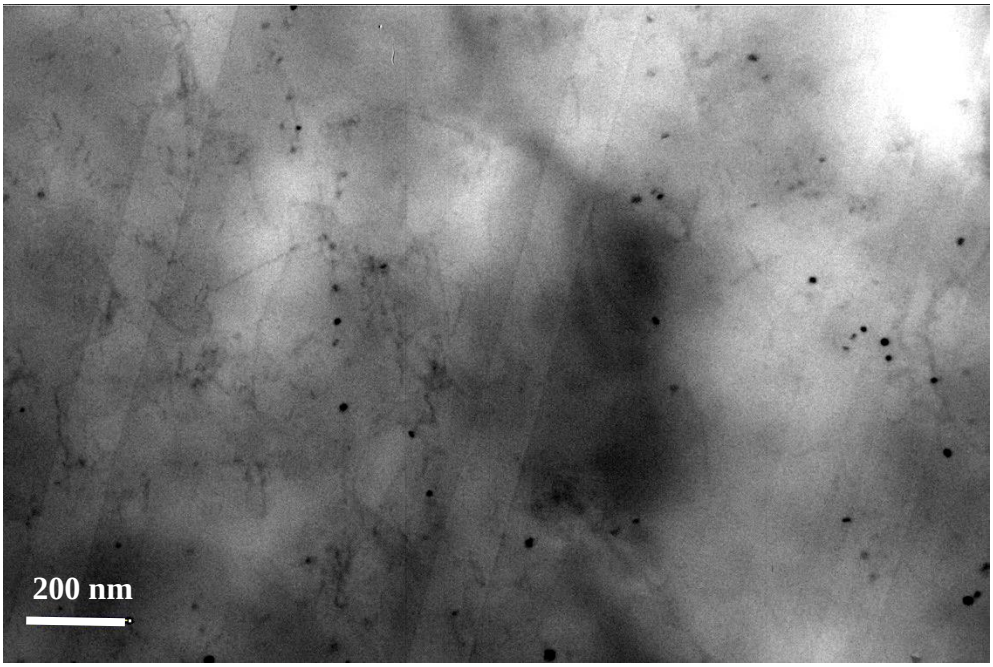

Figure 8-27 SIP shown in the deformed sample at °950 C, 0.45 strain, held for 25s

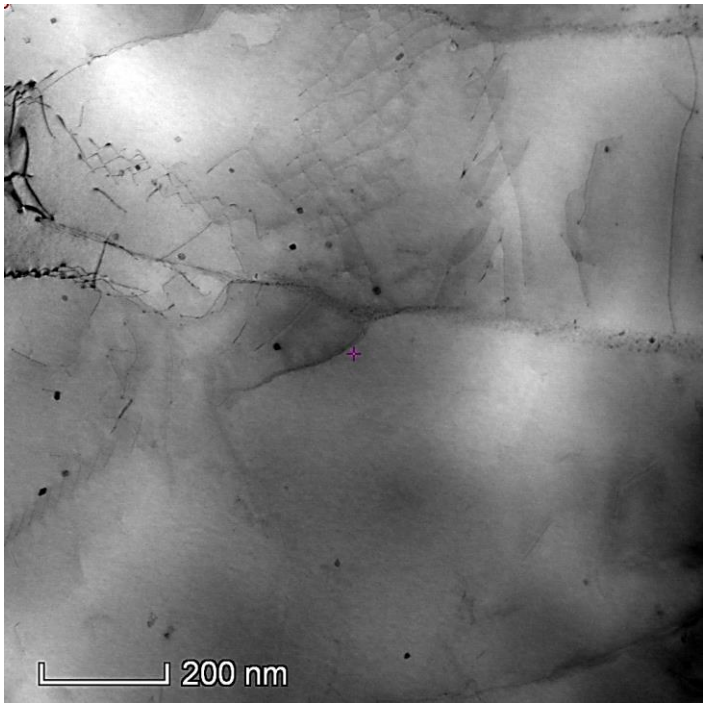

Figure 8-28 SIP size evolution at 850 °C, 0.35 strain for a Fe-30Ni-0.044 wt.% Nb steel 3000s

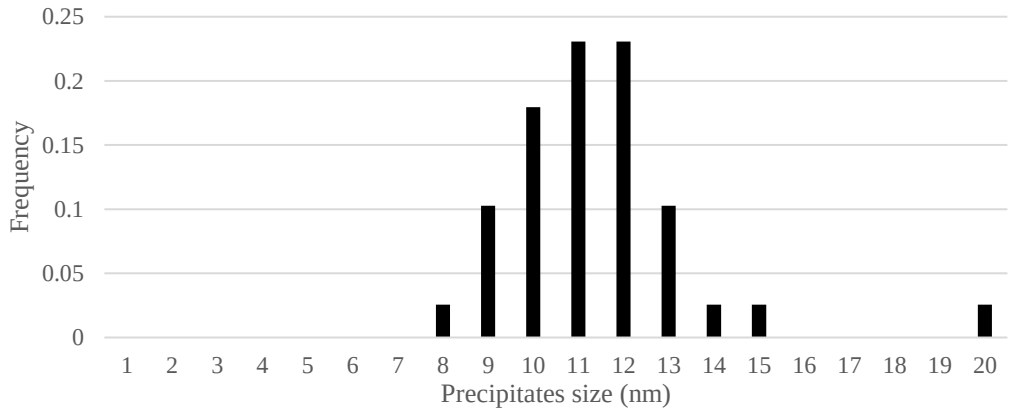

(a)

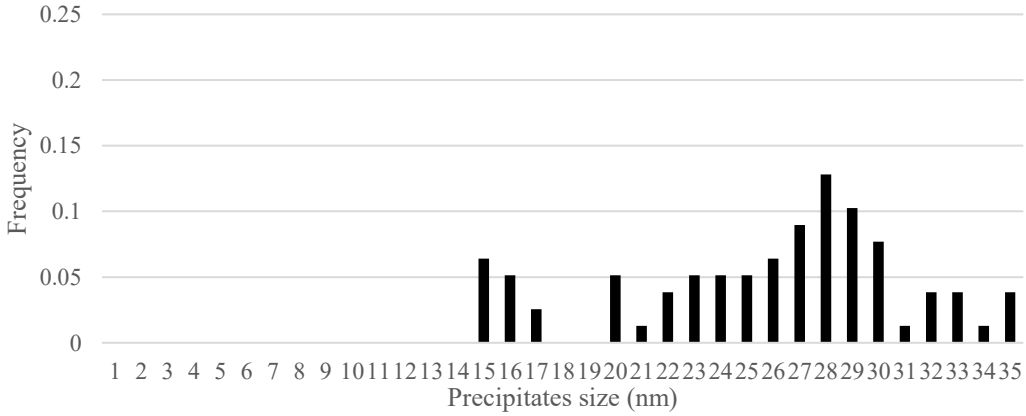

(b)

Figure 8-29 SIP size evolution 0.35 strain, deformed at 950 °C, (a) 25s (b) 300s

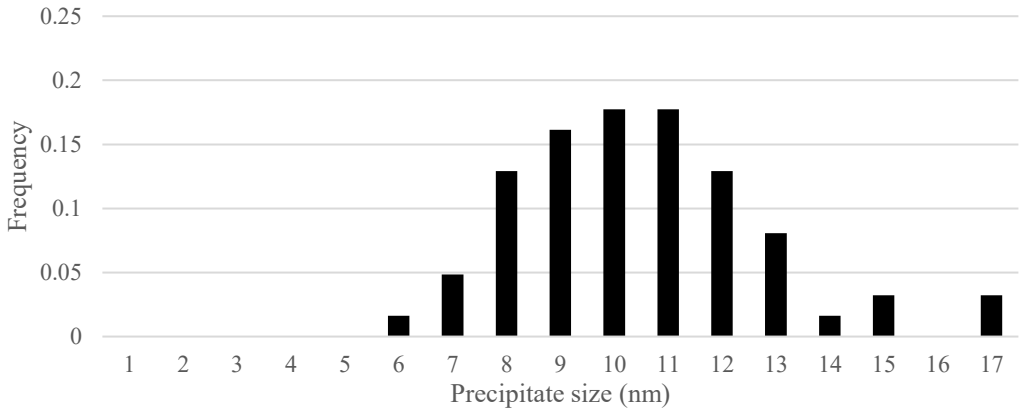

Figure 8-30 SIP size evolution 0.45 strain, deformed at 950 °C, 25s

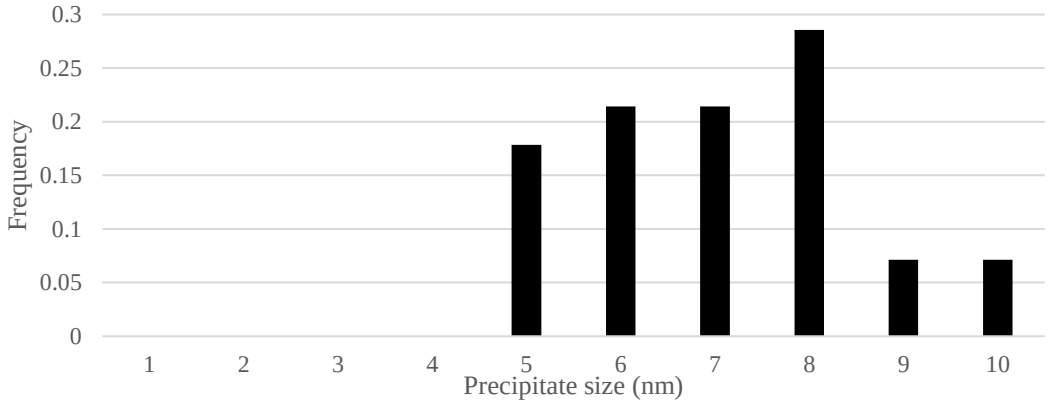

Figure 8-31 SIP size evolution 0.35 strain, deformed at 850 °C, 3000s

Table 8-9 Precipitates summary in the hot deformed condition

Temperature (ºC)	Strain	Time (s)	Average size (nm)	Number density ($\times 10^{21}$/ m^3)	Local pinning force (MPa)
950	0.35	25	12	0.12	0.04
		300	28	0.09	0.06
850	0.35	3000	8	0.47	0.1
950	0.45	25	11	0.11	0.04

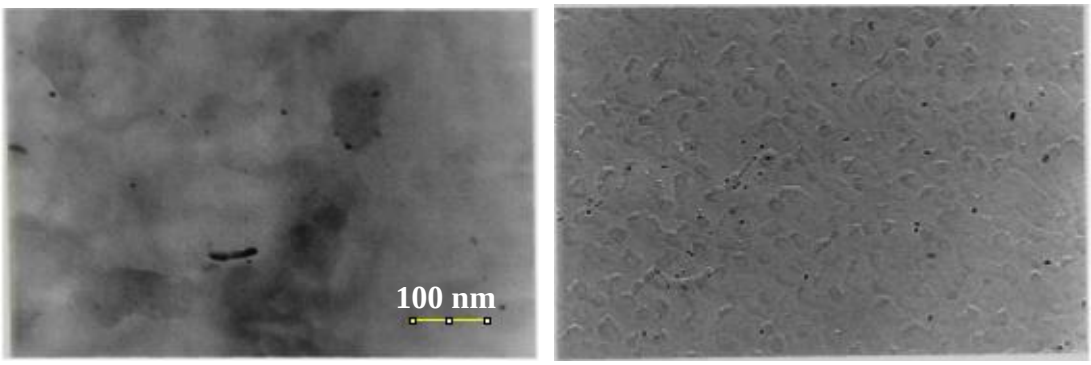

(a) (b)

(c)

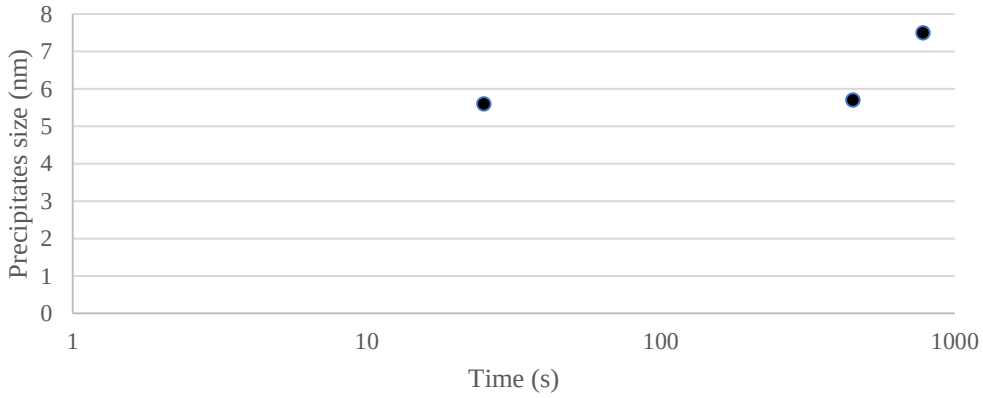

(d)

Figure 8-32 SIP size evolution at 850 °C, 0.25 strain reported for a Fe-30Ni-0.02 wt.% Nb steel, (a) 22s, (b) 450s and (c) 780s (d) Precipitates size evolution [11]

8.4 Summary

Fe-30Ni- 0.044 wt. % Nb recrystallisation kinetics at 0.3 - 0.2 cold strain and 0.45 - 0.3 hot strain within the annealing / holding temperature range of 950 - 850 °C have been measured. The Nb(C,N) precipitation kinetics and size evolution have also been examined. The results are summarised as follows:

For cold deformed then annealed samples:

1. Strain induced precipitation nucleation occurs before the onset of recrystallisation at 0.3 strain, 950 - 850°C, and growth and coarsening occurs during recrystallisation, whose rates are influenced by the temperature. With decreasing temperature, the growth and coarsening rates decrease.

2. The critical pinning force determined to slow down recrystallisation kinetics (strain 0.3, deformed at room temperature) is approximately 0.25 MPa, and the effective precipitates size to slow down recrystallisation is 6 nm.

3. The retardation of recrystallisation at 0.3 strain is attributed to both solute drag and strain induced precipitates. A model taking into account both the pinning force and solute drag has been used, and good agreements with the experimental results have been observed. The Avrami exponent prediction can also be achieved by taking the change of pinning force with time into consideration.

4. The effect of Nb on the Avrami exponent is dependent on the growth and coarsening rate of precipitates. At lower temperature, i.e. 850 °C, 0.3 strain, the slow precipitate coarsening rate leads to a prolonged pinning effect on recrystallisation and hence a lower Avrami exponent.

For hot deformed samples:

1. Strain induced precipitates are significantly larger in size (11 - 12nm) compared to cold deformed samples (4nm) after isothermal holding time of 25s at 950°C. Thus, the precipitation kinetics between cold and hot deformed samples are not equivalent.

2. Similarly, the recrystallisation kinetics are also considerably different, which has been attributed to the variation in both stored energy and pinning force, as a result, the cold and hot deformation recrystallisation times are not comparable.

3. The decreased Avrami exponent at 850°C, 0.35 strain is attributed to the slow precipitation kinetics, which agrees well with the observation in the cold deformed samples.

Table 8-10 Comparison of cold deformed and annealed and hot deformed tests

	Tests	Objectives	Transferrable knowledge	Non- transferrable knowledge
1	Hardness measurement during annealing	1. Softening behaviour with the presence of Nb in the cold deformed condition		1. It indicated that no significant precipitation strengthening occurred during the annealing process due to the low level of Nb content, i.e. low precipitates density and size (blow the detection limit of the TEM)
2	Optical analysis of recrystallisation evolution	1. Recrystallisation inhomogeneity for both cold and hot deformed samples. 2. Recrystallisation kinetics and Avrami exponents for both cold and hot deformed samples	1. Recrystallisation nucleation occurred along the grain boundary regions, and the recrystallisation growth rate was faster in the finer grains than the coarser grains for both cold and hot deformed samples. 2. Recrystallisation Avrami exponents were affected by the strain induced precipitation kinetics. Rapid coarsening of the strain induced precipitates have no effect on the recrystallisation Avrami exponent, whereas little coarsening leads to the decreasing in the recrystallisation Avrami exponent.	1. The absolute value of recrystallisation starting and finishing time is not equivalent/ transferrable between the cold and hot deformed samples, attributed to the variation in the stored energy level also the differences in the strain induced precipitation kinetics.
3	TEM observation of strain induced precipitation	1. EDS to confirm the composition of the precipitates	1. NbC precipitates have been observed in both cold and hot deformed samples.	1. Strain induced precipitation kinetics is faster in the hot deformed condition compared to the cold deformed condition.

		2. Precipitates size evolution and kinetics during annealing for both cold and hot deformed conditions		2. The SIP size is larger in the hot deformed

Chapter 9 Conclusions

Two major areas have been investigated in the project, which are the effect of the grain size distribution and the effect of Nb addition on the recrystallisation kinetics. A model Fe-30Ni alloy, heat treated to give two different initial grain size distributions, has been used as it retains its austenitic structure to room temperature allowing the representative both room temperature and high temperature deformation structures to be assessed along with the recrystallisation growth mechanisms.

Effect of grain size distribution on the recrystallisation kinetics

1. No macroscopic strain distribution was found for samples deformed to 0.3 strain at room temperature. Whereas the macroscopic strain inhomogeneity has been observed for hot deformed samples (strain 0.27- 0.45) attributed to the barrelling. Additionally, microscopic inhomogeneity of the deformed microstructure has been observed under both cold and hot deformation conditions. The grain boundary area and the triple points were more deformed than the grain interior. Also finer grains in the grain size distribution showed higher local misorientation (i.e. higher strain) than coarser grains.

2. Recrystallisation nuclei were non-randomly distributed, predominately along the grain boundaries. Impingement of growing recrystallised grains along the grain boundary occurs at an early stage of recrystallisation leading to a lower Avrami exponent that predicted theoretically assuming site saturated nucleation with three-dimensional growth with constant growth rate.

3. The heavily deformed regions have more stored energy and thus recrystallise first, then the lightly deformed regions recrystallise later. The recrystallisation rate of the region with high stored energy is considerably faster than the rest. It has also been observed that the finer grains recrystallise faster than the coarser grains due to both the higher stored energy and higher density of potential nucleation sites. As a result, the recrystallisation growth rate decreases with time, which also leads to a decreased Avrami exponent.

4. The recrystallisation Avrami exponent is affected by the grain size distributions within the temperature range of 950-850 °C and strain range 0.2- 0.3 (cold deformed condition), strain range 0.27- 0.35 (hot deformed condition). The wider grain size distribution, with grain size range of 20-340 µm (mode grain size 160 µm), gave an exponent of 1.1- 1.3 and the narrower distribution, with grain size range of 20-200 µm (mode grain size 100 µm) gave a value of 1.8- 2.2 in both cold and hot deformed conditions.

6. The Avrami exponents have been found to be independent of the strain and temperature within the temperature range of 950-850 °C, strain level 0.2- 0.3 for cold deformed condition, (strain level 0.27- 0.35 for hot deformed condition). The recrystallisation activation energy for the Fe-30Ni model alloy has been measured to be 192 kJ/ mol (cold deformation condition).

7. The Avrami exponent can be predicted well from the grain size distribution, with a simple approach considering the grain size at the 10% and 90% cumulative area fraction.

8. The final recrystallised grain size distribution has been predicted using approaches from the literature. The equation proposed by Kaonda et al [186], which considers each grain size class in the distribution individually, gave reasonably good agreement for the samples with initial mode grain size of 160 µm and 100 µm at 0.2 and 0.3 strain.

9. The Fe- 30Ni model alloy hot deformation tests have been applied to examine the effect of grain size distribution on recrystallisation Avrami exponent. The proposed model and the experimental Avrami exponents agreed well within the strain range of 0.27- 0.35, temperature range of 950- 850 °C. Nevertheless, it is worth noting that the recrystallisation kinetics between the cold and hot deformed conditions is not equivalent, which is attributed to the variation in the stored energy.

Effect of Nb addition on the recrystallisation kinetics

1. A delay in the onset of recrystallisation has been observed for the cold deformed then annealed Fe-30Ni-0.044wt.% Nb steel within the temperature range of 950-

850 °C, strain range 0.3-0.2. The effect of Nb solute drag and / or strain induced precipitates on recrystallisation kinetics is dependent on temperature and strain. The Avrami exponent was found to be independent from temperature after 0.2 strain, annealing at 950-850 °C, with the exponents being between 1.2- 1.4 and well predicted from the grain size distribution. At 0.3 strain, the Avrami exponent is also between 1.2-1.4 after annealing at 950- 900 °C, but it decreased to 0.9 at 850 °C.

2. Strain induced precipitates have been observed at 0.3 strain, 950-850 °C prior to and at the early stage of recrystallisation. The retardation in the onset of recrystallisation. was caused by the effect of strain induced precipitates and solute drag, but the Avrami exponent was not affected as the strain induced precipitates rapidly coarsened reducing the pinning force on recrystallisation at 950 – 900 °C. The decrease in Avrami exponent for 850 °C, 0.3 strain was attributed to the slow growth and coarsening rate of the strain induced precipitates meaning that they remained less than 6 nm resulting in a larger pinning force reducing the recrystallisation rate.

3. The retardation of onset of recrystallisation has also been observed for the hot deformed Fe- 30Ni- 0.044 wt.%Nb samples at 950- 850 °C, strain range 0.35- 0.45. The decreased recrystallisation Avrami exponent at 850 °C, 0.35 strain attributed to the slow precipitation growth and coarsening mechanism. However, thew recrystallisation kinetics between cold and hot deformed conditions is not transferrable due to the differences in both recrystallisation driving force, i.e. stored energy and the pinning force.

4. Strain induced precipitation growth and coarsening rate is significantly faster in the hot deformed condition compared to the cold deformed and annealed condtion. The SIP size was over 10 nm at 950 °C, 0.35- 0.45 strain after 25s for hot deformed samples, whereas it was only 3.5 nm at 950 °C, 0.3 strain after 25s for cold deformed samples.

5. The proposed model taken the recrystallisation driving force and the precipitation pinning force into consideration has given a good prediction of recrystallisation starting time at 0.3 strain (cold deformation condition). Additionally, the Avrami exponent can also be predicted by taking the change of pinning force into account, which has shown good agreements in this case.

Chapter 10 Future work

The following areas of further work have been identified:

1. The extent of strain inhomogeneity, both inter- granular and intra- granular, at different deformation temperatures requires further investigation. That is, dynamic recovery could consume more stored energy at heavily deformed regions, i.e. triple points and grain boundary area, as a result any strain inhomogeneity could be less significant compared to in a sample deformed at room temperature (when no recovery occurs).

2. The dislocation density has been estimated using hardness measurements for the cold deformed samples within the strain range of 0.3-0.2. Local misorientation measured by EBSD has been applied to qualitatively discuss the strain inhomogeneity at 0.3 strain. More accurate values of dislocation density at different strains are required to further improve the recrystallisation kinetics prediction. XRD and EBSD can be used to measure the dislocation density at different deformation conditions, i.e. strain, strain rate and temperature. Additionally, a quantitative relationship between the grain size and the dislocation density is highly desirable and could be obtained using EBSD. Then the recrystallisation rate could be linked directly to the dislocation density and the grain boundary length per unit area.

3. The recrystallisation activation energy, strain exponent, Avrami exponent and constant A were determined for Fe-30Ni model alloy by using Sellars apporach, which were cold deformed to 0.3 - 0.2 strain, and the Avrami exponent can be estimated by taking the grain size distribution into consideration. However, the Avrami exponent prediction approach was developed for two grain size distributions, i.e. 20-200 μm / mode grain size 100 μm and 20-340 μm / mode grain size 160 μm; more grain size distributions need to be tested to validate the proposed Avrami exponent prediction equation.

4. It has been seen in Chapter 7 that the recrystallised grains nucleate along the grain boundaries, and the growth rate for each individual recrystallised grain varies. As a result, the fully recrystallised grain microstructure varies in size. By using the Kaonda's approach, i.e. considering each grain size class individually, the prediction

of the recrystallised grain size distribution has been considerably improved, however some discrepancy has still been seen at 0.3 strain for the samples with grain size range of 20- 340 μm. The cause of the discrepancy is not evident from the current experiment therefore a wider strain level and different initial grain size distributions need to be examined to determine if the errors are experimental variability of if further modification of the empirically fitted parameters in the model is required.

5. The strain induced precipitates have been observed at 0.3 strain within the temperature range of 950- 850 °C prior and at the early stage of recrystallisation. The results indicated that both strain induced precipitates and solute drag retarded the onset of recrystallisation, but under most conditions the precipitates coarsen quickly and do not slow the rate of recrystallisation but the slow coarsening rate of strain induced precipitates at 850 °C, 0.3 strain leads to a decrease in the Avrami exponent. A wider strain and temperature range are required to fully establish the role of Nb on the recrystallisation kinetics and Avrami exponents. Additionally, the precipitation kinetics at more temperatures and strain levels need to be measured to validate the effect of strain induced precipitation coarsening rate on recrystallisation kinetics and Avrami exponent.

6. It has been shown that the coarsening rate of the precipitates were significantly faster than prediction assuming bulk diffusion within the temperature range of 950-850 °C, 0.3 strain. However, it is not clear whether the accelerated diffusivity of Nb is attributed to the dislocation network and/ or moving grain boundary during recrystallisation. Additionally, it is not clear whether the fast precipitation growth and coarsening mechanism in the hot deformed condition is attributed to the dynamic recovery. Atomic probe tomography can be used to characterise the Nb level at the moving boundary and the dislocation network. Once the Nb level at moving boundaries is established, the effect of solute drag can also be studied.

References

[1] F. Humphreys and M.Hatherly, Recrystallisation and Related Annealing Phenomena, 2nd ed., Oxford: Elsevier, 2004.

[2] I. Fernandez, P. Uranga, B. Lopez and J. M. Rodriguez- Ibabe, "Static recrystallisation behaviour of a wide range of austenite grain sizes in microalloyed steels," *ISIJ International,* Vol. 40, No. 9, pp. 893-901, 2000.

[3] A. F. Padilha, R. L. Plaut and P. R. Rios, "Annealing of Cold- Worked Austenitc Stainless Steels," *ISIJ International,* Vol. 43, No. 2, pp. 135-143, 2003.

[4] H. Takuda, N. Yamazaki and N. Hatta, "Influence of cold- rolling and annealing conditions on formability of aluminium alloy sheet," *Journal of Materials Science,* Vol. 30, pp. 957- 963, 1995.

[5] C. Scott, B. Remy, J. Collet, A. Cael, C. Bao, F. Danoix, B. Malard and C. Curfs, "Precipitation strengthening in high managanese austenitic TWIP steels," *International Journal of Materials,* Vol. 102, No. 5, pp. 538- 549, 2011.

[6] S. Misra, "Austenite Recrystallisation and Ferrite Formation in Hot Rolled Titanium Microalloyed Steels," Ph.D. thesis, University of Wollongong, Wollongong, Australia, 1986.

[7] C. H. Gur and J. Pan, "Physical Metallurgy of Thermal Processing," in *Handbook of Thermal Process Modeling Steels*, Boca Raton, CRC Press, 2008, p. 94.

[8] R. D. Doherty, D. A. Hughes, F. J. Humphreys, J. J. Jonas, D. J. Jensen, M. E. Kassner, W. E. King, T. R. McNelley, H. J. McQueen and A. Rollett, "Current issues in recrystallisation: a review," *Materials Science and Engineering A*, pp. 219-274, 1997.

[9] A. J. DeArdo, J. M. Gray and L. Meyer "Fundamental Metallurgy of Niobium in Steels," Porceeding of Niobium international symposium, University of Pittsburgh, Pittsburgh, 1984.

[10] P. Cizek, F. Bai, E. J. Palmiere and W. M. Rainforth, "EBSD study of the orientation dependence of substructure characteristics in a model Fe−30wt%Ni alloy subjected to hot deformation," *Journal of Microscopy,* Vol. 217, pp. 138-151, February 2005.

[11] A. Abdollah-Zadeh, "The Investigation Of Deformation, Recovery, Recrystallisation And Precipitation In Austenitic HSLA Steel Analogue Alloys," PhD thesis, University of Wollongong, 1996.

[12] A. Kundu, "Grain structure development during casting, reheating and deformation of Nb- microalloyed steels," Ph.D. thesis, University of Birmingham, Birmingham, UK, 2011.

[13] A. D. Rollett, "Overview of Modelling and Simulation of Recrystallisation," *Progress in Materials Science,* Vol. 42, pp. 79- 99, 1997.

[14] A. D. Rollett, D. J. Srolovitz, R. D. Doherty and M. P. Anderson, "Computer simulation of recrystallisation in non-uniformly deformed metals," *Acta metall. ,* Vol. 37, No. 2, pp. 627-639, 1989.

[15] X. Song, M. Rettenmayr, C. Muller and H. E. Exner, "Modeling of Recrystallisation after Inhomogeneous Deformation," *Metallurgical and Materials Transactions A,* Vol. 32A, pp. 2199- 2206, 2001.

[16] D. Chakrabarti, "Development of bimodal grain structures and their effect on toughness in HSLA steel," Ph.D. thesis, University of Birmingham, Birmingham, UK, 2007.

[17] S. H. Park, "Modelling and measurement of the continuous- cooling-precipitation kinetics of Nb(C,N) in HSLA steels," Montreal , 1992.

[18] M. F. Ashby, "The deformation of plastically non-homogeneous materials," *Philosophical Magazine,* Vol. 21, No. 170, pp. 399-424, 1970.

[19] R. E. Schramm and R. P. Reed, "Stacking fault Energy of FCC Fe-Ni Alloys by X- Ray Diffraction Line Profile Analysis," *Metallurgical Transactions A,* Vol. 7A, pp. 359- 363, 1976.

[20] X. Wang, H. Li, S. Lekakh and R. J. O. Malley, "Inverse Finite Element Modeling of the Barreling Effect on Experimental Stress-Strain Curve for High Temperature Steel Compression test," *Journal of Materials Processing Technology,* Vol. 243, pp. 465- 473, 2017.

[21] C. W. Price, "Use of Kolmogorov- Johnson- Mehl- Avrami Kinetics in Recrystallisation of Metals and Crystallization of Metallic Glasses," *Acta Metall. Mater.,* Vol. 38, No. 5, pp. 727- 738, 1990.

[22] R. A. Petkovic, M. J. Luton and J. J. Jonas, "Recovery and Recrystallisation of Carbon Steel Between Intervals of Hot Working," *Canadian Metallurgical Quarterly,* Vol. 14, No. 2, pp. 137- 145, 1975.

[23] H. E. Sasbzi, A. Z. Hanzaki, H. R. Abedi, R. Soltani, A. Mateo and J. J. Roa, "The effects of bimodal grain size distributions on the work hardening behavior of a Transformation-TWinning induced plasticity steel," *Materials Science & Engineering,* Vol. 678, pp. 23-32, 2016.

[24] E. A. Simielli, "Deformation and recrystallisation kinetics of microalloyed steels in the intercritcal region," Ph. D. thesis, McGill University, Montreal, Canada, 1990.

[25] N. Hansen, "Cold deformation microstructures," *Materials science and technology,* Vol. 6, pp. 1039- 1047, 1990.

[26] D. Hull and D. Bacon, Introduction to dislocation 3rd edition, UK: Pergamon Press, 1984.

[27] M. K. Rehman and H. S. Zurob, "A Novel Approach to Model Static Recrystallisation of Austenite During Hot Rolling of Nb Microalloyed Steel. Part I: Precipitate-Free Case," *Metallurgical and Materials Transaction A,* Vol. 44A, p. 1862, April 2013.

[28] R. Le Gall and J. J. Jonas, "Solute drag effects during the dynamic recrystallisation of nickel," *Acta materialia,* Vol. 47, pp. 4365-4374, 1999.

[29] R. O. Williams, "The stored energy of copper deformed at 24C," *Acta Metallurgica,* Vol. 13, pp. 163-168, 1965.

[30] M. H. Loretto and A. J. White, "THe influence of grain size on the energy stored in deformed copper," *Acta Metallurgica,* Vol. 9, pp. 512-513, 1961.

[31] J. E. Bailey, "The dislcaotion density, flow stress and stored energy in deformed polycrystalline copper," *Philosophical Magazine,* Vol. 8, No. 86, pp. 223-236.

[32] M. Kazeminezhad, "On the modeling of the static recrystallisation considering the initial grain size effects," *Materials science and engineering A,* Vol. 486, pp. 202-207, 2008.

[33] K. Marthinsen, O. Daaland, T. Furu and E. Nes, "The Spatial Distribution of Nucleation Sites and its Effect on Recrystallisation Kinetics in

Commercial Aluminum Alloys," *Metallurgical and Materials Transactions A,* Vol. 34A, p. 2705, 2003.

[34] R. D. Doherty, "Recrystallisation and texture," *Progress in Materials Science* , Vol. 42, pp. 39-58, 1997.

[35] P. Cizek, J. A. Whiteman, W. M. Rainforth and J. H. Beynon, "EBSD and TEM investigation of the hot deformation substructure characteristics of a type 316L austenitic stainless steel," *Journal of Microscopy,* Vol. 213, pp. 285-295, March 2004.

[36] F. J. Humphreys and M. G. Ardakani, "The Deformation of Particle-Containing Aluminium Single Crystals," *Acta Metall.,* Vol. 42, No. 3, pp. 794-761, 1994.

[37] R. O. Willams, "The stored energy in deformed copper: the effect of grain size and silver content," *Acta Metallurgica,* Vol. 9, pp. 949-957, 1961.

[38] R. O. Williams, "The stored energy in deformed copper at 24C," *Acta Metallurgica,* Vol. 13, pp. 163-168, 1965.

[39] I. Baker, L. Liu and D. Mandal, "The effect of grain size on the stored energy of cold work as a function fo strain for polycrystalline Nickel," *Scripta Metallurgica et Materiala,* Vol. 32, pp. 167-171, 1995.

[40] M. P. Black, "Microstructural evolution of austenite in a microalloyed Fe-30Ni alloy," University of Sheffield , Shefiield , 2002.

[41] E. J. Palmiere, "The Use of Model Systems Based on Fe- 30 wt% Ni for Investigate the Precipitation and Transformation Behaviour of Microalloyed Austenite," in *HSLA Steels 2015, Microalloying 2015 & Offshore Engineering Steels 2015,* 2016.

[42] R. M. Poths, W. M. Rainforth and E. J. Palmiere, "Strain Induced Precipitation in Model and Conventional Microalloyed Steels During Thermomechanical Processing," *Materials Science Forum,* Vols. 500-501, pp. 139-146, 2005.

[43] A. Das, "Revisiting Stacking Fault Energy of Steels," *Metallurgical and Materials Transactions A,* Vol. 47A, pp. 748- 768, 2016.

[44] S. Zaefferer, T. Baudin and R. Penelle, "A Study on the Formation Mechanisms of the Cube Recrystallisation Texture in Cold Rolled Fe- 36% Ni Alloys," *Acta Mater. ,* Vol. 49, pp. 1105-1122, 2001.

[45] Z. Husain, "The kinetics of recovery and recrystallisation of low alloy steels during warm working," European COmmunities , Luxembourg, 1998.

[46] L. Price, J. Sinto, E. Worrell, D. Phylipsen, X. Hu and J. Li, "Energy use and carbon dioxide emissions from steel production in China," 2002.

[47] D. Poddar, P. Cizek, H. Beladi and P. D. Hodgson, "Evolution fo strain-induced precipitates in a model austenitic Fe-30Ni-Nb steel and their effect on the flow behaviour," *Acta Materialia* , Vol. 80, pp. 1-15, 2014.

[48] A. Laasraoui and J. J. Jonas, "Prediction of steel flow stresses at high tempeature and strain rate," *Metallurgical transactions A,* Vol. 22A, p. 1545, 1991.

[49] P. J. Hurley, P. D. Hodgson and B. C. Muddle, "A study of deformation substructures in austenite using a model Ni- 30 wt.% Fe alloy," *Scripta Materialia,* Vol. 45, pp. 25-32, 2001.

[50] H. Beladi, P. Cizek and P. D. Hodgson, "Dynamic recrystallisation of austenite in Ni- 30 Pct Fe- model alloy: microstructure and texture evolution," *Metallurgical and materials transactions A,* Vol. 40A, pp. 1175- 1189, May 2009.

[51] W. Charnock and J. Nutting, "The effect of carbon and nickel upon the stacking- fault energy of iron," *Metal science journal,* Vol. 1, pp. 123-127, 1967.

[52] T. Furu, K. Marthinsen and E. Nes, "Modelling recrystallisation," *Materials Science and Technology* , Vol. 6, p. 1093, 1990.

[53] A. DeArdo, "Processing, Microstructure, and Properties of HSLA Steels," proceedings of an International Symposium on Processing, Microstructure and Properties of HSLA Steels, TMS Ferrous Metallurgy Committee, Warrendale, Pittsburgh, Pa. USA, 1988.

[54] H. P. Stuwe, A. F. Padilha and F. Siciliano, "Competition between recovery and recrystallisation," *Materials Science and Engineering A,* Vol. 333, pp. 361- 367.

[55] E. Nes, "Recovery Revisited," *Acta Metall. Mater.,* Vol. 43, No. 6, pp. 2189- 2207, 1995.

[56] P. R. Rios, H. R. Z. Sandim, "Nucleation and growth during recrystallisation," *Materials Research,* Vol. 8, No. 3, pp. 225-238, 2005.

[57] J. W. Martin and R. D. Doherty, Stability of microstructure in metallic systems, Cambridge: Cambridge University Press, 1976, pp. 7-10.

[58] B. Hutchinson, S. Jonsson and L. Ryde, "On the kinetics of recrystallisation in cold worked metals," *Scripta metallurgica,* Vol. 23, pp. 671- 676, 1989.

[59] F. Haessner, Recrystallisation of Metallic Materials, Stuttgart: Alle Rechie vorbehalten, 1970.

[60] R. K. Ray, W. B. Hutchinson and B. J. Duggan, "A study of the nucleation of recrystallisation using HVEM," *Acta Metallurgica,* Vol. 23, pp. 831-840, 1975.

[61] R. A. Vandermeer, D. J. Jensen and E. Woldt, "Grain boundary mobility during recrystallisation of copper," *Metallurgical and materials transactions A,* Vol. 28A, pp. 749-754, 1997.

[62] C. Capdevila, Y. L. Chen, A. R. Jones and H. K. D. H. Bhadeshia, "Effect of strain heterogeneity on recrystallisation of PM2000," in *Proceedings of the 21st Risø International Symposium on materials science: Recrystallisation- Fundamental Aspects and Relations to Deformation Microstructure,* Roskilde, Denmark, 2000.

[63] X. Song, M. Rettenmayr, C. Muller and H. E. Exner, "Modelling of recrystalllisation after inhomogeneous deformation," *Metallurgical and materials transactions A,* Vol. 32, No. 9, pp. 2199-2206, 2000.

[64] H. Nakamichi, F. J. Humphreys, P. S. Bate and I. Brough, "In- situ EBSD observation of the recrystallizatoin of an IF steel at high temperature," *Materials science forum,* Vol. 550, pp. 441-446, 2007.

[65] R. L. Gall, G. Liao and G. Saindrenan, "In- situ SEM studies of grain boundary migraiton during recrystallisation of cold- rolled nickel," *Scripta Materialia,* Vol. 41, No. 4, pp. 427-432, 1999.

[66] R. A. Vandermeer and D. J. Jensen, "Recrystallisation in hot vs cold deformed commercial aluminium: a microstructure path comparison," *Acta Materialia,* Vol. 51, pp. 3005- 3018, 2003.

[67] R. A. Vandermeer and D. J. Jenson, "On the estimation of cahn-hagel interface migration rates," *Scripta Metallurgica et Mateialia,* Vol. 30, No. 12, pp. 1575-1580, 1994.

[68] B. Dutta and C. M. Sellars, "Effect of composition and process variables on Nb(C,N) precipitation in Nb microalloyed austenite," *Materials science and technology,* Vol. 3, p. 197, 1987.

[69] S. Medina, A. Q. and M. Gomez, "Strain induced precipitation effect on austenite static recrystallisation in microalloyed steels," *Materials science and technology,* Vol. 19, No.1, p. 99- 108, 2003.

[70] C. M. Sellars and J. A. Whiteman, "Recrystallisation and grain growth in hot rolling," *Metal Science,* Vol. 13, No. 3-4, pp. 187-194, 1979.

[71] D. R. Barraclough and C. M. Sellars, "Static recrystallisation and restoration after hot deformation of Type 304 stainless steel," *Metal Science,* Vol. 13, No. 3-4, pp. 257-268, 1979.

[72] S. F. Medina and A. Quispe, "Improved model for static recrystallisation kinetics of hot deformed austenite in low alloy and Nb/ V microalloyed steels," *ISIJ International,* Vol. 41, pp. 774-781, 2001.

[73] P. Saidi, S. Shahandeh and J. J. Hoyt, "Relationship between recrystallisation kinetics and the inhomogeneity of stored energy," *Metallurgical and materials transactions A,* p. 2975, 2015.

[74] L. Backe, "Modelling the microstructural evolution during hot deformation of microalloyed steels," Ph. D. thesis, KTH Royal Institute of Technology, Stockholm, 2009.

[75] R. A. Vandermeer and B. B. Rath, "Microstructural Modeling of Recrystallisation in Deformed Iron Single Crystals," *Metallurgical Transactions A,* Vol. 20, No. 10, pp. 1399-1942, 1989.

[76] L. Llanos, B. Pereda, B. Lopez and J. M. Rodriguez-Ibabe, "Modelling of static recrystallisation behaivor of high manganese austenitic steels with different alloying contents," *ISIJ international,* Vol. 56, No. 6, pp. 1038-1047, 2016.

[77] D. G. Cram, H. S. Zurob, Y. J. M. Brechet and C. R. Hutchinson, "Modelling discontinuous dynamic recrystallisation using a physical based model for nucleation," *Acta Materialia,* Vol. 57, pp. 5218-5228, 2009.

[78] M. K. Rehman, "Modelling the microstructure evolution during hot deformation of microalloyed steels," Ph. D. thesis, McMaster University, 2014.

[79] H. Luo and S. V. D. Zwaag, "An analytical approach to model heterogeneous recrystallisation kinetics taking into account the natural spatial inhomogeneity of deformation," *Metallurgical and materials transactions A*, Vol. 47A, pp. 231- 238, 2016.

[80] M. A. Almojil, "Deformation and recrystallisation in low carbon steels," Manchester Materials Science Centre, Manchester, 2010.

[81] S. Vervynckt, K. Verbeken, B. Lopez and J. Jonas, "Modern HSLA steels and role of non-recrystallisation temperature," *International materials reviews*, Vol. 57, No. 4, p. 187, 2012.

[82] J. Cahn, "The impurity drag effect in grain boundary motion," *Acta Metallurgica*, Vol. 10, No. 9, pp. 789-798, 1962.

[83] H. Zurob, C. R. Hutchinson, Y. Brechet and G. Purdy, " Modeling od austenite grain size distribution in Nb microalloyed steels processed by thin slab casting and direct rolling," *Acta Materialia*, Vol. 50, pp. 3075-3092, 2002.

[84] J. J. Jonas, "High Strength Low Alloy Steels," *Proceedings High Strength Low Alloys Steels* , pp. 80-91, 1984.

[85] S. Yamamoto, C. Ouchi and T. Osuka, "The Effect of Microalloying Elements on the Recovery and Recrystallisation in Deformed Austenite", Thermomechanical Processing of Microalloyed Austenite, Pittsburgh, pp. 613- 639, 1982.

[86] N. Hansen, "New Discoveries in Deformed Metals," *Metallurgical and Materials Transactions A*, Vol. 32A, pp. 2917- 2935, 2001.

[87] C. M. Sellars, "Modelling microstructural development during hot rolling," *Materials science and technology*, Vol. 6, No. 11, pp. 1072-1081, 1990.

[88] A. Abdollah-Zadeh, "The Investigation Of Deformation, Recovery, Recrystallisation And Precipitation In Austenitic HSLA Steel Analogue Alloys," University of Wollongong, 1996.

[89] P. Cizek, F. Bai, E. J. Palmiere and W. M. Rainforth, "EBSD Study of the Orientation Dependence of Substructure Characteristics In a Model Fe-

30wt% Ni Alloy Subjected to Hot Deformation," *Journal of Microscopy*, Vol. 217, pp. 138- 151, 2005.

[90] M. K. M. Kaonda, "Prediction of the Recrystallised Grain Size Distribution after Deformation for the Nb Free and Nb Model Steel," PhD thesis, Birmingham, 2016.

[91] S. S. Hansen, G. B. V. Sande and M. Cohen, "Nionium carbonitride precipitation and austenite recrystallisation in hot- rolled microalloyed steels," *Metallurgical transactions A,* Vol. 11A, p. 387, 1980.

[92] D. A. Hughes and N. Hansen, "A comparison of the Evolution of Cold And Hot Deformation Microstructures and Textures in FCC Metals," in *Advances in Hot Deformation Textures and Microstructures*, Pittsburgh, 1993.

[93] A. S. Taylor, P. Cizek and P. D. Hodgson, "Orientation Dependence of the Substructure Characterisitics in a Ni- 30Fe Austenitic Model Alloy Deformed in Hot Plane Strain Compression," *Acta Materialia* , Vol. 60, pp. 1548- 1569, 2012.

[94] V. Randle, N. Hansen and D. J. Jensen, "The Deformation Behaviour of Grain Boundary Regions in Polycrystalline Aluminium," *Philophical Magazine A,* Vol. 73, No. 2, pp. 265-282, 1996.

[95] Y. Adachi, T. Tomida and S. Hinotani, "Dislocation Substructures in Hot-deformed Ni- based Alloys: Simulation for Structure Evolution of Hot-worked Austenite in Low Carbon Steels," *ISIJ International,* Vol. 40, pp. S194- S198, 2000.

[96] X. Wang, E. Brunger and G. Gottstein, "Microstructure characterization and dynamic recrystallisation in an Alloy 800H," *Materials Science and Engineering,* Vol. A290, pp. 180- 185, 2000.

[97] P. Cizek, J. A. Whiteman, W. M. Rainforth and J. H. Beynon, "EBSD and TEM investigation of the hot deformation substructure characteristics of a type 316L austenitic stainless steel," *Journal of Microscopy,* Vol. 213, pp. 285- 295, 2004.

[98] Q. Liu, D. J. Jensen and N. Hansen, "Effect of Grain Orientation on Deformation Structure in Cold- rolled Polycrystalline Aluminum," *Acta Mater.*, Vol. 46, No. 16, pp. 5819- 5838, 1998.

[99] X. Huang and G. Winther, "Dislocation structures. Part I. Grain orientation dependence," *Philosophical Magazine,* Vol. 87, No. 33, pp. 5189- 5214, 2007.

[100] B. Bay, N. Hansen, D. A. Hughes and D. K.-. Wilsdorf, "Evolution of FCC Deformation Structures in Polyslip," *Acta Metall. Mater.,* Vol. 40, No. 2, pp. 205- 219, 1992.

[101] G. Wu and D. J. Jensen, "Recrystallisation kinetics of aluminium AA1200 cold rolled to true strain of 2," *Materials Science and Technology,* Vol. 21, No. 12, pp. 1407- 1411, 2005.

[102] S. Kolupaeva and M. Semenov, "The stored energy of plastic deformation in crystals of face-centered cubic metals," *Materials Science and Engineering,* Vol. 71, No. 71, pp. 1- 6.

[103] H. J. McQueen, "Substructures in Aluminum from Dynamic and Static Recovery," *Czech. J. Phys. B,* Vol. 38, pp. 359- 372, 1988.

[104] K. Mukunthan and E. B. Hawbolt, "Modeling Recovery and Recrystallisation Kinetics in Cold- Rolled Ti- Nb Stablized Interstitial-Free Steel," *Metallurgical and Materials Transactions A,* Vol. 27A, pp. 3410- 3423, 1996.

[105] M. F. Abbod, P. Cizek and D. A. Linkens, "Modeling the Flow Behavior, Recrystallisation, and Crystallographic Texture in Hot-Deformed Fe-30 Wt Pct Ni Austenite," *Metallurgical and Materials Transactions A,* Vol. 38A, pp. 2400- 2409, 2007.

[106] M. Ji, "The Validity of Stress Relaxation Method on Characterising the Recrystallisation Behaviour of Nb- Microalloyed Steels," University of Birmingham, Project report, 2013.

[107] P. H. Shipway and H. K. D. H. Bhadeshia, "Mechanical Stablisation of bainite," *Materials Science and Technology,* Vol. 11, No. 11, pp. 1116-1128, 1995.

[108] C. Watson, "Modelling high integrity steel forgings for turbine applications in the power generation industry," The University of Birmingham, PhD thesis, 2015.

[109] Y. Li, E. Onodera and A. Chiba, "Friction coefficient in Hot Compression of Cylindrical Sample," *Materials Transactions,* vol. 51, no. 7, pp. 1210-1215, 2010.

[110] E. A. Brandes and G. B. Brook, Smithells Metals Reference Book, 7th ed., Oxford: Reed Educational and Professional Publishing, 1992, pp. 25-5.

[111] P. C. Maxwell, A. Goldberg and J. C. Shyne, "Stress- Assited and Strain-Induced Martensites in Fe- Ni- C Alloys," *Metallurgical Transactions* , Vol. 5, pp. 1305- 1318, 1974.

[112] G. Li, T. M. Maccagno, D. Q. Bai and J. J. Jonas, "Effect of initial grain size on the static recrystallisation kinetics of Nb microalloyed steels," *ISIJ International* , Vol. 36, pp. 1479-1485, 1996.

[113] P. D. Hodgson and R. K. Gibbs, "A mathematical model to predict the mechanical properties of hot rolled C-Mn and microalloyed steels," *ISIJ International* , Vol. 32, No. 12, pp. 1329-1338, 1992.

[114] Y. Lu, D. A. Molodov and G. Gottstein, "Recrystallisation Kinetics and Microstructure Evolution During Annealing of a Cold- rolled Fe-Mn-C Alloy," *Acta Materialia,* Vol. 59, pp. 3229- 3243, 2011.

[115] V. Torabinejad, A. Z.-. Hanzaki and S. Moemeni, "An Analysis to the Kinetics of Austenite Recrystallisation in Fe-30Mn-5Al Steel," *Materials and Manufacturing Processes,* Vol. 28, No. 1, pp. 36- 41, 2013.

[116] N. Tsuji, H. Takebayashi, T. Takiguchi, K. Tsuzaki and T. Maki, "Recrystallisation of Solidified Columnar Crystals In an Fe- 36%Ni Austenitic Alloy," *Acta Metall. Mater.*, Vol. 43, No. 2, pp. 755- 768, 1995.

[117] M. Strangwood, "Microstructure from processing: evaluation and modelling grain size control: Lecture 3," School of Metallurgy and Materials, University of Birmingham, Birmingham, 2015.

[118] I. Shon, S. Lee, Y. Seo, Y. Lee, Y. Jeong and C. Choi, " Effect of Initial Structure on Recrystallized Austenite Grain Size of Fe-32%Ni Alloy," *Materials Science Forum,* Vols. 475- 479, pp. 175- 178, 2005.

[119] P. Urganda, A. I. Fernandez, B. Lopez and J. M. Rodriguez- Ibabe, "Modeling of austenite grain size distribution in Nb microalloyed steels processed by thin slab casting and direct rolling (TSDR)," *ISIJ international,* Vol. 44, No. 8, pp. 1416- 1425, 2004.

[120] S. F. Medina, A. Quispe and m. Gomez, "Model for strain- induced precipitation kinetics in microalloyed steels," *Metallurgical and Materials Transactions A,* Vol. 45A, p. 1524, 2014.

[121] M. J. Jones and F. J. Humphreys, "Interaction of recrystallisation and precipitation: The effect of Al3Sc on the recrystallisation behaviour of deformed aluminium," *Acta materialia,* Vol. 51, pp. 2149- 2159, 2003.

[122] W. Yang, D. Yan and L. Rong, "The separation of recrystallisation and precipitation processes in a cold-rolled Al–Mg–Sc solid solution," *Scripta Materialia ,* Vol. 68 , p. 587–590, 2013.

[123] B. Dutta and E. J. Palmiere, "Effect of prestrain and deformation temperature on the recrystallisation behavior of steels microalloyed with Niobium," *Metallurgical and materials transactions A,* Vol. 34A, p. 1237, June 2003.

[124] B. Dutta, E. J. Palmiere and C. M. Sellars, "Modelling the kinetics of strain induced precipitation in Nb microalloyed steels," *Acta Mater.,* Vol. 49, pp. 785-794, 2001.

[125] N. Ryum, "Precipitation and Recrystallisation in an Al- 0.5 wt.% Zr-alloy," *Acta Metallurgica,* Vol. 17, pp. 269- 278, 1969.

[126] K. Huang, R. E. Loge and K. Marthinsen, "On the sluggish recrystallisation of a cold-rolled Al–Mn–Fe–Si alloy," *J Mater Sci ,* Vol. 51, p. 1632–1643, 2016.

[127] H. Zurob, C. Hutchinson, Y. Brechet and G. Purdy, "Rationalization of the softening and recrystallisation behaviour of microalloyed austenite using mechanism maps," *Materials Science and Engineering A,* Vol. 382, pp. 64-81, 2004.

[128] H. Yen, M. Huang, C. Scott and J. Yang, "Interactions between deformation-induced defects and carbides in a vanadium-containing TWIP steel," *Scripta Materialia ,* Vol. 66, pp. 1018- 1023, 2012.

[129] D. J. Powell, R. Pilkington and D. A. Miller, "The Precipitation Characteristics of 20 % Cr/ 25% Ni- Nb Stabilised Stainless Steel," *Acta Metall.,* Vol. 36, No. 3, pp. 713- 724, 1988.

[130] I. Weiss and J. J. Jonas, "Dynamic precipitation and coarsening of Niobium carbonitride during the hot compression of HSLA steels," *Metallurgical transactions A,* Vol. 11A, p. 403, 1980.

[131] R. M. Poths, W. Rainforth and E. J. Palmiere, "Investigating precipitation in microalloyed austenite during thermomechanical processing," *Materials science forum* , Vols. 426-432, pp. 1255-1260, 2003.

[132] I. B. Haroe, A. Rosen and I. W. Hall, "Evolution of Microstructure of AISI 347 Stainless Steel During Heat Treatment," *Materials Science and Technology,* Vol. 9, No. 7, pp. 620- 626, 1993.

[133] A. T. Davenport, L. C. Brossard and R. E. Miner, "Precipitation in microalloyed high- strength low- alloy steels," *Journal of metals,* Vol. 27, No. 6, pp. 21-27, 1975.

[134] W. C. Liu, Z. L. Chen and M. Yao, "Effect of Cold Rolling on the Precipitation Behavior of Sigma Phase in INCONEL 718," *Metallurgical and Materials Transactions A,* Vol. 30A, pp. 31- 40, 1999.

[135] A. LeBon, J. R. Vernis and C. Rossard, "Recrystallisation and precipitaion during hot working of a Nb- Bearing HSLA steel," *Metal science,* Vol. 9, p. 36, 1975.

[136] M. J. Luton, R. Dorvel and R. A. Petkovic, "Interaction between deformation, recrystallisation and precipitation in niobium steels," *Metallurgical Transactions A,* Vol. 11 A, pp. 411-420, 1980.

[137] G. R. Love, "Dislocation pipe diffusion," *Acta Metallurgica* , Vol. 12, pp. 731- 737, June 1964.

[138] E. J. Palmiere and B. Dutta, "Strain induced precipitation of Nb(CN) in low carbon steels: modelling and experiment validation," *Materials Science forum,* Vols. 426-432, pp. 1237-1242, 2003.

[139] A. R. Jones, P. R. Howell and B. Ralph, "The precipitation of niobium carbide at grain boundaries in an austenitic stainless steel," *Journal of Materials Science,* Vol. 11, No. 9, pp. 1593- 1599, 1976.

[140] E. J. Palmiere, C. I. Garcia and A. J. DeArdo, "Compositional and Microstructural Changes Which Attend Reheating and Grain Coarsening in Steels Containing Niobium," *Metallurgicia and Materials Transactions A,* Vol. 25A, pp. 277- 286, 1994.

[141] R. C. Sharma, V. K. Lakshmanan and J. S. Kirkaldy, "Solubility of Niobium Carbide and Niobium Carbonitride in Alloyed Austenite and Ferrite," *Metallurgical Transactions A*, pp. 545-553, 1984.

[142] M. G. Akben, I. Weiss and J. .. Jonas, "Dynamic Precipitation and Solute Hardening In a V Microalloyed Steel and Two Nb Steels Containing High Levels of Mn," *Acta Metallurgica*, Vol. 29, pp. 111- 121, 1980.

[143] J. K. Irvine, B. F. Pickering and T. Gladman, "Grain refined C- Mn steels," *J. Iron steel inst*, Vol. 205, No. 2, pp. 161-182, 1967.

[144] K. Narita, "Physical Chemistry of the Groups IVa (Ti, Zr), Va (V, Nb, Ta) and the Rare Earth Elements in Steel," *ISIJ International*, Vol. 15, p. 145, 1975.

[145] R. Smith, "The Solubility of Niobium (Columbium) Carbide in Gamma Iron," *Transactions of the Metallurgical Society of AIME*, Vol. 236, No. 2, p. 220, 1966.

[146] V. Lakshmanan, "Solubility Product for Niobium Carbide in Austenite," *Metall. Trans.*, Vol. 15A, No. 3, p. 545, 1984.

[147] V. Nagarajan, E. J. Palmiere and C. M. Sellars, "New approach for modelling strain induced precipitation of Nb(C,N) in HSLA steels during multipass hot deformation in austenite," *Materials Science and Technology*, Vol. 25, No. 9, pp. 1168- 1174, 2009.

[148] B. Dutta, E. Valdes and C. M. Sellars, "Mechanism and kinetics of strain induced precipitation of Nb(C,N) in austenite," *Acta metall. mater.*, pp. 653-662, 1992.

[149] S. Okaguchi and T. Hashimoto, "Computer model for predictoin of carbonitride precipitation during hot working in Nb- Ti bearing HSLA steels," *ISIJ International*, Vol. 32, No. 3, pp. 283- 290, 1992.

[150] N. Fujita, "Modelling carbide precipitation in alloy steels," University of Cambridge, Cambridge, 2000.

[151] Y. J. Wang and H. S. Zurob, "The precipitation of NbC on dislocation in austenite," *Applied physics A Materials science and processing*, Vol. 74, pp. 1213-1215, 2002.

[152] N. Stanford and D. P. Dunne, "Effect of NbC and TiC Precipitation on Shape Memory in an Iron- Based Alloy," *J. Mater. Sci.,* Vol. 41, pp. 4883-4891, 2006.

[153] K. B. Kang, O. Kwon, W. B. Lee and C. G. Park, "Effect of precipitation on the recrystallisation behaviour of a Nb containing steel," *Scripta Materialia* , Vol. 36, pp. 1303-1308, 1997.

[154] O. Kwon and A. J. DeArdo, "Interaction between recrystallisation and precipitation in hot- deformed microalloyed steels," Backe pp. 529-538, 1991.

[155] A. R. Jones, P. R. Howell and B. Ralph, "Quantitative Aspects of Precipitation at Grain Boundaries In an Austenitic Stainless Steel," *Journal of Materials Science,* Vol. 11, pp. 1600- 1606, 1976.

[156] Y. J. Wang and H. S. Zurob, "The precipitation of NbC on dislocation in austenite," *Applied Physics A,* Vol. 74, pp. 1213-1215, 2002.

[157] E. Pereloma, B. Crawford and P. Hodgson, "Strain-induced precipitation behaviour in hot rolled strip steel," *Materials Science and Engineering A,* Vol. 299, p. 27, 2001.

[158] J. Takahashi, K. Kawakam, J. Hamada and K. Kimura, "Direct observation of niobium segregation to dislocations in steel," *Acta Materialia,* Vol. 107, pp. 415- 422, 2016.

[159] A. Kisko, J. Talonen, D. A. Porter and L. P. Karjalainen, "Effect of Nb Microalloying on Reversion and Grain Growth in a High-Mn 204Cu Austenitic Stainless Steel," *ISIJ International* , Vol. 55, No. 10, pp. 2217-2224, 2015.

[160] S. Vervynckt, K. Verbeken, P. Thibaux and Y. Houbaert, "Recrystallisation–precipitation interaction during austenite hot deformation of a Nb microalloyed steel," *Materials Science and Engineering A,* Vol. 528, pp. 5519-5528, 2011.

[161] J. Herman, B. Donnay and V. Leroy, "Precipitation kinetics of microalloyed additions during hot- rolling of HSLA steels," *ISIJ International* , Vol. 32, No. 6, p. 779, 1992.

[162] S. Medina, "From heterogeneous to homogeneous nucleation for precipitation in austenite of microalloyed steels," *Acta Materialia,* Vol. 84, pp. 202-207, 2015.

[163] C. Ouchi, T. Sampei and I. Kozasu, "The effect of hot rolling condition and chemical composition on the onset temperature of austenite- ferrite transformation after hot rolling," *Transactions ISIJ,* Vol. 22, p. 214, 1982.

[164] W. M. Rainforth, M. P. Black, R. L. Higginson, E. J. Palmiere, C. M. Sellars, I. Prabst, P. Warbichler and F. Hofer, "Precipitation of NbC in a model austenitic steel," *Acta Materialia ,* Vol. 50, pp. 735-747, 2002.

[165] F. Shi, X. Li, Y. Qi and C. Liu, "Aging Precipitation and Recrystallisation Behavior After Cold Compression By 10% in High- Nitrogen Austenitic Stainless Steel," in *The 8th Pacific Rim International Congress on Advanced Materials and Processing*, Hawaii, 2013.

[166] W. F. Smith, Structure and properties of Engineering alloys, New york: McGraw- Hill, 1993.

[167] T. F. Majka, D. K. Matlock and G. Krauss, "Development of microstructural banding in low- alloy steel with simulated Mn segregation," *metallurgical and materials transaction A,* Vol. 33A, p. 1627, 2002.

[168] L. J. Cuddy, "Microstructure developed during thermomechanical treatment of HSLA steels," *Metallurgical Transactions A,* Vol. 12A, p. 1313, 1981.

[169] A. F. Smith and R. Hales, "Diffusion of manganese in Type 316 austenitic stainless steel," *metal science,* Vol. 9, No. 1, pp. 181-184, 1975.

[170] M. H. Loretto and A. J. White, "The influence of grain size on the energy stored in deformed copper," *Acta Metallurgicda,* Vol. 9, pp. 512-513, 1961.

[171] P. M. Kelly, A. Jostsons, R. G. Blake and J. G. Napier, "The determination of foil thickness by scanning transmission electron microscopy," *Phys. stat. sol. ,* Vol. 31, p. 771, 1975.

[172] D. B. William and C. B. Carter, Transmission electron microscopy, Spring- Verlag US, 2009.

[173] S. M. Allen and F. L. Hall, "Foil thickness measurements from covergent-beam diffraction patterns," *Philosophical magazine A,* Vol. 46, No. 2, pp. 243- 253, 1982.

[174] M. F. Ashby and D. R. H. Jones, Engineering Materials, Pergamon Press, 1980.

[175] H. M. Ledbetter and R. P. Reed, "Elastic Properties of Metals and Alloys, 1. Iron, Nickel and Iron- Nickel Alloys," *J. Phys. Chem. Ref. Data,* Vol. 2, No. 3, p. 531, 1973.

[176] Y. Tanji, Y. Shirakawa and H. Moriya, "Young's modulus, shear modulus and compressibility of Fe- Ni (fcc) alloys," Research Institute for Iron, Steel and Other Metals, 1970.

[177] C. Donadille, R. Valle, P. Dervin and R. Penelle, "Development of Texture and Microstruture During Cold- rolling and Annealing of F.C.C Alloys: Example of An Austenitic Stainless Steel," *Acta Metall.,* Vol. 37, No. 6, pp. 1547-1571, 1989.

[178] M. Kaonda, C. Slater, M. Strangwood and C. Davis, "Modelling the recrystallised grain size distribution after deformation," University of Birmingham, Birmingham, 2016.

[179] A. Laasraoui and J. J. Jonas, "Prediction of temperature distribution, flow stress and microstructure during the multipass hot rolling of steel plate and strip," *Transaction of the iron and steel institute of Japan,* Vol. 31, No. 1, pp. 95-105, 1991.

[180] T. Chandra, I. Weiss and J. J. Jonas, "Effect of static recrystallisation on the growth of Nb(CN) in a 0.07 % Nb HSLA steel," *Canadian Metallurgical Quarterly,* Vol. 20, No. 4, pp. 421-428, 1981.

[181] L. Llanos, B. Pereda and B. Lopez, "Interaction between recovery, recrystallisation, and NbC strain- induced preciptation in high- Mn steels," *Metallurgical and materials transaction A,* Vol. 46A, p. 5248, 2015.